Young Researchers' Forum II: Construction Materials

19th February 2014

University College London, London, WC1E 6BT

EXTENDED ABSTRACTS

Editors

R J Mangabhai, Y Bai and C I Goodier

The Institute of Concrete Technology is leading this event
with the support of:

PREFACE

This is the second Young Researchers Forum for early-career scientists and engineers working in the field of construction materials to be held at Department of Civil, Environmental and Geomatic Engineering, University College London, London. The first meeting was organised by the Construction Materials Group, The Society of Chemical Industry in May 2012.

The aims of this joint meeting are:

- To provide an opportunity to speak to a friendly audience of young researchers (research students and those recently appointed in industry).
- To raise the level of contact and communication between people in the early stages of their careers, from both industry and academia.
- To increase each individual's understandings of how skills and facilities are distributed across the country.
- To provide an opportunity to learn more about the organisations hosting the event and their roles in research and industry.

The response to the call for papers for this meeting was excellent, with 42 abstracts received from the Czech Republic, Italy, Kenya, Lebanon, Netherlands, Poland, Spain, UK and USA. We therefore decided to provide the students with Oral and Poster presentations to accommodate the response. The extended abstract demonstrate a strong continued interest and progression in research in the construction industry.

The extended abstracts have been divided in oral and poster presentations in the following themes.

- Timber for Structural Applications
- Use of Waste Materials In Construction
- Materials for Nuclear Waste Immobilisation
- Cement Hydration
- Durability of Structures
- Materials Testing
- Concrete Technology

We wish to thank all the authors for their hard work in preparing their contributions and meeting, tight deadlines that have enabled the production of extended abstracts.

We would like to thank David Ball Group, Grace, Isolearn, Sika and Zwick-Roell for supporting the Young Researcher’s Forum II.

The Institute of Concrete Technology extends its thanks to Construction Materials Group of SCI, The Institute of Materials, Minerals and Mining, The Institute of Asphalt Technology and The Mineralogical Society for supporting the event.

We wish to thank Adrian Blacker (Chairman of Construction Materials Group, SCI) and Dr Mark Tyrer (Chairman of Cementitious Materials Group, The Institute of Materials, Minerals and Mining) for their help, and thank ICT, SCI, IOM^3 and Quartz Scientific for contributions towards the prizes.

Finally to University College London for hosting the event, and Jun Ren and Yanfei Yue for their help in setting up the website and compiling the extended abstracts.

The editors express the wish, on behalf of all authors, that readers find the extended abstracts topical, and useful in their work, also that it stimulates further work on construction materials.

Raman Mangabhai	Chairman of Events & Marketing, Institute of Concrete Technology
	Mangabhai Consulting /Cement and Concrete Science
Dr Yun Bai	Senior Lecturer in Materials, University College London
Dr Chris Goodier	Senior Lecturer, Loughborough University

Feb 2014

SUPPORTING ORGANISATIONS

www.davidballgroup.com

Chris Howard

Chris.Howard@davidballgroup.com

www.grace.com

Graham Moorfield

Graham.Moorfield@grace.com

www.isolearntraing.com

Des O'Connor

isolearn@gmail.com

www.sika.com

Phil Scarlett

scarlett.phil@uk.sika.com

www.zwick.co.uk

Alan Thomas

Alan.Thomas@zwick.co.uk

CONTENTS **Page**

Chairman: Dr Yun Bai, University College London

SESSION 6: MATERIALS TESTING

POSTER PRESENTATIONS

1: TIMBER FOR STRUCTURAL APPLICATIONS

2: USE OF WASTE MATERIALS IN CONSTRUCTION

3: CONCRETE TECHNOLOGY

4: CEMENT HYDRATION

5: DURABILITY OF STRUCTURES

6: MATERIALS TESTING

ORAL PRESENTATIONS

POST-TENSIONING OF TIMBER BEAMS WITH BASALT FIBRE REINFORCED POLYMER

E. McConnell, Dr D. McPolin, Prof S. Taylor
Queens University Belfast
emcconnell10@qub.ac.uk, d.mcpolin@qub.ac.uk, s.e.taylor@qub.ac.uk

ABSTRACT: Development of the structural performance of glulam timber beams by the inclusion of reinforcing materials has the potential to improve service performance and ultimate capacity. In recent years research focusing on the addition of fibre reinforced polymers to strengthen members has yielded positive results. However, the FRP is still a relatively expensive material and its full potential has not been realised. This paper describes a series of four-point bending tests that were conducted to failure on reinforced and post-tensioned glulam timber beams where the reinforcing tendon used was 12 mm diameter BFRP (Basalt Fibre Reinforced Polymer). The research was designed to evaluate the additional benefits of including an active type of reinforcement, by post-tensioning the BFRP tendon, as opposed to the previously discussed passive approach of simple reinforcement.

From the laboratory investigations, it was established that there was a 16% increase in load carrying capacity when the post-tensioned members were compared to those with the passive reinforcement. Furthermore, when members containing the BFRP composite are contrasted against control timber specimen's stiffness is increased, with a 14% reduction of deflection under service loads. Further reductions are evident when the induced precamber is considered, with a net reduction in deflection of 40% on average. Additionally a more favourable ductile failure mode was witnessed compared to the brittle failure of an unreinforced timber beam. The results support the assumption that by initially stressing the embedded FRP tendon the structural benefits experienced by the timber member increase in a number of ways, indicating that there is significant scope for this approach in practical applications.
Keywords: BFRP, Four-point Bending, Glulam, Timber, Post-tension.

INTRODUCTION

Despite the many benefits offered by timber use over other construction materials it remains underused in the industry, 'timber is not widely used for primary structural elements' [1]. The underuse of timber as a structural material may be attributed to the naturally occurring defects within its structure. Undesirable characteristics include the presence of knots and grain defects, susceptibility to the effects of moisture and other time dependent vulnerabilities, such as the occurrence of creep, which will affect the materials structural capabilities.

Recently, extensive research has been completed regarding the reinforcement of timber using both various metals and novel fibre reinforced polymers as an attempt to enhance the timber's strength and stiffness [2-4].

BFRP is a corrosion resistant, composite material particularly suited to use within timber reinforcement as it has a low elastic modulus and therefore the two materials will have high strain compatibility. Additionally it has excellent tensile strength, approximately 2.5 times stronger than steel while also being 3.7 times lighter [5].

Although extensive work reinforcing timber has been previously undertaken, many researchers have concluded that the addition of the expensive FRP reinforcement is similar to the addition of a single timber lamina, making this method ineffective and uneconomical [4&6]. It is therefore arguable that the FRP's utilised in these investigations are not being fully exploited as only a fraction of their structural potential is used. By initially tensioning the material and therefore using active reinforcement a number of advantages may be further realised as, 'prestressing effectively increases flexural strength by introducing an initial compressive stress into the timber fibres that in service are under tension' [7].

RESEARCH OBJECTIVES

This research was initiated to evaluate the feasibility of strengthening timber beams by the addition of a post-tensioned basalt fibred reinforced polymer rods. Throughout the full investigation, a combination of unreinforced and post-tensioned GL28 timber beams, with unbonded and bonded rods, were tested experimentally to determine the structural advantages. This paper discusses the investigation of unreinforced and BFRP reinforced timber sections. Extensive material testing and theoretical investigations examining the various stresses occurring throughout the materials, during the testing process, were undertaken and analysed to allow the creation of a theoretical stress model capable of accurately predicting the behaviour of the system.

EXPERIMENTAL TESTING

Test Variables

The instrumentation and test set-up shown in Figure 1 illustrates the flexural tests conducted on each beam within the series. As timber is a particularly variable material it was crucial to conduct numerous service load tests at each stage of the process to allow direct comparisons to be drawn between the results. To facilitate this each beam was tested in the following way;

1. Timber with 16mm void
2. Timber with 12mm BFRP rod slotted, slack, through the void
3. Timber with 12mm BFRP post-tensioned to 20kN, unbonded
4. Timber with 12mm BFRP post-tensioned to 20kN, bonded

The sets of tests discussed within this paper are;

- 5 No. 45x155x3000mm timber beams, tested both elastically and to failure, (C1-C5)

- 5 No. 45x155x3000mm timber beams reinforced with unbonded post-tensioned 12mm diameter BFRP bar, tested elastically
- 5 No. 45x155x3000mm timber beams reinforced with bonded post-tensioned 12mm diameter BFRP bar, tested both elastically and to failure (B1-B5)

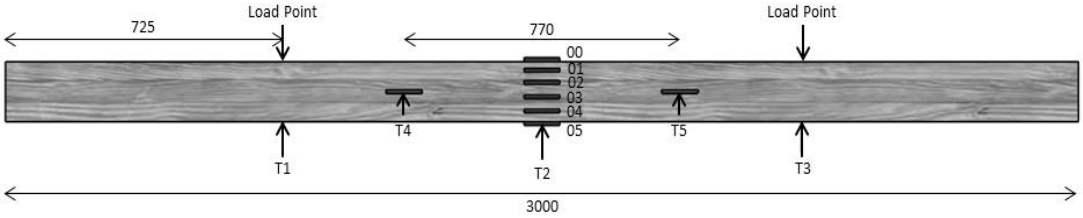

Fig. 1: *Test Instrumentation and Flexural Test Set-up*

Flexural Test Procedure

Beams were tested using the four point bending method in accordance to BS EN 408[8]. The beams were supported on rollers, as was the spreader bar under the loading point. For safety lateral supports were provided to prevent lateral torsional buckling in the beams as they were tested. There was sufficient clearance to ensure they did not alter the behaviour of the test.

For elastic tests, an initial load of 10kN was applied twice as the settlement load in increments of 1kN with data recorded at each interval on all instrumentation. The 10kN load was held for five minutes, unloaded incrementally and all load removed for a further five minutes prior to the second elastic loading test which proceeded in the same manner. The tests to failure were carried out using the same process following the previous elastic tests and subsequently loaded to failure. The response was monitored both through instrumentation, but additionally documented using digital imagery.

Material Testing

Preliminary material tests were completed to test the feasibility and accuracy of the test procedures rather than gain a comprehensive representation of the timber properties, at this stage. Tensile and compressive tests were carried out in accordance with BS EN 408 (2010). Compressive blocks, 45x155x270mm, were crushed parallel to the grain using a Dartec actuator, while 9x12mm tensile dog bones were failed using a Zwick static material testing machine.

RESULTS

Material Testing Results

Table 1 & 2 below show a sample of the material testing results gathered from the compressive and tensile tests. As is true for clear timber, timber with no visible defects such as knots, the tensile and compressive stress values are similar indicating that these results may be representative of the material. However, as timber frequently fails because of the presence of natural defects further material testing is planned to allow both the mean and characteristic values of the structural properties to be calculated. Preliminary theoretical calculations have been completed using the average results listed below as these were significantly higher than the values accordingly to the specific strength class.

Table 1. *Preliminary compressive test results*

Sample No.	Failure Load (kN)	Compressive Stress (N/mm^2)
1	264.94	37.4
2	281.78	39.8
3	247.63	34.9
4	273.41	38.6
5	260.26	36.7
Average	265.60	37.5

Table 2. *Preliminary tensile test results*

Sample No.	Failure Load (kN)	Tensile Stress (N/mm^2)
1	3.65	33.8
2	3.68	34.1
3	3.33	30.8
4	5.02	46.48
5	5.77	53.4
Average	4.29	39.7

Flexural Testing Results

Unreinforced Beams

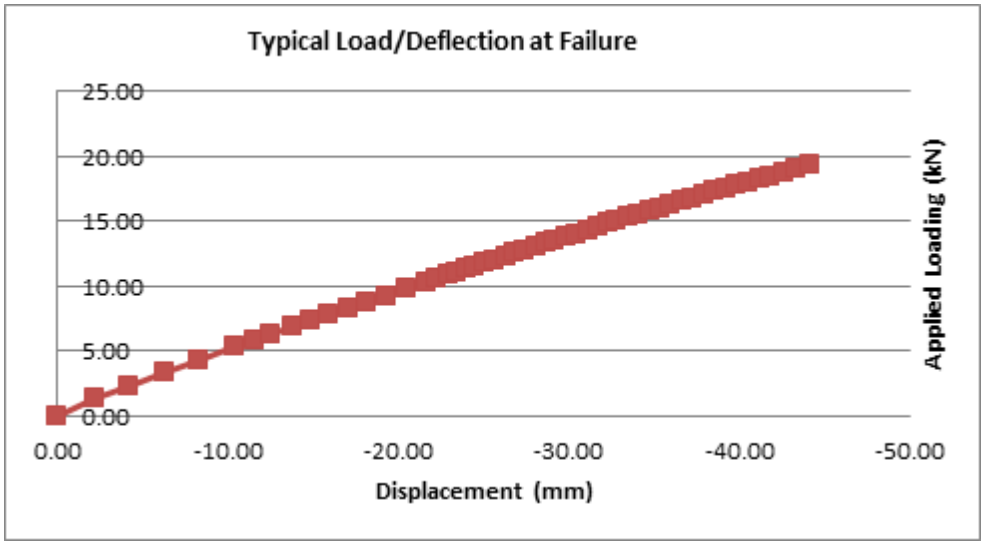

Fig. 2: *Load Deflection of an Unreinforced Timber Beam to Failure*

Figure 2 represents the typical deflection response of an unreinforced timber beam used throughout the experimental programme. As is evident from the figure the typically proportional trend line continues until the failure of the beam indicating that the failure mode was sudden and brittle.

Using a simple beam deflection formula, Equation 1, and by assuming that the four point bending method yields a 10% greater deflection than the application of a

UDL the modulus of elasticity can be calculated for the average unreinforced timber beam tested.

$$\Delta = \frac{1.1\ (5.w.L^3)}{384.E.I} \qquad (1)$$

By using the average results yielded from this series of experiments a value of 9200N/mm^2 is obtained. This value is considerably lower than the expected from a GL28 sample, however it may be used to quickly calculate and compare the relative increase in stiffness, EI, that the post-tensioning process causes.

Post-tensioned Beams

Figure 3 shows the typical load deflection response of a beam at various stages of construction, under service loading. It is initially evident that with the application of post-tensioning, both with the tendon bonded and unbonded, there is an increase in stiffness, particularly evident under the 10kN applied load. From the figure above it can be seen that there is approximately a 4mm reduction, approximately 14%, in service deflection between the solid timber beam and the post-tensioned beam with the BFRP tendon bonded in place at a 10kN applied load. BFRP was chosen for this investigation due to its relatively low modulus of elasticity meaning that it should respond to load in a similar way to the timber.

The figure supports this theory, that there is very little difference in the response between the solid timber beam and the beam with a slack BFRP rod slotted through its length. This further indicates that the increase of stiffness and the resulting advantages, seen throughout these experiments, can be attributed to the post-tensioning process. The graph represents the typical deflection response of the beams under service loading with the precamber induced by the post-tensioning ignored, meaning that there are further benefits offered by the post-tensioning process that initial evident from the figure.

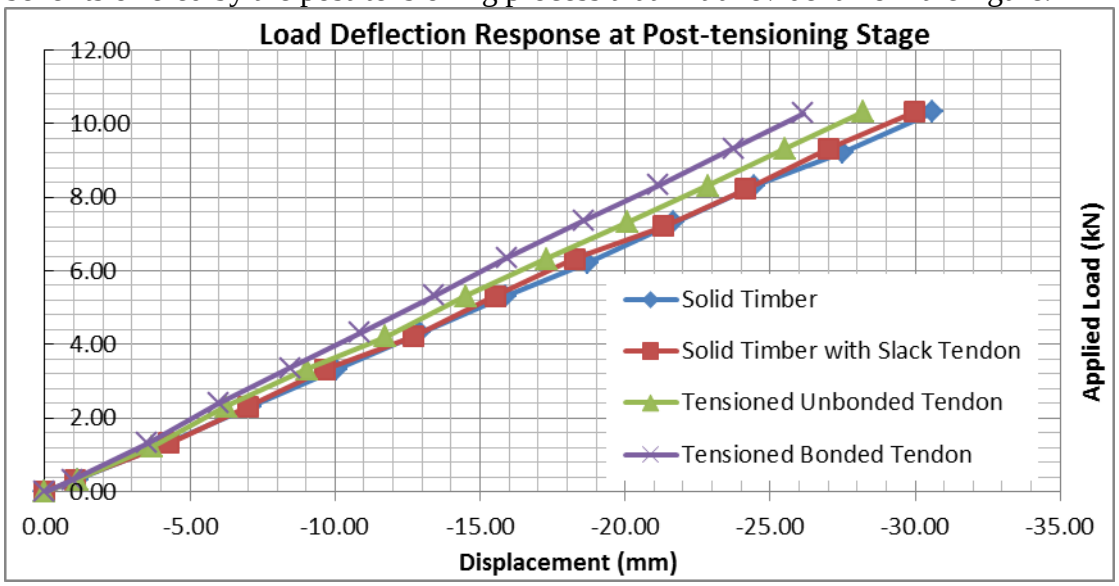

Fig. 3: *Load Deflection Response under Service Loading*

Table 3. *Collapse Load & Predicted Capacity of Unreinforced and Post-tensioned Beams*

Beam No.	Failure Load (kN)	Failure Mode	Predicted Capacity (kN)
C1	16.25	tensile split on soffit	21.10
C2	19.25	tensile split on soffit	
C3	23.75	tensile split on soffit	
C4	22.50	tensile split on soffit	
C5	17.50	tensile split on soffit	
Av. C	19.85		
B1	22.00	tensile split along tendon position	25.97
B2	20.00	tensile cracking near load points	
B3	24.00	tensile split along tendon position	
B4	22.50	knot on soffit opened and split	
B5	26.00	compressive cracking on top under load points	
Av. B	22.90		

Table 3 highlights the difference between the unreinforced timber and the timber post-tensioned to 20kN at the point of failure. Initially considering the failure loads it is evident that there is an increase in capacity when timber is post-tensioned. In this particular series of experiments there is a 16% increase in strength and a reduction in the variability of the materials performance. Although timber is not strictly comparable in this manner, due to the inherent variability of its nature, these results indicate a positive shift in the materials capabilities when post-tensioned using a BFRP tendon.

Additionally the results correspond accurately with the predicted capacity calculated for each experimental investigation. The theoretical process is discussed further in overleaf and although preliminary the results are encouraging.

THEORETICAL PREDICTIONS

The principle and behaviour of linear elastic stress is a well-understood theory commonly used within the concrete industry. As a preliminary investigation the theory has been applied to this process and, as shown in Table 3, has yielded positive results.

The stresses induced by the application of both a post-tensioning force and a load where considered separately, as shown in Figure 4. By using the timbers material properties, compressive and tensile strength, it was possible to calculate the force required to remove the elastic stress reversal caused by the post-tensioning. This then indicated the additional loading that the timber would be able to support following post-tensioning and thus the increase in strength.

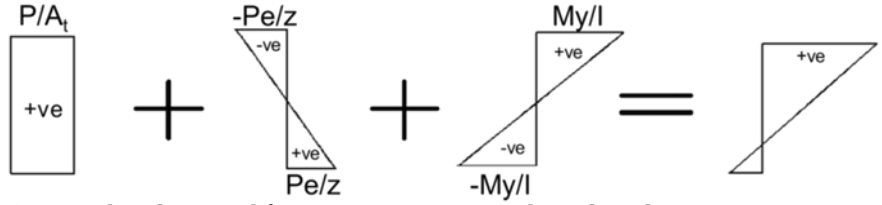

Fig. 4: *Induced Stressed from Post-tensioning and Load Application*

CONCLUSIONS

Although the small number of samples must be considered when evaluating the following conclusions the process of post-tensioning offers a number of advantages when applied to timber. Examining the data set indicated that there was an overall flexural strength gain of 16%. This value corresponded reasonably with the theoretical investigations that have been carried out to date. All beams tested, with the exception of B5, failed in an elastic-type tension failure with splitting occurring near the soffit. This would indicate that further structural improvements may be possible through post-tensioning as it has the potential to encourage a compressive, plastic failure within the timber.

The stiffness results of the various beams tested are positive; the BFRP having a low modulus of elasticity increased the stiffness of the beams under a 10kN applied load by 14% nevertheless. When considering the precamber the advantages increase making post-tensioning a viable and worthwhile process in the attempts to strengthen timber. Furthermore the failure mode of the post-tensioned beams exhibited a more ductile form, due to the presence of the BFRP rod, indicating further benefits that the development of post-tensioned timber would afford the industry.

REFERENCES

[1] Gilfillan, J.R., Gilbert, S.G. & Patrick, G.R.H., The use of FRP composites in enhancing the structural behaviour of timber beams, Journal of Reinforced Plastics and Composites, 22(15):1373-1388. 2003

[2] Patrick, G., The structural performance of FRP reinforced glued laminated beams made from homegrown Sitka spruce, Thesis. Ph.D. (Faculty of Engineering), Queen's University of Belfast. 2004

[3] Plevris, N. and Triantafillou, T. FRP-Reinforced Wood as Structural Material. Journal of Material Civ. Eng., 4(3): 300–317. 1992

[4] Martin, Z.A. Stith, J.K. & Tingley, D.A. Commercialisation of FRP reinforced glulam beam technology. Proceedings of the 6th world conference on timber engineering. Whistler Resort, Canada, UBC Press. 2000.

[5] Information on http://magmatech.co.uk/

[6] Negrao, J. Brunner, M. & Lehmann, M. Pre-stressing of Timber. Bonding of Timber: Core document of the COST Action E34. Vienna: University of Natural Resources and Applied Life Sciences. 2008.

[7] Brady, F. & Harte, A. Prestressed FRP Flexural Strengthening of Softwood Glue-Laminated Timber Beams, 10th World Conference on Timber Engineering (WCTE), 2 - 5 June 2008.

[8] British Standards Institution, 2010. BS EN 408:2010 Timber structures. Structural timber and glued laminated timber. Determination of some physical and mechanical properties: BSI

MECHANICAL CHARACTERIZATION OF ENGINEERED GUADUA-BAMBOO PANELS USING DIGITAL IMAGE CORRELATION

Hector F. Archila
Department of Architecture and Civil Engineering, University of Bath, Bath, UK.
H.F.Archila.Santos@bath.ac.uk

Martin P. Ansell
Department of Mechanical Engineering, University of Bath, Bath, UK.

Pete Walker
Department of Architecture and Civil Engineering, University of Bath, Bath, UK.

ABSTRACT: Engineered panels were manufactured by cross laminating heat and pressure treated strips of *Guadua angustifolia Kunth* (Guadua). Cross laminated Guadua (CLG) panels comprised of three and five layers glued with a high performance epoxy resin. Large specimens of these panels were tested in compression and their elastic mechanical properties evaluated. The digital image correlation (DIC) method was applied to measure strain variations in the X, Y (in-plane) and Z (out of plane) axes on the surface of 600 mm^2 CLG panels. Strain results were analysed using VIC 3D software and used to calculate the elastic values of the panels. Moduli of elasticity (MOE) values from DIC for three and five ply panels were 13.50 GPa and 22.59 GPa in the main direction (E_0) and 5.28 GPa and 12.54 GPa in the transversal direction (E_{90}). While predicted MOE values for three and five ply panels were 21.43 GPa and 19.51 GPa in the main direction (E_0) and 11.83 GPa and 13.75 GPa in the transversal direction (E_{90}). This study is part of a research project that aims to develop standardised industrial structural products from Guadua and to measure and predict their mechanical behaviour.
Keywords: Bamboo, cross laminated panels, digital image correlation, *Guadua angustifolia Kunth*, thermo-hydro-mechanical modification.

INTRODUCTION

Guadua has remarkable eco-credentials when compared to conventional building materials and exceptional advantages when compared to wood forest products. As with other bamboo species, Guadua is a fast growing non-wood forest resource that renews itself; it also has a high yield per hectare and captures and fixes more carbon than most softwood trees [1]. Vogtländer *et al* [2], identified bamboo as one the best renewable resource in terms of yield when used in durable applications. Comparison of the annual yield of Guadua in m^3/ha for products such as MDF is very similar to that of Eucalyptus

and Radiata Pine [2] which makes Guadua a competitive alternative material. Furthermore, bamboos in general have a considerable strength to weight ratio which is comparable to mild steel. Average values of elastic modulus per unit density (specific modulus) of bamboo are very similar to those of steel (25 x 10^6 m^2/s^2) [3]. However, factors such as the bamboo species, its variation in density across and along the culm and anisotropic mechanical properties hinder its use in stiffness-driven applications where steel has been widely used. Engineered bamboo products are scarce and require complex manufacturing processes. For instance, fabrication of laminated Guadua products results on an energy intensive process due to the machining of round culms into rectangular strips that produces high amounts of waste [2, 4]. Therefore, the development of engineered Guadua products needs to exploit its remarkable features, tackle the issues regarding manufacture and improve durability.

Studies on heat treatments applied to bamboo have shown improvements on the mechanical properties and resistance to termites and fungal decay [5, 6]. These studies and primary experimentation with THM treatments showed that temperatures below 160^{o}C had a positive effect on the mechanical properties of Guadua and provided a dimensionally stable flat sheet material with a densified profile [3]. Thus, THM modifications were used as a way of reducing machining and producing durable engineered Guadua panels with improved mechanical properties. The panels were subjected to a testing programme with the aim of characterising their mechanical properties and results from compression tests of large CLG panels were assessed using the DIC method. This paper reports on the development of CLG panels at the University of Bath, manufactured using straightforward densification and assembly methods that could be easily applied industrially.

MANUFACTURE OF THE PANELS

Preparation of the Material

Round culms of Guadua were cut to the required length and its outermost layer was removed using a professional burnisher fitted with a 100 mm x 289 mm x 40 grit Zirconium cloth belt. This highly abrasive belt was used to remove about 100μm of the tough cutinized layer that covers the cortex of Guadua. Subsequently the peeled lengths of cylindrical Guadua were radially cut into six to eight strips (depending on the diameter) and the inner pith cavity membrane was also removed.

The strips were stored under controlled temperature (27^o C ± 2^o C) and relative humidity (70 ± 5 %) in a conditioning room, enabling them to reach equilibrium at 12% moisture content (MC). By following the above mentioned process a reduction of 27% of wasted material was achieved [3].

Densification

Following immersion in water for 24 hours, the strips were subjected to an open thermo-hydro-mechanical (THM) treatment for 20 minutes using a daylight opening hot press with 1000 square mm oil heated platens. Pressure on the hydraulic press was computer controlled using PressMAN software and applied across the radial direction. Maximum pressure, temperature and compression set were fixed to 50 kg/cm^2, 150^{o}C and 45%

respectively. The compression set C is defined as C = (Ro-Rc)/Ro where Ro and Rc are the thickness of the samples before and after compression respectively.

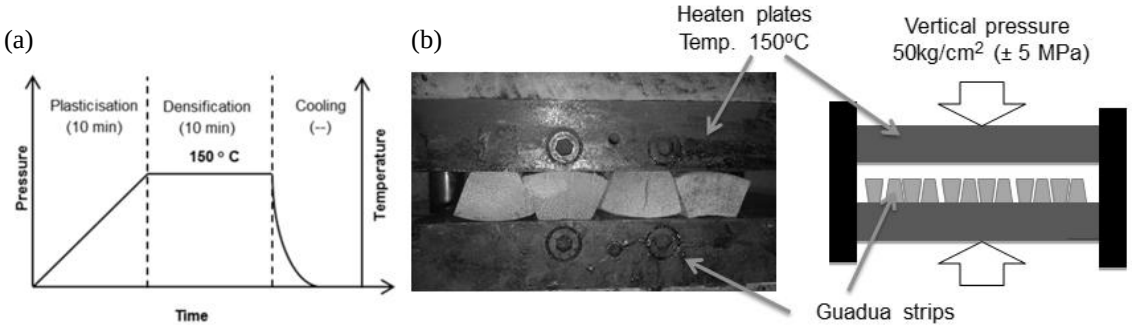

Fig. 1: *(a) THM diagram (b) Image and diagram of the heat and pressure process.*

As can be seen in Figure 1, THM modification occurred in two stages; the first is a plasticisation stage where temperature and pressure on the strips of Guadua is increased for 10 minutes. The second is the densification stage, where maximum pressure and temperature were maintained for 10 minutes. This densification process provided densified flat Guadua strips (FGS) with improved mechanical properties (Table 1), as previously reported on [3]. A slight reduction in the dry weight of the strips was recorded post-THM treatment; however the MC was not markedly affected (-0.5%).

Table 1. *MOE and Poisson's ratio of Guadua strips pre and post THM modification* [3]

	(a) Pre THM (control sample)	**(b) Post THM (FGS)**
Fibre fraction area	25.53 %	47. 78 %
E_L	16.21 GPa ± 0.76	31.04 GPa ± 0.47
E_T	-	2.22 GPa
Density (ρ)	540 kg/m^3	830 kg/m^3
Specific stiffness $_{(L)}$ (average)	29.84 x 10^6 m^2/s^2	37.58 x 10^6 m^2/s^2

Lamination

FGS were used to form the individual plies of three and five layer cross laminated Guadua panels, which were labelled CLG-3, CLG-5 respectively. The plies were glued with a mix of wood epoxy resin (Sicomin SR 5550) and wood gap filler (Wood fill 250), which also increased the viscosity of the mix. The content of resin by total weight of the composite was 4% and the spreading rate was 215 g/m^2. Cold pressure of about 35 kg/cm^2 was applied to the panels until the resin was set (Figure 2b) and then left to cure in a conditioning room for about 20 days before machining.

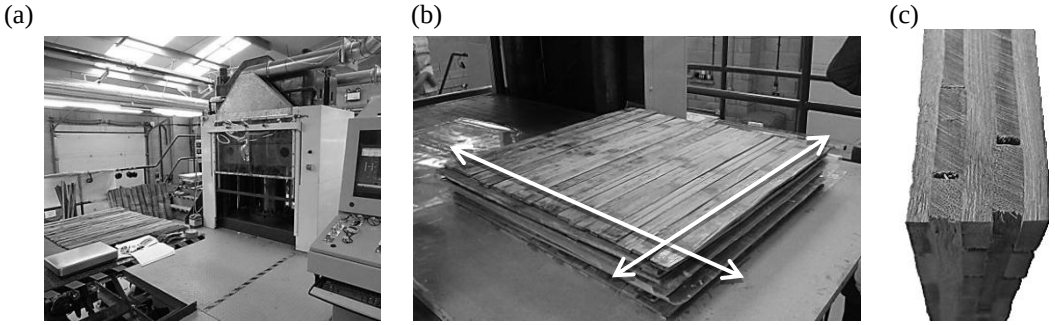

Fig. 2: *a) PressMAN hot press b)Lamination of the CLG panel c)Cross section of a CLG-5 panel.*

The symmetrical composition of the laminate was determined by the odd number of layers (three and five) and the lamination of alternating layers with regular thicknesses (5.5±0.3) at 0^o and 90^o. For structural analysis the manufactured CLG-3 and CLG-5 panels are considered as shell elements under plane stress conditions and their orthotropic elastic properties need to be evaluated (MOE, shear modulus and Poisson's ratio).

The longitudinal orientation of the CLG panels corresponds to its load bearing direction and is defined by the orientation of Guadua fibres in the outer layers (Figure 3a). This also represents the highest number of layers orientated in X_1 and a ratio of 2 to 3 for CLG-3 and 3 to 5 for CLG-5.

EXPERIMENTS AND ANALYSIS

Compression test

CLG-3 and CLG-5 panels of 600 mm x 600 mm were tested in compression in the X_1 (longitudinal) and X_3 (transversal) directions as illustrated in Figure 3. The panels were tested according to the BS EN 789:2004 [7] standard for structural timber elements. Compression tests of the panels were carried out in a 200 kN Mayes universal test machine (Figure 4a) at a rate of 0.5 mm/min. Ten loading series below the elastic limit were undertaken per panel and special test fixtures were used to anchor the panels to the test machine.

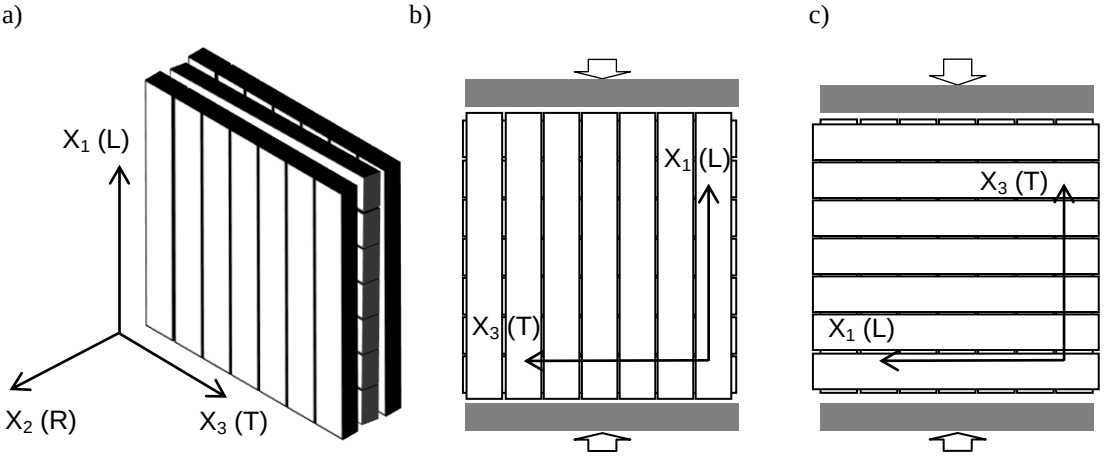

Fig. 3: *a) Geometric (X_1, X_2, X_3) and orthotropic (L, R, T) axis of the CLG panel b) Diagram of the compression test on the longitudinal direction of the panel c) Diagram of the compression test on the transversal direction of the panel.*

Digital Image Correlation Method

During mechanical testing, two monochrome high speed cameras (Fast Cam SA3) recorded simultaneous images of a speckle pattern painted on the surface of the panel at a rate of one frame per second (Figure 4). These sets of paired images were analysed using VIC3D-2009 software and 3D strain maps were produced (Figure 4b and 4c). A virtual extensometer (A-B) was placed on the face of the panel with the speckle pattern and the axial strain variations per image were recorded. Figures 4b and 4c illustrate the area analysed and the location of the extensometer.

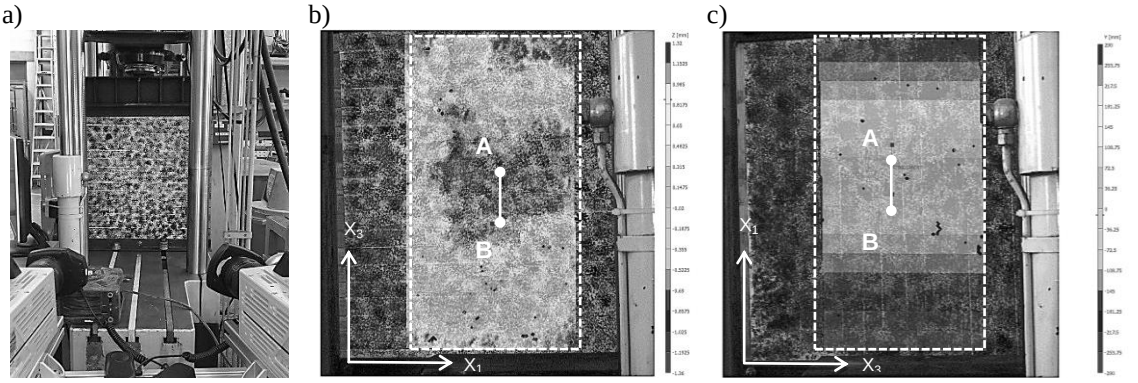

Fig. 4: *a) Panel mounted on the test machine b) Strain map in X_2 (z)of a CLG tested on the transversal axis c) in z of a transversal CLG Typical strain-stress graph of the compression test carried on CLG panels*

Determination of MOE

Strain values from the DIC method were used to calculate the MOE of CLG-3 and CLG-5 panels in the longitudinal (E_0) and transversal direction (E_{90}). Typical stress-strain response obtained from the compression test of three and five layers CLG panels was plotted and a linear regression analysis performed (Figure 5). The longest portion of the graph with a correlation coefficient $\geqslant 0.60$ was used to determine MOE.

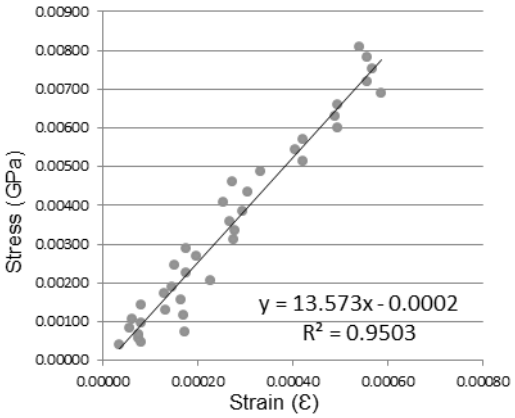

Table 2. *MOE results*

	MOE Predicted values	**MOE Test values**	**Correlat. Coeff. (R^2)**
$E_{0,\ CLG\text{-}3}$	21.43 Gpa	13.50 GPa	0.94
$E_{90,\ CLG\text{-}3}$	11.83 GPa	5.28 GPa	0.84
$E_{0,\ CLG\text{-}5}$	19.51 GPa	22.59 GPa	0.95
$E_{90,\ CLG\text{-}5}$	13.75 GPa	12.54 GPa	0.63

Fig. 5: *Typical strain-stress graph for CLG-5 panels tested in the longitudinal direction.*

Results for E_0 and E_{90} from the compression test of CLG-3 and CLG-5 panels are presented in Table 2 together with predicted values using data from previous tests reported in [3]. E_0 and E_{90} values depend on the number of layers and the stiffness's of the individual layers (E_L and E_T).

Predicted MOE values were generally higher than the MOE values obtained through the DIC method. CLG-3 and CLG-5 panels longitudinally oriented presented a load capacity between 1.5 and 2.5 times their transversal orientation in both predicted and test results. No permanent deformation (post-test) in any axis was recorded by the DIC; however, 3D strain maps showed areas prone to deformation in the X_2 (R) direction that presented gaps or fabrication defects.

CONCLUSIONS

Flat cross-laminated Guadua (CLG) panels for use in construction were manufactured using a simplified process that reduced the wastage produced during conventional lamination processing by 27%.

The elastic mechanical properties of engineered bamboo panels were characterised using digital techniques and compared to predicted values using data from previous tests [3]. Similar MOE values ($E_{0,5ply}$ = 14 GPa) have been reported by [8] for cross laminated bamboo products using different techniques. However, validation of the obtained results will require further testing using physical strain measurement systems. DIC methods allowed for a qualitative assessment of the structural behaviour of the panels but difficulties were encountered on the quantitative analysis of their mechanical properties.

ACKNOWLEDGEMENT

The first author is grateful to AMPHIBIA GROUP LTD and COLCIENCIAS, sponsors of his studies at the University of Bath, UK.

REFERENCES

[1] Lou, Y. Li, Y. Buckingham, K. Giles, H. Zhou G. *Bamboo and Climate Change Mitigation Bamboo: a comparative analysis of carbon sequestration.* INBAR Technical Report No. 32. Beijing, 2010.

[2] Vogtländer J, van der Lugt P, Brezet H. *The sustainability of bamboo products for local and Western European applications.* LCAs and land-use. J. Clean. Prod. Elsevier Ltd; 2010 (September) 18(13):1260–9.

[3] Archila-Santos, H., Ansell, M., Walker, P. *Elastic properties of thermo-hydro-mechanically modified bamboo (Guadua angustifolia Kunth) measured in tension.* Accepted to Key Engineering Materials, 2013.

[4] Flander K, Rovers R. *One laminated bamboo-frame house per hectare per year.* Constr. Build. Mater. 2009 (January) 23(1):210–8.

[5] Zhang YM, Yu YL, Yu WJ. *Effect of thermal treatment on the physical and mechanical properties of phyllostachys pubescen bamboo.* Eur. J. Wood Prod., 2012 (November) 71(1):61–7.

[6] Manalo RD, Garcia CM. *Termite Resistance of Thermally-Modified Dendrocalamus asper (Schultes f.) Backer ex Heyne.* Insects. 2012 (March) 3(4):390–5.

[7] British Standards Institution. *Timber structures. Test methods. Determination of mechanical properties of wood based panels.* BS EN 789:2004. BSI, London, 2004.

[8] Verma CS, Chariar VM. *Development of layered laminate bamboo composite and their mechanical properties.* Compos. Part B Eng. Elsevier Ltd; 2012 (April) 43(3):1063–9.

EFFECT OF CALCINING ON THE PROPERTIES OF CERAMICS PRODUCED FROM FINE INCINERATOR BOTTOM ASH

Athanasios Bourtsalas, Sue Grimes and Chris Cheeseman
Department of Civil and Environmental Engineering, Imperial College London, South Kensington Campus, London, SW7 2AZ, UK

Luc Vandepperre
Department of Materials, Imperial College London, South Kensington Campus, London, SW7 2AZ, UK

Nickolas Themelis
Earth Engineering Centre, Columbia University, New York, NY 10027, USA

ABSTRACT: Incinerator bottom ash (IBA) is normally processed to extract ferrous and non-ferrous metals with the coarse mineral fraction used to produce secondary aggregate. This processing also produces significant volumes of fine IBA particles, typically less than 4 mm, which are problematic because reuse options for this material are limited. Fine IBA particles can be transformed milling and calcining into a raw material suitable for the production of ceramics that exhibit low shrinkage during firing. The processing involves the addition of glass to aid liquid phase sintering, milling to reduce the particle size and increase reactivity and calcining to limit volatile loss and control shrinkage during firing. Calcining changes the crystalline phases present in fine IBA from predominantly quartz (SiO_2), calcite ($CaCO_3$) gehlenite ($Ca_2Al_2SiO_7$) and hematite (Fe_2O_3) to diopside ($CaMgSi_2O_6$), clinoestatite ($MgSiO_3$) and andradite ($Ca_3Fe_2Si_3O_{12}$). Pressed calcined powders exhibit low shrinkage (<5%) during sintering and produce dense (2.78 g/cm^3), hard ceramics that exhibit negligible water absorption when fired at 1080 °C. The research demonstrates the potential for transforming the problematic fraction of fine IBA particles into a raw material suitable for the manufacture of ceramics such as tiles, with potential for use in urban applications.
Keywords: Incinerator bottom ash, energy from waste, resource efficiency, circular economy, sintering, ceramics.

INTRODUCTION

There are currently 454 energy from waste (EfW) plants operating in Europe, the vast majority of which combust residual waste. The combustion process produces incinerator

bottom ash (IBA) that is normally quenched on exiting the combustion chamber. After ageing and weathering IBA forms a loosely agglomerated granular material. Typically 250-320 kg of IBA is produced per tonne of input residual waste to an EfW plant. IBA processing typically uses standard drum or flat screen decks with different mesh sizes to sort size fractions, with further metal recovery using magnetic and eddy current separators. The metals extracted have significant value and the mineral fraction greater than 4 mm is extensively used as secondary recycled aggregate. IBA also contains approximately 45 wt. % of fine particles significantly less than 4mm in diameter, which are not ideal for use as aggregate. There are currently limited alternative beneficial reuse options for this material which is typically either blended into IBA aggregate or disposed of to landfill neither of which is ideal.

Previous research has used IBA for the production of ceramics and glass-ceramics. Ceramic manufacturing typically involves sintering compacted powder samples. In the glass-ceramic process raw materials are melted to form a glass at relatively high temperatures and this is followed by subsequent heat treatment at lower temperatures to promote crystallisation effects. An advantage of these processes is that they encapsulate heavy metals in the ceramic or glass-ceramic formed so that metal leaching is limited (Rawlings et al., 2010).

This research has investigated the potential for transforming the fine (<4 mm) fraction of IBA into a raw material suitable for the production of sintered ceramic tiles, that exhibit high density and hardness and low shrinkage during firing.

EXPERIMENTAL

Characterisation of the fine IBA fraction

A representative 50 kg batch of <4 mm processed IBA was obtained from a major supplier of secondary IBA aggregate in SE England (Day Group, Brentford facility). The chemical composition of the fine IBA fraction was determined by X-ray fluorescence analysis (XRF Spectro 2000 Analyser). The milled powder sample was also characterised by X-ray diffraction (Philips PW 1830 diffractometer) to identify the crystalline phases present. The effect of temperature on the milled powder was investigated by thermogravimetric analysis (TG/DTA, Stanton Redcroft, STA-1500 Series) on 25µg samples using a ramp rate of 10 $^{o}C.min^{-1}$.

Ceramic processing

Previous work demonstrated that the addition of 20 wt. % of recycled soda lime silica glass significantly improved liquid phase sintering of fine IBA. 500g sample batches of 80 IBA: 20 glass were therefore prepared with 1 wt. % of polyethylene glycol (PEG-8000) added as binder. This was wet milled for 24 hours in a porcelain ball mill, rotating at 40 rpm using high-density alumina milling media, a water to charge ratio was 2 and a milling media to charge ratio of 5. The particle size distribution of milled slurry samples was determined by laser diffraction (Beckman Coulter, LS-100 Series).

Milled slurries were dried overnight at 105°C, and lightly ground to pass through a 500 µm sieve to form powders suitable for pressing. Tile samples (110 x 55 x 20mm) and disc samples (40 mm diameter) were formed by uniaxial pressing at 48 MPa (Nannetti S hydraulic press) using a steel die. Pressed samples were then sintered in an electric laboratory furnace (Lenton Eurotherm 2416CC) at a heating rate of 6 °C/ min to

temperatures between 1020 and 1100°C with a 1 hour dwell time at peak temperature.Following wet ball milling and drying the IBA powders were calcined in aluminum crucible at temperatures between 600 and 1100 °C. The powders were then lightly ground in a mortar and pestle to produce ceramic powders suitable for processing into ceramics using the same procedures as for the un-calcined powder.

Property characterisation

The linear shrinkage was calculated from disc samples by comparing the diameter before and after firing using:

$(D_o – D_s)*100/ D_o$

where D_o is the diameter of the green disc and D_s the diameter of the sintered disc.

The relative density of the sintered samples was determined using Archimedes method taking into account of the effect of temperature on the specific gravity of water.

The water absorption of sintered samples was determined from the increase in weight of dried samples after immersion in water for 24 hours under a vacuum to remove the air entrapped within the open porous of the sample.

The Vickers micro-hardness of sintered samples was measured with a Leitz Wetzlar 8423 microhardness tester using a 25 g load. The Vickers number (HV) with units of kg mm^{-2}, is calculated from:

$HV= 1.854 (F/ D^2)$

where F is the applied load (kgf) and D^2 the area of the indentation measured in mm^2 .

Microstructural analysis used scanning electron microscopy (SEM, Jeol JSM-5610LV) to examine gold coated fracture surfaces of sintered samples.

RESULTS AND DISCUSSION

As-received fine IBA

Chemical composition data obtained by XRF is given Table 1. Approximately 80% w/w of the fine fraction of IBA consists of oxides of Si, Ca, Fe and Al. XRD data given in Figure 2 shows that the major crystalline phases present are quartz (SiO_2), calcite ($CaCO_3$), gehlenite ($Ca_2Al_2SiO_7$) and hematite (Fe_2O_3).

Table 1. *Chemical composition of the less than 4 mm fine fraction of IBA*

	CaO	**SiO_2**	**Al_2O_3**	**MgO**	**Fe_2O_3**	**K_2O**	**Na_2O**	**TiO_2**	**ZnO**	**P_2O_5**	**Others**
IBA	33.7	21.2	8.7	2.2	18.4	1.9	3.0	1.6	1.6	1.5	6.2

Thermogravimetric analysis data (Figure 3) shows that from ambient temperature to 120 °C weight loss occurs due to evaporation of moisture. Significant weight loss occurs between 600 and 770 °C, related to an endothermic peak centred at 765 °C and this results from the decomposition of calcite ($CaCO_3$) to CaO and CO_2. The weight loss of 1.7% between 1020 and 1100 °C is from the decomposition of alkali metal sulphates and evolution of SO_2. The endothermic peak in the DTA curve is also associated with melting. The peak identifies the energy consumption associated with the physical change from solid glass to a liquid.

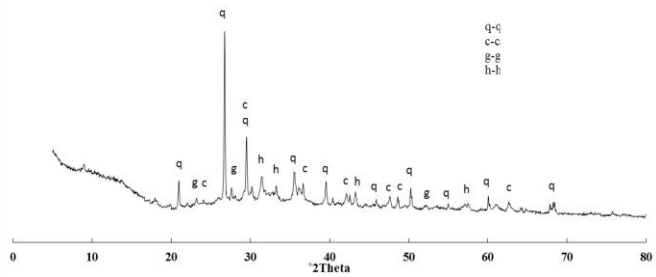

Fig. 2: *X-ray diffraction data of IBA/ glass*

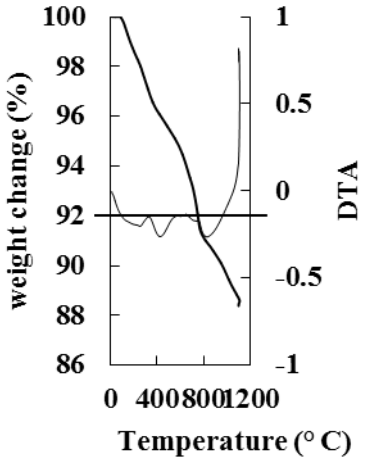

Fig. 3: *TG/ DTA of IBA/ glass*

Physical properties of IBA ceramics

The effect of sintering temperature on the density and shrinkage of sintered samples is shown in Figure 4(a). Maximum average densities of approximately 2.5 g/cm^3 were obtained for samples sintered at 1040 °C. However, sintering at 1080 °C resulted in lower water absorption, higher Vickers micro hardness and an improved appearance, and on this basis this was selected as optimum temperature. Linear shrinkage was relatively high ~20% and this tended to cause deformation and warping of tile samples during sintering

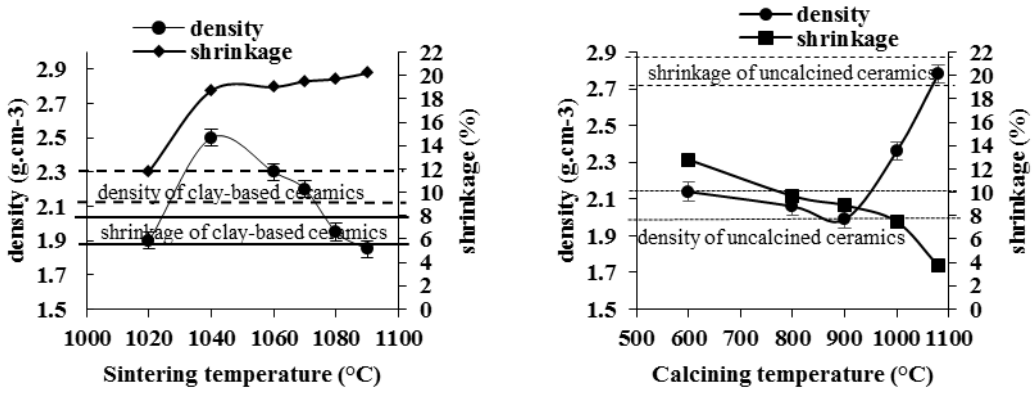

Fig. 4: *Effect of: (a) sintering and, (b) calcining temperature on the density and shrinkage of ceramics produced from uncalcined IBA glass powders.*

Maximum average densities of 2.8 g/cm^3 were obtained from the mixture calcined at 1080 °C and this had a linear shrinkage of just 3.7% which is significantly lower than that for typical clay based ceramics. Sintering the uncalcined samples at 1080 °C produced a ceramic with 4.1 GPa Vickers micro hardness, while ceramic tiles prepared from calcined powder had a hardness of 4.5 GPa hardness when sintered at 1080 °C (Figure 5). Water absorption of the IBA glass ceramics was negligible for samples sintered at temperatures above 1070°C.

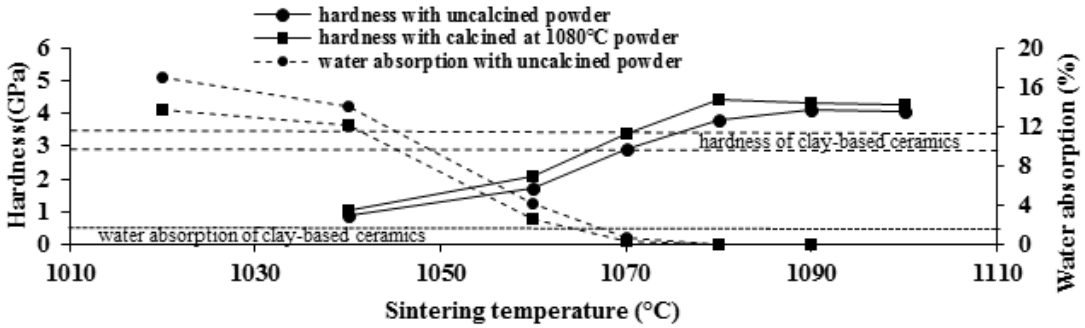

Fig.5: *Effect of sintering temperature (1 hour dwell) on the Vickers micro hardness and water absorption of ceramics produced from uncalcined and calcined at 1080 °C IBA glass powders*

X-ray diffraction data for milled IBA and glass mixes calcined at 800, 900, 1000 and 1100 °C are shown in Figure 7. While quartz (SiO_2), calcite ($CaCO_3$), hematite (Fe_2O_3) and ghelenite ($Ca_2Al_2SiO_7$) are the major crystalline phases identified in the as-received IBA new crystalline phases are found in powders calcined above 800°C, with diopside ($CaMgSi_2O_6$), clinoestatite ($MgSiO_3$) and andradite ($Ca_3Fe_2Si_3O_{12}$) the major crystalline phases in powders calcined at 1080 °C.

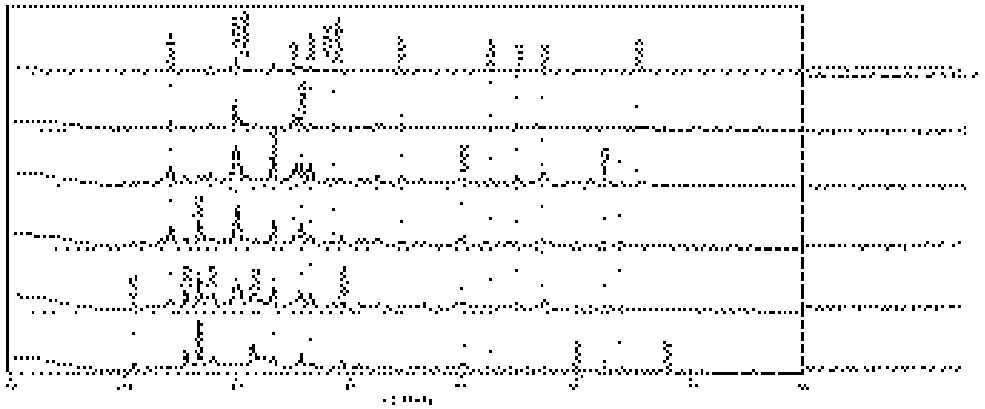

Fig. 6: *X-ray diffraction data of IBA glass wet ball milled for 24 hours, calcined IBA and glass powder at 800, 900, 1000 and 1080 °C and ceramic sintered at 1080°C with calcined at 1080°C powder*

Ceramics produced without calcining have extensive closed porosity in agreement with the density data, as shown in the SEM images in Figure 7.

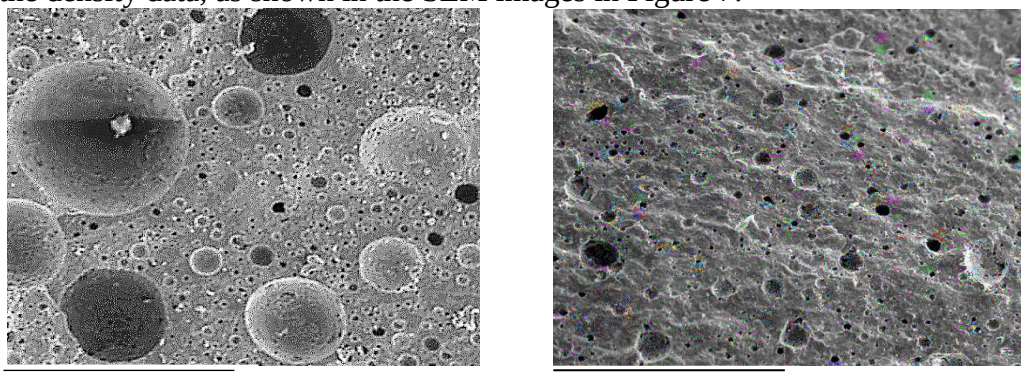

a) ceramic without calcining *b)ceramic with calcined at 1080°C*

Fig.7: *SEM micrographs of sintered at 1080 °C ceramics produced from IBA glass powder: (a) without calcining, (b) calcined at 1080°C*

CONCLUSIONS

Powders can be produced from the fine fraction of IBA that are suitable for manufacturing pyroxene group ceramics. The process involves milling the IBA mixed with glass and calcining. The sintering conditions control the physical, mechanical, mineralogical and microstructural properties of the ceramics formed. Sintering IBA powders without calcining results in excessive shrinkage during firing which is likely to be problematic for the production of ceramic tiles. Increasing the calcining temperature increased the density of sintered ceramics and reduced firing shrinkage. Ceramics with densities of 2.78 g/cm^3, negligible water absorption, 4.5 GPa Vickers micro hardness and approximately 4% linear shrinkage was obtained by sintering compacted powders at 1080 °C. While quartz and calcite were the major crystalline phases in the as-received fine IBA diopside and clinoenstatite were the major crystalline phase present in calcined powders and ceramics sintered at 1080 °C.

ACKNOWLEDGEMENTS

This research was funded by the Global Waste to Energy Research and Technology Council (WTERT), Wheelabrator Technologies Inc., Martin Gmbh and a Dixon Scholarship. We also wish to acknowledge the support of Adam Day of Day Group and Dave Parks from Monier Group Gmbh.

REFERENCES

Aloisi M., Karamanov A., Taglieri G., Ferrante F., Pelino M., 2006. Sintered glass ceramic composites from vitrified municipal solid waste bottom ashes. J. Hazard Mater, 137, 138-143.

Appendino P., Ferraris M., Matekovits I., Salvo M., 2004. Production of glass-ceramic bodies from the bottom ashes of municipal solid waste incinerators. J. Eur. Ceram. Soc., 24, 803-810.

Barbieri L., Corradi A., Lancellotti I., Manfredini T., 2002. Use of municipal incinerator bottom ash as sintering promoter in industrial ceramics. Waste Manag, 22, 859-863.

Baruzzo D., Minichelli D., Bruckner S., Fedrizzi L., Bachiorrini A., Maschio S., 2006. Possible production of ceramic tiles from marine dredging spoils alone and mixed with other waste materials. J. Hazard Mater, 134, 202-210.

Bethanis S., Cheeseman C.R., Sollars C.J., 2004. Effect of sintering temperature on the properties and leaching of incinerator IBA. Waste Manag Res., 22, 225-264.

Cheeseman C.R., Monteiro da Rocha S., Sollars C.J., Bethanis S., Boccaccini A.R., 2003. Ceramic processing of incinerator bottom ash. Waste Manag., 23, 907-916.

Ferraris M., Salvo M., Smeacetto F., Augier L., Barbieri L., Corradi A., Lancellotti I., 2001. Glass matrix composites from solid waste materials, J. Eur. Ceram. Soc., 21, 453-460.

Polettini A., Pomi R., Fortuna E., 2009. Chemical activation in view of MSWI IBA recycling in cement base systems, J. Hazard Mater., 162, 1292-1299.

Rawlings R.D., Wu J.P., Boccaccini A.R., 2006. Glass ceramics: Their production from wastes - A review. J Mater Sci., 41, 733-761.

Schabbach L.M., Andreola F., Barbieri L., Lancellotti I., Karamanova E., Ranguelov B., Karamanov A., 2012. Post-treated incinerator bottom ash as alternative raw material for ceramic manufacturing. J Eur Ceram Soc., 32, 2843- 2852.

COMPARISON OF LIGHTWEIGHT MORTARS MANUFACTURED WITH VIRGIN OR RECYCLED POLYSTYRENE

Chiara Giosuè
Department of Sciences and Engineering of Matter, Environment and Urban Planning , Università Politecnica delle Marche, 60131, Ancona, IT
c.giosue@univpm.it

Alessandra Mobili
Department of Sciences and Engineering of Matter, Environment and Urban Planning , Università Politecnica delle Marche, 60131, Ancona, IT

Costanzo di Perna
Department of Industrial Engineering and Mathematical Sciences , Università Politecnica delle Marche , 60131, Ancona, IT

Francesca Tittarelli
Department of Sciences and Engineering of Matter, Environment and Urban Planning , Università Politecnica delle Marche, 60131, Ancona, IT

ABSTRACT: In recent years, energy saving in buildings prescribes limits on thermal transmittance of opaque structures that can be achieved with the use of materials with low thermal conductivities. Mortars and concretes lightened with polystyrene pearls belong to this class. In this work, the performance of lightweight mortars manufactured with virgin polystyrene is compared with that of mortars manufactured with recycled granules of polystyrene at the same volume dosage.

Six mortar mixtures with water/cement = 0.55 by replacing the 33% - 66% - 100% of sand volume with virgin or recycled polystyrene are manufactured.

The obtained results show that, at the same volume dosage, the replacing of virgin polystyrene with recycled one improves the mechanical performance of mortars without significant variation in the capillary water absorption and water vapour permeability. The use of recycled polystyrene increases the equivalent thermal conductivity of mortars that can be compensated with a higher dosage of polystyrene. The use of recycled polystyrene allows a significant economical savings during the production phase of mortars and a certain insulation degree.
Keywords: Building energy efficiency, lightweight aggregates, mortar, recycled polystyrene, waste.

INTRODUCTION

The importance of energy building efficiency is more and more relevant. Actually, the global energy use contributed by buildings is about 40% [1]. In the last years, European directive 2002/91/CE [2] and following prescribe limits about the transmittance value. It is possible to reach this objective using building materials with low value of transmittance as example cementitious materials with virgin polystyrene. If the dosage of polystyrene is increased, it is possible to obtain lightweight structural mortar with density: δ= 1400 ÷ 2000 kg/m^3 and compressive resistance (R_c) more than 18 MPa, lightweight concrete with low strength, δ = 800 ÷ 1400 kg/m^3 and R_c = 7 ÷ 18 MPa, and lightweight mortar with thermal properties with δ = 300 ÷ 800 kg/m^3 and R_c = 0.5 ÷ 7 MPa [3].

Nowadays, it is also necessary to reuse wastes and by-products: recycling plastic is a possible option [4] so decreasing both the volume of waste in dump and the consumption of raw materials is viable. In this way industries producing polystyrene packaging use to shred waste polystyrene into granules before the disposal. The exponential growth in plastic waste from packaging incited a search for alternative means of recycling [5] and a possible solution is the substitution of virgin (commercial) polystyrene with recycled polystyrene.

SCOPE

The scope of this study is to compare fresh and hardened properties as density, strength, durability and thermal conductivity of mortars made with different dosage of virgin and recycled expanded polystyrene (EPS) used in substitution of a certain quantity of sand during the preparation of mortar (33%, 66% and 100% by volume).

EXPERIMENTAL PROGRAM

Materials and methods

Materials

A commercial Portland-limestone blended cement CEM II/A-L 42.5 R according to EN 197-1:2011 (Cement–Part 1: composition, specifications and conformity criteria) is used.

Table 1. *Cement Chemical Composition.*

Component	TiO_2	Al_2O_3	Fe_2O_3	MgO	SiO	CaO	SO_3	K_2O	Na_2O	Loss on Ignition
Percentage (%)	0.09	3.74	1.8	1.15	29.67	59.25	3.25	0.79	0.26	11.62

The Blaine fineness of cement is 0.41 m^2/g and its specific gravity is 3.05 g/cm^3. The chemical composition is indicated in Table 1. Fig. 1 shows the grain size distribution curves of aggregates. A calcareous natural sand, with 6 mm maximum diameter is used. Specific gravity is 2.65 g/cm^3. Two different types of polystyrene are used: virgin and recycled (Fig. 2). For both the specific gravity is 0.012 g/cm^3. Sand has the best distribution, virgin polystyrene has a regular spherical shape and more than

90% of particles have a diameter from 2 to 4 mm. Recycled polystyrene has particles with a less regular surface and a more distributed grain size between 1 and 8 mm.

An Air Entraining Agent (AEA) based on tensio-active agents is added both in mixtures virgin and recycled with 66 % and 100 % of polystyrene at the dosage of 0.1 and 0.3% by cement weight to inhibit segregation.

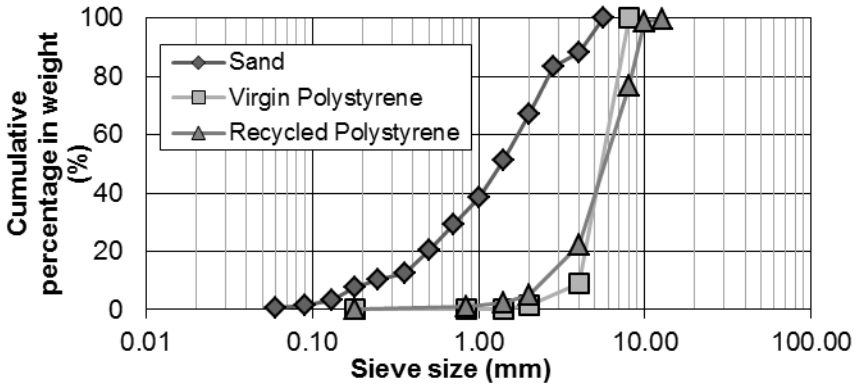

Fig. 1: *Grain size distribution of aggregates: sand, virgin polystyrene and recycled polystyrene.*

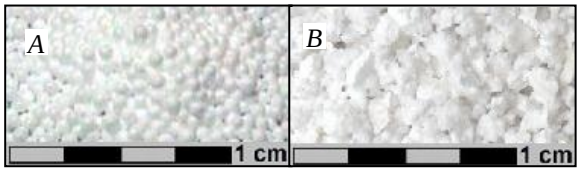

Fig. 2: *Virgin Polystyrene (A) and Recycled Polystyrene (B).*

The mixtures are prepared following the standard UNI EN 1015-2:2007 (Methods of test for mortar for masonry-Part 2: Bulk sampling of mortars and preparation of test mortars) with the proportions shown in Table 2. The water/cement ratio is 0.55. The volume of aggregate is constant in each mixture. After the preparation, the specimens are cured as described in UNI EN 1015-11:2007 (Methods of test for mortar for masonry-Part 11: Determination of flexural and compressive strength of hardened mortar).

Table 2. *Mix design (Kg/m^3).*

Code	Cement (Kg)	Water (Kg)	AEA (Kg)	Sand (Kg)	Virgin Poly. (Kg)	Recycled Poly. (Kg)	Slump (mm)	Mortar density (Kg/m^3)
V33	320	176	-	1257	2.74	-	120	1800
V66	320	176	0.32	610	5.23	-	116	930
V100	320	176	0.96	-	7.69	-	110	290
R33	320	176	-	1257	-	2.74	115	1900
R66	320	176	0.32	610	-	5.23	120	1370
R100	320	176	0.96	-	-	7.69	115	600

Test Methods

The workability is measured according to UNI EN 1015-3:2007 (Methods of test for mortar for masonry-Part 3: Determination of consistence of fresh mortar). Flexural (R_f) and compressive (R_c) strength of mortars are measured according to UNI EN 1015-11:2007. Prismatic specimens are prepared for each mixture, 40 x 40 x 160 mm in size, and tests are performed after 2, 7 and 28 days.

Water absorption due to capillary action of porous microstructure can decrease mortar durability. The Water Absorption Coefficient (CA) is evaluated with UNI EN

1015-18:2004 (Methods of test for mortar for masonry-Part 18: Determination of water absorption coefficient due to capillary action of hardened mortar). The water flux by capillarity through the specimen is measured by partial immersion (5-10 mm) in distillate water. The difference of weight by 10 and 90 minutes is the water absorbed due to capillarity action, 40 x 40 x 40 mm is the size for the specimen used.

Cylindrical specimens with diameter 140 mm and 25 mm high are prepared to evaluate the water vapour transmission W according to UNI EN 1015-19:2008 (Methods of test for mortar for masonry-Part 19: Determination of water vapour permeability of hardened rendering and plastering mortars).

Thermo characterization test is made by the experimental determination of thermal conductivity λ though cylindrical specimens (diameter 200 mm, thickness 25 mm) following the standard UNI EN 12667:2002 (Thermal performance of building materials and products - Determination of thermal resistance by means of guarded hot plate and heat flow meter methods-Products of high and medium thermal resistance). The radial heat flow is used to determine λ. The simulation of one-dimensional flow is generated by two thermocouple placed on the sides of the specimen.

RESULTS AND DISCUSSION

All the mixtures have stiff consistence (slump Φ = 11.5 ÷ 12.5 cm). Fig. 3 shows mechanical results at 2, 7 and 28 days. R_c decreases when the dosage of polystyrene is higher but with the same concentration the recycled polystyrene mortar resistance is up to 5 times greater than the virgin polystyrene mortar. The better grain size distribution and the uneven surface (Fig. 1 and Fig. 2) contribute to obtain these results. There is a good exponential correlation between R_c at 28 days and density (Fig. 4).

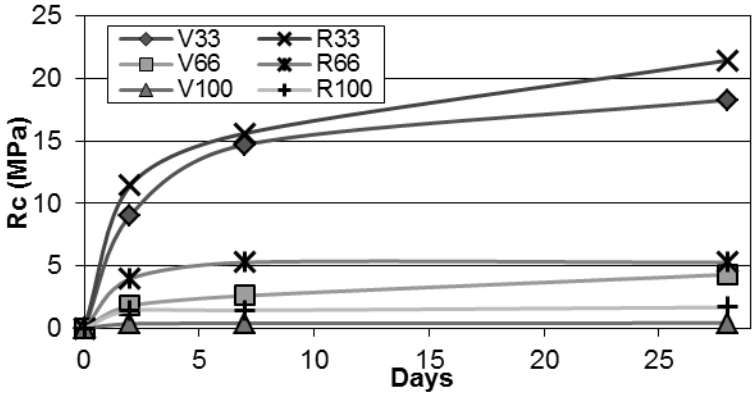

Fig. 3: *Compressive strength (R_c) development of virgin and recycled polystyrene mortars.*

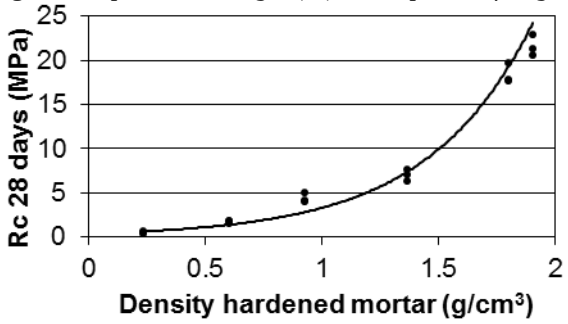

Fig. 4: *Relation between R_c after 28 days of curing and density of different hardened mortars.*

Water absorption due to capillarity at 33% of dosage is lower in recycled (Fig. 5) than in virgin polystyrene mortar. This result is due to the recycled polystyrene irregular shape that not being an absorbent material increases the tortuosity of the path of the water. At higher level of polystyrene the trend is the opposite because in virgin polystyrene mortar there are more macroporosities caused by regular spherical shape of grain than in recycled polystyrene one (Fig. 6). There is no cement paste in that pores so the water cannot be intake.

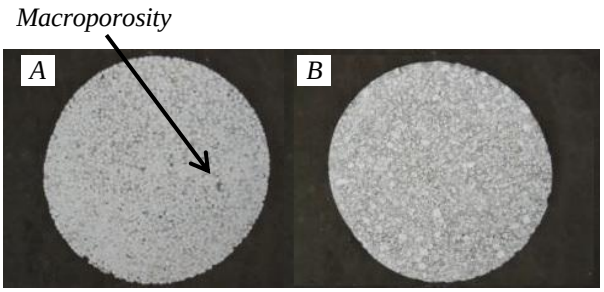

Fig. 6: *100% Virgin Polystyrene mortar (A), 100% Recycled Polystyrene mortar (B).*

The water vapour permeability W between the two types of specimens is not significantly (Fig. 7). The greater is that measured in V100 mortar due to the high presence of macroporosities. Anyway, the use of a hydrophobic admixture could decrease the capillary water absorption of mortar with recycled polystyrene and increase its permeability to water vapour [6, 7].

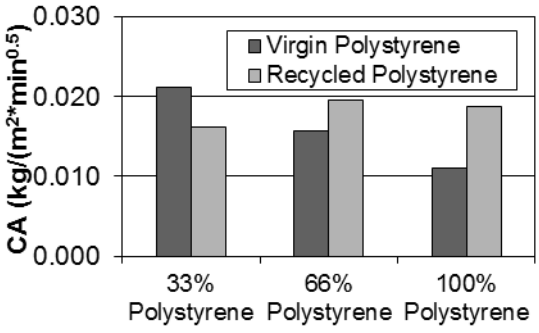

Fig. 5: *Water absorption coefficient due to capillary action of virgin and recycled polystyrene mortars.*

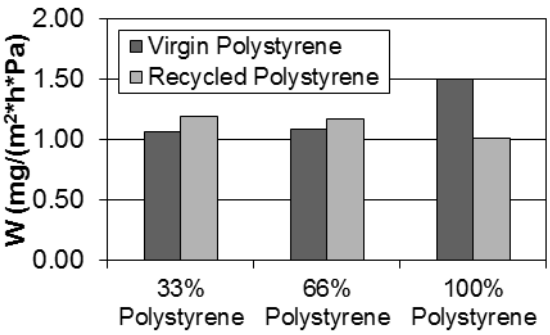

Fig. 7: *Water vapour permeability of virgin and recycled polystyrene mortars.*

For what concerns thermal properties, at the same dosage of polystyrene there is a decrease in performance for the recycled polystyrene mortar. However, there is a good linear relation between thermal conductivity λ and the percentage of polystyrene (Fig. 8).

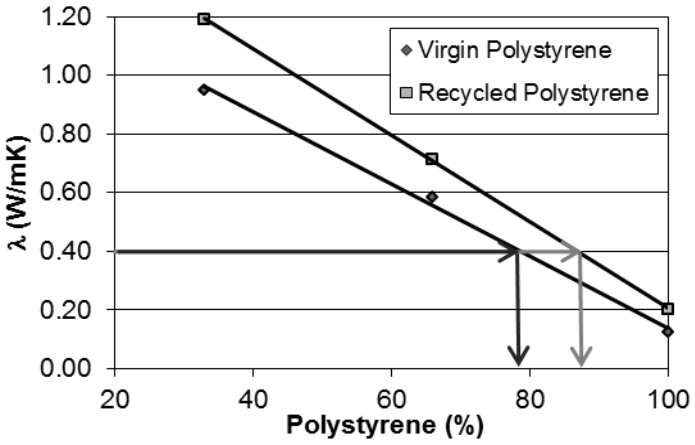

Fig. 8: *Relation between thermal conductivity λ and percentage of polystyrene in different mortars.*

This relation is useful to know how much virgin or recycled polystyrene it is necessary to add to the mixture to obtain a certain value of λ. As example to prepare a mortar with λ = 0.4 W/mK, according to the trend line in Fig. 7 it is necessary to replace 79% of sand volume with virgin polystyrene or 87% of sand volume with recycled polystyrene.

The comparison between the prices shows that at the same value of λ, to prepare mortar with recycled polystyrene is more convenient than to prepare it with virgin polystyrene. The price for recycled polystyrene is 8 €/m^3 and the price for virgin polystyrene is 25 €/m^3, therefore a saving more than 25% can be achieved.

CONCLUSIONS

The manufacturing of lightweight mortar with recycled polystyrene instead of virgin polystyrene, at the same volume dosage, implies:

- an increase in the mechanical properties;
- a decrease in capillary water absorption at low dosage of polystyrene (33% by volume of sand) but a certain increase at higher dosages (66% - 100% by volume of sand);
- no significant differences on water vapour permeability;
- an increase in the equivalent conductivity, compensated by an increase in the percentage of polystyrene;
- that to obtain mortar with a certain thermal insulating capacity, the use of recycled polystyrene is more economical convenient than virgin one.

REFERENCES

[1] Wang S, Yan C and Xiao F. *Quantitative energy performance assessment methods for existing buildings*. Energy and Buildings. 2012, 55 (December) 873-888.

[2] European Directive 2002/91/Ce, Directive 2002/91/EC of the European Parliament and of the Council of 16 December 2002 on the energy performance of buildings.

[3] Collepardi M. Collepardi S, Troli R. *The new concrete*. [Italian version], ENCO SRL Press, 01/2009

[4] Saikia N, de Britio J. *Use of plastic waste as aggregate in cement mortar and concrete preparation: A review*. Construction and Building materials, 2012, 34 (September) 385-401.

[5] Marzouk O Y, Dheilly R M, Queneudec M. *Valorization of post-consumer waste plastic in cementitious concrete composite*. Waste Management. 2007, 27, 310-318

[6] Tittarelli F, Moriconi G. *Comparison between surface and bulk hydrophobic treatment against corrosion of galvanized reinforcing steel concrete*. Cement and Concrete Research. 2011, 41.6 (June) 609-614.

[7] Mailvaganam N P. Miscellaneous Admixtures, Concrete Admixtures Handbook. VS Ramachandran (Ed), Noyes Publications, Park Ridge, New Jersey, USA, (1984) 518-524.

USE OF INDUSTRIAL WASTES IN THE PREPARATION OF ADVANCED PHOTOCATALYTIC BUILDING MATERIALS

J. Balbuena, M. Cruz-Yusta, J. Morales and L. Sánchez
Departamento de Química Inorgánica, Facultad de Ciencias – Universidad de Córdoba, Córdoba, Spain.
luis-sanchez@uco.es

I. Mármol
Grupo Puma S.L., Avda. Agrupación Córdoba nº 17, Córdoba, Spain

D. Kovandzic
Agencia de Obra Pública de la Junta de Andalucía, c/ Diego Martínez Barrio, Sevilla, Spain

ABSTRACT: Appropriate waste management is one of the main requisites for sustainable development at present. This task is nowadays tackled by the material construction industry. A preliminary study about the proper valorization of the husk of steel lamination process (HSL) for the production of advanced photocatalytic building materials is here presented.

The HSL waste, being generated on the steel industry (HSL), is constituted by Fe_2O_3 (41.9 %), SiO_2 (10.6 %) and CaO (8.9 %), Cr (7.6 %), Al_2O_3 (6.8 %) and MgO (4.1 %). The high presence of iron oxides was used to develop photocatalytic properties through their thermal transformation into α-Fe_2O_3. The enrichment in hematite phase in waste composition accounted at temperatures of 600 ºC, HSL-T.

Mortar specimens containing HSL-T as photocatalyst admixture let the preparation of self-cleaning and de-polluting materials. These mortars exhibited good behavior towards the photochemical degradation of organic dyes, rhodamine-B (RhB). Conversely, the use of wastes for the preparation of materials enhancing the photocatalytic oxidation of NO_x gases resulted more interesting. Moreover, building materials with enhanced photocatalytic properties were prepared using the synergistic effect of TiO_2 and HSL-T photocatalysts. Finally, the preparation of sustainable building materials is demonstrated through an adequate reuse of steel lamination process wastes.
Keywords: Mortar, waste, photocatalysis, self-cleaning, NOx de-pollution.

INTRODUCTION

The chemical industry is a very important sector contributing to ensure the continuous improvement in the Sustainable Development. Currently, there are a variety of co-products and wastes which could provide − through the proper treatment − a range of materials with new features, including photocatalysis. It is known that construction industry is one of the best targets for solid waste reconversion due to the consumption of large amounts of raw materials and the large volume of the final products. Recently, considerable interest has been aroused in the implementation of photocatalysts in building materials, like TiO_2, because it involves additional benefits such as the self-cleaning of pollutants attached on surface or the de-polluting action over the environmental air pollutants.[1-3]

In that concerning to air purification, the presence of nitrogen oxides (NO_x = NO + NO_2) in the atmosphere is a great concern for modern society, due to the several adverse and harmful effects of these compounds on human health. TiO_2-containing materials are interesting thanks to their ability to promote photocatalytic oxidation (PCO) of these gases. Thus, by using TiO_2 as an efficient photocatalyst, NO_x oxidation is easily promoted using only atmospheric oxygen, water and UV-A solar radiation.[4] This simple mechanism is the basis for the preparation of de-polluting building materials. Nevertheless, because TiO_2 is an expensive additive, the high cost of these advanced construction materials precludes its widespread use, and therefore, promising applications of this type of materials will be limited in our cities. An alternative to mitigate this shortcoming could be the preparation of a semiconductor photocatalyst from industrial wastes. Of the metal oxides which commonly appear in these wastes, iron-based products are interesting because they could be transformed into photocatalytic materials, as previously reported by our research group.[1,5] Hematite (α-Fe_2O_3) is the most stable iron oxide with n-type semiconducting properties under ambient conditions. Even though its photocatalytic activity is lower than that of the TiO_2 anatase phase, this oxide can absorb visible light (1.9−2.2 eV band gap). This absorption ability has attracted a strong interest in its potential applications for the photocatalytic degradation of pollutants in water and air.[6]

An interesting waste is that produced during the steel lamination process, industrial activity producing this solid waste in large amounts. Because the content in iron oxide is high in this waste, it can be used to prepare a raw material with potential photocatalytic properties. This work shows a preliminary study about the proper valorization of the husk of steel lamination process (HSL) for the production of new self-cleaning and de-polluting materials, more specifically cementitious materials.

EXPERIMENTAL

The as-received HSL samples were dried at 110 °C until constant weight. In order to homogenize the particle size, the samples were grinded using a planetary mill (300 rpm; 1 h). The chemical composition was determined by X-ray fluorescence analysis (XRF). The mineralogical and crystalline phases identification was performed using X-ray diffraction (XRD). The particle size distribution (PSD) curves for the overall mixed raw materials were determined with a laser analyser (Mastersizer 2000 LF, Malvern, UK).

A flooring mortar was studied to evaluate the use of HSL samples as additives for the preparation of self-cleaning and de-polluting materials. Mortar specimens were prepared by using cement (Portland BL I 52.5 R), silica and dolomite sands, calcite as a filler, and organic additives (dispersible polymer powders, plasticizer and superplasticizer). The different formulations were adjusted to obtain an appropriate consistency and acceptable workability (UNE-EN 1015-3 and 1015-2). The mortar specimens were cast in 40x40x160 mm molds, using a cement/sand ratio of 1:2. After 48 h, the specimens were demolded and cured at 20 ºC at 65 ± 5% relative humidity (RH). Specimens were tested after 28 curing days.

The evaluation of the self-cleaning property of mortar with the HSL was performed according to the standard UNI 11259.[7] Thus, the specimens were stained on the surface with rhodamine-B (RhB, red dye). The variations in color during light exposure were measured with a CM-5 colorimeter from Konica Minolta. The degradability of RhB is represented by the R_{26} index: $R_{26} = [a^*(0h) – a^*(26\ h) / a^*(0h)] \times 100$, where a*(0h) and a*(26 h) denote the value of a* – the green (–) → red (+) axis CIE color parameter – before and after 26 h of irradiation.

Concerning the air de-polluting action, the photocatalytic oxidation of nitrogen oxide, NO, was studied. The NO oxidation tests were carried following the methodology described in to ISO 22197-1, which is applicable to photocatalytic materials produced for air purification. However, some of the specifications described on this standard were modified in order to obtain the better performance with the samples object of this study. Thus, the tests were carried out on 50 x 50 mm mortar samples placed in a laminar flow reactor and irradiated with artificial sunlight (25 and 580 W/m^2, UV and visible irradiance, respectively). Air was supplied with a relative humidity of 50 ± 10%. Air and NO gas streams were mixed to obtain the desired concentration, 500 ppb NO, and sent to the photoreactor (Q = 0.75 L/min). The removal rate (%) of NO_x was defined according to the following equation:

$$NO_x \text{ removal rate (\%)} = [NO_X]_{inlet} – [NO_X]_{outlet} / [NO_X]_{inlet} \times 100$$

RESULTS AND DISCUSSION

Waste characterization and transformation

The large number of HSL samples studied exhibited the following common composition: Fe_2O_3 (41.9 %), SiO_2 (10.6 %) and CaO (8.9 %), Cr (7.6 %), Al_2O_3 (6.8 %) and MgO (4.1 %) as the main components with 11.6 % of L.O.I.

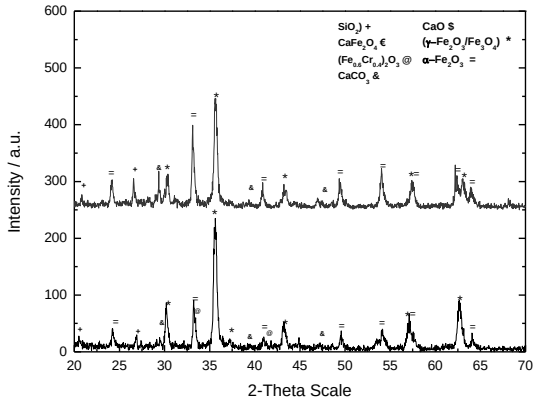

Fig. 1: *XRD patterns for original and heated waste: HSL (down), HSL-T (up).*

The chemical analysis was in agreement with the XRD pattern recorded for the HSL waste, Figure 1. Thus, iron oxides (Fe_3O_4/γ-Fe_2O_3/α-Fe_2O_3) were present as the main crystalline phases. Chromium appears as $(Fe_{0.6}Cr_{0.4})_2O_3$ avoiding the existence of Cr(VI). A clear enrichment in hematite was noted after heating the waste at 600 ºC (4h), Figure 1. This sample is hereafter designated as HSL-T.

Mortar formulation and mechanical properties

The importance of internal microstructure in the mechanical and photocatalytic properties of cement based mortars have been previously reported.[8,9] Taken into account this, we have examined eight different formulations using aggregates of different nature, siliceous (1 to 4) and dolomitic (5) sands, and particle size and keeping constant the percentage of cement and additives, Table 1.

Table 1. *Mortar formulations (wt %).*

Mortar components	M-1	M-2	M-3	M-4	M-5	M-6	M-7	M-8
Sand 1 (400 - 3000 µm)	22.23	12.23	22.23	-	-	12.23	22.23	43.47
Sand 2 (200 - 1500 µm)	43.47	43.47	20	43.47	20	20	-	12.23
Sand 3 (150 - 800 µm)	-	-	-	-	23.47	23.47	43.47	-
Sand 4 (100 - 500 µm)	-	-	23.47	-	-	-	-	-
Sand 5 (300 - 3000 µm)	-	10	-	22.23	22.23	10	-	-
Filler	-	-	-	-	-	-	-	10
BL I 52.5 R	33	33	33	33	33	33	33	33
Redispersible polymer	1	1	1	1	1	1	1	1
Surfactant wetting	0.05	0.05	0.05	0.05	0.05	0.05	0.05	0.05
Fluidifying	0.25	0.25	0.25	0.25	0.25	0.25	0.25	0.25

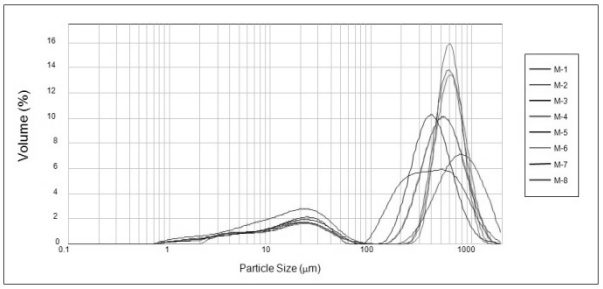

Fig. 2: *Particle size distributions of different mortars.*

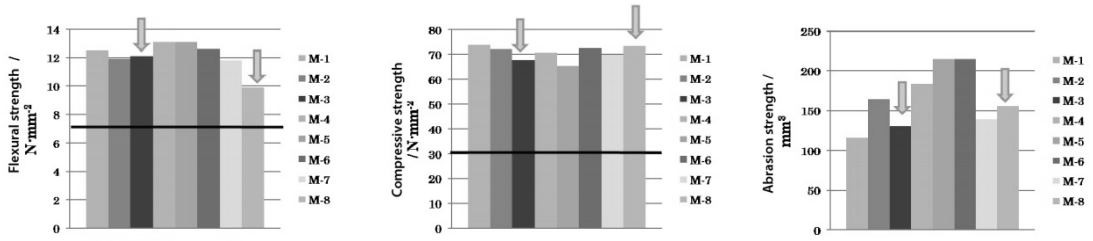

Fig. 3: *Mechanical strengths of the studied mortars after 28 days of curing.*

Figure 2 shows the particle size distribution of the dry formulations M1 to M8. The values of flexural, compression and abrasion resistances were obtained for the eight mortars after 28 days of curing. In all the cases, the values were higher than 7 N/mm^2 (flexural strength) and 30 N/mm^2 (compressive strength) and lower than 400 mm^3 (abrasion resistance), optimal values deduced from the experience in the applications of flooring mortars.[10] We conclude that the most appropriate formulations are the M3 and M8, because the particle size distribution of the finer aggregates is most similar to that of the HSL-T (0.3-110 μm) to be introduced in the new the formulation of the mortar.

Self-cleaning and de-polluting materials

Subsequently, the potential applications of new cement-based photocatalytic mortars containing the transformed wastes were examined. Table 2 shows the percent composition of the mortars studied. In the new formulations of mortars M3 and M8, the $CaCO_3$ filler and Sand 4 were partially replacing by 5% HSL-T. The presence of this new admixture does not origins significant changes on the mechanical properties, Table 2. Therefore, the use of HSL-T in mortars does not preclude their practical application.

Table 2. *Composition of the studied mortars (wt%)*

Mortar	SiO_2	Cement	Filler/Sand 4	Additives	HSL-T	TiO_2
M3	55.7	33	23,47	1.3	--	--
M3-5HSL	55.7	33	18,47	1.3	5.0	--
M8	55.7	33	10	1.3	--	--
M8-5HSL	55.7	33	5	1.3	5.0	--

Table 3. *Mechanical strengths of the studied mortars after 28 days of curing.*

Mortar	Flexural / $N \cdot mm^{-2}$	Compressive / $N \cdot mm^{-2}$	Abrasion / mm^3
M3	9,3	68,9	156,0
M3-5HSL	9,4	64,7	123,0
M8	9,6	76,4	89,0
M8-5HSL	10,3	67,1	123,0

Rhodamine-B (RhB) degradation test was used to check the ability of these building materials as self-cleaning pollutants based on their photocatalytic properties. The red stain was reduced down after irradiation (Figure 4). Table 4 shows the R_{26} index values as a quantitative evaluation of RhB dye photodegradation being the M3-5HSL the mortar exhibiting the best self-cleaning performance.

Table 4. *RhB photodegradation in the studied mortars*

Mortar	R_{26} / %
M3	--
M3-5HSL	44,28
M8	--
M8-5HSL	21,70

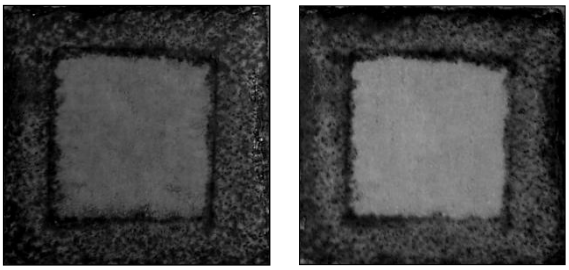

Fig. 4: *M8-5HSL before (left) and after irradiation (right).*

The use of a photocatalytic flooring mortar is of interest in order to reduce the urban pollution through the photocatalysis. On this sense, Ai et al. reported that the removal of NO_x accounts for its photocatalytic oxidation (PCO) to NO_2^-/NO_3^-.[11] In the mortars object of this study the PCO is clearly enhanced by the presence of the HSL-T in the mortar formulation, Figure 5. The removal of NO_x was higher for the sample M8-5HSL. In order to enhance the photocatalytic properties, 0.25 or 0.5 % wt of TiO_2 Evonik-P25 was also added to the M8-5HSL formulation (mortars M8-5HSL-0.25T and M8-5HSL-0.25T, respectively). It is observed that HSL-T and TiO_2 works synergistically, which is ascribed to the optical absorption ability of TiO_2 and α-Fe_2O_3 oxides in the longer wavelength region.[1]. Thus, the PCO efficiency of M8-5HSL-0.25T is better to that of M8-0.25T sample and similar to the M8-0.5T sample.

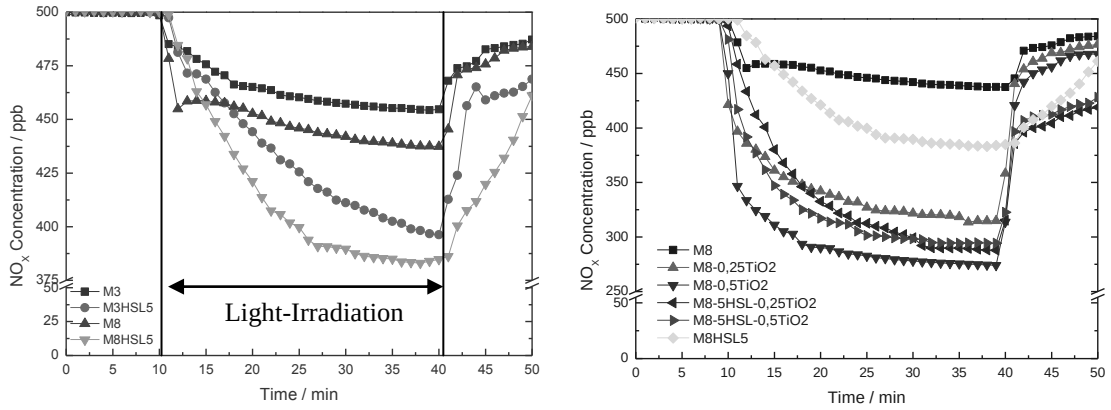

Fig. 5: *NO_X concentration profiles obtained during the photocatalytic degradation of NO gas over MHSL (left) and MHSL-TiO_2 (right) mortars under artificial solar light.*

CONCLUSIONS

Appropriate HSL waste management was performed for its reuse as a new value-added admixture in the preparation of sustainable photocatalytic materials. The preparation of advanced photocatalytic materials exhibiting self-cleaning and de-polluting properties was possible by the inclusion of HSL-T and HSLT/TiO_2 admixtures.

ACKNOWLEDGEMENTS

The authors would like to thank the FEDER of European Union for financial support via project "*Preparación de materiales de construcción de última generación para la mejora de la sostenibilidad ambiental en entornos urbanos: disminución de gases contaminantes (NO_X) emitidos por los sistemas de transporte*" of de "*Programa*

Operativo FEDER de Andalucía 2007-2013". We also thank all Agency of Public Works of Andalusia Regional Government staff and researchers for their dedication and professionalism.

REFERENCES

[1] R. Sugrañez, M. Cruz, I. Mármol, F. Martín, J. Morales, L. Sánchez, *ChemSusChem* 2012, *5*, 694-699.
[2] J. Chen, C.S. Poon, *Build. Environ.* 2009, *44*, 1899-1906.
[3] G. Hüsken, M. Hunger, H.J.H Brouwers, *Build. Environ.* 2009, *44*, 2463-2474.
[4] A. Folli, S.B. Campbell, J.A. Anderson, D.E. Macphee, *J. Photoch. Photobio. A* 2011, *220*, 85-93.
[5] R. Sugrañez, M. Cruz-Yusta, I. Mármol, J. Morales, L. Sánchez, *ChemSusChem* 2013, *6*, 2340-2347.
[6] N.T. Hahn, H.C. Ye, D.W. Flaherty, *ACS Nano* 2010, 4,1977-1986.
[7] UNI 11259, "Determination of the photocatalytic activity of hydraulic binders. Rhodamine test method", Ente Nazionale Italiano di Unificazione, 2008.
[8] R. Sugrañez, J.I. Álvarez, M. Cruz, I. Mármol, J. Morales, L. Sánchez. *Constr Build Mater* 2013, 41, 139-145.
[9] R. Sugrañez, J.I. Álvarez, M. Cruz, I. Mármol, J. Morales, J. Vila, L. Sánchez *Build Environ* 2013, 69, 55-63.
[10] Internal communication from GRUPO PUMA, http://www.grupopuma.com
[11] Z. Ai, W. Ho, S. Lee, L. Zhang, *Environ. Sci. Technol.* 2009, *43, 4143-4150.*

EFFECT OF HYDROTHERMAL CONDITION ON PC-$BaSO_4$ SYSTEM AS A HIGH DENSITY SUPPORT MATRIX FOR DEEP BOREHOLE GEOLOGICAL DISPOSAL OF NUCLEAR WASTES

O. H. Hussein, S. A. Bernal, C. A. Utton, H. Kinoshita
Department of Materials Science and Engineering, The University of Sheffield, Mappin Street, Sheffield, S1 3JD, UK
mt1oh@sheffield.ac.uk

ABSTRACT: Cementitious grout is one of the candidate materials for the high density support matrix (HDSM) for the deep borehole geological disposal (DBGD) of nuclear wastes, so that the waste containers can withstand mechanical stress when the HDSM has solidified around them. The HDSM then has to maintain its integrity for a long time under severe condition, for instance the temperature of surrounding environment can rise up to approximately 180ºC within 28 days of emplacement due to the heat produced from radioactive wastes. We have studied the effect of hydrothermal condition on the PC-$BaSO_4$ system as a candidate material for HDSM. The products had a significant level of porosity and strength regression under the hydrothermal curing compared to those cured at ambient conditions. It was found that C-S-H and monosulphate initially formed were replaced by more stable lime rich phases such as jaffeite and reinhardbraunsite under hydrothermal conditions. These phase evolution appeared to be the cause of the significant level of porosity, and strength regression after the hydrothermal curing.
Keywords: $BaSO_4$, hydrothermal condition, phase evolution, strength regression

INTRODUCTION

Deep borehole geological disposal is an alternative methodology for the disposal of nuclear waste to increase the geological barriers for the radionuclide transport to the geosphere (Fig.1) [1, 2]. One of key components in the deep borehole disposal system (DBDS) is the high density support matrices (HDSM) which keep the canisters safely together without creating stresses that could lead to the release of the radionuclides to the environment and also can be used for sealing the deep borehole. Physical integrity of the cementitious HDSM placed in the borehole is of importance, especially under hydrothermal condition. The heat produced by the radioactive wastes can raise the temperature of the surroundings up to 180ºC within 28 days [1, 2], meaning that cement matrix has to withstand this temperature and high pressure.

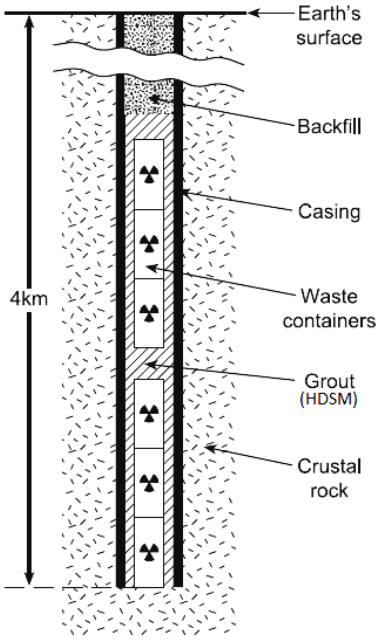

Fig. 1: *Schematic diagrams of deep borehole geological disposal* [1, 2]

The present study investigated the effect of hydrothermal condition on the PC-$BaSO_4$ system as a candidate material for HDSM. $BaSO_4$ has been used an effective aggregate for the shielding concrete of radiation owing to its high density [3] and also known to be stable at high temperatures up to over 1000 ^oC. PC-$BaSO_4$ systems were cured either under ambient and hydrothermal conditions, and their product phases, microstructure and compressive strength were investigated. A neat PC system was also studied for comparison.

EXPERIMENTAL

The Portland cement used in the study were a type CEM I (Castle Cements product UK) with a fineness of 352 m^2/kg Blaine. Analytical grade $BaSO_4$ of particle size of <1 µm with 98 % purity (Acros organics) was also used both as in powder form and granulated form. The $BaSO_4$ granules were prepared by mixing $BaSO_4$ powder with water (water/$BaSO_4$ ratio = 0.5 on a mass basis); drying the slurry in an oven at 90 °C for 24 hrs; sintered in an Elite (UK) furnace in air at 1000°C for 24 hrs; and crushing the solid to 0.6-5 mm. The formulations of the specimens produced are given in Table 1. These formulations were selected based on the results obtained in a previous study conducted by the authors [4].

Table 1. *Formulation of cement samples*

Sample ID	PC (g)	$BaSO_4$ powder (g)	$BaSO_4$granule (g)	Water (g)	w/c	w/s
PC	100	0	0	53	0.53	0.53
12P48G	40	12	48	21.2	0.53	0.41

The cement pastes were prepared in accordance with the standard mixing procedure described in previous study [4]. After mixing, a portion of pastes were placed in a sealed plastic container and cured at 40^oC for 28 days. Another portion pastes were cured at 180°C and left for 7 and 28 days in a sealed Teflon pot contained in a stainless-steel vessel. After the required curing time, selected samples were subjected to the immediate compressive strength test. The other materials were broken into smaller pieces and submerged in acetone for 3 days to arrest hydration reactions, then dried and and stored in sealed containers prior to analysis to avoid carbonation. The product phases were analysed using Xray diffraction (XRD) and thermogravimetry (TG) after ground to <63 µm using mortar, pestle and a sieve. The microstructures of the products were studied using scanning electron microscopy (SEM) on a carbon coated polished surface of small pieces moulded in epoxy resin. Mercury intrusion porosimetry (MIP) was also used on small cement pieces.

RESULTS AND DISCUSSION

Neat PC

The crystalline phases identified in the XRD data for the sample cured at 40°C (Fig. 2 a) were unhydrated alite (A) and belite (B), with portlandite (P), monosulphate (MS) and calcite (C). In the hydrothermal curing (Fig. 2 b), in addition to the alite (A), belite (B), portlandite (P) and calcite (C), hydrogarnet (Hg) was observed instead of monosulphate (MS). Formation of lime-rich phases, Jaffeite (J: $C_6S_2H_3$), reinhardbraunsite (R: C_5S_2H), and α-dicalcium silicate hydrate (Z: α-C_2SH) was also observed, which must be related to the decomposition/dehydration of C-S-H. It has been reported that C-S-H is not stable at high temperatures and often replaced by such crystalline phases with a high Ca/Si ratios [5-8].

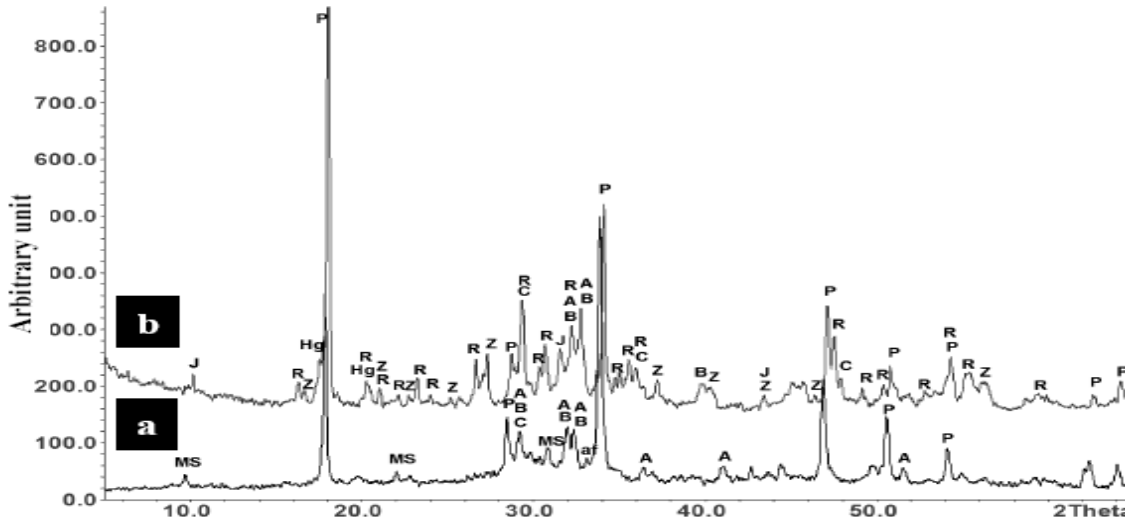

Fig. 2: XRD *trace of neat PC samples: (a) cured at 40°C, (b) cured under hydrothermal condition*

The lack of the water loss below 300°C in TG and DTG data (Fig. 3) in the PC cured under hydrothermal condition confirms the absence of the C-S-H and AFm phases. The presence of hydrogarnet (Hg) and portlandite (CH) are confirmed by a shoulder in the DTG curve at 370°C and a clear peak at approximately 450°C, respectively. Further small weight loss at around 500°C is due to the decomposition of α-dicalcium silicate hydrate to dicalcium silicate which is slightly different from clinker phase (β-C_2S) [8]. The decomposition of calcium carbonates is also observed as a broad peak at 600-700°C.

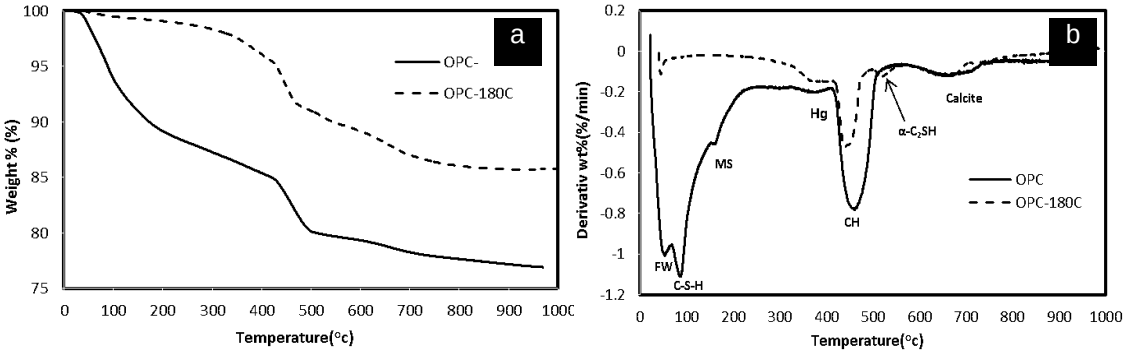

Fig. 3: *TG (a) and DTG (b) of neat PC cured at 40 °C and under hydrothermal condition*

The microstructure of the PC was clearly affected by the hydrothermal condition as shown in Fig. 4. The sample is much more porous when cured under hydrothermal condition. This porous microstructure is likely attributed to the lack of the usual C-S-H gel. The C-S-H gel formed in the early hydration reaction of C_3S is known to lose its interlayer water under a similar condition (high pressure steam, 100-300°C) [5], which can be accompanied by a shrinkage of the interlayer thickness [20] and the formation of crystalline silicate hydrate phases with a high Ca/Si ratio such as jaffeite and reinhardbraunsite by reacting with portlandite [9, 10].

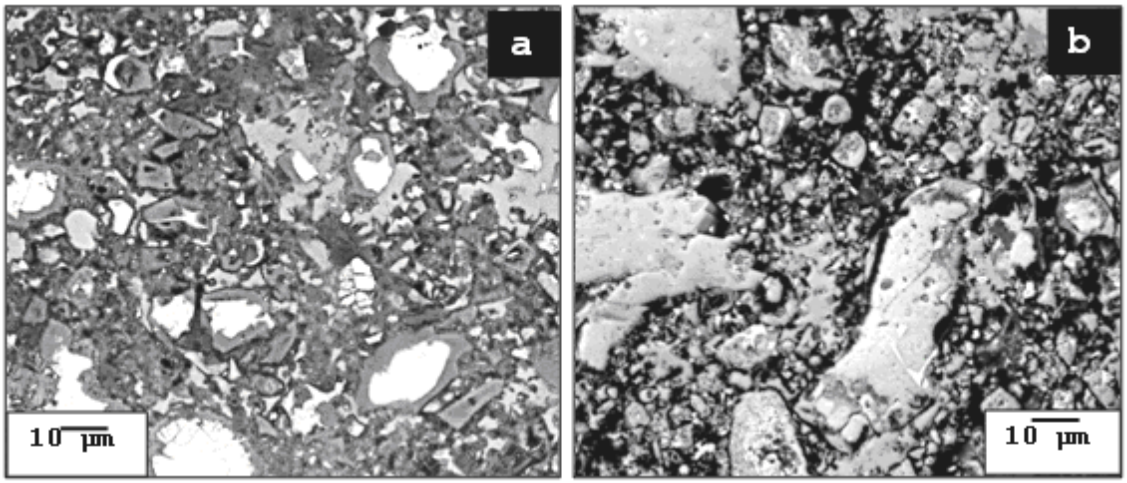

Fig. 4: *BSE images of PC, w/c=0.53: (a) cured at 40°C, (b) under hydrothermal condition at 180°C*

PC-$BaSO_4$ system

The XRD and TG results (not shown) confirmed that reaction products in the PC-$BaSO_4$ system were similar to those in the neat PC. The clear differences were the presence of peaks attributed to $BaSO_4$ in XRD data, and less weight loss in TG data associated wit the less PC in the system. The effect of curing time on the hydration reaction under hydrothermal curing can be seen in the TG data shown in Fig. 5. The sample cured for 7 days showed the conventional cement hydration phases i.e. C-S-H and AFm whereas at 28 days, as already discussed, neither C-S-H nor AFm was observed. This suggests that the C-S-H phase progressively disappears during the hydrothermal curing and replaced by more stable phases with a higher Ca/Si ratio with a possible CH consumption [5]. The total weight loss of PC- $BaSO_4$ system cured for 7 days was also significantly larger than that cured for 28 days.

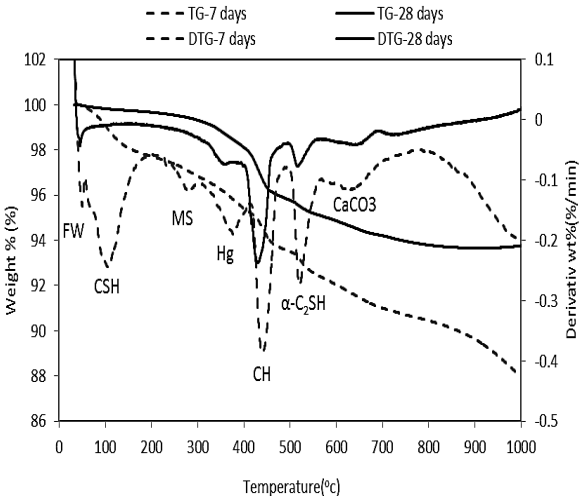

Fig. 5: *TG and DTG of 12P48G cured in hydrothermal condition for 7 and 28 days.*

The microstructure of 12P48G (Fig. 6) was less heterogeneous compared with the neat PC after the hydrothermal curing(Fig. 4). The possible reason is the filler effect of

fine $BaSO_4$ particles. The large surface area of $BaSO_4$ powder can enhance the hydration reaction and fill the porous interfacial transition zone between the cement paste and $BaSO_4$ granule, resulting in more homogenous microstructure.

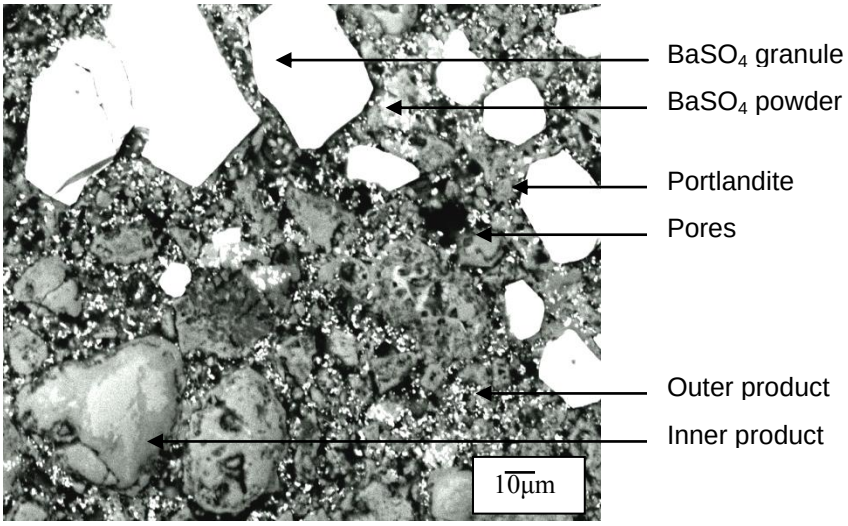

Fig. 6: *BSE images of 12P48G cured under hydrothermal condition for 28 days.*

Strength regression

The mechanical strength was clearly decreased when samples were hydrothermally cured (Fig. 7 a), compared to when cured at 40°C. This strength regression must be attributed to the loss of the main binding phase (C-S-H) as a result of the hydrothermal curing and formation α-C_2SH. The α-C_2SH has been known to increase in the permeability and strength reduction due to the volume reduction as a consequence of the formation of this phase [11, 12]. The strength regression was more significant in the neat PC (76%) whereas the 12P48G showed a less strength regression of 59%, probably because the less PC content in this system compared with the neat PC system. Corresponding to the strength data, the total porosity was greater after hydrothermal curing in both systems, but the 12P48G showed a slightly less porosity.

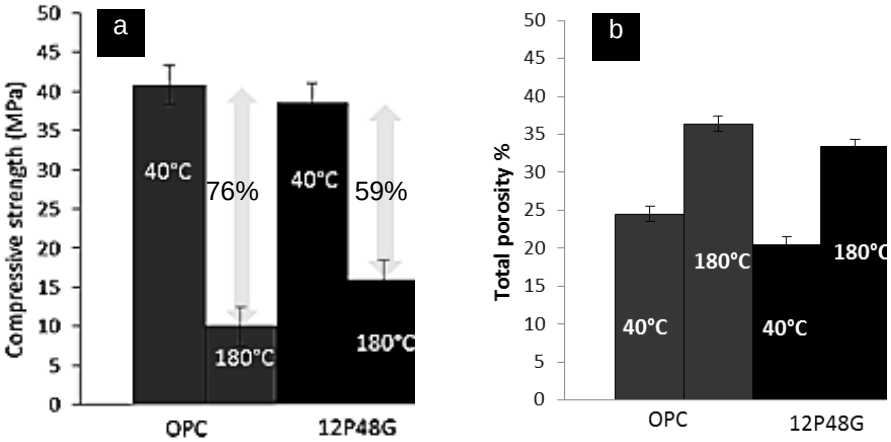

Fig. 7: *Compressive strength (a) and total porosity (b) of the samples cured at 40 °C and hydrothermal condition for 28 days.*

CONCLUSIONS

The obtained results revealed that the neat PC and PC-$BaSO_4$ systems show a similar response towards the hydrothermal curing at 180°C for 28 days. Both systems did not contain C-S-H or monosulphate phase, but showed the presence of Jaffeite, reinhardbraunsite, and α-dicalcium silicate hydrate. It was found that initially C-S-H and monosulphate forms through the conventional hydration of PC cement, in addition to α- C_2SH through direct hydration of C_2S. These phases are then replaced by more stable lime rich phases such as Jaffeite and reinhardbraunsite, possibly with a partial consumption of CH and α- C_2SH. The significant level of porosity after the hydrothermal curing is probably due to this phase evolution.

REFERENCES

[1] F. G. F. Gibb, K. P. Travis, N. A. McTaggart, and D. Burley, *A model for heat flow in deep borehole disposals of high-level nuclear waste.* Journal of Geophysical Reaearch, 2008. **113**: p. B05201.

[2] F. G. F. Gibb, N. A. McTaggart, K. P. Travis, D. Burley, and K. W. Hesketh, *High-density support matrices: Key to the deep borehole disposal of spent nuclear fuel.* Journal of Nuclear Materials 2008. **374** p. 370–377.

[3] I. Akkurt, H. Akyıldırım, B. Mavi, S. Kilincarslan, and C. Basyigit, *Photon attenuation coefficients of concrete includes barite in different rate.* Annals of Nuclear Energy, 2010. **37**: p. 910-914.

[4] O. Hussein, C. Utton, M. Ojovan, and H. Kinoshita, *The effects of BaSO4 loading on OPC cementing system for encapsulation of BaSO4 scale from oil and gas industry.* Journal of Hazardous Materials, 2013. **261**: p. 11-20.

[5] K. Luke, *Phase studies of pozzolanic stabilized calcium silicate hydrates at 180C.* Cement and Concrete Research, 2004. **34**( ): p. 1725 – 1732.

[6] E. R. Buckle and H. F. W. Taylor, *The hydration of tricalcium and dicalcium silicates in pastes under normal and steam curing conditions.* Appl. Chem. , 1959. **9**: p. 163–172.

[7] A. C. Jupe, A. P. Wilkinson, K. Luke, and G. P. Funkhouser, *Class H cement hydration at 180 °C and high pressure in the presence of added silica.* Cement and Concrete Research, 2008. **38**: p. 660–666.

[8] K. Yanagisawa, X. H. A. Onda, and K. Kajiyoshi, *Hydration of β-dicalcium silicate at high temperatures under hydrothermal conditions* Cement and Concrete Research, 2006. **36**: p. 810–816.

[9] F. Meducin, H. Zanni, C. Noik, G. Hamel, and B. Bresson, *Tricalcium silicate (C3S) hydration under high pressure at ambient and high temperature (200 °C).* Cement and Concrete Research, 2008. **38**: p. 320–324.

[10] H. Taylor, *Chapter 11: Admixtures and special uses of cements*, in *Cement chemistry*. 1990, Academic Press: London. p. 365-371.

[11] V. S. Ramachandran, *Application of differential thermal analysis in cement chemistry*. 1969, New York: Chemical publishing company. 308.

[12] G. Bye, *Portland cement*, ed. 2. 1999: Thomas Telford.

MODELLING THE EFFECT OF ELECTRICAL CURRENT FLOW ON THE HYDRATION PROCESS OF CEMENT-BASED MATERIALS

A. Susanto, D.A. Koleva and K. van Breugel
Faculty of Civil Engineering and Geosciences, Delft University of Technology, Section of Materials and Environment, Stevinweg 1, 2628 CN Delft, The Netherlands
a.susanto@tudelft.nl; d.a.koleva@tudelft.nl; k.vanbreugel@tudelft.nl

E.A.B. Koenders
Faculty of Civil Engineering and Geosciences, Delft University of Technology, Section of Materials and Environment, Stevinweg 1, 2628 CN Delft, The Netherlands

Civil Engineering Department-COPPE, Federal University of Rio de Janeiro, 68506 Rio de Janerio, Brazil
e.a.b.koenders@tudelft.nl

ABSTRACT: Stray current is essentially an electrical current "leakage" from metal conductors and electrical installations. When it flows through cement-based systems, electrical energy is converted to thermal energy that causes increasing temperature due to Joule heating phenomena. The aim of this paper is to shed light on the influence of electrical current flow on cement hydration, morphological and structural changes of cement-based systems, emphasizing on the potentially altered temperature effects when electrical current flow is involved. Calorimetry tests show that degree of cement hydration increases as a results of temperature increase due to electrical current flow through cement-based systems. To evaluate the influence of electrical current on the hydration mechanisms in cement-based systems, HYMOSTRUC will be used as a modelling approach, where temperature effects due to electrical current flow are implemented in the existing numerical simulation.
Keywords: Cement hydration, cement-based materials, microstructure, stray current, temperature

INTRODUCTION

Cement hydration plays a critical role in the microstructural development of cement-based systems. Cement hydration is a complex exothermic chemical process, encompassing several phases which are linked to the contribution of different clinker minerals. The hydration process presents a series of chemical and physico-chemical reactions, accompanied by heat generation and heat evolution, which depend on cement composition, cement fineness, and ambient temperature as main factors [1, 2]. This

process is a transformation from a high energy state to a lower one, where the energy is transmitted as heat [3]. By determining the heat of hydration, information about the temperature development during the cement hydration process can be obtained. Temperature is a parameter which significantly affects materials properties and performance of cement-based systems at early age such as strength [4, 5], thermal stress [6] and distress (i.e. cracking) [7, 8].

The temperature development in a cement-based system is not only effected by the above-mentioned internal factors but also related to external factors (i.e. surrounding environment, stray current flow etc.). Stray current can flow in the surrounding medium through conductive paths and can therefore also flow through concrete and reinforced concrete structures. The effects of stray current (both AC and DC) are well recognized in the engineering practice from the view point of steel-corrosion initiation and propagation. However, the influence of stray current and electrical current in general on hydration mechanisms or micro-mechanical properties of concrete structures is not well understood and reports are limited. Electrical energy produced from electrical current flow can be converted to thermal energy that causes increasing temperature in the cement-based systems due to Joule heating phenomena. The amount of released heat is proportional to the square of the electrical current, flowing through the system [9]. The altered heat release will have a potential effect on ion and water transport which will influence the hydration process and the microstructure development. This paper aims to shed light on the influence of electrical current flow on cement hydration, emphasizing on the potentially altered temperature effects when electrical current flow is involved. To evaluate the influence of electrical current on the hydration mechanisms in cement-based systems, HYMOSTRUC will be used as a modelling approach, where temperature effects due to electrical current flow are implemented in the existing numerical simulation. Additionally, isothermal calorimetric tests were performed to evaluate the hydration properties of cement-based systems at early-age. In this paper, the hydration properties are evaluated from hydration parameters including heat release, temperature development and degree of hydration.

EXPERIMENTAL MATERIALS AND METHODS

Materials

The studied specimens were cement paste, cast from Ordinary Portland Cement (OPC CEM I 42.5N), water-to-cement ratio of 0.5. The chemical composition (in wt. %) of OPC CEM I 42.5N (ENCI, NL) is as follows: CaO 63.9%; SiO_2 20.6%; Al_2O_3 5.01%; Fe_2O_3 3.25%; SO_3 2.68%; K_2O 0.65%; Na_2O 0.3 %.

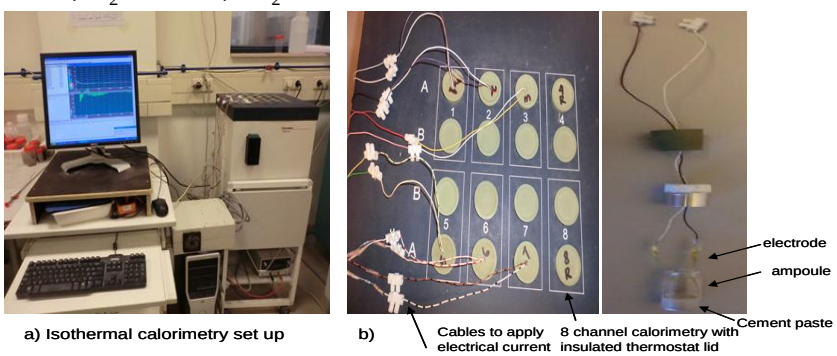

Fig. 1: *(a) Isothermal calorimeter (TAM-Air-314) used to measure heat release of cement paste; (b) Schematic pictures of the holders for "under current" regime*

Methods

Isothermal calorimetry test. The rate of hydration of cement paste was measured by Thermometric isothermal conduction calorimeter (TAM-Air-314) (Figure 1), using 10 ± 0.01g samples and appropriate amounts of mixing water (± 5g); w/c ratio of 0.5 was employed. Before mixing, all the materials were tempered in the oven for at least 12 hours at the desired testing temperature i.e. 20°C. The cement paste was cast into capped glass vials (ampoules) and afterwards placed in the calorimeter. The specimen preparation and experimental procedure followed well known methodology [10], except for the modifications related to the application and monitoring the effect of electrical current flow. The tests were performed on three groups of samples: control (reference) group, "10 mA/m^2" group and "1A/m^2" group, where electrical current flow on the aforementioned levels was relevant for the last two groups. For the "under current" samples, the same ampoules as for the control cases were used, but designed in a way to include two metal electrodes as electrical current conductors (schematic pictures in Fig.1b). Electrical current was applied immediately after samples' casting from an external source. The duration of the measurements was about 10 days. The isothermal heat of hydration was derived by integration of the rate of heat evolution.

Based on the result of heat of hydration from isothermal calorimetry tests, degree of hydration at time *t* can be calculated using the following equation [11, 12]:

$$\alpha = \frac{Q(t)}{Q_{max}} \qquad (1)$$

where Q(t): heat liberated at time t (J/g)- obtained from calorimetry test

Q_{max}: maximum amount of heat liberated at complete hydration (J/g)

Due to electrical current flow through the specimens, maximum amount of heat liberated at complete hydration is calculated as follows:

$$Q_{max} = (Q_{max})_{cem} + (Q_{max})_{el} \qquad (2)$$

where

$(Q_{max})_{cem}$: maximum heat of hydration of Portland cement at complete hydration (J/g)

$(Q_{max})_{el}$: maximum amount of heat liberated by electrical current flow at complete hydration (J/g)

Calculation of maximum heat of hydration of Portland cement ($(Q_{max})_{cem}$) has been proposed by Verbeek [12]:

$$(Q_{max})_{cem} = q_1.(C_3S) + q_2.(C_2S) + q_3.(C_3A) + q_4.(C_3AF) + q_5.(C) + q_6.(M_gO) \qquad (3)$$

where q_1.. q_2: heat of hydration of the constituents considered.

For maximum amount of heat liberated by electrical current flow $(Q_{max})_{el}$ can be calculated using the following equation:

$$(Q_{max})_{el} = I^2 R\, t/m_c \qquad (4)$$

where I is electrical current flow (in Ampere), R is resistance of cement (in Ohm), t is final time (in second) and m_c is mass of cement.

EXPERIMENTAL RESULTS

The effect of electrical current flow on the rate of heat release of cement paste, determined by isothermal calorimetry at 20°C is depicted in Figure 2. The tests were

continued for a longer than the generally accepted time-frame of 3-5 days (i.e. for 250h) in order to evaluate possible current-induced alterations in heat release on later stages. As seen from Fig. 2, the electrical current flow in both current regimes exerts higher heat release within the first hours of cement hydration, compared to the control specimen. Higher current density (1A/m^2) leads to a higher heat release, compared to lower current density (10mA/m^2). What can be also observed is that this influence is not proportional to the amount of current, flowing through the specimens i.e. the difference between values for "10 mA" and "1A" regimes is not as significant as compared to the control case. The result can be attributed to effects on microstructural properties as pore network connectivity and permeability. When electrical current flow is involved, ion and water migration in the matrix takes place, rather than diffusion-related ion and water transport only. Therefore, different levels of current flow will lead to different rates of hydration products formation and distribution. Microstructural analysis is necessary to evaluate these effects, which is an on-going investigation and not subject to this contribution. The results from isothermal calorimetry are in good agreement with the hypothesized effects on ion and water migration, the heat released being proportional to the square of the electrical current, flowing through the cement-based systems. An increasing heat release due to current flow can be seen at about 2 to 60 hours during the hydration process, namely the main peaks at about 11 to 14 hours (Fig.2). There is only a moderate effect in the dormant period of cement hydration (at about 2 hours after mixing). At later stage (> than 150h), the effect of electrical current is not obvious, although slightly higher values were recorded until the end of the test.

Figure 3 shows heat capacity and the temperature development for the control specimens and those under current flow, calculated from calorimetry data. Heat capacity of the systems that contributes to the temperature development was calculated using the following equation:

$$C_{psystems} = \{m_w(1-\alpha)\}C_{pw} + \{m_{ci} + \alpha m_w\}\, C_{pc} \quad (5)$$

where, m_w is mass of water (kg), m_{ci} is initial mass of cement (kg), C_{pw} is heat capacity of water (J/kg K), C_{pc} is heat capacity of cement (J/kg K), and α is degree of hydration.

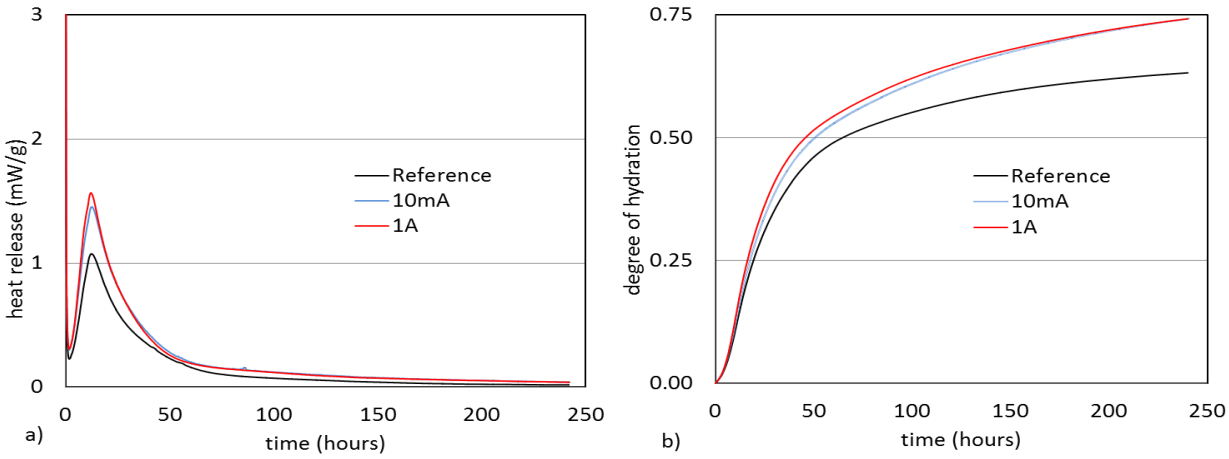

Fig. 2 Heat released (a) and degree of hydration (b) as function of time for cement paste with w/c 0.5

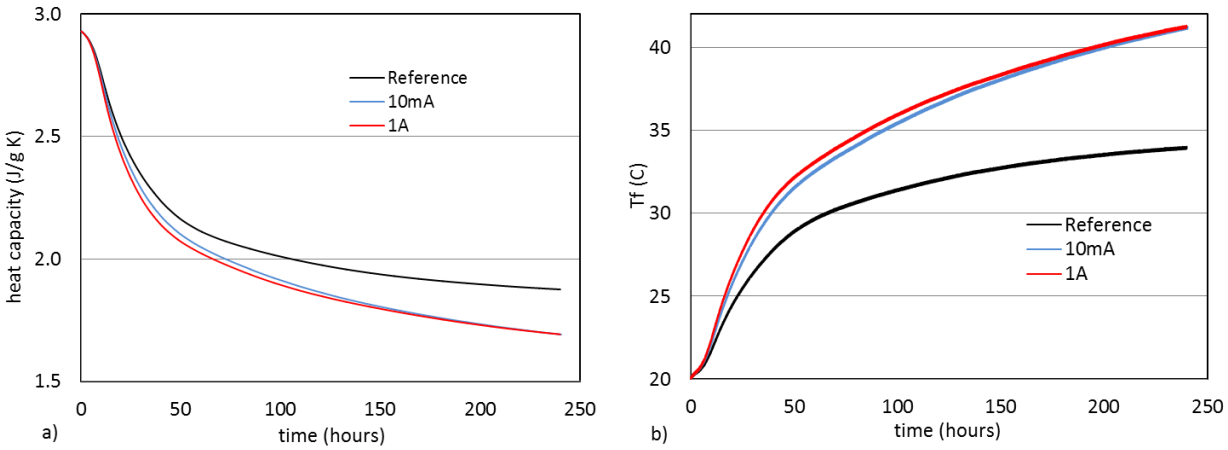

Fig.3: *Heat capacity (a) and temperature development (b) for control and "under current" samples, calculated from calorimetry test.*

Fiq. 3 shows that temperature increase with decreasing heat capacity of the cement-based systems. The trend of temperature development due to current flow in the cement-based materials is in line with the recorded heat evolution. Basically, the hydration of cement paste is accompanied by heat release, which causes a temperature rise in the cement paste. The more pronounced temperature increase in groups "10 mA" and "1A" can be associated with the electrical current, flowing through the samples. Temperature increases due to electrical current flow (Fig. 3) can be extracted from the calorimetry test data using equation (6):

$$T_f = \frac{1}{m_c} \int_{t_o}^{t_n} \frac{P(t)}{c(t)}\, dt + T_i \qquad (6)$$

where c is heat capacity of cement (J/kg. K), m_c is mass of cement (kg), P(t) is thermal power (Watt), Q(t) is thermal energy per mass (J/g), T_i is initial temperature before electrical current applied (K) and T_f is final temperature after electrical current applied (K).

Q(t) can be calculated using the following equation:

$$Q(t) = \frac{1}{m} \int_{t_o}^{t_n} P(t)dt \qquad (7)$$

Figure 4 shows the temperature increase in the cement-based systems due to electrical current flow as a comparison of the two current regimes. It accelerates the degree of cement hydration. This phenomena follows Arrhenius' equation that indicate temperature dependence of reaction rates (i.e. degree of hydration).

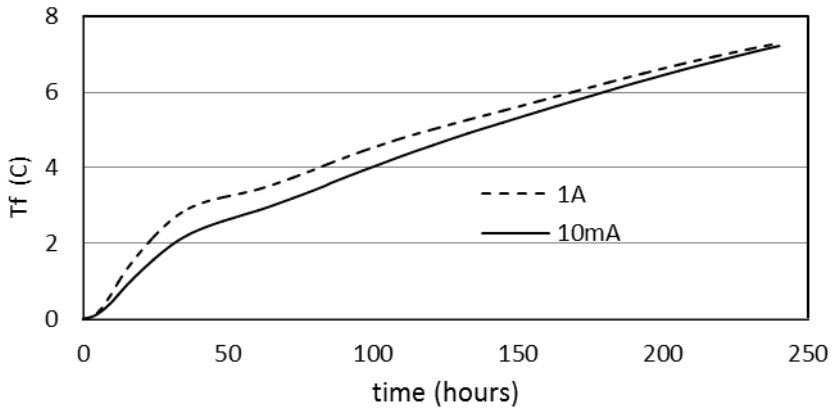

Fig. 4: *Temperature increase in the cement-paste samples due to electrical current flow*

MODELING APPROACH

The temperature development has a significant influence on the hydration process of cement-based systems. It influence the quality and performance of concrete structures. Electrical current flow has the potential to enhance the related temperature increase due acceleration of ion and water migration and thus overall cement hydration rate, including the Joule heating effect. Therefore, with regard to risks when structures are potentially exposed to electrical current (including stray current) flow, it is necessary to predict the temperature development in order to avoid thermal stresses or risk of early age cracking. If electrical current is applied to the cement-based materials with electrical resistance R, mass m, and heat capacity c, the temperature will increase following the equation below:

$$T_f(t) = \frac{I^2\ R(t)\ t}{m_c\ c\ (t)} + T_i \qquad (8)$$

The resistance (R) is a function of time and depends on several physical parameters such as porosity, degree of hydration, chemical composition and ionic strength of the pore solution etc. At this stage, the modeling approach considers only porosity as a factor, influencing the resistance development. The general relationship between resistance and electrical resistivity is as follows:

$$R = \frac{\rho\ l}{A} \qquad (9)$$

where R is electrical resistance in ohm, ρ is electrical resistivity in ohm.m, A is the cross section of the cement paste in m^2, and l is the length in m. Electrical resistivity is linked to porosity via the following equation as well [13-15]:

$$\rho\left(\phi\,(t)\right) = \rho_0\ a\ \phi_t^{-m} \qquad (10)$$

Considering equations (8), (9) and (10) the following final dependence can be extracted:

$$T_f(t) = \frac{I^2\ t}{m_c\ c\ (t)}\ \frac{\rho_0\ a\ \phi_t^{-m}\ l}{A} + T_i \qquad (11)$$

where $\rho\left(\phi\,(t)\right)$ is electrical resistivity as function of porosity at time t, ρ_o is resistivity of the pore water in concrete, c is total heat capacity (J/(kg.K)), m is cementitious factor, l is length of the sample (m), A is surface area (m^2), ϕ is porosity, and a is constant.

The above considerations can be substituted in the HYMOSTRUC model, by implementing the effects of electrical current flow on temperature effects. The effect of temperature-induced morphological and structural changes due to electrical current flow, and the ratio between the volume of reaction product and reactant (ν-factor) [11] can be presented as follows:

$$\nu\left(T_f\right) = 2.2 * e^{-28\ .10^{-6}\ \left\{T + \frac{I^2\ t}{m_c\ c\ (t)}\ \frac{\rho_0\ a\ \phi_t^{-m}\ l}{A} + T_i\right\}^2} \qquad (12)$$

This relation will be applied to each individual cement particle in the cement system and will affect the amount of outward growth of the calcium silicate hydrate (C-S-H) gel, depending on the strength of the electrical current flow. With this, the microstructure formation will respond to the electrical current in terms of porosity changes, which will implicitly affect the strength. Less outward expansion of the C-S-H gel will cause less internal bonding between the hydrating cement particles and affect mechanical properties. The porosity increase will be a way to measure the quantitative effect of it. This is one of the experimental techniques that will be used to validate the implementation.

CONCLUSIONS

This paper discussed the influence of electrical current flow on the hydration process of cement-based materials. The following conclusions can be summarized:

1. Electrical current, flowing through cement-based systems accelerates the degree of cement hydration as a result of temperature increase.
2. By implementing the effect of electrical current flow on temperature, resistivity and porosity of the cement matrix, a modified equation for the ratio between the volume of reaction product and reactant (the ν-factor) can be introduced in the HYMOSTRUC model. The model will predict the temperature-induced morphological and structural changes due to electrical current flow. The evolution of cement hydration and microstructural changes can be simulated in time. The modeling results will be validated by experimental tests for porosity, pore size distribution and permeability.

REFERENCES

[1] Hewlet PC, *Lea's chemistry of cement and concrete*, 4th ed. Oxford: Butterworth-Heinemann, 2004.

[2] Taylor HFP, Cement chemistry, 2nd ed. London: Thomas Telford, 1997.

[3] Mindess S., Young J.F., Darwin D. (2003). *Concrete*: Prentice-Hall, Upper Saddle River, New Jersey, USA.

[4] W.M. Hale, T.D. Bush, B.W. Russell, S.F. Freyne, *Effect of curing temperature on hardened concrete properties*, Transportation Research Record: Journal of the Transportation Research Board 1914 (2005) 97–104.

[5] R.C. Tank, The rate constant model for strength development of concrete, Ph.D. Dissertation, Polytechnic University, Brooklyn, New York, 1988.

[6] H.T. Yu, L. Khazanovich, M.I. Darter, A. Ardani, *Analysis of concrete pavement responses to temperature and wheel loads measured from instrumented slabs*, Transportation Research Record 1639 (1998) 94–101.

[7] T. Nishizawa, T. Fukuda, S. Matsuno, K. Himeno, *Curling stress equation for transverse joint edge of a concrete pavement slab based on finite-element method analysis*, Transportation Research Record 1525 (1996) 35–43.

[8] A.R. Mohamed, W. Hansen, *Effect of nonlinear temperature gradient on curling stress in concrete pavements*, Transportation Research Record: Journal of the Transportation Research Board 1568 (1997) 65–72.

[9] Alexandra von Meier, *Electric power systems: a conceptual introduction*, p67, 2006, John Wiley & Sons, USA.

[10] L. Wadso, An experimental comparison between isothermal calorimetry, semi-adiabatic calorimetry and solution calorimetry for the study of cement hydration, NORDTEST Report 522

[11] van Breugel K. (1991), *Simulation of hydration and formation of structure in hardening cement-based materials*, PhD thesis, Delft University of Technology, the Netherlands.

[12] Verbeek, G.J., 1960, 4th [SCC, Washington, Paper IV-3, pp. 453-465.

[13] P.J. Tumidajki, A.S. Schumacher, S. Perron, P. Gu and J.J. Beaudoin, *On the relationship between porosity and electrical resistivity in cementitious systems*, Cement and Concrete Research, Vol. 26, No. 4, pp. 539-544, 1996.
[14] F. Hunkeler, *The resistivity of pore water solution-a decisive parameter of rebar corrosion and repair methods*, Construction and Building Materials, Vol. 10, No. 5, pp. 381-389, 1996.
[15] H.W. Whittington, J. McCarter, M.C. Forde, *The conduction of electricity through concrete*, Magazine of Concrete Research: Vol. 33, No. 114 : March 1981.

MICROSTRUCTURE AND PHASE ASSEMBLAGE OF LOW-CLINKER CEMENTS DURING EARLY STAGES OF CARBONATION

J. HERTERICH, L. Black and I. Richardson
Institute for Resilient Infrastructure, School of Civil Engineering, University of Leeds, Leeds. LS2 9JT.
cn08j6h@leeds.ac.uk

ABSTRACT: The use of Supplementary Cementitious Materials (SCMs) in the cement industry has become common practice, however, such systems hydrate more gradually than pure Portland Cement (PC) systems. Design models established for PC systems are acceptable when low levels of replacement are used, but may be unsuitable if higher levels of replacement are used. In such systems an understanding of the complex relationship between composite cement hydration, drying of the sample surface and phase carbonation kinetics is imperative. This study investigates the effects of curing length and RH level on very early age composite cement samples (48 hours) cured for periods of 72 hours or less. The data indicates modifications in carbonation behavior compared to 'idealised'/28 day cured systems. Furthermore, the rate of carbonation and nature of the carbonate species formed is dependent on the relative humidity (RH).

INTRODUCTION

Increasing and widespread use of Supplementary Cementitious Materials (SCMs) in the cement industry has become common practice. The use of these composite cements is advantageous in both environmental and engineering aspects, acknowledging the ever rising pressures to further reduce carbon production associated with cement manufacture. It has been well established that utilising SCMs leads to significant reductions in associated CO_2 emissions in addition to notable improvements in terms of durability through enhancement of the cement microstructure; however, development of superior technological properties is reliant on adequate curing. Composite cements exhibit reduced rates of hydration, making them dependent upon extended periods of moist curing. It is demonstrated extensively throughout the literature [1-2] that composite cement materials are more adversely affected by poor and inadequate curing methods than traditional CEMI systems. Failure to adhere to these prolonged curing guidelines by early removal of formwork in construction practice may impact on both durability and strength gain. Information regarding material performance is needed, especially at these very early ages.

Pulverised Fuel Ash (PFA) and Ground Granulated Blast Furnace Slag (GGBS) are industrial waste products and have become the common convention for use as SCMs. Though it is well established that a reduced rate of hydration is observed with both materials, owing to their pozzolanic and latent hydraulic properties, both the PC and the SCM will hydrate simultaneously, yet there is still a significant lack of knowledge regarding the early age kinetics of the reactions taking place. This becomes

of great importance when considering the early removal of formwork in practice where the reliance on models established for PC systems may no longer be suitable. Under such conditions, hydration will be very much incomplete, with previous research indicating minor or no reaction of PFA up to hydration periods of 7 days [3,4] and only slightly faster reaction rates for GGBS[5]. In both cases the result will be an underdeveloped and exposed microstructure, vulnerable to ingress and attack from aggressive species.

The expected retardation of the rate of CO_2 ingress typically observed in PC systems is as a result of densification of the microstructure. This, however, is not concurrent with the behaviour exhibited in high replacement SCM cements, which are adversely affected by a coarser microstructure and greater porosity upon carbonation.

EXPERIMENTAL

Four systems (CEMI, 30% PFA, 30% GGBS & 60% GGBS) at a w/b ratio of 0.57 were investigated in this study, data was collected for paste samples only. A CEM I 52.5R cement (with no additional limestone) was used in all the samples. In order to mimic the procedures commonly followed in practice, curing lengths/t_0 values between 0-72 hours were selected; 24 hours, 72 hours and the time at which a sample had developed a compressive strength of 11MPa. Preliminary testing indicated that a minimum compressive strength of 11Mpa would be required for sample preperation, the equivalent curing lengths for the CEMI, 30% PFA, 30% GGBS and 60% GGBS systems are 17, 72, 24 and 72 hours respectively.

Samples were cast in small plastic vials and cured in a water bath at 20^{o}C +/- 1^{o}C, before being cut to a thickness of 0.5mm and subjected to carbonation at ambient conditions (300-400ppm CO_2, approx. 24^{o}C) for a period of 48 hours at different RH levels (30%, 40%, 55%, 75% & 85%).Characterisation was performed on all the samples at ages of t_0 and 48 hours.

Simultaneous Thermal Analysis (STA) data was collected using a Stanton Redcroft Simultaneous Thermal Analyser STA 780, under a N_2 atmosphere, heating to 1000^{o}C at a rate of 20^{o}C/min. Attenuated Total Reflectance Fourier Transform Infrared Spectroscopy (ATR-FTIR) data was collected using a Thermo Scientific Nicolet Is10 spectrometer, fitted with a Thermo Scientific Smart Diamond ATR sampling accessory, over a wave number range of 0 – 4000cm^{-1}. Data was collected for t_0 samples and RH levels of 40%, 55% and 75%. X-Ray Diffraction (XRD) data was collected using a Bruker D2 Phaser (5^o – 70^o, Cu Kα radiation, 2θ with step size 0.008 and time 1.0s).

RESULTS AND DISCUSSION

Table 1 displays the increase in $CaCO_3$ contents calculated from the TGA data. An increase in carbonation extent with increasing RH level is evident for all the samples, however at the higher humidity levels of 75% and 85%, this was considerably more pronounced.

For optimum carbonation to occur, atmospheric RH levels should lie between 50 – 70%. Low levels of RH induce drying of the capillary pores, greatly reducing the rate of carbonation by reducing the ability for dissolution of both CO_2 and the hydrated

phases. Conversely, high levels of humidity delay hydration by decreasing the rate of CO_2 diffusion through the cement pore structure as a result of water condensation in the capillary pores[6]. The results in Table 1 suggest maximum carbonation at a slightly higher RH range. This is likely to be a result of the very early ages of the samples, compared to the often reported results on 28 day systems. Systems subjected to curing lengths of only a few days, however, will exhibit open and underdeveloped microstructures, and hence be more porous, in which carbonation rate will not be delayed in the same way. This change in behaviour between 'idealised'/28 day lab cured samples and a more realistic curing length, further highlights the necessity for updated carbonation models and approaches.

Table 1. *Calculated $CaCO_3$ content from TGA data showing change in $CaCO_3$ content from t_0*

		Change in CaCO3 content from t0 (%)				
		RH Level				
		30%	40%	55%	75%	85%
72 hr cured	CEMI (0.57)	0.0	0.0	0.8	10.0	7.7
	30% PFA (0.57)	0.7	2.8	4.0	16.4	17.0
	30% GGBS (0.57)	0.5	1.8	3.5	17.3	13.2
	60% GGBS (0.57)	1.9	2.5	7.4	17.8	14.1
24 hr cured	CEMI (0.57)	0.9	2.7	3.6	20.8	17.8
	30% PFA (0.57)	1.3	2.8	5.3	18.9	25.1
	30% GGBS (0.57)	1.1	5.3	4.5	19.8	22.1
	60% GGBS (0.57)					
11MPa cured	CEMI (0.57)	2.2	3.1	8.7	26.6	25.9
	30% PFA (0.57)	0.7	2.8	4.0	16.4	17.0
	30% GGBS (0.57)	1.1	5.3	4.5	19.8	22.1
	60% GGBS (0.57)	1.9	2.5	7.4	17.8	14.1

Effects of curing duration on carbonation behaviour have also been demonstrated. Samples cured for 72 hours display the greatest extent of carbonation at 75% RH, whereas the composite systems display higher levels at 85%. In general the systems cured for 24 and 72 hours show an increase in carbonation for the composite materials at all RH levels. Samples cured to an equivalent compressive strength of 11MPa show decreased carbonate contents with increasing curing lengths. It is evident that carbonation begins almost immediately upon exposure to ambient conditions. The results indicate that, at these very early ages, curing lengths have a sizeable effect on resistance to carbonation, and curing samples for even an additional 48 hours (from 24 hours) demonstrates a marked decrease in carbonation extent. The TGA data plots for the 30% GGBS (0.57) sample cured for 72 hours are displayed in Figure 1(a). It should be noted that Figure 1(a) and 1(b) are representative of all the TGA results obtained.

Typically 3 decomposition modes are associated with carbonation; mode I (780^o – 990^oC), mode II (680^o – 780^oC) and mode III (550^o – 680^oC). The highest decomposition temperature range, mode I, is attributed to the decomposition of well crystallised $CaCO_3$, i.e calcite[6]. Figure 1(a) exhibits a much greater proportion of mass loss at a higher temperature for both 75% and 85% RH. This is also evident in the DTA data for the same samples (Figure 1(b)), in which we can see an increase in decomposition temperature at 75% and 85% RH. This clear shift in decomposition temperature indicates the presence of better structured/crystallised $CaCO_3$, or calcite. The literature suggests decomposition modes I and II may be responsible for the

crystalline polymorphs of $CaCO_3$ (calcite, aragonite & vaterite), while mode III could be associated with amorphous $CaCO_3$. What is clear is a slightly altered mechanism of carbonation depending on the level of humidity.

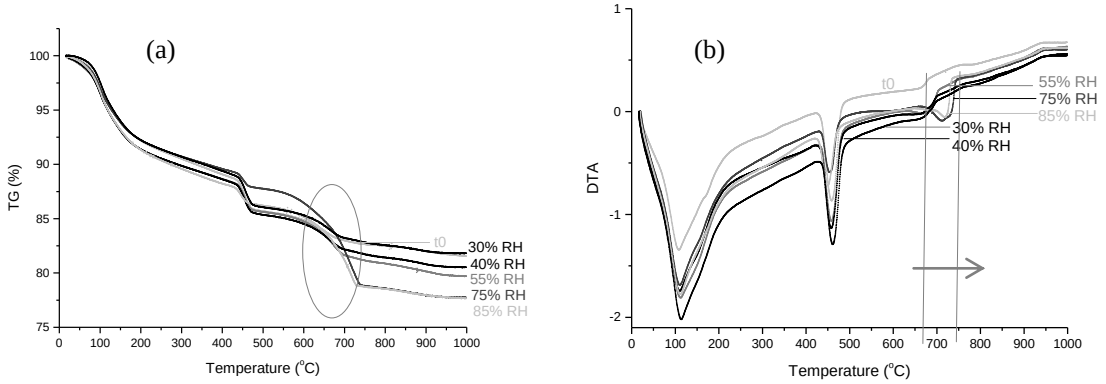

Fig. 1: ***(a)*** *TGA plot for 30% GGBS (0.57) – 72 hour cured at t_0 and RH levels of 30, 40, 55, 75 & 85%* ***(b)*** *DTA plot for 30% GGBS (0.57) – 72 hour cured at t_0 and RH levels of 30, 40, 55, 75 & 85%*

Figure 2 displays the ATR-FTIR data collected for the same sample. The characteristic absorbance band for carbonates lies between 1400 – 1500cm^{-1}, Figure 2 shows that a very clear increase in $CaCO_3$ content is evident with increasing RH level, results consistent with those obtained from STA. Additionally, the ATR-FTIR data displays a change in the shape of the carbonate band, where with increasing humidity a transformation into a much sharper asymmetrical peak is observed. Peak sharpening is an indication of a more crystalline compound, the peak is expected to be narrow if the phases are crystalline, and therefore, conversely, band broadening indicates a phase with a less ordered structure[7]. Furthermore, the nature of various carbonate species can be determined from the shape of the carbonate band. Comparing the spectra obtained for the samples with infrared spectra collected for amorphous $CaCO_3$ and calcite [8] it is clear that both crystalline and non-crystalline phases are present.

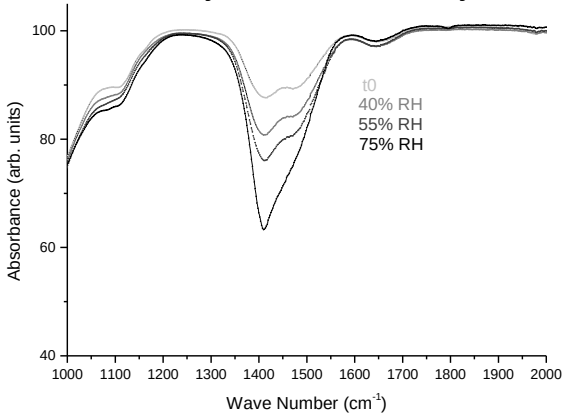

Fig. 2: *ATR-FTIR data for 30% GGBS (0.57) – 72 hour cured showing $CaCO_3$ content between 1000 – 2000cm^{-1}*

At the lower RH levels an amorphous $CaCO_3$ component is present, however a predominantly crystalline $CaCO_3$ phase is formed as the level increases. This verifies the behaviour observed in both the TGA and DTA data where a shift in decomposition temperature suggests the presence of crystalline $CaCO_3$. The ATR spectra confirms the

presence of calcite at 75% RH, and TGA and ATR data both indicate the presence of an amorphous $CaCO_3$ component at lower RH levels.

XRD data (Figure 3) indicates only very minimal change in calcite content at the lower RH levels, however a significant increase is observed at 75% and 85% RH. This, firstly, corroborates the shift to a higher decomposition mode observed in the DTA data, and secondly suggests the presence of an amorphous $CaCO_3$ phase. The $CaCO_3$ content detected using XRD is much lower compared to that indicated by TGA and ATR analysis. As XRD measurements only detect crystalline components, the $CaCO_3$ not accounted for must be, again as previously suggested, poorly crystalline/amorphous.

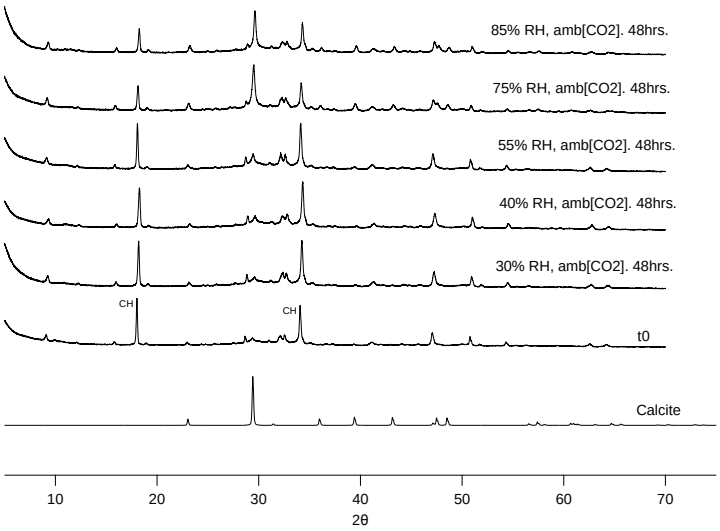

Fig. 3: *XRD data for 30% GGBS (0.57) – 72 hour cured at t_0 and RH levels of 30, 40, 55, 75 & 85%*

Finally, XRD displays a decrease in $Ca(OH)_2$ content with increasing RH, behaviour also observed in TGA and ATR-FTIR data, though not shown here. Silicate bands in the infrared data showed no indication of consumption of C-S-H, whereas a decrease in portlandite content was evident at higher humidity levels. TGA data displayed the lowest calculated $Ca(OH)_2$ levels for the highest carbonation levels, further suggesting that these very early ages it is only the $Ca(OH)_2$ taking place in the carbonation reaction. With increasing exposure length, $Ca(OH)_2$ is expected to be completely consumed and carbonation of C-S-H will be observed.

CONCLUSIONS

- Changes in carbonation behaviour observed between samples cured under ideal conditions, i.e. 28 days, and those cured for very short periods of time, i.e. <72 hours. Carbonation also occurs to a much greater extent in the composite systems, behaviour attributed to a more porous material with a less developed microstructure.
- The mechanism of carbonation appears to be slightly different depending on the level of RH. Higher RH levels, and therefore greater levels of carbonation, gave rise to the production of a more crystalline $CaCO_3$ polymorph (calcite) whereas at lower levels of humidity an amorphous polymorph was observed.
- Curing length has a marked effect on carbonation extent, with even a small increase in curing time showing reduced carbonate contents.

- At these very early ages, it is the $Ca(OH)_2$ involved in the carbonation reaction, as indicated by reduced portlandite contents with increasing carbonate contents.

ACKNOWLEDGEMENT

Acknowledgment would like to be given to Nanocem for the funding and support of this research.

REFERENCES

[1] Poon, C.S., Y.L. Wong, and L. Lam, The influence of different curing conditions on the pore structure and related properties of fly-ash cement pastes and mortars. Construction and Building Materials, 1997. 11(7–8): p. 383-393.

[2] Çakır, Ö. and F. Aköz, Effect of curing conditions on the mortars with and without GGBFS. Construction and Building Materials, 2008. 22(3): p. 308-314.

[3] Fraay, A.L.A., J.M. Bijen, and Y.M. de Haan, The reaction of fly ash in concrete a critical examination. Cement and Concrete Research, 1989. 19(2): p. 235-246.

[4] Deschner, F., et al., Hydration of Portland cement with high replacement by siliceous fly ash. Cement and Concrete Research, 2012. 42(10): p. 1389-1400.

[5] Escalante, J.I., et al., Reactivity of blast-furnace slag in Portland cement blends hydrated under different conditions. Cement and Concrete Research, 2001. 31(10): p. 1403-1409.

[6] Thiery, M., Villain, G., Dangla, P., Platret, G., 2007. Investigation of the carbonation front shape on cementitious materials: Effects of the chemical kinetics. Cement and Concrete Research, 37(7): 1047-1058.

[7] Rikard Ylmen, U.J., 2013. Carbonation of Portland Cement Studied by Diffuse Reflection Fourier Transform Infrared Spectroscopy. International Journal of Concrete Structures and Materials 7(2): 119-125.

[8] Flemming A Andersen, L.B., 1991. Infrared Spectra of Amorphous and Crystalline Calcium Carbonate. Acta Chemica Scandinavica, 45: 1018-1024.

ASSESSING THE RESPONSE OF REINFORCED CONCRETE STRUCTURES WITH SURFACE MOUNTED FIBRE BRAGG GRATING SENSORS

Soretire Okufi
School of Civil and Building Engineering, Loughborough University, Loughborough, LE11 3TU, UK

Chris Goodier
Loughborough University, School of Civil and Building Engineering, Loughborough, LE11 3TU, UK

Vangelis Astreinidis
Civil Engineering Monitoring Ltd, Unit 1, Palmer Business Court, Manor House Road, Nottingham, NG10 1LR

Simon Austin
Loughborough University, School of Civil and Building Engineering, Loughborough, LE11 3TU, UK

Nigel Davison
Civil Engineering Monitoring Ltd, Unit 1, Palmer Business Court, Manor House Road, Nottingham, NG10 1LR

ABSTRACT: The use of fibre Bragg grating (FBG) sensors in field applications is an area of great potential, although it is still in its infancy. This paper evaluates the reasons behind the rapid increase in FBG for structural instrumentation, as well as addressing the adaptability and the limitations of FBG sensors. These points are addressed through a review of three case studies, where FBG sensors are implemented in the instrumentation and assessment of bridges under dynamic loadings. The strain data collected using FBG sensors were compared with other equipment capable of monitoring strains to evaluate the reliability of the FBG sensors. This provides a load history, thus providing historical data to build more sophisticated models. FBG sensors have proved useful in field applications despite their limitations, where the quality of the protective materials is important in reducing the risk of damage to FBG sensors. The major reasons behind their rise in popularity are their versatility and the stability of their readings. The strong correlation between various methods of strain data collection was encouraging, highlighting the repeatability of this technique. This demonstrates that FBG sensors can from part of a bespoke maintenance plan, improving the residual structural life.

Keywords: Fibre optic sensors, installation of sensors, reinforced concrete, strain monitoring, surface mounted sensors.

INTRODUCTION

The demand for fibre optic sensing (FOS) technology has thrived due to the structural state of aging infrastructure. This, coupled with the inherent advantages of fibre optic sensors and recent developments in this field, have led to the transition from laboratory investigations to field applications. The US market for FOS is predicted to triple from year 2011 to 2016 [9] and this figure may not account for the reduction in material costs as the technology improves.

Fibre optic sensors are particularly associated with assessing the structural health of bridges. Their ability to transmit a strong signal over large distances, as well as their resistance to corrosion and electromagnetic interference, have enabled their application in other fields, such as geotechnics and the oil and gas industry. Davies and Buenfeld [2] describe the future potential of FOS in smart buildings, where actuators are installed on the structure and linked to a computer system. This feedback loop can be used to make automated adjustments to the structure which can be controlled remotely.

However, the structural life of a building could potentially exceed that of a sensor, because although the fibre Bragg grating (FBG) sensors can be protected with materials of higher durability, the fibres cannot be manufactured from better materials. The fibre core is made of silica, which would eventually fail due to the aggressive, alkaline environment of concrete. This is one driver behind the investment in designing sensors that are capable of self-assessment.

According to Maaskant et al [7], FBG sensors are increasingly implemented in assessing the performance of new structural materials. This is due to the desire to understand their short term and long term performance, as well as their structural response. A network of researchers in Canada called Intelligent Sensing for Innovative Structures (ISIS) [5] and the Hong Kong Highways Department [1] are championing the integration of fibre optic sensors in the long term assessment of structures.

The research questions in this paper are: (1) what are the reasons behind the increase of FBG sensors in the field instrumentation of structures; and (2) what are the in situ limitations of FBG sensors and how reliable are they? These questions are addressed through reviewing studies where FBG sensors have been used in the instrumentation of three bridges. Chan et al [1] monitored the Tsing Ma Bridge in China, Rodrigues et al [5] investigated the Leziria Bridge on the Portuguese highway (A10) and Maaskant et al [7] monitored the Beddington Trail Bridge in Canada.

THE CASE STUDIES

Chan et al [1] monitored the Tsing Ma Bridge, a large suspension bridge in China with a span of over 1300 m, carrying both railway and highway traffic. The bridge comprises a double deck configuration, the upper carrying six lanes of traffic, and the lower two railway lines and an additional two traffic lanes. A hybrid configuration was adopted, combining a steel truss and box forms. The lateral bending stiffness is provided through cross frames of Vierendeel trusses at 4.5 m centres, where every fourth frame is supported by a suspending cable. A bespoke Wind and Structural Health Monitoring System (WASHMS) was installed after commission in 1997, consisting of approximately 800 sensors to monitor the structural health of the bridge. These include: strain gauges, accelerometers, temperature sensors and level sensors.

Chan et al [1] aimed to assess the performance of a new demultiplexing/interrogation system (DEMINSYS). The data collected from the DEMINSYS system was then compared with the data from the WASHMS system.

Rodrigues et al [5] review evaluates the performance of the Leziria Bridge in Portugal. This 30 m wide, eight-span single prestressed concrete box girder highway bridge opened in 2007. In total, 92 FBG sensors were installed to monitor the structural behaviour of the 970 m main span, including strains, deflections and temperature. Strain gauges were installed at 15 locations on the top and bottom surfaces of the bridge deck.

Maaskant et al [7] monitored the Beddington Trail Bridge in Canada with a span of 42 m. The deck of this three lane bridge is supported by 26 bulb-T girders with a depth of 1.1 m. Six of the girders had carbon fibre reinforced plastic tendons (CFRP). A total of 18 FBG sensors were installed on the tendons, 12 of these on CFRP tendons. Maaskant et al [7] aimed to evaluate the structural response of the structural tendons, manufactured from various materials with different mechanical and thermal properties. The data in this study was collected over 18 months.

Rodrigues et al [5] study had a similar aim to Chan et al [1] to assess the performance of the novel FBG transducers. This bridge already had a built in electrical strain gauge system, so the data collected using these two systems were compared. Both of these studies stemmed from a desire to build a system utilising FBG sensors in structural health monitoring (SHM), under normal loading conditions.

Multiplexing sensors are an attractive feature of FBG as relatively large structures can be monitored with a single interrogator, this tactic was employed by Rodrigues et al [5] and Chan et al [1]. The disadvantage of multiplexing is all sensors past a point of fractures are rendered useless and specialist equipment is required to detect the point of failure, so it is important to specify a suitable protection system. Maaskant et al [7] opted to avoid multiplexing the sensors, this could be due to the relatively small size of the Beddington Trail Bridge. None of the case studies discussed in this paper installed redundancy into the FBG sensing system, this means critical data will be lost if a sensor installed on a critical section fails.

PERFORMANCE OF THE SENSING SYSTEMS

The FOS systems proved to be reliable method of monitoring structural health, under multiple loading conditions. Their high survival rate and its versatility have demonstrated the potential of FBG in SHM. Maaskant et al [7] reported a problem of unreliable equipment, where data on the early behaviour of carbon fibre reinforced plastics (CFRP) tendons was lost. They tested the FBG sensors on a scale model in laboratory conditions, giving the author increased confidence of their performance. Strains of up to 8000 micro strains could be experienced in the reinforcing tendons, which made it difficult to install sensors to verify the performance FBG sensors.

The data acquisition rate utilised depends on the target parameters and the loading conditions. This is demonstrated in table 1, where Chan et al [1] employed a high sampling frequency of 500 Hz to collect strain data under dynamic train loading. Rodrigues et al [5] monitored the impact of dynamic loads utilising a data acquisition rate of 200 Hz, where the bridge was loaded with a truck travelling at 80 km/h. Data on parameters such as temperature and creep can be collected at a low sampling rate, as these parameters are relatively static in comparison to the evolution of strain.

Table 1. *A summary of the data acquisition rates utilised under multiple projects, N/A = not available*

Bridges	Leziria Bridge [5]	Tsing Ma Bridge [1]	Beddington Trail Bridge [7]	West Mill Bridge [11]	Luiz I bridge [6]
Data sampling rate of strain (Hz)	200	500	N/A	100	5
Number of sensors	92	40	18	40	128

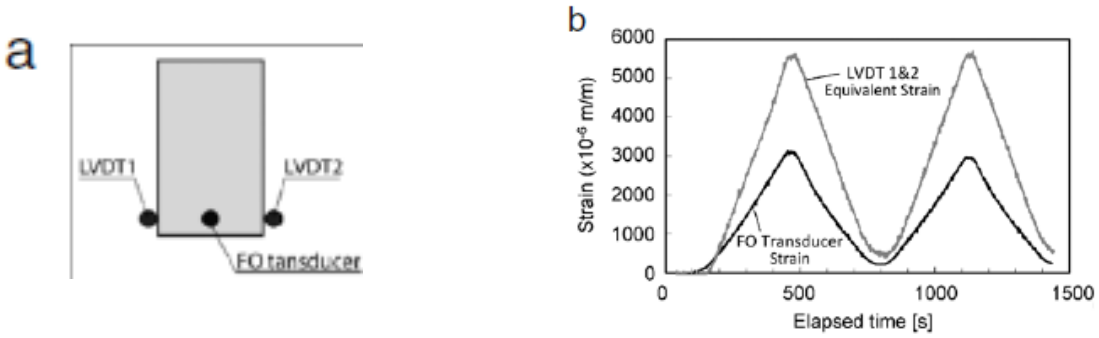

Fig.1: *(a) Location of the FBG sensor and LDVT on the concrete sample; (b) the correlation between the LVDT and FBG sensors (Rodrigues et al [5])*

Figure 1 shows strong correlation between the strain readings collected in laboratory conditions with FBG sensors LVDTs under flexural loading. The difference in magnitude is due to the relative positions of the sensor.

The performance of the DEMINSYS system [1] was assessed by comparing the results with that obtained from the preinstalled strain gauges, this information is presented in figure 2. Again, these sensors are both installed on the same structural member and are in close proximity with each other, the data shows a strong correlation.

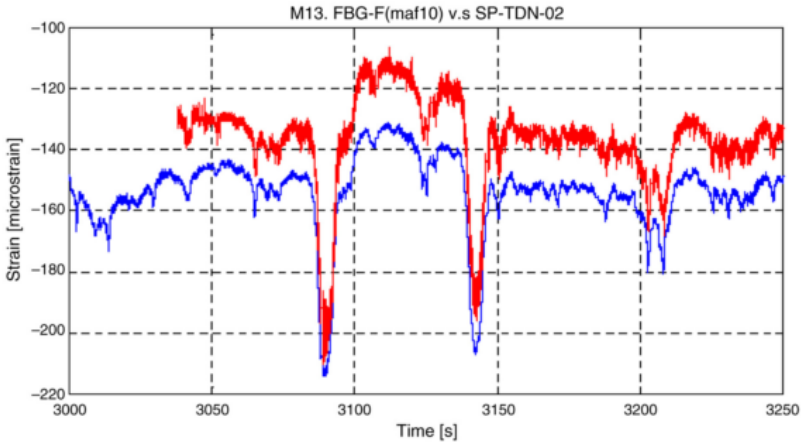

Fig.2: *Comparison between the DEMINSYS (upper) and WASHMS (lower) strain gauges on the truss section (Chan et al [1]).*

FBG sensors also proved versatile, where all case studies utilised bespoke FBG sensors. FBG sensors are attractive as their readings are immune to power fluctuations, proving accurate and repeatable results.

TEMPERATURE CORRECTION OF THE SENSORS

Fibre Bragg gratings (FBGs) are intrinsic sensors, where the grating site on the fibre is photosensitive. When light passes through the fibre core at zero strain, the Bragg wavelength is reflected and this data is captured by an interrogator. As the host material is strained, the attached FBG is also strained, shifting the reflected wavelength; this data can be used to determine the strain of the host material. Davies and Buenfeld [2] explain the influence of temperature and strain on the Bragg wavelength as follows.

The temperature response of the FBG sensor and its substrate differ, so it is important to compensate for this. Sensors are attached to a substrate, hence temperature compensation becomes a necessity. Common practise involves the choice of a jacket and adhesive with a close temperature-response match to the host material. The bridge studied by Maaskant et al [7] utilised prestressed concrete girders, the reinforcing tendons were made of: steel and two reinforcement bars manufactured from two forms of carbon fibre reinforced plastic (CFRP). The materials used all possessed alternative temperature responses to the sensor. The ambient temperature characteristics of the entire structure was utilised in order to make effective compare the behaviour of the materials.

Maaskant et al [7] chose to normalise the strain data to the expected values at 20 ^{o}C. Data on the strain of the tendons were collected on four occasions, of these the ambient temperature was 0 ^{o}C and 6 ^{o}C respectively. The approach to normalise this data to the standard of 20 ^{o}C would rely on empiric formulas and extrapolation, this will provide an estimate rather than information on the actual measured strain. Rather than normalising the data to 20 ^{o}C, an alternative approach would have been to assess the performance of the CFRPs at low temperatures, particularly the effect of freeze thaw on the structural reinforcement material, due to the lack of knowledge of the long term performance of these materials.

Chan et al [1] and Rodrigues et al [5] employed identical techniques to compensate for temperature. Both installed separate FBG strain and temperature sensors, and this information was then utilised to compensate for the temperature response of the structure.

CONCLUSIONS

This paper reviewed three studies where in situ FBG sensors were employed. The advantages of FBG sensors such as its versatility, reliability and multiplexing abilities are discussed in this paper and are the major reasons for the increased interest in FBG sensors. The limitations of this sensor were also highlighted, providing a balanced view for engineers who require structural instrumentation. A common theme amongst the case studies was the high correlation of data between FBG sensors and strain gauges, both on site and in field applications, highlighting the reliability of FBG sensors.

Fibre optic sensors have proved their potential value in the field of SHM. A potential application of FBG sensors would be to provide an alternative method to visual inspection, providing an objective and automated approach to SHM. Concrete is a heterogeneous material, making it difficult to predict the exact location of crack propagation. Visual inspections will be necessary until a solution to this problem is found.

FBG sensors are often suggested as a method of evaluating the effectiveness of composite materials in the rehabilitation of concrete structures. This ambition has proved more difficult than noted in the study by Maaskant et al [7]. Lau et al [10] developed a mathematical model to predict the interaction between the adhesive layer and an optical sensor. Further work on refining the model to describe this relationship would be helpful in improving the quality of in-situ data collected. Of particular interest would be developing a model describing the behaviour of a sensor where two adhesives are employed, as implemented on the Tsing Ma Bridge by Chan et al [1].

REFERENCES

[1] Chan T H T, Yu L, Tam H Y, Ni Y Q, Liu S Y, Chung W H and Cheng L K. Fibre Bragg grating sensors for structural health monitoring of Tsing Ma bridge: Background and experimental observation. *Engineering Structures,* 2006, 28 (May) 648–659.

[2] Lau K, Yuan L, Zhou L, Wu J and Woo C. Strain monitoring in FRP laminates and concrete beams using FBG sensors. *Composite Structures,* 2001, 51 (January) 9–20.

[3] Li H-N, Li D-S and Song G-B. Recent applications of fibre optic sensors to health monitoring in civil engineering. *Engineering Structures,* 2004, 26 (November) 1647–1657.

[4] Majumder M, Gangopadhyay T K, Chakraborty A K, Dasgupta K and Bhattacharya D K. Fibre Bragg gratings in structural health monitoring—Present status and applications. *Sensors and Actuators A: Physical,* 2008, 147 (January) 150–164.

[5] Rodrigues C, Félix C, Lage A and Figueiras J. Development of a long-term monitoring system based on FBG sensors applied to concrete bridges. *Engineering Structures,* 2010, 32 (February) 1993–2002.

[6] Costa B J A and Figueiras J A. Fiber optic based monitoring system applied to a centenary metallic arch bridge: Design and installation. *Engineering Structures,* 2012, 44 (June) 271–280.

[7] Davies R D and Buenfeld N R. *Automated Monitoring of the Deterioration of Concrete Structures.* DTI/CIRIA Report, 2007.

[8] Maaskant R, Alavie T, Measures R M, Tadros G, Rizkalla S H and Guha-Thakurta. A Fibre-optic Bragg grating sensors for bridge monitoring. *Cement and Concrete Composites,* 1997. 19 (January) 21–33.

[9] Peach M. Fiber-optic sensors set for ‘impressive’ sales growth 20 Jun 2012. Available at: http://opticsorg/news/3/6/27/.

[10] Lau K, Yuan L, Zhou L, Wu J and Woo C. Strain monitoring in FRP laminates and concrete beams using FBG sensors. *Composite Structures,* 2001, 51 (January) 9–20.

[11] Gebremichaela Y M, Lia W, Boylea W J O, Meggittb B T, Grattana K T V, McKinleya B, Fernandoc G F, Kisterc G, Winterc D, Canningd L and Luked S. Integration and assessment of fibre Bragg grating sensors in an all-fibre reinforced polymer composite road bridge. *Sensors and Actuators A,* 2005, 118 (August) 78–85.

RESIDUAL BOND STRENGTH BEHAVIOUR OF CORRODED REINFORCEMENT IN NATURAL CORROSIVE ENVIRONMENT

Jaya Nepal and Hua-Peng Chen*
School of Engineering, University of Greenwich, Chatham Maritime, Kent, UK
j.nepal@greenwich.ac.uk and * Corresponding author: h.chen@greenwich.ac.uk

ABSTRACT: This paper aims to investigate the effects of the reinforcement corrosion on the residual bond strength behaviour of corrosion damaged reinforced concrete structures in natural corrosive environments. The analytical solutions of residual bond strength of corroded concrete structures are used to evaluate the bond behaviour of Ullasund bridge, Norway, which was demolished in 1998. The results obtained from the study have been examined with the published field data. The study concludes that the bond strength in concrete increases in low level of corrosion (<1%) and decreases significantly with further increase in corrosion due to longitudinal cracking of the concrete cover. The proposed approach is capable of assessing the bond strength behaviour of corrosion affected concrete structures.
Keywords: Bond strength; concrete cracking; deterioration; reinforcement corrosion.

INTRODUCTION

Reinforcement corrosion is one of the most common causes of deterioration in reinforced concrete (RC) structures. It affects the bond strength at steel-concrete bond interface by changing mechanical interlocking and frictional force between concrete and reinforcement (rebar) [1] . This ultimately affects the performance of the RC structures. Many investigations have been undertaken in the past for the evaluation of residual bond strength of corroded RC structures in controlled conditions using accelerated corrosion technique. However these works are performed on the artificially corroded RC specimens [2,3]. They do not resemble the actual behaviour of specimens which are corroded for long time in the natural environment. Therefore, in order to obtain the better understanding of the bond behaviour in reality, it is necessary to investigate the bond behaviour of RC structures corroded naturally. This study aims to investigate the bond behaviour of corroded RC structures in natural aggressive environment. A case study of the Ullasund bridge, Norway, demolished in 1998 is therefore discussed.

CORROSION – INDUCED CONCRETE CRACKING

Assuming the constant current density i_{corr}, the uniform corrosion depth or the radius loss of the rebar is defined as $x = R_b - R_{rb}$ in which R_b = initial radius of the rebar and R_{rb} = reduced rebar radius. Its corresponding corrosion level is defined as $x_p = (W_o - W_s)/W_o \times 100\%$ where W_o is the original weight of the rebar and W_s is the remaining weight of the corroded rebar.

The corrosion products formed are expansive in nature. Due to its expansive nature, radial and hoop stresses are developed at the rebar surface. When this hoop stress on the concrete surface reaches the tensile strength of concrete, radial splitting cracks are formed at the bond interface and these cracks propagate until they reach the concrete surface R_c. The concrete cracking process due to reinforcement corrosion was investigated analytically by [4,5]. Considering thick walled cylinder model as shown in Fig. 1 and bilinear tension softening law of cracked concrete, the normalised crack width at the rebar surface can be expressed as [5]

$$W_b = \frac{1}{b(l_o - R_b)}\left(\frac{E}{f_t}u_b - aR_b\right) \quad (1)$$

where *a* and *b* are the coefficients of bilinear softening curve depending on w_{cr} = critical crack width and w_u= ultimate cohesive crack width; $l_o = \frac{n_c l_{ch}}{2\pi b}$ is the material constant in which n_c is the number of crack taken as 4 for thick walled cylinder model and l_{ch} is the characteristic length; E = effective modulus of elasticity of the concrete; f_t = tensile strength of the concrete and u_b = axis symmetric radial displacement at the rebar surface. The relation between normalised crack width W and actual crack width is defined as $W = f_t w(r)/G_f$ where G_f is the fracture energy of the concrete; $w(r)$ is the actual crack width at any point r between R_b and R_c and its value does not exceed w_u. w_{cr} and w_u depends on the concrete strength and the maximum aggregate size D_a [6].

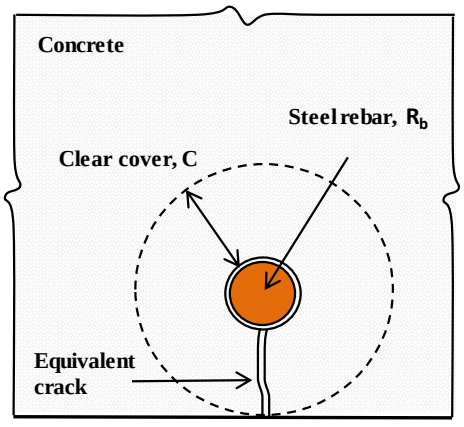

Fig.1 *Idealisation of cover concrete as thick-walled cylinder model for predicting concrete crack development and bond strength evolution.*

The mass of the corrosion product responsible for the radial displacement u_b and reduced radius of the rebar R_{rb} could be estimated from

$$M_r = \frac{\pi}{\alpha_m}\left(2R_b u_b + {u_b}^2\right) \quad ; \quad R_{rb} = \left(R_b^2 - \frac{\alpha M_r}{\pi}\right)^{1/2} \quad (2)$$

where $\alpha_m = \frac{1}{\rho_r} - \frac{\alpha}{\rho_s}$ in which ρ_s is the density of the steel; and $\rho_r = \frac{\rho_s}{\alpha\alpha_1}$ is the density of the corrosion product in which α and α_1 are the molecular weight ratio and the volume ratio of the corrosion products respectively [7].

BOND STRENGTH BEHAVIOUR

The design bond strength of any RC structures is the function of the compressive strength of the concrete f_{ck} [6,8], estimated from one of the following

$$T_{ubo} = 0.894\sqrt{f_{ck}} \quad ; \quad T_{ubo} = 0.315{f_{ck}}^{2/3} \qquad (3a,b)$$

The ultimate bond strength for corroded reinforcement at any corrosion level is the total contribution of three types of stresses acting at the bond interface [1]

$$T_{ub}(x_p) = T_{ad} + T_{cnf} + T_{corr} \qquad (4)$$

The adhesion stress acting between rebar and concrete is given by

$$T_{ad} = \frac{n_{st}\, A_r f_{coh}\, [cot\, \delta_o + tan(\delta_o + \varphi)]}{\pi D_{rb} S_r}$$

where n_{st} is the number of stirrups; $A_r = \pi D_{rb} h_r$ is the rib area; D_{rb} = reduced diameter of the rebar; $h_r = 0.07 D_{rb}$ is the reduced rib height of the rebar; $f_{coh} = 3.41 - 21.21(x - x_c)$ is the adhesion strength coefficient in which x_c is the corrosion depth corresponding to the through cracking of the concrete cover; δ_o and φ are the orientation of the rib and the angle of friction between steel and concrete respectively ; $S_r = 0.6 D_b$ is the rib spacing in which D_b is the original diameter of rebar [9] and $tan(\delta_o + \varphi)$ can be estimated from $1.57 - 0.785x$.

The confinements stress $T_{cnf} = k_{cnf} P_{cnf}$ where k_{cnf} is the coefficient of confinement stress evaluated from $n_{st}\, C_r tan(\delta_o + \varphi)/\pi$ in which C_r is the shape factor constant taken as 0.8 for crescent shape rebar. P_{cnf} is the the total confinement stress contributed by the concrete and the stirrups. For thick walled cylinder model P_{cnf} given by [10] can be expressed as

$$P_{cnf} = \left[\frac{C - u_b}{R_{rb}}\right] \times f_t \frac{1 - \frac{w_b}{w_u}}{1 + \frac{k.w_b}{D_a}} + \left[\frac{n_{st} a_{st}}{D_{rb}\, \Delta z}\right] \times E_{st} \sqrt{\frac{a_2 w_b^2}{\alpha^2 d_{st}^2} + \frac{a_1 w_b}{\alpha d_{st}} + a_o} \qquad (5)$$

where $C = R_c - R_b$ is the clear cover depth; k is the constant taken as 167; w_b is the actual crack width at rebar surface; a_{st} is the cross-section area of stirrup leg with diameter of d_{st} ; Δz is the spacing of stirrup; E_{st} is the modulus of elasticity of steel; α is the shape factor of stirrup taken as 2; a_2, a_1 and a_o are coefficients related to trilateral local bond-slip law of the stirrup.

Corrosion stress due to accumulating corrosion product at rebar surface is defined as $T_{corr} = \mu P_{corr}$, in which μ is the coefficient of friction between corroded rebar and cracked concrete defined as $0.37 - 0.26(x - x_c)$ and P_{corr} is the corrosion pressure. The corrosion pressure acting at rebar surface is given by [5]

$$P_{corr} = \frac{f_t}{1 - \vartheta^2}\left\{(a - bW_b)\left(1 + \nu\sqrt{\beta_b}\right) + b(l_o - R_b)\frac{dW}{dr} + \nu\sqrt{\beta_b}\frac{l_o}{R_b} bW_b\right\} \qquad (6)$$

where $W = c_1\delta(l_o,r) + c_2$ is the normalised crack width in which $\delta(l_o,r) = \frac{1}{l_o(l_o-r)} - \frac{1}{l_o^2} ln\frac{|l_o-r|}{r}$; c_1 and c_2 are the functions of W_b to be determined by two boundary conditions $W\big|_{r=r_h} = W_b$ and $W\big|_{r=r_c} = W_c$; $\beta_b = 1/\left(1 + \frac{bl_oW_b}{(a-bW_b)R_b}\right)$ is the stiffness reduction factor and ϑ is the Poisson's ratio of concrete. Once normalised crack width W is available other parameters such as dW/dr and actual crack width at the cover surface w_c can be calculated.

CASE STUDY

In order to investigate the effectiveness of the proposed approach, the analyses are now carried out by taking published field data of Ullasund bridge, Norway. It was demolished in 1998, only after 29 years of service in harsh environments [11]. From the pieces of concrete collected from Ullasund bridge, 22 cubic specimens with dimensions of 150 mm × 150 mm × 150 mm and single ribbed rebar were prepared. The yield strength of the rebar was 400 MPa and the compressive strength of the concrete was 40.3 MPa. Bond strength of each specimen was determined by pull-out test and the corresponding corrosion products were determined by sandblasting. Material properties required for this analytical model are assumed: total crack number $n_c = 4$; Poisson's ratio ϑ = 0.18; creep coefficient $\emptyset_c$ = 2.0 and i_{corr} = 1 μA/cm^2; G_f =200 N/m; ρ_s = 7850kg/m^3; α_1= 2.0; and α= 0.725. Equivalent critical crack width w_{cr} = 0.2 mm and ultimate crack width w_u = 1.6 mm have been obtained from [6] for adopted maximum aggregate size D_a = 16 mm. Other parameters such as f_t = 4.6 MPa; E_c = 37.1 GPa are obtained from [8]. The comparison of predicted results with the field data of Ullasund bridge and design bond strength according to [6,8] have been shown in Fig. 2.

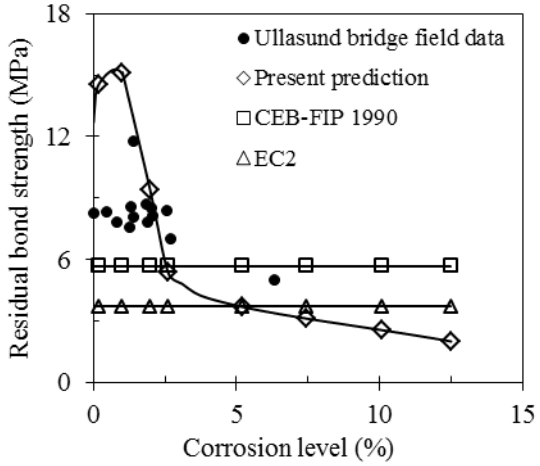

Fig.2: *Residual bond strength vs. corrosion level.*

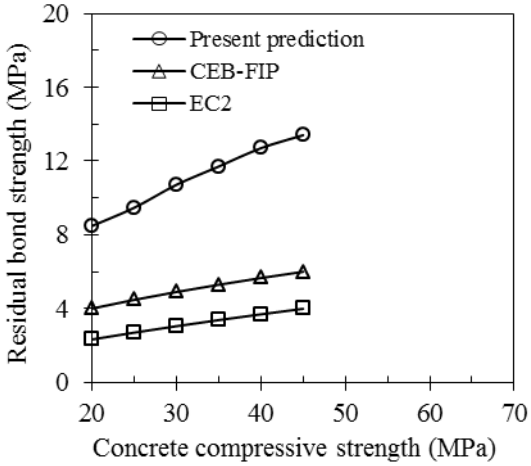

Fig.3: *Residual bond strength vs. concrete compressive strength.*

It can be seen from the comparison, the results obtained from the present study are in good agreement with the field data. The predicted bond strength in low corrosion level (<1%) is slightly higher than field data, this may be due to the difference between the material properties of the concrete assumed in the present model and the actual material properties of Ullasund bridge. The difference may be also due to the

complexity of the reinforcement corrosion and cover cracking mechanism in reality. It is clear from the Fig. 2 that at the low level of corrosion(<1%) there is slight increase in bond strength, but further increase in corrosion leads to significant reduction in bond strength as observed in the field data caused by the longitudinal cracking of the concrete cover. It is interesting to see that at about 2.5% corrosion level the specimen reaches the design bond strength as given by [6] whereas at about 5% corrosion level it reaches the design bond strength value as given by [8].

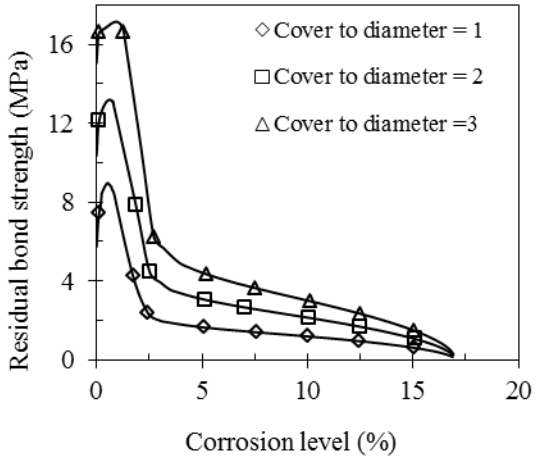

Fig.4: *Residual bond strength vs. corrosion level for different cover to rebar diameter ratios.*

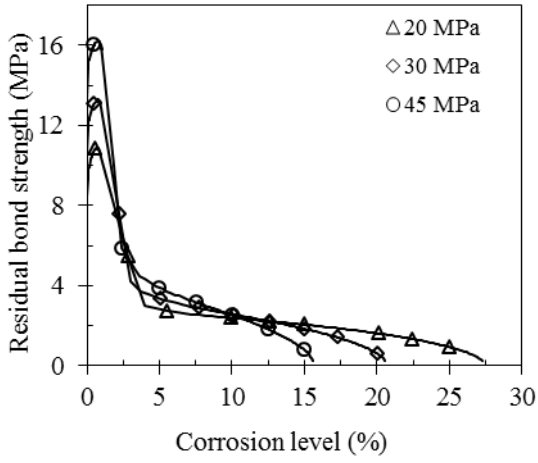

Fig.5: *Residual bond strength vs. corrosion level for different compressive strengths of the concrete.*

Fig. 3 shows the variations between the predicted bond strength and the design bond strength of the un-corroded rebar for different compressive strengths of the concrete. The predicted results are higher than the design bond strength. This may be due to the fact that the design bond strengths are only based on the compressive strength of concrete whereas the predicted results are based on mechanical as well as geometrical properties of both the rebar and the surrounding concrete. Fig. 4 and Fig. 5 show the influence of cover to rebar diameter ratio and the compressive strength of the surrounding concrete on the bond strength deterioration process, respectively. From Fig. 4, bond strength at the rebar surface increases as the cover to rebar diameter ratio increases. This may be due to the increase in resistance created by the larger cover depth. The results from Fig. 5 show that at low level of corrosion residual bond strength increases with higher value of compressive strength but the residual bond strength decays faster for higher compressive strength at relatively lower corrosion level. This may be due to the acceleration of cover cracking process caused by increase in the modulus of elasticity of the concrete and decrease in ultimate crack width for higher compressive strength.

CONCLUSIONS

On the basis of the results from the case study involving the residual bond strength strength behaviour of corrosion damaged RC structure exposed to the natural corrosive environment, the following conclusions are noted: a) At low level of corrosion (<1%) , ultimate bond strength increases, following by considerable decrease as corrosion

progresses; b) At corrosion level of about 2-5% , it reaches its design bond strength value; c) Bond strength decreases significantly when concrete is fully cracked; d) Increase in concrete strength or cover depth, the bond strength increases; e) With only low mass loss of reinforcement there is significant reduction in bond strength; f) The proposed approach can be an effective and useful tool in evaluating residual strength of any types of corroded RC structures exposed in aggressive environments, however more research is required to understand the bond strength deterioration in natural aggressive environments.

REFERENCES

[1] Coronelli D. Corrosion cracking and bond strength modelling for corroded bars in reinforced concrete. *ACI Structural Journal*, 2002, 99(3) 267–276.

[2] Law D W, Tang D, Molyneaux T K C and Gravina R . Impact of crack width on bond: confined and unconfined rebar. *Materials and Structures*, 2011, 44(7) 1287-1296.

[3] Lee H S, Noguchi T and Tomosawa F. Evaluation of the bond properties between concrete and reinforcement as a function of the degree of reinforcement corrosion. *Cement and Concrete Research*,2002, 32(8) 1313-1318.

[4] Chen H P and Alani A M . Optimized maintenance strategey for concrete structures affected by cracking due to reinforcement corrosion. *ACI Structural Journal*, 2013, 110(2) 229-238.

[5] Chen H P and Xiao N. Analytical solutions for corrosion-induced cohesive concrete cracking. *Journal of Applied Mathematics*, 2012, Article ID 769132.

[6] Comité Euro-international du Béton - Fédération International de la Précontrainte (CEB-FIP). *Design code*. Thomas Telford, London, 1990.

[7] Bhargava K, Ghosh A K, Mori Y, and Ramanujam S. Model for cover cracking due to rebar corrosion in RC structures. *Engineering Structures*, 2006, 28(2) 1093–1109.

[8] Eurocode 2. *Design of concrete structure*. European comitee for standardization, Brussels, 2002.

[9] Wang X and Liu X . Modelling effects of corrosion on cover cracking and bond in reinforced concrete. *Magzine of Concrete Research*, (2004), 56(4) 191-199.

[10] Giuriani E, Plizzari G, and Schumm C. Role of stirrups and residual tensile strength of cracked concrete on bond. *Journal of Structural Engineering ASCE*, 1991, 117(1) 1-18.

[11] Horringmoe G, Saether I, Antonsen R and Arntsen B. *Laboratory investigations of steel bar corrosion in concrete Background document SB-3.10*. Sustainable Bridges, Norut Technology, 2007.

DEVELOPMENT OF MICROENCAPSULATED HEALING AGENTS FOR SELF-HEALING CEMENTITIOUS COMPOSITES

C Litina, A Kanellopoulos, A Al-Tabbaa
Engineering Department, University of Cambridge, Trumpington Street, Cambridge CB2 1PZ, UK
cl519@cam.ac.uk, *ak880@cam.ac.uk*, *aa22@cam.ac.uk*

ABSTRACT: Concrete is susceptible to numerous environmental factors which generate cracking that propagates through the material causing damage to accumulate and lead to failure. Traditional design is based on the prevention and delay of those first instances of cracking allowing for subsequent external application of post-damage repair works. However that does not offer a sustainable solution for the management and maintenance of infrastructure installations and in particular in the case of remote, often costly, systems.

Our research proposes the application of natural concepts of adaptability and self-healing on cementitious composites for damage control and recovery of functionality. An intrinsic self-sustained recovery system is suggested based on the inclusion of repair agents within the concrete matrix. Thus defects will be detected and recovered spontaneously by mobilising the appropriate healing agent in the damaged location. Micron-sized polymeric vessels are utilised as carriers of healing agents and are embedded in the cement matrix. These hinder the accumulation of damage by bonding the crack surfaces and controlling the propagation of cracks within the material. Moreover the versatility of the shells allows the inclusion of a wide range of materials capable of targeting specific degradation mechanisms, such as corrosion.
Keywords: Cement composites, interfacial polymerisation, methyl methacrylate, microencapsulation, self-healing, urea-formaldehyde

INTRODUCTION

Structural materials undergo a wide variety of defects, due to mechanical or environmental loading. These defects induce damage in the form of cracks which might subsequently propagate leading to accelerated failure and will consequently significantly decrease their service life.

A proposed solution evolves the development of an adaptable engineered autonomic self-healing system through the incorporation of a composite encapsulated liquid healing compound and catalyst. Generally the concept of microencapsulation of self-healing agents has been widely investigated as far as polymers and polymeric composites are concerned [1–4]. However these concepts have been only recently expanded to the field of cementitious composites [5].

Here, we report on the design and characterisation of Urea-Formaldehyde (UF) capsules containing a methyl methacrylate core for use in self-healing cementitious composites. UF has been considered to meet the demanding criteria required for use in previous research on self-healing materials [2,4,5]

MATERIALS AND METHODS

Microcapsule materials

Core material used in the encapsulations is methyl-methacrylate (SAFC), used as received. The microcapsule wall-forming materials include urea, resorcinol, formalin (37% formaldehyde in water) (Fisher) and ammonium chloride (ACROS Organics). Two different emulsifiers/stabilisers were used; poly(ethylene-alt-maleic anhydride) (EMA) (Aldrich) and Span 85 (Sigma). EMA powder was added to deionised water and sheared for 10 min (3000rpm) at room temperature to obtain a 2.5% (wt/vol) aqueous surfactant solution. Similarly an aqueous emulsion, 5% (vol/vol), of Span 85 was prepared. An IKA T25 ULTRA TURRAX homogeniser was employed for the dispersion of surfactants in the aqueous phase.

Characterisation of microcapsules

Thermal stability of produced microcapsules was tested using Thermogravimetric Analysis (TGA) on a Perkin Elmer STA 6000. Small amounts of microcapsules (10-20 mg) were heated from 30 to 500 ^{o}C at a rate of 10 ^{o}C/min in air.

Verification of the chemical composition of the produced microcapsules was performed on a computerised Fourier Transform Infrared Spectrophotometer (SPECTRUM 100, Perkin Elmer) in transmission mode. The number of scans was 16 and the resolution was 1 cm^{-1}.

Images of dried microcapsules were obtained using scanning electron microscopy (EVO LS 15, Carl Zeiss). Capsule diameter measurements and size distribution was estimated using ImageJ analysis software. Samples were prepared by dropping an aliquot (ca. 40 ul) of the particle suspension onto a SEM stub (12.5 mm diameter) and oven drying at 40^{o}C for 30min. The resulting powder sample was sputter coated with a thin layer of gold (~10 nm).

Encapsulation procedure

Microcapsules containing MMA were prepared by an *in situ* urea-formaldehyde microencapsulation procedure adapted from previously reported shell walls [1,4–6]. Two different non-ionic surfactants were used. The two methods are presented in Table 1.

At room temperature, 100ml of deionised H_2O was placed in a 600 ml beaker, along with 25 ml of 2.5% (wt/vol) EMA (Method A) or 25 ml of 5% (vol/vol) Span 85 (Method B). Subsequently, 2.5 gr urea, 0.25 gr ammonium chloride and 0.25 gr resorcinol were diluted in the aforementioned solution. After the addition of the wall-forming materials the pH was adjusted to 3.5 by the drop-wise addition of sodium hydroxide and hydrochloric acid. The beaker was then placed on a combined magnetic stirrer hot-plate equipped with a stir bar (40 mm diameter) and the core phase of 30 ml of MMA was dispersed in the beaker at a desired agitation rate (800 rpm) for 10 min. After 10 min, 6.33 gr formalin was added and the temperature was increased from ambient to 55 ^{o}C. The reaction proceeded under continuous agitation (350 rpm) at

constant temperature (55 ^{o}C) for 4 h. After 4 h the beaker was removed from the hot-plate and allowed to cool to ambient temperature. The microcapsule suspension was vacuum filtered and washed with deionised water and ethanol to remove unreacted wall forming and residual core materials. Microcapsules were oven-dried for 3 hours at 40 ^{o}C and kept in sealed containers prior to further analysis.

Table 1. *In situ UF encapsulation methods used in this work for preparation of microcapsules*

Method	Aqueous phase	Urea (g)	Resorcinol (g)	Ammonium chloride (g)	Formalin (g)	pH
UF-A	100 ml H_2O, 25 ml 2.5% EMA, 30 ml core	2.5	0.25	0.25	6.33	3.3
UF-B	100 ml H_2O, 25 ml 5% Span 85, 30 ml core	2.5	0.25	0.25	6.33	3.3

RESULTS AND DISCUSSIONS

Microcapsule size and distribution

The high shear rate that was applied for the emulsification of the aqueous phase lead to submicron capsules. The size distribution confirms previous findings [1,7,8] of asymmetric shift towards smaller capsule diameters (Fig. 1).

SEM images revealed spherical structures, with non-porous rough shell walls (Fig. 2). Capsules produced with SPAN 85 appear agglomerated, tending to fuse compared to the separated structures produced with EMA.

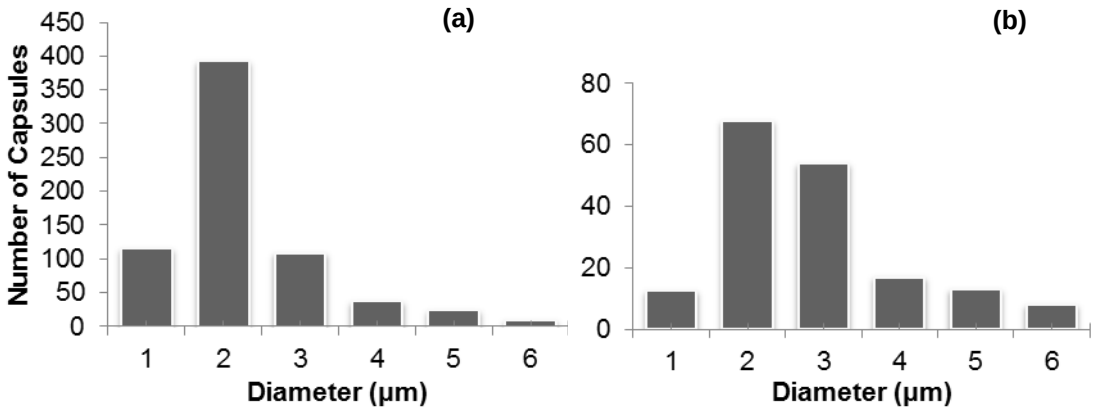

Fig. 1. *Representative histogram of capsule diameter submicron capsules prepared using (a) EMA and (b) SPAN 85 emulsifier*

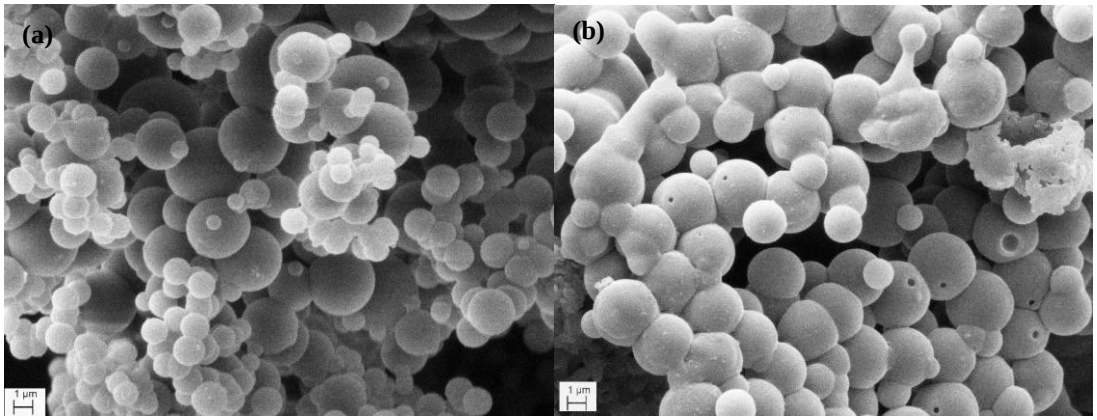

Fig. 2. *SEM images of UF capsules prepared with (a) EMA and (b) SPAN 85*

Yield analysis

Microcapsule yield, shown in Table 2, was measured by the mass of capsules collected as a solid residue at the end of the experimental process compared to the mass of solids used in the encapsulation (i.e. shell forming materials and core). The yield appears dependent on the surfactant used, ranging from a low 20.6% to 54.3% when EMA is used. Conversely the mean diameter indicates

Table 2. *Yield and mean diameter for each UF combination prepared at 350rpm.*

Capsule type	Microcapsule yield (%)	Mean diameter (μm)
UF-A	54.3	1.9±1.06
UF-B	20.6	2.6±1.33

Thermal analysis and stability

In order to evaluate the chemical composition and stability of the produced microcapsules, TGA analysis of the samples was conducted. Indicative mass loss and heat flow curves of the produced UF capsules are presented in Fig. 3. Two distinct transitions were observed in the TGA curves following accordingly the endothermic and exothermic peaks of the heat flow [9]. Two endothermic peaks are observed between 250-350 ^{o}C. These could be attributed to the evaporation of water and free formaldehyde at lower temperatures and the decomposition of the UF shell as the temperature increases [10]. The latter is accompanied by a steep weight loss. Concurrently two exothermic peaks, the first at 240 ^{o}C and the second between 380-400 ^{o}C manifest curing of the core material and continuous polymerisation. Further fragmentation of the residuals is evident above 450^{o}C.

Nonetheless, the microcapsules appear chemically stable bellow 200 °C, with only small evaporation of moisture occurring between 70 and 100 ^{o}C, indicating that the suggested composition offers good thermal viability.

Chemical characterisation

IR sprectrum suggests bands which can be assigned to both urea-formaldehyde polymers and MMA, namely the shell and core materials (Fig. 4). Characteristic peaks of an N-H stretching vibration at 1544 cm^{-1}, a C=O stretching vibration at 1630 cm^{-1}, C-H stretching vibrations at 1380 cm^{-1} and 2900 cm^{-1}, C-N stretching vibrations at 1249

and 1047 cm^{-1} suggest the formation of UF. Besides we can assume the presence of typical bands of MMA such as 2988 cm^{-1} and 892 cm^{-1}. The latter infers the presence of encapsulated MMA.

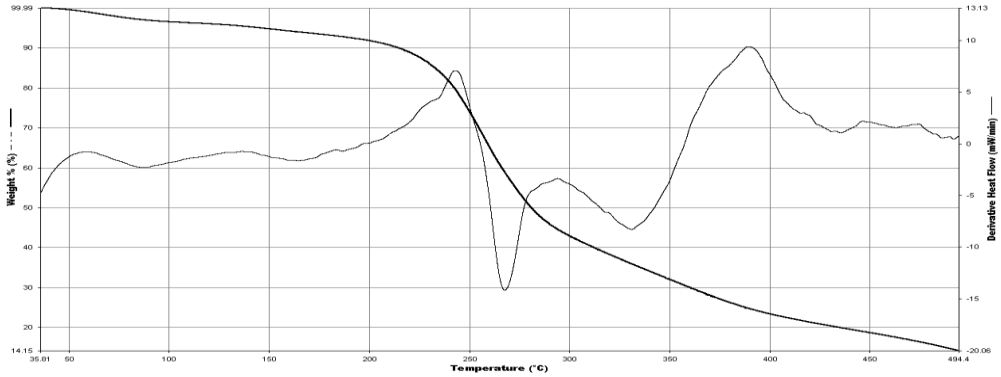

Fig. 3. *Mass loss and heat flow as a function of temperature.*

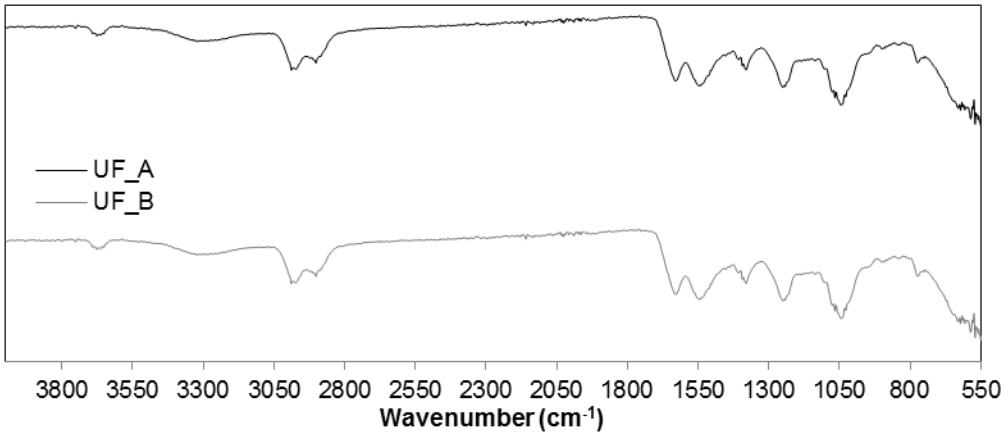

Fig. 4. *Transmission infrared spectra of produced microcapsules*

CONCLUSION

The microencapsulation of MMA by UF membrane using an in situ interfacial polymerization method was achieved successfully. FTIR analysis confirms the presence of both the core and shell materials while the stability of the proposed structures is confirmed by TGA experiments. Although the size of the microcapsules lies within the range of submicrons the suggested composition appears robust for use in self-healing applications.

Investigation is under way for testing the behaviour of the capsules within a cementitious matrix.

ACKNOWLEDGEMENTS

Financial support from the Engineering and Physical Sciences Research Council (EPSRC) and the Hellenic States Scholarship Foundation for the PhD study of the first is gratefully acknowledged.

REFERENCES

[1]. Blaiszik B, Sottos NR, White SR. Nanocapsules for self-healing materials. Composites Science and Technology [Internet]. 2008 Mar; 68(3-4):978–86. Available from: http://dx.doi.org/10.1016/j.compscitech.2007.07.021

[2] White SR, Sottos NR, Geubelle PH, Moore JS, Kessler MR, Sriram SR, et al. Autonomic healing of polymer composites. Nature [Internet]. 2001 Mar 15;409(6822):794–7. Available from: http://www.ncbi.nlm.nih.gov/pubmed/11236987

[3] Youngblood JP, Sottos NR. Bioinspired Materials for Self-Cleaning and Self-Healing Self-Cleaning Surfaces : MRS Bulletin. 2008;33(August):732–41.

[4] Blaiszik BJ, Caruso MM, McIlroy DA, Moore JS, White SR, Sottos NR. Microcapsules filled with reactive solutions for self-healing materials. Polymer [Internet]. 2009 Feb;50(4):990–7. Available from: http://dx.doi.org/10.1016/j.polymer.2008.12.040

[5] Gilford J, Hassan MM, Rupnow T, Barbato M, Okeil A, Asadi S. Dicyclopentadiene (DCPD) and Sodium Silicate Microencapsulation for Self-Healing of Concrete. Journal of Materials in Civil Engineering [Internet]. American Society of Civil Engineers; 2013 Jul 12;130712025159006. Available from: http://ascelibrary.org/doi/abs/10.1061/(ASCE)MT.1943-5533.0000892

[6] Brown EN, Kessler MR, Sottos NR, White SR. In situ poly(urea-formaldehyde) microencapsulation of dicyclopentadiene. Journal of Microencapsulation [Internet]. 2003;20(6):719–30. Available from: http://sottosgroup.beckman.illinois.edu/papers/nrs034.pdf

[7] Brown EN, Sottos NR, White SR. Fracture testing of a self-healing polymer composite. Experimental Mechanics [Internet]. Springer Boston; 2002 Dec 24;42(4):372–9. Available from: http://www.springerlink.com/content/2071611057486036/

[8] Blaiszik BJ, Sottos NR, White SR. Nanocapsules for self-healing materials. Composites Science and Technology [Internet]. 2008;68(3):978–86. Available from: http://www.sciencedirect.com/science/article/pii/S0266353807002941

[9] Liao L, Zhang W, Xin Y, Wang H, Zhao Y, Li W. Preparation and characterization of microcapsule containing epoxy resin and its self-healing performance of anticorrosion covering material. Chinese Science Bulletin [Internet]. 2011 Mar 1;56(4-5):439–43. Available from: http://link.springer.com/10.1007/s11434-010-4133-0

[10] Camino G, Operti L, Trossarelli L. Mechanism of thermal degradation of urea-formaldehyde polycondensates. Polymer Degradation and Stability [Internet]. 1983 May;5(3):161–72. Available from: http://dx.doi.org/10.1016/0141-3910(83)90007-1

CALCIUM ALUMNATE CEMENT AS THE MODIFIER OF LIME BINDERS DESTINED FOR THE ARCHTECTURE RESTORATION

Agnieszka Defus
Department of Building Materials, Faculty of Material Science and Ceramics, AGH University of Science and Technology, Kraków, Poland
defus@agh.edu.pl

ABSTRACT: Lime binder, perceived as historical building material, was modified with the defined quantity of calcium aluminate cement and anhydrite. The main research was based on the observation of the influence of CAC on the binder. The general assumptions take account the transformation of metastable hydrates into stable phases (hydrogarnet) which causes the increase of porosity, that would enable a quick water evaporation from the historic wall and the growth of mortar durability. The addition of anhydrite leads to the formation of ettringite, which crystallizes in the capillary pores and causes the strength development. X ray diffraction was used to quantify the phases generated in the binder samples, SEM analysis was used to evaluate the microstructure of the samples. Also porosity was determined by the use of MIP. On the mortars samples the rate of water absorption and compression strength was measured.
The objective of conducted investigations was to modify lime binders with the additives of different calcium aluminate cements and anhydrite and determine its usability as the restoration mortars for historical architecture.
Keywords: calcium aluminate cements, conservation, historic mortars, lime binders, restoration.

INTRODUCTION

Lime based binders and mortars have been used as a building materials for centuries. During the ages they were modified by various natural additives, which eventually caused the materials' quality improvement. Restoration and conservation of historic building materials requires its full characteristics, as well as the proper knowledge of currently produced binding materials, enabling effective and profitable enhance of chemical, physical and structural compatibility with historical building materials.

Application of cement, as an additive to restoration materials can raise multiple problems, mostly because of the mechanical incompatibility of both materials, hardening process resulting the release of soluble salts, limited elasticity and shorter durability in comparison to lime binders. Because of those features, the maximum amount of 5% cement additive in restoration mortar has been specified [1].

Calcium aluminate cements comprise a potential usage alternative, when it comes

to modification of lime binders with the purpose of architecture restoration. Quick setting and hardening can be governed by accelerated hydration of calcium aluminates, also the porosity value can increase, due to the transformation of metastable hydrates into stable phases. The supplementary addition of anhydrite into the mixture leads to the formation of ettringite, which in this case can be also perceived as a desirable phase.

MATERIALS AND METHODS

Samples Preparation

In this study, three composition of binders were considered. Hydrated lime is the main ingredient in all of the samples comprising 92.5% quantity. CAC contains 5% of the sample, three types of CACs were used depending on the quantity of aluminates: Górkal 70 (70% Al_2O_3), Górkal 40 (40% Al_2O_3), Fondu (40% Al_2O_3). The amount of anhydrite equates 2.5% of the composition. All of the samples were mixed with water in the W/C ratio of 1.0. The composition of the samples is shown in the Table 1 below.

Table 1. *Composition of binder tested on the experimental part.*

Sample	CAC	Anhydrite	Hydrated Lime
S1	5% F	2.5%	92.5%
S2	5% G70	2.5%	92.5%
S3	5% G40	2.5%	92.5%

The samples prepared for the compressive strength and water absorption tests were mixed with sand in the volumetric dosage of 1:1:3 (water:binder:sand) and kept in accordance with PN-EN 1015-11:2000 [4].

Fresh Samples Characterisation

Fresh mortar was subjected to the test of flow table consistency based on PN-EN 1015-3:2000 [3]. The mortar displacement was registered after 15 shots of the flow table within 15 seconds. The value of flow reached 171 mm, which was consistent with the requirements (170 ± 5 mm) [1].

The density of the fresh mortar was obtained by the use of the 1 litre volume container. The value reached 1.94 kg/dm^3(measured for S2 sample).

Hardened Samples Characterisation

The samples composition was determined by the X-ray diffraction using Philips X'Pert Pro MD, after drying grinding to a fineness < 0.063 mm.

SEM observation determining a morphology of samples was carried out on a fractured surfaces using Scanning Electron Microscope JROL 5400.

Samples were tested using Mercury Intrusion Porosimetry (MIP) by the use of PoreMaster 60, Quantachrome Instruments.

Water absorption was performed based on PN-EN 1015-18:2003 method [5].

Compressive strength development was evaluated after 28 and 90 days (setting time proposed by standards [4]) and executed on a hydraulic press Toni Technik.

RESULTS AND DISCUSSIONS

X-ray Diffraction

XRD investigations shown in Fig. 1 demonstrate that apart from predominant presence of portlandite, ettringite was formed, also some amount of gypsum and hydrogarnet occurred.

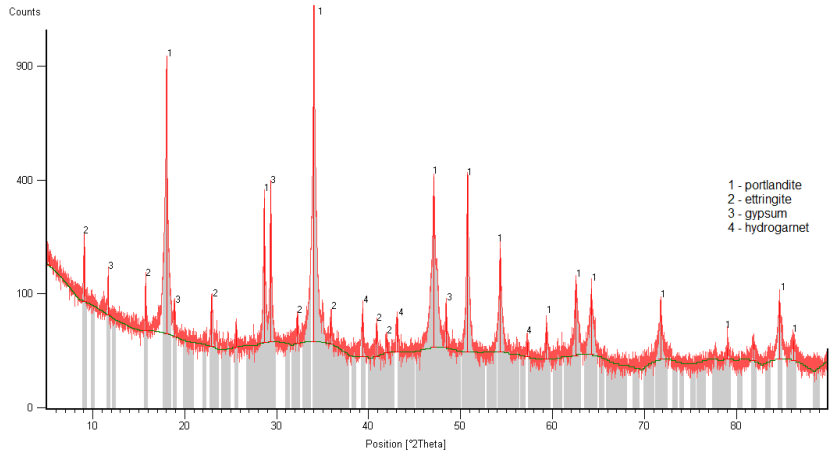

Fig. 1: *XRD pattern of S1 sample showing the presence of specified phases (S2 and S3 patterns did not demonstrated much difference).*

The appearance of ettringite in samples is connected with the reaction that occurs while mixing CAC with gypsum [2]:

$$3CA + 3C\bar{S}H_2 + 33H \rightarrow C_3A \cdot 3C\bar{S} \cdot H_{32} + 2AH_3$$

In the presence of hydrated lime AH_3 transforms into CAH_{10}:

$$AH_3 + CH + 6H \rightarrow CAH_{10}$$

CAH_{10} can easily continue to react with gypsum (in presence of CH), eventually leading to ettringite formation:

$$CAH_{10} + 2CH + 3C\bar{S}H_2 + 14H \rightarrow C_3A \cdot 3C\bar{S} \cdot H_{32} + 2AH_3$$

SEM Analysis

The results obtained from SEM photographs (Fig. 2) display two different homogenously mixed structures – ettringite with its needle shaped crystals and portlandite from the hardened lime binder. This fact states in agreement with XRD results (Fig. 1).

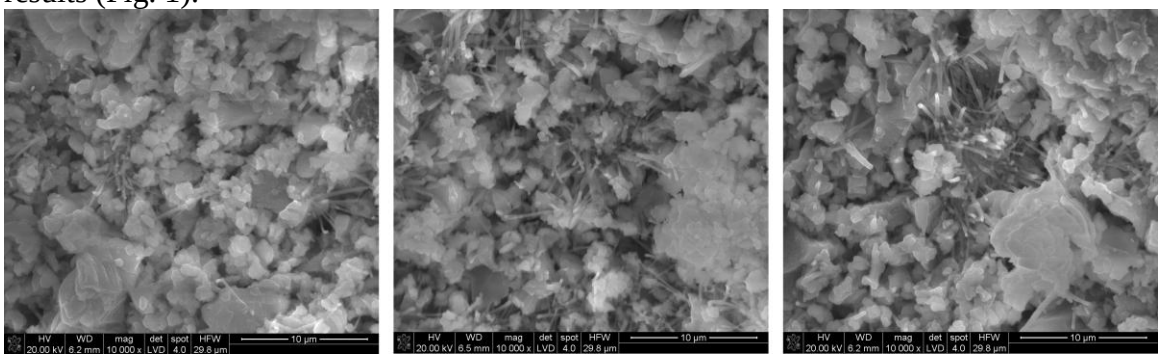

Fig. 2: *SEM pictures showing the morphology of each sample (S1, S2 and S3 from the left).*

MIP Characterization

In Fig. 3 the relative pore size distribution measured by mercury intrusion is displayed, Fig. 4 shows the cumulative intrusion of samples. The porosity of each sample is shown in the Table 2 below. The percentages reached over 40%, which is required value for restoration mortars specified in [1].

Table 2. *Porosity of samples tested on MIP.*

Sample	S1	S2	S3
Porosity, %	48.37	64.41	47.50

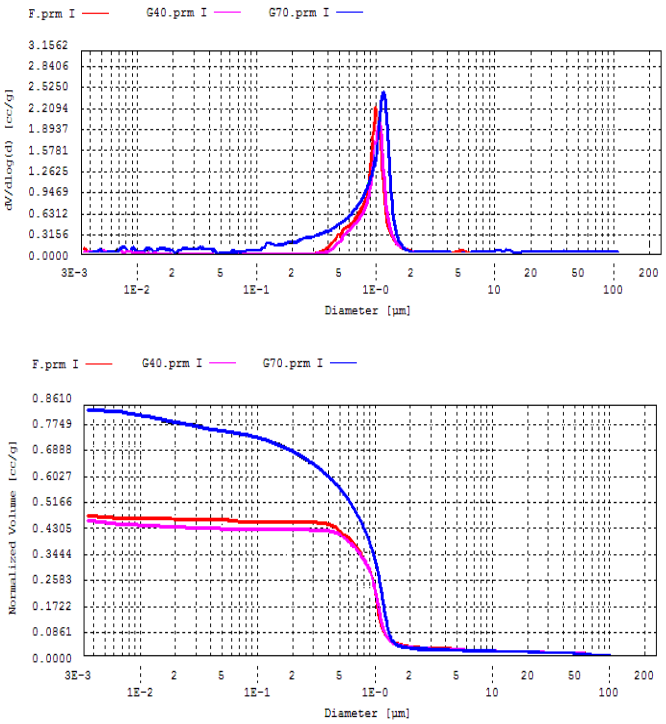

Fig. 3: *Pore size distribution curves (above)* and *cumulative intrusion curves (below).*

It can be seen (Fig. 3) that the majority of pore sizes can be placed between 0.1 µm and 2.0 µm, mostly the peak concentration of pores is found around 1.0 µm. In general, pore size distribution in such range is responsible for high capillary action, it also allows ettringite crystallization within them, causing pore size reduction.

An examination of the cumulative intrusion curves states, that the percentage of pores increases rapidly as pore sizes reduces to below around 0.5 µm.

Absorption of Water

Results of water absorption tests are displayed in Table 3. Water absorption coefficients were obtained according to [5].

Table 3. *Water absorption characteristics of samples.*

Sample	Apparent density, g/cm^3	Water absorption after 24h, %	Water absorption coefficient (1), kg/m^2·min$^{0.5}$	Water absorption coefficient (2), kg/m^2
S1	1.59	20.56	2.30	26.50
S2	1.57	22.08	2.23	28.13
S3	1.59	22.15	2.32	28.69

It is essential to note, that mortars have relatively low apparent density, which is considered as an advantage for the restoration purpose (lack of supplementary weight at original materials).

Water absorption coefficient (2) achieved high values, which is an explicit effect of high porosity level. It can be perceived as both advantageous and disadvantageous feature. High water absorption level contributes to quick water evaporation from a historic wall, but it can also accelerate a salt decay process.

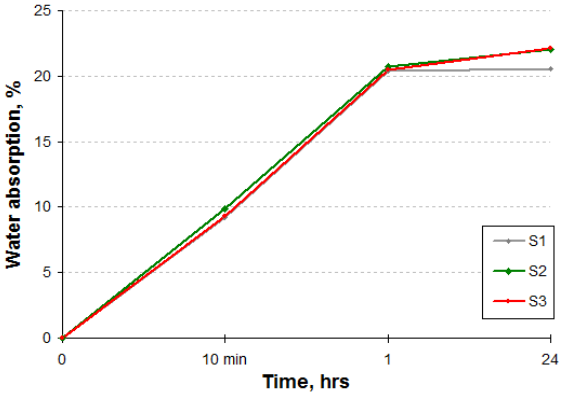

Fig. 5: *Water absorption changes in time.*

The diagram on the left side (Fig. 5) presents the change of water absorption in time. An uptake speed decrease proceeds in logarithmic dependency, meaning that the water absorption speed after first 1-2 hours reduces rapidly and after a while achieves a normalized level.

Compressive Strength Development

The results of measurements of the compressive strength development are shown in Table 4. All tested mortars characterise a low compressive strength (1.25-1.75 MPa), what makes them compatible with restoration purposes.

Table 4. *Compressive strength after 28 and 90 days of curing.*

Sample	Breaking force after 28 days, k*N*	Breaking force after 90 days, k*N*	Compressive strength after 28 days, *MPa*	Compressive strength after 90 days, *MPa*
S1 - 1 S1 - 1	2.0 2.0	2.8 2.4	1.25	1.62
S2 - 2 S2 - 2	2.6 3.0	3.4 4.2	1.75	2.38
S3 - 3 S3 - 3	2.2 2.2	2.8 3.0	1.38	1.82

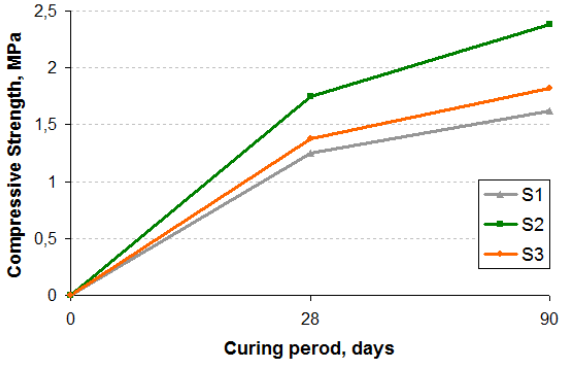

Fig. 6: *Strength development in mortar samples.*

The strength development of mortars is displayed on Fig. 6. After 90 days compressive strength of each sample increased around 30% against the values reached after 28 days. S2 sample achieved moderately higher values of compressive strength (30-45% more), which comes from higher aluminate content.

According to the requirements obtained strength values should range between 1.5 and 5 MPa [1].

CONCLUSIONS

Presented binders and mortars tested in laboratory demonstrate the possible use in the activity of conservation and restoration of historical architecture. They achieved low apparent density (~1.6 g/cm^3), low compressive strength (~1.5 MPa, up to max. 2.3 MPa) and high porosity values (over 40%). High level of water absorption can be perceived as questionable value, because of the possibility of quick salt decay. To avoid this problem adding some specified (e.g. natural) additives can be considered.

The main purpose of modifying lime binders with CAC and anhydrite was to obtain an ettringite supporting the compressive strength during early stages of use and to gain higher porosity using the mechanism of transformation from metastable to stable phases in CAC hydration. Some amount of ettringite was registered during XRD and SEM tests, moderately higher quantity of this phase crystallized in S2 sample, which contained higher amount of aluminates. That dependency can also be acknowledged in compressive strength test. The transformation of CAC hydrates did not occurred or occurred only in a minor level (as shown in XRD characteristics), but the porosity of each sample reached satisfactory level. To achieve the benefits coming from CAC hydrates transformation, increasing the curing temperature or modifying the mixture composition should be considered.

Further investigations should be conducted concerning salt resistance and efflorescences sensibility tests determining the actual usability of such binders for conservation and restoration purposes.

ACKNOWLEDGEMENTS

The X-ray diffraction test was performed at the XRD Structural Researches Laboratory (WIMiC AGH), MIP test was performed at the Department of Ceramics and Refractiores (WIMiC AGH), the SEM/EDS test was performed at the Scanning Electron Mincroscopy and X-ray Analysis Laboratory (WIMiC AGH). Prof. M. Bućko, Mrs B. Trybalska, M.Sc.Eng. and Mrs A. Łabuz, M.Sc.Eng. are gratefully acknowledged.

REFERENCES

[1] Rokiel M, Wymagania stawiane tynkom renowacyjnym. Available at: www.abc-sciany.pl (enter the publication title in the search field).
[2] Szeląg H (2008), Czynniki determinujące naprężenia w cemencie ekspansywnym, Doctoral Dissertation, pp. 7-9.
[3] PN-EN 1015-3:2000 Metody badań zapraw do murów. Określenie konsystencji świeżej zaprawy (za pomocą stolika rozpływu).
[4] PN-EN 1015-11:2000 Metody badań zapraw do murów. Określenie wytrzymałości na zginanie i ściskanie stwardniałej zaprawy.
[5] PN-EN 1015-18:2003 Metody badań zapraw do murów. Określenie współczynnika absorpcji wody spowodowanej podciąganiem kapilarnym stwardniałej zaprawy.

SAFETY INNOVATIONS IN MATERIALS TESTING FOR TUNNEL CONSTRUCTION

K Ledzion
BBMV, C510 Liverpool Street and Whitechapel Station Tunnels, TUCA Laboratory, Lugg Approach, Ilford, London, UK
Karol.ledzion@bbmv.co.uk

ABSTRACT: It is accepted that tunnel environments present high levels of risk associated with the confined nature of this type of project, especially during the construction phase. Therefore it is essential that high quality product and workmanship are maintained at all stages. In order to achieve this, only the most suitable materials and highly skilled personnel should be used.

One area often overlooked or addressed as an afterthought is the inspection and testing regimes of the materials in both temporary and permanent states. By operating a high level of control through adopting best practice test methods and timely reporting systems, it is possible to better manage risk to operatives and provide surety for the long term performance required for these expensive infrastructure projects.

The identification and implementation of best practice and innovative test methods, together with the short and long term benefits of extensive research undertaken are covered by this paper.

Keywords: Inspection, materials, risk, test, tunnel.

INTRODUCTION

Materials' testing is commonly seen as an intrusive activity, not popular with the site team and at best, a necessary evil! However, it must be understood that such testing helps to control the risks associated with tunneling where materials failures can lead to tragedy and can have a major impact on the completion of the project. Through robust testing regimes we are able to control the risk and ensure the best quality of the finished product. Due to the nature of the activities, some of the sampling and testing techniques described have inherent safety risks associate with them, either within the procedure, or location and it is important to understand and manage these.

The examples that follow are mainly related to the A3 Hindhead Tunnel constructed by Balfour Beatty and the Crossrail C510 project at Whitechapel and Liverpool Street Station, constructed by the BBMV consortium (Balfour Beatty, Morgan Sindall, Alpine BeMo and Vinci). These contracts consist principally of sprayed concrete lining (SCL) and this will be discussed in more detail.

TRIALS

Concrete Mixes used in tunneling tend to be very expensive in comparison to more conventional structural mixes. In the case of SCL mixes, they are often required to be pumped for long distances and maintain workability over extended periods of time. In the case of precast segments, there will be other key requirements.

Producing satisfactory mixes that meets the many requirements is a difficult process. For Crossrail C510, extensive laboratory trial mixes were undertaken to assess a wide range of constituent materials for suitability and compatibility. Once this has been completed, arrangements were made to carry out a series of full scale trials using appropriate equipment and trained personnel in order to further refine the mixes. Only at this stage it was also possible to make initial assessments of ease of spraying and rebound percentage, as well as technical compliance. One factor that greatly assists the trial process is the acceptance by the Client to allocate time and money, in advance of the main programme. In the case of Crossrail C510 the full scale trial programme lasted for several months.

Once the onsite batching plants had been established and commissioned, a further programme of trials were undertaken on site to ensure the quality of each mix produced closely matches the design parameters. At this time, the full process can be reviewed, including operation of any pumping and spraying equipment and it gives an opportunity for the production team to begin working with the concrete mix.

TESTING

SCL mixes require high level of quality control/monitoring to ensure the best results are achieved, including checks on constituents, fresh concrete and hardened concrete. The testing regime generally consists of:

1. Concrete constituents must be tested on a regular basis for compliance. Constituents such as cement and admixtures are routinely tested by the suppliers under their own QA schemes, and test results supplied on a regular basis, the methods generally not being suited to on-site checks. However, it is good practice to undertake regular testing of the aggregates used in the mix to ensure compliance. Aggregates for sprayed concrete especially tend to be produced to much finer tolerances than general concrete aggregates and the final mix can suffer heavily if they fall outside the agreed envelope.
2. The ‘base’ mix produced at the batching plant needs to be checked before it is pumped to the location of spraying. It is important that regular flow tests are undertaken to check the consistence, but checks also need to be made to ensure that the steel fibre content is within limits, a test that can only be made whilst the concrete is fresh. Samples are also taken at this stage for routine compressive strength and density tests, as well as less frequent tests such as shrinkage.
3. Very soon after the accelerator is added to the concrete and it has been sprayed, early age testing is undertaken to ensure the adequate initial strength gain. This is controlled by needle penetration test in first 60 minutes following spraying and through HILTI pull out tests for between one and twelve hours after spraying.
4. Sprayed concrete compliance is generally assessed by compressive strength of cores. These core samples can be obtained from either direct coring of the in-situ

hardened lining or by coring of panels that have been sprayed adjacent to the works. Whilst it may cause some disruption to the production activities, it is best practice to obtain samples directly from the lining since these give a much more accurate representation of the strength as well as enabling visual assessment of workmanship. Another key parameter that can be assessed is the fibre content of the cores to ensure the correct dosage has been incorporated in the fresh concrete and not lost through rebound.

Fig. 1: *Early-age assessment of sprayed concrete strength using needle penetrometer.*

5. As a further stage of inspection, the cores are visually assessed on site by dedicated Quality Engineers and inspectors before being dispatched to the testing laboratory located in Ilford, at the Tunneling and Underground Construction Academy (TUCA). All cores are then photographed and logged including an assessment of the quality of joints, compaction and distribution of fibres, as well as encapsulation of reinforcement, if found. On a typical day, between 15 and 20 individual cores are photographed and logged. If any anomalies are detected, copies are immediately sent to the engineering team for review and discussion at the daily review meetings.

Fig. 2: *Coring of sprayed concrete lining within the tunnel, Crossrail C510.*

TEST LABORATORY

It is essential that any major tunneling project has access to a dedicated testing laboratory and team of well trained, qualified, technicians that are available at all hours, 24/7 if required. The key advantages of having dedicated testing facilities include:

1. Control. The competent personnel based on site can ensure that the materials used are compliant with the design requirements through both routine testing as well as visual inspection.
2. Flexibility. The laboratory technicians are always available to asses and test the materials produced without unnecessary delay.
3. Competency. By having a dedicated team, the experience and competency of each person can be ensured. In the case of Balfour Beatty, the technicians are NVQ qualified and extensively trained. They have a full understanding of UKAS and the quality systems that they operate.
4. Safety. The site based teams have better awareness of the risks through familiarity with the project as well as attendance site safety briefings. The process of obtaining a Tunnel Skills card as well as training in confined space working can be time consuming and expensive, so a high turnover of staff is to be avoided. When external test houses are used, there can be a greater range of people who could attend the site.
5. Impartiality. Accurate and unbiased testing and reporting is essential. Accreditation by the United Kingdom Accreditation Service (UKAS) is essential to demonstrate that correct systems and methods are being followed, and that the management systems are robust.
6. Quick reporting. It is essential that reporting is undertaken as quickly as possible following the completion of the test, There is no point undertaking a wide range of tests on site and in the laboratory, if information is not available to review by those who need to make decisions.
7. Trials and innovation. Having a suitably equipped laboratory on site enables additional trials and development to be undertaken as the contracts progress.

A key aspect listed above is safety. When the project has a dedicated testing laboratory on site, it enables best practice to be implemented and drives initiatives. Examples of key successes on the Crossrail C510 contract have been the assessment of drilling equipment for extracting cores, to enable this process to be undertaken as safely as possible. As well as the risk associated with the rotating barrel, it has been possible to reduce manual handling of equipment through the use of mobile hydraulic platforms, whilst at the same time increasing output of sampling. Another area where safety has been improved is in relation to the sawing and preparation of the core samples for compressive strength testing. No longer is sulfur capping undertaken on site, with the related risks of irritating fumes, but all samples are now prepared by grinding to meet the tight limits on flatness. The bench saws have also been modified with a cradle and clamps to eliminate any risk of harm through contact with the blade. Once again, in addressing safety risks, it has enabled improvement in outputs and efficiency.

Where there is a steady workforce associated with a construction project, those people develop an awareness of key safety risks and are more likely to recognize any issues that require addressing. Training is expensive and time consuming and gives better value when the recipient remains for longer periods. As a result, all laboratory

supervisory personnel have completed the 5 day Site Management Safety Scheme (SMSTS) qualification, and a rate of one trained first aider for every four technicians.

REPORTING

There is little benefit in undertaking compliance tests on either the constituents or finished product if there is not a suitable system that enables a quick and accurate reporting of test results. It is essential that any reporting mechanism identifies the compliance status of the results and that they are available without delay. The use of an open network drive accessible to all those who require access to the information, including contractor, designer and client is the best way of achieving this goal. The current system has been developed by Balfour Beatty over a number of years and is used on all major construction projects and has been identified by the UK Highways Agency on their Innovation Schedule as industry best practice.

As well as reviewing individual test results, it is essential to operate a system that enables visual identification of trends in the form of control charts or graphs. In the case of concrete compressive strength, long term trends can be monitored that may indicate changes to constituent materials or plant wear that may be detrimental to the mix.

CONCLUSION

In the case of major construction projects, especially sprayed concrete lined tunnels, the presence of an on-site testing laboratory and team of trained and competent technicians is essential in order to manage risks. However, it is not just undertaking the testing correctly that is important, but ensuring that the testing is done safely and without delay to the project, and that there is a suitable system available to distribute the information to all interested parties.

CHARACTERISATION OF FRIEDEL'S SALT IN CEMENTITIOUS MATERIALS WITH RAMAN SPECTROSCOPY

Yanfei Yue and Yun Bai
Department of Civil, Environmental and Geomatic Engineering, University College London, London, UK
yun.bai@ucl.ac.uk

Jing Jing Wang and John J. Boland
Centre for Research on Adaptive Nanostructures and Nanodevices, Trinity College Dublin, Dublin, Ireland

P. A. Muhammed Basheer
School of Planning, Architecture and Civil Engineering, Queen's University Belfast, Belfast, UK

ABSTRACT: Friedel's salt ($C_3A{\cdot}CaCl_2{\cdot}H_{10}$), a product formed between chloride ions (Cl^-) and calcium aluminates (C_3A), is usually believed to be responsible for the chemical binding of chloride ions in hardened cement matrix. Therefore, characterising the condition of the Friedel's salt formed in cementitious materials can improve the understanding of the interactions between chloride and the aluminate phases in concrete and, thus, facilitate the prediction of service life of reinforced concrete structures because only those 'free' chloride can initiate the corrosion of reinforcing bar in concrete. Raman spectroscopy, a vibrational spectroscopy worked on the principle of inelastic scattering, is an outstanding analytical tool which combines both qualitative and quantitative analysis capacities. However, up-to-date, there is no research on the application of Raman spectroscopy for the characterisation of Friedel's salt. In the current study, a bench-mounted Raman spectrometer was employed to characterise the pure Friedel's salt synthesized under controlled lab condition as well as the Friedel's salt formed in a Portland cement paste after being exposed in NaCl solution. Under Raman spectroscopy, various fingerprint bands of Friedel's salt were successfully identified. The results obtained clearly indicate that Raman spectroscopy is adequate to characterise Friedel's salt in cementitious materials.
Keywords: Cementitious materials, chloride ingress, Friedel's salt, Raman spectroscopy.

INTRODUCTION

Chloride ingress is the most significant factor causing the steel bars corrosion in reinforced concrete structures, especially those exposed to marine environment, de-icing

salts and brackish groundwater [1, 2]. The '*total chloride*' ions can exist in concrete in two forms, i.e. '*bound chlorides*' and '*free chlorides*' [3]. The former are either chemically bound by the reactions with calcium aluminate (C_3A) to form the so-called Friedel's salt (FS salt) [4, 5], i.e. calcium chloroaluminate ($3CaO.\ Al_2O_3.\ CaCl_2.\ 10H_2O$), or physically bound by adsorption on the surface of the gel pores; whilst the latter are those dissolved in concrete pore solution. Although only these free chlorides can initiate the corrosion of reinforcing bars, chloride binding can remove the chloride ions from the pore solution and, thus, can delay the penetration of chloride ions into concrete. Hence, understanding the formation and molecular structure of the FS salt can facilitate the prediction of service life of reinforced concrete structures.

Raman spectroscopy, a vibrational spectroscopy, can provide 'fingerprint' information of molecular structures for solids, liquids and gases[6]. It works on inelastic scattering that the scattered light occurs at wavelength (frequency) shifted up or down from the incident laser light. As this wavelength shift is specific to the chemical bonds and the symmetry of molecules, Raman scattered signal can thus be used to identify substances. Application of Raman spectroscopy in cement and concrete was first demonstrated by Bensted in 1976[7], after which various research were reported and related information can be summarised as follows, (i) identification of anhydrous cement/clinker minerals (C_3S, β–C_2S, C_3A and C_4AF)[8, 9], and their hydration phases (CH, CSH, AFt and AFm)[8, 10-13]; (ii) characterisation of concrete deterioration products, such as sulphate-bearing phases (i.e. AFt, gypsum and thaumasite)[10, 14] and calcium carbonate polymorphs (i.e. calcite, vaterite and aragonite)[15, 16]; (iii) some specific applications such as study of the structural feature of vaterite and CSH[16], characterisation of dehydration mechanism and high pressure properties of gypsum[17, 18] and the high-temperature phase transformation of C_2S[19]. However, no attempts have been made so far to apply Raman spectroscopy for identifying FS salt.

In the current paper, Raman spectroscopy was first employed to characterise a synthesized pure FS salt so that the fingerprint of the Raman bands of FS salt can be collected and assigned, which was then used as bench-mark information to characterise the FS salt formed in the PC paste sample subjected to accelerated chloride ingress. Based on the results, the potential for Raman spectroscopy to characterise FS salt in cementitious materials are discussed.

EXPERIMENTS

Materials

The Portland cement (PC) used in this study was CEM I (in accordance with BS EN 197-1:2011) supplied by QUINN Cement. Its chemical composition is reported in Table 1 below. The cement pastes were manufactured at a water-to-cement ratio (W/C) of 0.35. After 24 hours initial curing in plastic tubes, the specimens were removed from the tube and then covered with a water saturated hessian, which were sealed in plastic sample bags and stored in a curing room at temperature of 20±1 ℃ for around 6 months. At the end of sixth month, selected pastes were ground into powder to a fineness of 63 μm and then subjected to chloride ingress in 2.8 M NaCl solution for 14 days. The samples were then dried in a vacuum desiccator. The pure FS salt was synthesized under controlled conditions at laboratory. Both the pure FS salt and the FS salt formed under accelerated chloride ingress were identified with Raman spectroscopy.

Table 1. *Chemical composition of PC*

Oxides/%	SiO_2	Al_2O_3	Fe_2O_3	CaO	MgO	K_2O	Na_2O	SO_3
PC	23.00	6.15	2.95	61.30	1.80	0.68	0.22	2.50

Raman spectroscopy

The Raman analysis was performed under back-scattered geometry using a Renishaw micro-Raman spectrometer equipped with a Charged Coupled Device (CCD) detector. A 514.5 nm single-line (Argon ions) laser with output power of 25.5 mW was employed as the excitation source. The laser beam was focused through an objective with 50X magnification, and then interrogated the sample. Measured power at the sampling level was around 4.1 mW. To improve the signal-to-noise ratio (SNR), Raman spectra were recorded with exposure time of 10s and accumulations of 10.

RESULTS AND DISCUSSIONS

Raman spectroscopy characterisation of pure FS salt

As abovementioned, Raman spectroscopy has not been applied for characterising the FS salt before. Hence, in the current study, a synthesized pure FS salt was analysed first so that the Raman bands collected and assigned can be used as bench-mark to analyse the PC paste sample later. To clearly identify the molecular vibration modes in FS salt, extended scan mode was employed in an attempt to record all the detectable Raman bands.

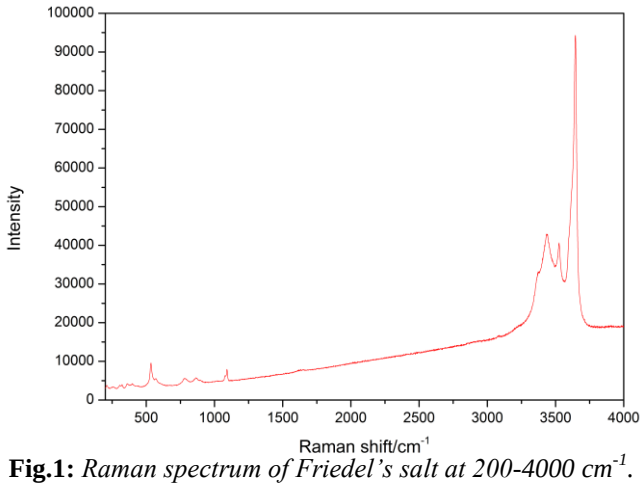

Fig.1: *Raman spectrum of Friedel's salt at 200-4000 cm^{-1}.*

Fig.1 represents the full Raman spectrum of FS salt under extended scan mode between 200-4000 cm^{-1}. Obviously, as shown in Fig.1, except the crystalliferous water bands located at the high frequency regions of about 3200-3800 cm^{-1}, the remaining Raman bands were mainly located at the low frequency region, i.e. 200-1100 cm^{-1}. Hence, a Raman spectrum between 200-1700 cm^{-1} is presented separately in Fig. 2(a). As shown in Fig. 2(a), sloping backgrounds were observed, which imposes a strong disturbance to the Raman spectrum. Those backgrounds could be the troublesome fluorescence

induced by the uncertain impurities in the raw materials used to synthesize the FS salt. Hence, baseline correction using OriginPro 8.6 was applied to reduce the background effect and the resultant spectrum is shown in Fig. 2(b).

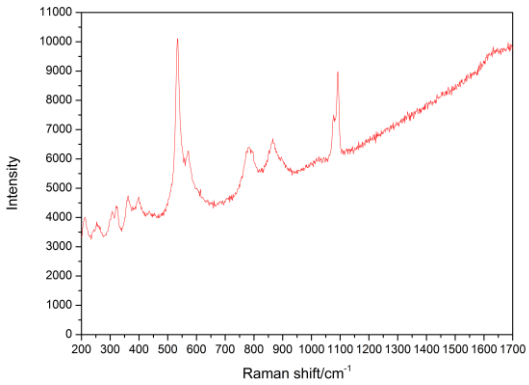

Fig. 2(a): *Raman spectrum of FS salt.*

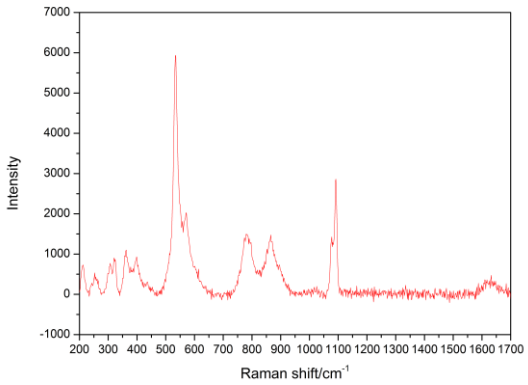

Fig. 2(b): *Raman spectrum of FS salt after subtracting background.*

As can be seen from Fig. 2(b), the distinct peak at 534 cm^{-1} and also its shoulder at 568 cm^{-1}, which could be assigned to the bending vibration mode of Al-OH (γ_3 Al-OH) [5, 20, 21] in FS salt, can be clearly observed. At the same time, the band located at 783 cm^{-1}, which could be attributed to the stretching vibration of Al-OH (γ_1 Al-OH), also can be noticed. Some minor bands at 200-500 cm^{-1} were also identified, i.e. the bands at 212 cm^{-1} and 255 cm^{-1} [lattice vibration (LV)], the doublet at 305/323 cm^{-1} [translation mode of T(H_2O, Ca)] and 362/397 cm^{-1} (molecular rotation and translation). Furthermore, the hump located at the high frequency region, namely, 1629 cm^{-1}, could be attributed to the H-O-H bending vibration (γ_2 H_2O) of interlayer water molecules in the FS salt. The sharp peaks at 1077 cm^{-1} and 1092 cm^{-1} could be assigned to the γ_1 symmetric stretching vibration of [CO_3] in the carbonates. These could be the carbonates formed due to the carbonation during sample preparation. The above results would suggest that Raman spectroscopy is adequate to identify different molecular vibration modes of FS salt.

Raman spectroscopy characterisation of FS salt formed in the PC paste

The synthesized pure FS salt is in white colour, which could be easily identified under Raman spectroscopy. However, the FS salt formed in the PC paste sample is in grey colour. This, coupled with the heterogeneous nature of the cementitious materials, could potentially be troublesome for Raman spectroscopy. Fig. 3(a) shows the Raman spectrum of the chloride attacked PC paste sample.

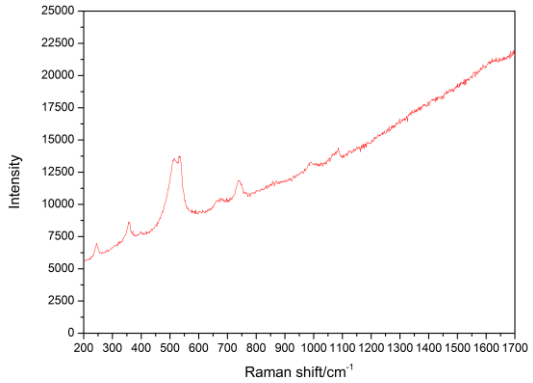

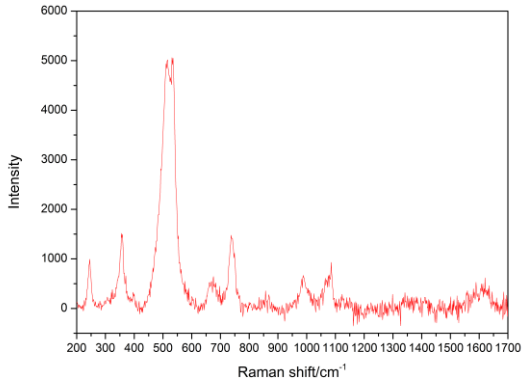

Fig. 3(a): *Raman spectrum of FS salt in PC paste.* **Fig. 3(b)**: *Raman spectrum of FS salt in PC paste after subtracting background.*

As expected, strong sloping backgrounds were emerged from 200 cm^{-1} onwards in the spectrum. Hence, background was again subtracted and the resultant spectrum is presented in Fig. 3(b). The most intense doublet at 513/536 cm^{-1} could be attributed to the bending vibration mode γ_3 Al-OH in FS salt, while the band at 740 cm^{-1} to the Al-OH stretching vibration mode (γ_1 Al-OH) in FS salt. At the same time, two peaks at the low frequency region, i.e. 245 cm^{-1} and 356 cm^{-1}, could be assigned to the LV and T(H_2O,Ca) vibration mode respectively. Furthermore, the vibration bands of the cement hydration products, such as calcium silicate hydrate (CSH), were observed at 673 cm^{-1} which was assigned to the Si-O-Si symmetric bending in the Q^2 units. The carbonation bands were again observed at 1076 cm^{-1} [γ_1 (CO_3)]. In addition, the hump located at 1607 cm^{-1} due to the H-O-H bending vibration of the interlayer waters in FS salt was also recognised. The above results indicated that the typical Raman bands of FS salt formed in the chloride attacked PC paste also can be characterised, illustrating huge potential for applying Raman spectroscopy to characterise the FS salt formed in deteriorated concrete.

CONCLUSIONS

Friedel's (FS) salt is a chloride bearing product in cementiotious materials. By characterising the FS salt formed under chloride attack, we can obtain useful information on the chloride binding capacity of concrete which will eventually facilitate the prediction of service life of reinforced concrete structures. So far, there is no research about the application of Raman spectroscopy for the characterisation of FS salt. In the current study, Raman spectroscopy was successfully employed to identify the pure FS salt and also the FS salt formed in the PC paste subjected to chloride attack. The typical fingerprint bands which could be inferred from the molecular structure of FS salt have been successfully identified in this study at a mean Raman shift of 534 cm^{-1} (γ_3 Al-OH). The results indicated that Raman spectroscopy is adequate to characterise the FS salt formed in cementitious materials due to the ingress of chloride ions.

ACKNOWLEDGEMENTS

The authors would like to acknowledge the support received from the EPSRC UK-China Science Bridge project, China Scholarship Council and Faculty of Engineering Postgraduate Research Scholarship at University College London (UCL). The CEM I Portland cement used in this research was supplied by Quinn Cement.

REFERENCES

[1] Papadakis, V.G., Effect of supplementary cementing materials on concrete resistance against carbonation and chloride ingress. *Cement and concrete research*, 2000. 30(2): 291-299.
[2] Neville, A.M., Properties of Concrete (5th edition). 2012.
[3] Mohammed, T.U. and H. Hamada, Relationship between free chloride and total chloride contents in concrete. *Cement and concrete research*, 2003. 33(9): 1487-1490.

[4] Luping, T. and L.-O. Nilsson, Chloride binding capacity and binding isotherms of OPC pastes and mortars. *Cement and concrete research*, 1993. 23(2): 247-253.
[5] Birnin-Yauri, U.A. and F.P. Glasser, Friedel's salt, $Ca_2Al(OH)_6(Cl,OH)\cdot 2H_2O$: its solid solutions and their role in chloride binding. *Cement and concrete research*, 1998. 28(12): 1713-1723.
[6] Larkin, P.J., IR and Raman Spectroscopy: Principles and Spectral Interpretation. 2011: Elsevier.
[7] Bensted, J., Uses of Raman spectroscopy in cement chemistry. *Journal of the American Ceramic Society*, 1976. 59(3-4): 140-143.
[8] Ibáñez, J., et al., Hydration and carbonation of monoclinic C2S and C3S studied by Raman spectroscopy. *Journal of Raman Spectroscopy*, 2007. 38(1): 61-67.
[9] Tarrida, M., et al., An *in-situ* Raman spectroscopy study of the hydration of tricalcium silicate. *Advanced Cement Based Materials*, 1995. 2(1): 15-20.
[10] Black, L., et al., *In situ* Raman analysis of hydrating C 3 A and C 4 AF pastes in presence and absence of sulphate. *Advances in applied ceramics*, 2006. 105(4): 209-216.
[11] Garbev, K., et al., Structural features of C–S–H (I) and its carbonation in air—a Raman spectroscopic study. Part I: fresh phases. *Journal of the American Ceramic Society*, 2007. 90(3): 900-907.
[12] Frías, M. and S. Martínez-Ramírez, Use of micro-Raman spectroscopy to study reaction kinetics in blended white cement pastes containing metakaolin. *Journal of Raman Spectroscopy*, 2009. 40(12): 2063-2068.
[13] Martinez-Ramirez, S., M. Frías, and C. Domingo, Micro-Raman spectroscopy in white portland cement hydration: long-term study at room temperature. *Journal of Raman Spectroscopy*, 2006. 37(5): 555-561.
[14] Brough, A. and A. Atkinson, Micro-Raman spectroscopy of thaumasite. *Cement and concrete research*, 2001. 31(3): 421-424.
[15] Martinez-Ramirez, S., et al., Micro-Raman spectroscopy applied to depth profiles of carbonates formed in lime mortar. *Cement and concrete research*, 2003. 33(12): 2063-2068.
[16] Behrens, G., et al., Raman spectra of vateritic calcium carbonate. *Spectroscopy letters*, 1995. 28(6): 983-995.
[17] Prasad, P., A. Pradhan, and T. Gowd, *In situ* micro-Raman investigation of dehydration mechanism in natural gypsum. *Current Science-Bangalore*, 2001. 80(9): 1203-1207.
[18] Knittle, E., W. Phillips, and Q. Williams, An infrared and Raman spectroscopic study of gypsum at high pressures. *Physics and Chemistry of Minerals*, 2001. 28(9): 630-640.
[19] Remy, C., B. Reynard, and M. Madon, Raman Spectroscopic Investigations of Dicalcium Silicate: Polymorphs and High-Temperature Phase Transformations. *Journal of the American Ceramic Society*, 1997. 80(2): 413-423.
[20] Leroux, F., J. Ravaux, and G. Renaudin, Crystal structure of Kuzel's salt $3CaO\cdot Al_2O_3\cdot 1/2CaSO_4\cdot 1/2CaCl_2\cdot 11H_2O$ determined by synchrotron powder diffraction. *Cement and concrete research*, 2011. 41: 504-509.
[21] Wu, Y., et al., Effective removal of selenate from aqueous solutions by the Friedel phase. *Journal of Hazardous Materials*, 2010. 176(1–3): 193-198.

POSTER PRESENTATIONS

COMPOSITE MATERIAL MODEL FOR BAMBOO

M.C. Godina, R.Lorenzo and B. Sargeant
Department of Civil, Environmental and Geomatic Engineering, University College London, WC1E 6BT, London, UK
martha.godina.12@ucl.ac.uk

ABSTRACT: This research on bamboo as a composite material is part of a long term broader ongoing research on bamboo structural systems, with the aim of exploring the correlation between structural systems and material performance. It is therefore essential to fully understand the material behaviour. This paper presents the proposed methodology to develop a material model for bamboo based on composite materials theory, including the use of digital image correlation techniques to determine the inherently variable elastic constants of this natural material. Experimental tests have been designed to determine the elastic constants in a simple, accurate and transferrable basis. Preliminary compressive tests on small specimens were carried out on a single bamboo culm of the species Phyllostachys Pubescens (Moso bamboo). The scope of this set of preliminary tests was to determine the modulus of elasticity in the longitudinal direction (E_1). The results obtained from the central portion of the culm wall under compressive load were congruent with values available in the literature. The outcome of this preliminary test shows the potential to adopt this technique as an efficient means to obtain bamboos properties.
Keywords: Bamboo, composite material theory, digital image correlation, modulus of elasticity, variability.

INTRODUCTION

Bamboo is one of the oldest construction materials; through many centuries it has demonstrated its great potential as a structural material (1). As a natural material bamboo can be regarded as a responsible source for constructions; the ratio between the energy required for production per unit stress in use is 30, 80, 240 and 1500 for bamboo, wood, concrete and steel respectively (2). However, it has not yet seized the interest of most contemporary builders and designers, possibly due to the lack of information in material properties, standards, testing and construction techniques compared to conventional construction materials such concrete or steel. The current requirement to contribute to a sustainable built environment along with the continuous changes in architectural practice is challenging the role of construction materials in architecture.

The idea of linking the structural capabilities of bamboo with the morphology of a structural system needs to be addressed in a material model. Therefore, the interest to represent a material model that best characterises the real behaviour of bamboo. Composite material theory which is mainly used to develop engineering materials is

taken as the basis for the modelling of the bamboo behaviour. The main advantages are the high strength to weight ratio and high stiffness to weight ratio (3). A wide variety of composite materials can be found in nature such as wood, insects cuticle, plants, quills, horns, etc. (4,5). The efficiency of these materials in comparison with engineering materials is superior if one compares the density against the modulus of elasticity (6).

Composite theory consists of the analysis of laminates, which are two or more laminas bonded together. The advantage of laminates relies on the different combinations that it offers, since the laminas can have different orientations and material properties. Bamboo has the same orientation (0 degree) in all layers of the cross section; however the properties between the outside and inside wall vary.

BAMBOO STRUCTURE

Bamboo culms are natural grasses with variable properties that are organised as complex structures. This variation in physical and mechanical properties occurs along the culm, among each culm and between species. Mechanical properties are strongly linked to the anatomical structures of the bamboo. Macroscopically, bamboo culms are tapered hollow tubes. They are structured in nodes and internodes. At the internodes, fibres run along the culm axis, while in the nodes fibres bend towards the inside part of the culm in order to reach the lacuna and create the diaphragm providing transverse connection (7), Fig.1.

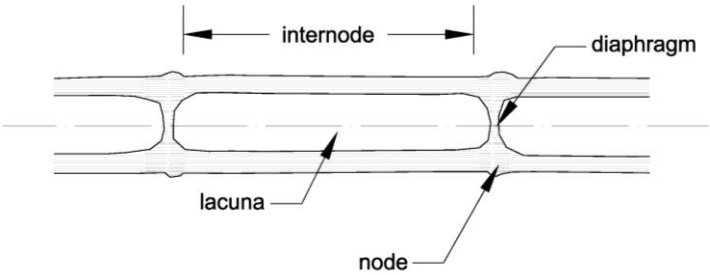

Fig. 1 *Longitudinal section of bamboo culm*

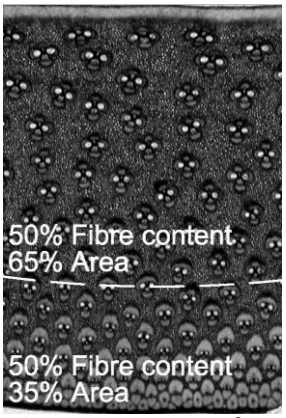

Fig. 2 *X-ray image of a cross section of bamboo culm.*

At the microscale, the constituents of bamboo culms can be considered as a fibre and a matrix. The average constituents in a bamboo culm of the species Phyllostachys Pubescens consists of 54% parenchyma (matrix), 38% fibres and 8% conducting tissue. In general, about 50% of the fibres are concentrated in the outer third of the wall (7). The distribution of fibres and matrix of Moso bamboo is clearly visible in Fig. 2; the image was captured by the Department of Medical Physics and Bioengineering using an x-ray phase contrast imaging technique. The distribution of fibres in the wall thickness is concentrated in the outer wall, therefore the strength, stiffness and density of the material increase from the inner to the outer layers of the culm.

MATERIAL MODEL

Composite materials are systems made up by adding one or more additional phases to the former phase. The synergy between the phases creates a material with greater mechanical properties than the sum of each of the constituents separately. Phases are the constituents of the composite material, that is, fibres and matrix. In the case of high-performance composites such as bamboo, the unidirectional and continuous fibres provides the strength and stiffness required to support loads, whereas the matrix bonds the fibres together, provides protection and distributes the loads between the fibres (8).

The properties of the composite material depend on the properties of each of the phases, the distribution of them and the geometrical properties (fibre volume and distribution). All composite materials are inhomogeneous, therefore they are subject to different scales of anisotropy (8). Bamboo can be considered as a transversely isotropic material, which is described as an orthotropic material that has two orthogonal directions with the same mechanical properties, Fig. 3. This means that the plane transverse to the fibre direction behaves as an isotropic material (9).

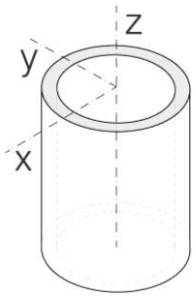

Fig. 3 *Orthotropic tube with the plane x-y as the plane of isotropy*

Composite material theory is classified in micromechanics and macromechanics. Micromechanics regards the properties of each of the constituents of the material in order to analyse the structure (e.g. fibre and matrix). Macromechanics deals with a material where the properties of its constituents are averaged (8).

In order to describe the assumptions taken into account for the material model regarding a single lamina, we first take an orthotropic material, which has three orthogonal planes of symmetry. Nine elastic constants describe this model (9):

$$E_1, E_2, E_3, v_{12}, v_{13}, v_{23}, G_{23}, G_{13}, G_{12} \quad (1)$$

Furthermore the isotropic behaviour of the plane perpendicular to the fibres (i.e. a transversely isotropic material) leads to the following relationships (9):

$$E_2 = E_3, \qquad v_{12} = v_{13}, \qquad G_{12} = G_{13}, \qquad G_{23} = \frac{E_2}{2(1+v_{23})} \quad (2)$$

Hence only five elastic constants are need for a transversely isotropic model (9):

$$E_1, E_2, G_{12}, v_{12}, v_{23} \quad (3)$$

Additionally, if we analyse a single lamina (considering that bamboo has the same properties through the wall thickness) and assume that the material is under the plane-stress condition (i.e. normal stress and out-of-plane shear stresses in z direction are zero.) the elastic constants are reduced to four (9):

$$E_1, E_2, G_{12}, v_{12} \quad (4)$$

The stiffness matrix in terms of engineering constants for a single lamina under plane-stress condition is (9):

$$[Q] = \begin{bmatrix} \frac{E_1}{D} & \frac{v_{12}E_2}{D} & 0 \\ \frac{v_{12}E_2}{D} & \frac{E_2}{D} & 0 \\ 0 & 0 & G_{12} \end{bmatrix} \quad (5)$$

Ultimately, in order to take into account the variability of the bamboo across the culm, it is necessary to consider the material model as a laminate, where two or more layers are bonded together. The stiffness and compliance matrix respectively for an orthotropic thin laminate are (9):

$$\begin{bmatrix} A_{11} & A_{12} & 0 & B_{11} & B_{12} & 0 \\ A_{12} & A_{22} & 0 & B_{12} & B_{22} & 0 \\ 0 & 0 & A_{66} & 0 & 0 & B_{66} \\ B_{11} & B_{12} & 0 & D_{11} & D_{12} & 0 \\ B_{12} & B_{22} & 0 & D_{12} & D_{22} & 0 \\ 0 & 0 & B_{66} & 0 & 0 & D_{66} \end{bmatrix}, \quad \begin{bmatrix} \alpha_{11} & \alpha_{12} & 0 & \beta_{11} & \beta_{12} & 0 \\ \alpha_{12} & \alpha_{22} & 0 & \beta_{12} & \beta_{22} & 0 \\ 0 & 0 & \alpha_{66} & 0 & 0 & \beta_{66} \\ \beta_{11} & \beta_{12} & 0 & \delta_{11} & \delta_{12} & 0 \\ \beta_{12} & \beta_{22} & 0 & \delta_{12} & \delta_{22} & 0 \\ 0 & 0 & \beta_{66} & 0 & 0 & \delta_{66} \end{bmatrix} \quad (6)$$

where [A] matrix is the relation between the in-plane stiffness and in-plane forces, [D] matrix relates the bending stiffness with the moments, and [B] matrix is the in plane-out-of-plane coupling. The geometry of the cross-section is also considered in this approach. The tensile and bending stiffness for a beam with an orthotropic and unsymmetrical cross-section are (9):

$$EA = 2R\pi \frac{1}{\alpha_{11}} \quad (7)$$

$$EI_{yy} = EI_{zz} = \pi \left(R^3 \frac{1}{\alpha_{11}} + R \frac{1}{\delta_{11}} \right) \quad (8)$$

This material model allows the input of variability across the culm, from the inside to the outside wall. The number of layers required to model bamboo depends on the level of accuracy required.

EXPERIMENTAL TEST

The main aim of the experimental tests is to obtain the modulus of elasticity of the centre portion of the wall thickness of the bamboo by applying new technologies with the potential to be transferred to the bamboo construction industry. Digital image correlation is a technique that uses optical measurements, and is capable of measuring displacements and strains. The potential of this technique, besides promoting more accessible methods of determining bamboo properties, relies on the possibility of achieving further data from tests in order to model the variances from a small bamboo specimen.

The test was designed for a small specimen of 12x12x6 mm, under a compressive load parallel to the fibres. The reason for selecting a small specimen was to evaluate the feasibility of applying this technique to the measurement of the properties across the wall thickness of the culm, and at the same time assess whether the properties of a small specimen are representative of a whole culm section.

Procedure

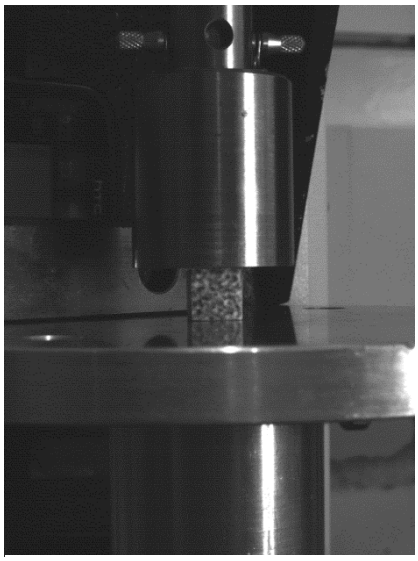

Fig. 4 *Set up of the specimen on the Instron machine.*

The specimens were cut 12 mm x 12 mm gauge length and 6 mm approx. of wall thickness and measured with a Vernier to an accuracy of 0.01 mm. A speckle pattern image was attached to the wall thickness of the specimen, Fig.4. The compressive load was applied by a testing machine Instron 3345 of 5 kN capacity and was set up with a maximum load of 4.9 kN at a crosshead speed rate of 0.60 mm/min. Two pairs of Kodak Megaplus ES 1.0 camera with Fujinon-TV lenses were set up in front of the Instron, level with the specimen height and triggered to a rate of two images per second. The lenses were high quality, stable and with relatively short focal lengths, allowing the enlargement of the area of the image we are interested in. The images were processed with VIC-3D software from Correlated Solutions, in order to obtain the displacements.

Results

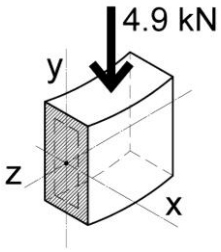

Fig. 5 *Specimen set up*

The compressive modulus of elasticity measured across the wall thickness of the specimen in the y axis was 5.81 kN/mm^2. It must be noted that the measurement area does not correspond to the total area of the wall thickness, since an offset from all the edges of the specimen (i.e. the total area of the speckle pattern) is required to calculate the position of each pixel in the speckle pattern. Therefore, the results showed only the centre portion of the wall thickness; see dash line from Fig. 5.

The modulus of elasticity presented by K.F.Chung et al (10) of whole bamboo culms Phyllostachys Pubescens (Mao Jue), under compressive load were 9.4 and 6.4 kN/mm^2 (average) from dry and wet bamboo respectively. Although the effective area measured was reduced, the displacements track is clearly congruent with the expected results.

In addition, in order to estimate the variability of bamboo across the culm wall, we can take the value of 5.81 kN/mm^2 as the average. Assuming that the stiffness is proportional to the fibre content of the wall, and that the fibres are concentrated in the outer third of the wall, we can calculate the modulus of elasticity representative for each layer:

$$F = \frac{\delta E}{l} A_I + 1.857 \frac{\delta E}{l} A_O \qquad (9)$$

Where F is the applied force, δ is the displacement, E is the modulus of elasticity, l is the original length, A_I is the inner layer area, A_O is the outer layer area, and 1.857 is the ratio between the inner and outer layers in area (i.e. 65 and 35% respectively, see Fig. 2). Accordingly the modulus of elasticity for the inner and outer layers is 4.27 and 7.94 kN/mm^2 respectively.

CONCLUSIONS

Theory of composite laminates is suggested as a material model for bamboo in order to predict the material behaviour. From the results we can conclude that digital image correlation is a very good technique to obtain the elastic constants of bamboo. The level of data possible to acquire with this technique will enable to measure not only displacements on the longitudinal axis, but also in the horizontal and off-axis orientations required to obtain the four elastic constants E_1, E_2, G_{12}, v_{12}. The level of accuracy to model a laminate (number of layers) will be determined based on feedback with future experimental work, as well as comparison of results between digital image correlation and strain gages techniques.

ACKNOWLEDGEMENTS

The authors would like to thank Dr. Paul Diemoz and Marco Endrizzi from the UCL Department of Medical Physics and Bioengineering for the X-ray image.

REFERENCES

[1] Dunkelberg K. IL 31 Bambus-Bamboo. Institute for Lightweight Structures (IL); 1985.
[2] Janssen JJA. Bamboo in building structures. 1981.
[3] Young WC, Budynas RG, Sadegh AM. Roark's Formulas for Stress and Strain. Eighth Edi. United States of America: McGraw-Hill; 2012: 873–918.
[4] Vincent J. Structural Biomaterials. Revised Ed. Princeton, New Jersey: Princeton University Press; 1990.
[5] Vincent JFV. Biomechanics materials, a practical approach. Rickwood D, Hames BD, editors. United States: Oxford University Press; 1992.
[6] Ashby MF, Gibson LJ, Wegst U, Olive R. The mechanical properties of natural materials . I . Material property charts. 2013;450(1938):123–40.
[7] Liese W. The anatomy of bamboo culms [Internet]. INBAR; 1998.
[8] Daniel IM, Ishai O. Engineering mechanics of composite materials. Second Edi. New York, New York: Oxford University Press, Inc.; 2006.
[9] Kollar LP, Springer GS. Mechanics of composite structures. United Kingdom: Cambridge University Press; 2003.
[10] Chung KF, Yu WK. Mechanical properties of structural bamboo for bamboo scaffoldings. Eng. Struct. [Internet]. 2002 Apr;24(4):429–42.

BENEFITS OF ULTRA-FINE FLY ASH ON CONCRETE

Bruce K. T. Kandie
Department of Civil and Structural, Masinde Muliro University of Science and Technology, Kakamega, Kenya.
brucekandie@yahoo.co.uk

Pilakoutas Kypros
Department of Civil and Structural Engineering, University of Sheffield, Sheffield, United Kingdom.
k.pilakoutas@sheffield.ac.uk

ABSTRACT: This paper presents an experimental investigation on the benefits of Ultra-Fine Fly Ash (UFFA) application up to 50% partial replacement for cement in concrete. UFFA is a new generation fine coal fly ash, which is double-classified to obtain the finer particles from the classified bulk. The effects on fresh (water demand, setting time, flow and air), porosity of mid to high strength, medium workability concrete mixes (designed for equal 28-days strength) and compared with concrete mixes with Ordinary Portland Cement (OPC), Micro-Silica (MS) and Seven BS 3892 Part 1 Pulverized Fly Ashes (PFA).

The research study shows that UFFA has an immense significant higher pozzolanicity than all United Kingdom (UK) fly ashes tested and significantly reduced the water demand and decreased air content and porosity of concrete. The compressive strength results indicated that a partial replacement of OPC with UFFA can not only reduce the total binder content required to obtain target strength at specific ages irrespective of curing, but also increased the efficiency of combination binder by up to 50% at latter ages. A high strength of 130 N/mm^2 was attained at 28 days for blend of UFFA/MS/OPC concrete with a combination of selected aggregates sizes proportions.

The incorporation of UFFA improved durability due to the enhanced resistance to Chloride attack and Carbonation compared to equal strength concrete made with OPC and UK PFA, irrespective of curing environment.

INTRODUCTION

Usage of green concrete worldwide is being adopted in reducing both CO_2 emission and cost of energy consumption and using of industrial waste as cement replacement is embraced by many governments.

Ultra-Fine Fly Ash is a new style of Class F Fly Ash to ASTM 311. Which is double classified at the source to produce a product consisting at only the very finest fly ash particles, typically with a mean particles size of 2.32 μm and a specific surface area of 30,000 cm^2/g.

EXPERIMENTAL INVESTIGATIONS

Materials

The cement was Portland Cement confirming to BS 12 1996, class 42.5 N/mm^2. Seven UK Class F fly ashes confirming to BS 3892, Part 1: 1997. Micro Silica was an aqueous slurry (50/50 by weight) and UFFA used a commercially available Class F fly ash confirming to BS 3892 Part 1: 1997. The chemical compositions are shown in Table 1. The aggregates were 10 and 20 mm river aggregates and sand. A Naphthalene-base superplasticizer to BS 5075, Part 3 was used to achieve a concrete workability level at 125 mm slump. Figure 1 shows the various Class F ashes researched on.

Table 1. *Chemical Properties of the cementitious materials used*

PERCENTAGE COMPOSITION											
Chemical composition			**UK BS 3892 Part 1: PFAs**								
Oxides	**OPC***	**UFFA**	**1**	**2**	**3**	**4**	**5**	**6**	**7**	**MS***	**GGBS***
Silica dioxide (SiO_2)	20.7	53.4	55.1	53	54.3	55.6	48.6	51.2	50.6	92	35.84
Aluminum oxide (Al_2O_3)	5.7	32.3	25.1	25.1	23.1	25	24.6	26.1	26.1	1	13
Ferric oxide (Fe_2O_3)	2.3	4.09	10.7	10.2	9.2	10.4	13	7.8	9.4	1	0.55
Calcium oxide (CaO)	64.8	5.05	1.6	3.8	4.1	1.9	2.8	6.4	3.7	0.3	39.53
Magnesium oxide (MgO)	1.1	1.29	1.5	2	2	1.6	1.7	1.9	2.2	0.6	8.28
Sodium oxide (Na_2O)	0.19	<.05	0.4	0.2	0.2	0.4	0.4	0.4	0.5	0.3	0.35
Potassium oxide (K_2O)	0.6	0.08	0.1	0.1	0.1	0.2	0.1	0.1	0.2	0.8	0.5
Sulphate (SO_3)	3.21	0.32	1.2	0.9	1.4	1.1	1.3	1.4	1.3	0.3	0.1
Equivalent alkali	0.58	0.10	0.47	0.27	0.27	0.53	0.47	0.47	0.63	0.83	0.68
Titanium oxide (TiO_2)	-	1.97	1	1.2	1	1.1	1.1	1.6	1.2	-	-
Loss of inginition (LIO)	0.92	0.23	3.1	4.9	5.8	2.5	6.1	3.3	4.7	-	-

*Provided by the manufacturer

Fig. 1: *UFFA and various types of UK PFAs.*

Determination of particle distribution

A laser Malvern Mastersizer E was used to measure the particle size and surface area of the various pozzolans and cementitious materials.

Determination of water demand

This test was undertaken in accordance to BS 3892: Part 1: 1993. Fine, medium and coarse sand was mixed in accordance to BS EN 196: Part 1: 1987.

Determination of compressive strength

The compressive strength in accordance to BS 1881: Part 116: 1983 on three 100 mm cubes at 7 and 28 days of full water immersion samples. The air-cured cubes were saturated prior to test by immersion in water tank for 24 hours (7 day test) or 48 hours (28 day test).

RESULTS AND DISCUSIONS

Particle size distributions

Table 2 and figure 2 shows the particle size distribution of the various pozzolans used. From this table, it is clear that UFFA has higher specific surface area than the UK. BS 3892 Part 1 PFA and GGBS which was in the range of 340 to 715 m^2/kg and 1,448 m^2/kg respectively, but SM had the highest surface area. UFFA had a fineness of 0% with a mean particle size of 2.32 µm and 90% of the particles were 5.25 µm, this was less than that obtained from BS 3892 Part 1 PFA and GGBS but similar to MS.

Table 2. *Mineral admixture lazar particle properties.*

Cementitious Material	Sp. Surface Area m²/Kg	Carbon Content (%)	Fineness >45(µm)	Particle Diameter D[v,0.1]	D[v,0.5]	D[v,0.9]	Span
UFFA	2,893	0.23	0	0.4	2.32	5.28	2.1
PFA1	715	3.1	6.5	1.5	8.47	36.81	4.17
PFA2	359	4.9	11.1	3.37	15.82	46.33	2.72
PFA3	509	5.8	10.1	2.14	12.18	44.56	3.48
PFA4	681	2.5	6.3	1.58	9.2	36.5	3.8
PFA5	448	6.1	14.3	2.43	14.97	52.1	3.32
PFA6	499	3.3	9.3	2.24	12.79	42.91	3.18
PFA7	340	4.7	14.2	3.65	15.28	52.19	23.05
MS*	4,952	-	0	0.25	1.03	22.27	21.36
GGBS*	1,448	-	0.5	0.9	6.64	19.52	2.8

* for comparison

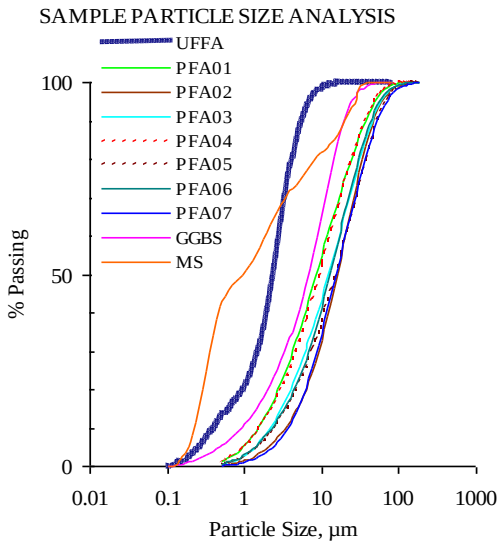

Fig. 2: *Particle size distribution Analysis*

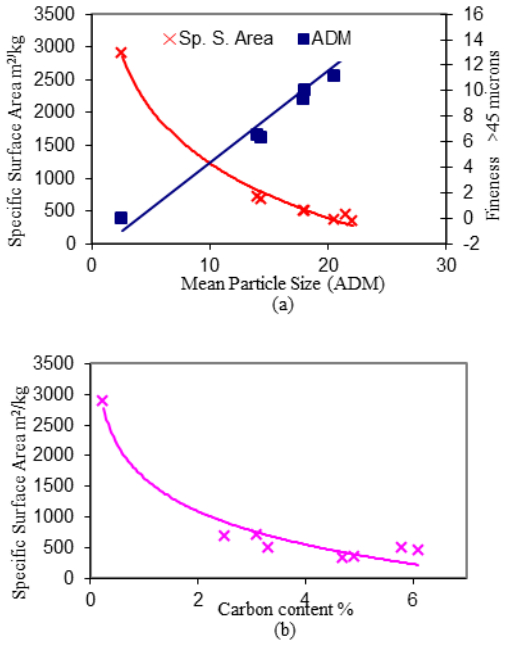

Fig. 3: *Fly ash physical characteristics*

Figure 3 (a) shows that there is a linear relationship between the mean particle size and the fineness of fly ash and similarly with every increase in fineness there is an increase in the carbon content (Figure 3 (b)). The relationship between the specific surface area and the mean particle size was not linear but a curve, which was decreasing with the increase in the mean particle size due to the fly ash particle being more coarser in it morphology.

A global fly ash characteristic may be predicted from figure 3 by knowing one of the elements of any type of fly ash.

Water demand

Figure 4 shows the water demand for cement, various pazzolans and the cementitious materials that were used in this investigation. UFFA had the lowers water demand and 29% was the maximum water reduction at 95% replacement level of PC42.5N.

The seven UK fly ashes had a variation of water demand and these were between the upper and lower bound zone. GGBS showed a slight reduction in the water demand up to a maximum reduction of 4% while MS increased the water demand as its partial replacement level of PC 42.5N was increased, with an increase of 20% and 71% for 5% and 10% replacement level.

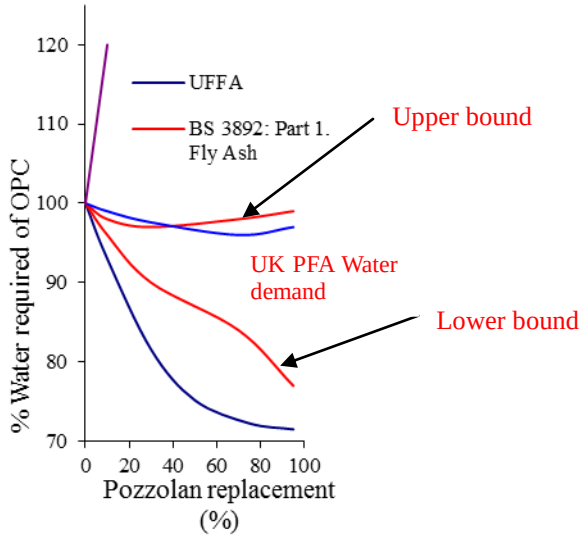

Fig. 4: *The water demand*

The specific surface area, unburned carbon content and the replacement levels were the factors responsible for the high and low water dement for the UFFA, seven UK fly ashes, GGBS and MS. We note that as both the specific surface area for the fly ashes and the replacement levels of cement are increased the water demand is decreased. This was directly opposite with the increase in carbon content increasing the water demand. This clearly shows that the particle shape, the low level of carbon and the fineness of UFFA may be the influencing factors to this reduction in water. This was not similar to SM despite it having a high surface area and its irregular surface texture resulted to this high water demand. GGBS having a high surface area did not show any significant water reduction.

Workability

All the concrete mixes were designed for a slump of 125 mm for an equal 28 days compressive strength. The workability was measured at different rates using the Tattersall two-point workability test and the flow table. From figure 5, we note that as the percentage of UFFA replacement of cement increased, there was a reduction in yield value *(g)* and plastic viscosity *(h)*.

This reduction of *g* and *h* was due to UFFA replacement levels is as a result of an UFFA supplying additional lubricant round the grains of aggregates, due to the "ball bearing effect" of the ultra fine particle size, spherical shape and low carbon content of UFFA. The application of superplasticizers also aided the decrease in both *g* and *h* value for all the cementitious materials. The workability of concrete containing UFFA was enhanced compared to BS 3892 Part 1 PFA and that of MS. Despite the fineness of MS, the workability was low, this may be as a result of the surface area texture and its high reactivity, resulting in a high *g* and *h* value due to MS reacting with the mixing water right from the moment it comes in contact with water and a little of the mixing water is left for lubricating the concrete despite the application of the superplasticizer.

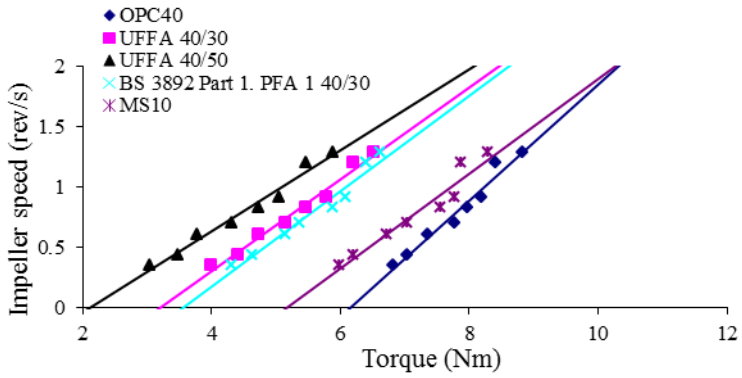

Fig. 5: *Workability of fresh concrete*

Pozzolanicity

The pozzolanic activity of the fly ashes was determined in terms of strength activity index shown on Figure 6. UFFA pozzolanicity was higher than UK BS 3892 Part 1 and OPC.

The seven UK fly ashes pozzolanic indexes are between the lower and upper bound zone. UFFA pozzolanic activity was enhanced by the ultra-fine particle size, high content of CaO and Al_2O_3, the low carbon content and it high pozzolanicity reactivity compared to those of the seven UK fly ashes.

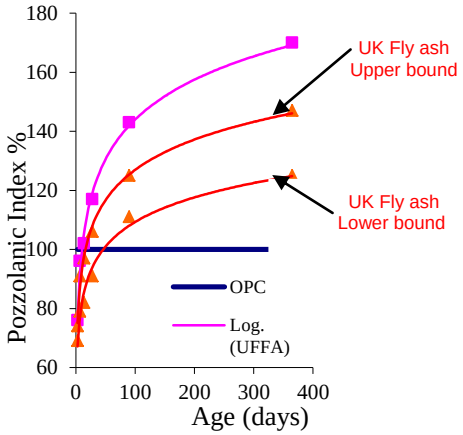

Fig. 6: *Pozzolanicity of the pozzolans*

Concrete compressive strength

The mixes designs and the strength results are given in Table 3. Incorporation of cementitious material resulted in a reduction in water-to-binder ratio of the UFFA/MS concrete mixes. The strength of UFFA/MS concrete is higher than those of OPC concrete. This strength development showed that crushed gravel is better that river gravel. Due to the river gravel shearing faster than the crushed gravels. A combination of 15 mm crushed gravel and 5 mm of sub sand resulted in the highest strength which was 129.5 N/mm^2 at 526 kg/m^3 binder at 28 days of testing. This was higher than 120 N/mm^2 attained by Price (1996) and Tsartsari (2002) at 28 days. The 5 mm coarse aggregates seemed to fill the voids between the coarse aggregates, a view that is supported by Kaplan (1959) who stated that compressive strength of concrete is higher than that of mortar and indicated that the mechanical interlocking of the coarse aggregate contributes to this. The binder of UFFA/MS had 153 kg/m^3 cement saving.

Table 3. *Composition and the compressive strength of concretes*.

MIX CODE	Mix composition kg/m^3											Compressive Strength (Mpa)	
	OPC	UFFA	MS	Cement Save	w	w/b	Aggregates					Age of testing (days)	
							20mm	15mm	10mm	5mm	Sand	7	28
OPC$^-$	522				120	0.23	770	0	340	0	778	84.6	95.1
UFFA/MS 1*$^-$	368	79	79	153	100	0.19	770	0	340	0	702	97	111.3
UFFA/MS 2*$^+$	368	79	79	153	100	0.19	0	770	340	0	702	98.4	116.6
UFFA/MS 3*$^+$	368	79	79	153	100	0.19	0	1110	0	156	546	102.5	129.5

* This were blend of 70% OPC 15%UFFA and 15%MS; + crushed gravel ; - river gravel

CONCLUSSIONS

1. UFFA as a cement binder improved the workability of concrete and this increased with the partial replacement levels of OPC as shown by reductions in '*g*' and '*h*' of these blended concrete.
2. UFFA had a maximum water reduction of 29% at 95% partial replacement level of PC42.5N, which was higher than that achieved by UK BS3892 Part 1 fly ashes and

MS, which was in the upper and lower limit range and an increase of 71% respectively.

3. At the upper limits of conventional replacement level (40%) UFFA reduced water content by 23% whilst the best UK PFA tested reduced water demand by 11%.
4. UFFA has 0.4 μm and 5.28 μm of its particles size less than 10 % and 90% by volume respectively. This was finer that the particles sizes of the seven UK fly ashes, GGBS and MS.
5. The application of UFFA, improved the durability of concrete due to its pozzolanic reaction, refinement of the pores and filling the capillaries, particularly with extended water curing.
6. The highest compressive strength achieved was 129.5 N/mm^2 by a blend of UFFA and MS at 15% partial cement replacement by weight. The w/b ratio was 0.19 and the aggregates used were crushed gravel of maximum size 15 mm.

REFERENCES

[1] Bouzoubaâ, N. and M. Lachemi, M. 2001. Self-compacting concrete incorporating high volumes of class F fly ash: Preliminary results. *Cement and Concrete Research, Volume 31, Issue 3, Pages 413-420.*

[2] Bouzoubaâ, N. Zhang, M. H. and Malhotra, V. M. 2000. Laboratory-produced high-volume fly ash

[3] Çelik, T. and Marar, K. 1996. Effects of crushed stone dust on some properties of concrete. *Cement and Concrete Research, Volume 26, Issue 7, July 1996, Pages*

ALKALI-THERMAL ACTIVATION OF RED MUD FOR PREPARATION OF ONE-PART GEOPOLYMER

Xinyuan Ke
School of Environmental Science and Engineering, Huazhong University of Science & Technology, Wuhan 430074, China
Department of Materials Science and Engineering, University of Sheffield, Sheffield S1 3JD, UK
xke2@sheffield.ac.uk

Nan Ye and Jiakuan Yang
School of Environmental Science and Engineering, Huazhong University of Science & Technology, Wuhan 430074, China

Susan A. Bernal and John L. Provis
Department of Materials Science and Engineering, University of Sheffield, Sheffield S1 3JD, UK

ABSTRACT: Red mud is a highly alkaline residue from the alumina industry. With a current worldwide disposal stockpile of approximately 2.7 billion tonnes, increasing by 120 million tonnes p.a., effective disposal and utilisation approaches are needed. In seeking suitable high-volume precursors for the production of geopolymer construction materials, red mud appears to be a feasible alternative if its reactivity can be controlled. In this study, a one-part "just add water" geopolymer has been synthesised by using alkali-thermal activation of red mud, to avoid the need for addition of a secondary alkaline solution when preparing geopolymers. The results show that alkali-thermal activation process largely improved the efficiency of red mud, as treated red mud acts as an Al-Si source for the formation of new phases with latent hydraulicity. An optimum 7 day strength of 10 MPa was attained.
Keywords: Alkali-thermal activation, geopolymer, hydraulic material, red mud.

INTRODUCTION

As the main binder used for concrete production, Portland cement is responsible for around 5% of worldwide CO_2 generation [1]. In seeking economic and environmental friendly alternative materials, it is necessary to develop and study alternative construction material such as alkali-activated binders [2, 3].

Alkali-activated materials, also referred to as 'geopolymers', have been studied in the past decades as alternative binders to traditional Portland cement [4]. Most geopolymer materials are synthesised from calcined clays such as metakaolin, industrial by-products such as fly ash derived from the coal combustion process, or metallurgical slags from the iron making process [5], along with an alkaline activator which induces a chemical reaction process

to form a hardened solid with desirable properties. The alkaline activator can be included in the mix as a solution, or as a powder mixed with the raw material [6]; however, it is usually included as a highly alkaline solution, but these solutions are difficult to handle, transport and store. Therefore, it is more desirable and convenient for commercial usage to develop one-part "just add water" geopolymer formulations. Studies focused on synthesizing one-part geopolymers are relatively limited [7-10]. One plausible way to produce one-part geopolymers is to synthesize them with a precursor already containing high contents of alkalis that can be easily released when the water is added, to give the early burst of reaction needed for rapid setting and strength development.

Red mud is a highly alkaline residue derived from the alumina extraction process. Bauxite (impure Al_2O_3) ore is digested in NaOH solution via the Bayer process, leaving a significant quantity of NaOH entrained in the residual iron-rich solids, called red mud for their colour and consistency. The worldwide annual production of red mud is estimated at around 120 million tonnes, which makes its disposal an issue of great environmental importance. As red mud is rich in aluminosilicates, synthesis of construction materials via geopolymerisation is a plausible method of utilisation, if the alumina content (which is often relatively unreactive, because the Bayer process is designed specifically to extract alumina from the ore, and so removes anything which is readily soluble) can be unlocked. A recent study has shown that thermal treatment is an effective way to make red mud more reactive for production of geopolymers when using liquid alkaline solutions [11] .

In this study, a "just add water" geopolymer is produced from red mud through an alkali-thermal pretreatment process. The effects of temperature and alkali addition on the red mud during the alkali-thermal activation process are studied by alkali leaching tests. The microstructure of the alkali-thermally treated red mud before addition of water is studied through X-ray diffraction, and compressive strength of the hydrated geopolymer samples is also determined.

EXPERIMENTAL DETAILS

Materials

The red mud used in this study originated from the alumina plant of CHALCO, Henan Branch, Zhengzhou, China, and was dried and stored at room temperature. The main chemical composition determined by X-ray fluorescence is: 20.4 wt.% SiO_2, 24.5 wt.% Al_2O_3, 12.9 wt.% CaO, 11.5 wt.% Na_2O, 9.5 wt.% Fe_2O_3.

Sample preparation and testing methods

The red mud was sieved (-300 μm) and dried in an oven at 45°C for 24 hours. Two groups of red mud precursors were then prepared:

- The first group was prepared by mixing the dried red mud with 15 wt.% Na_2O as sodium hydroxide, and heating to 600℃, 700℃ and 800℃.
- The second group was prepared by mixing the dried red mud with 5 wt.%, 10 wt.% and 15 wt.% Na_2O as sodium hydroxide, and heating to 800℃.

Heating was conducted at a ramp rate of 5℃/min, and holding at the peak temperature for 1 hour before cooling to room temperature (25℃).

The solubility of the red mud precursors was determined by mixing 0.25±0.02g solids with 25mL 5N NaOH solution at 25±1℃ for 24h, using a bath shaker. After filtration, the contents of Si and Al in the solution were determined by chemical titration. The leachabilities (η) of Si and Al were calculated according to Eqs. (1) and (2), where m_c is the mass of Si or Al

calculated from titration tests, m_0 is the mass of each element supplied by the original red mud, m is the mass of alkali-thermal treated red mud and $a(\%)$ is the addition of alkali. *LOI* (loss on ignition) was recorded at 1000°C.

$$\eta = \frac{m_c}{m_0} \times 100\% \quad (1)$$

$$m_0 = \frac{m}{(1 - LOI)} \times \frac{1}{(1 + a)} \times Chemical\ Composition(\%) \quad (2)$$

X-ray diffraction of the powders after treatment was carried out using a D/Max-3B X-ray diffractometers operated at 40 kV, 40 mA, with Ni-filtered Cu K_α radiation.

The one-part mix red mud-geopolymer paste was then prepared by adding water to the solid alkali aluminosilicate precursor at a water/binder ratio of 0.6. The fresh paste was put into 40×40×40mm mould, sealed, and cured at 20±1℃ and a relative humidity of 95%. After 1, 3 and 7 days of curing, compressive strength of the cubes were tested. Each value reported corresponds to the average of 2 samples.

RESULTS AND DISCUSSION

Solubility in alkaline medium

Determination of the solubility of geopolymer precursors in an alkaline medium is an efficient way of evaluating the potential chemical reactivity of the Al-Si source[12]. Si is the most essential framework forming element, while the presence of Al accelerates the early setting of the paste and leads to a cross-linked, insoluble final solid product [5,13]. The availability of both of these two elements illustrates the potential gel-forming properties of a given precursor.

It can be seen from Fig. 5(A), that with a fixed alkali addtion, the solubility of Al rose as the thermal activation temperature increased, while the solubility of Si increased from 600℃ to 700℃ but decreased at higher temperatures. Fig. 5(B) shows that, in specimens thermally activated at 800℃, the solubility of Al also increased with alkali addition. This indicates that within the range of experimental parameters selected in this study, the heating treatment and the temperature used have a stronger influence in the leachability of Al and Si than the degree of alkali addition beyond 10 wt.%.

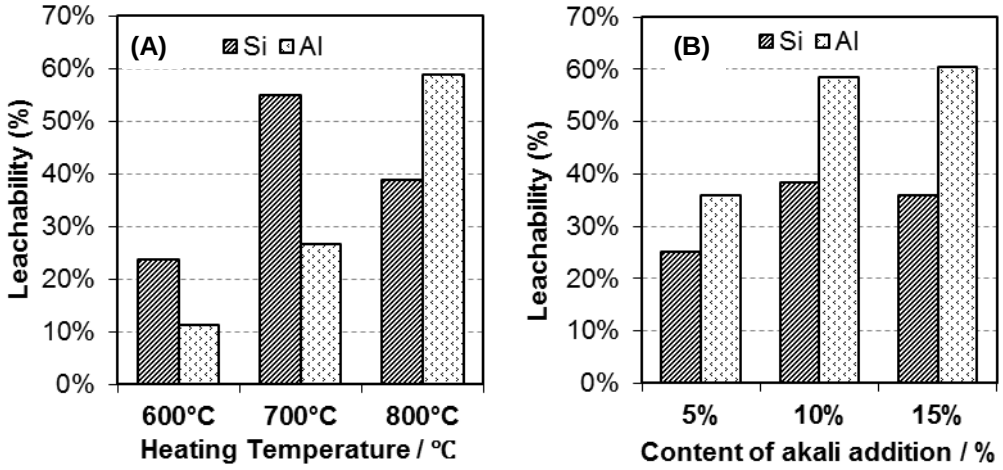

Fig. 5: *Content of solubility of Si and Al in 5N NaOH solutions from (A) red mud mixed with 15 wt.% Na_2O (as NaOH), heated at different temperatures, (B) red mud mixed with different alkali additions (expressed as wt.% Na_2O, added as NaOH), for samples heated at 800℃.*

In designing a geopolymer precursor, balanced availability of both Si and Al should be taken into consideration. Thus, the optimum alkali-thermal activation condition for the red mud used here appears to be 700 to 800℃, with 10 to 15 wt.% Na_2O.

Mineralogical characterisation

X-ray diffractograms of red mud-derived geopolymer precursors produced under different alkali-thermal conditions are shown in Fig. 6. Cancrinite (powder diffraction file (PDF) # 00-034-0176) and an alkali-rich (peralkaline) disordered Na-aluminosilicate ($[Na_2O]_x \cdot [Na(AlSiO_4)]_6$; x>0, PDF# 01-076-2385) are the main products of alkali-thermally activated red mud. Cancrinite is the dehydrated and decarbonated product derived from the cancrisilite (PDF#00-046-1381) which was previously identified in the unreacted red mud used in this study [14]. Increasing the heating temperature or alkali addition of the alkali-thermal activation process favours the decomposition of cancrisilite towards formation of the Na-aluminosilicate identified, which showed potential hydraulicity after mixing with water, instead of forming cancrinite. Belite (α_L-C_2S, PDF#00-033-0303) is also observed in the RM800-15 wt.% Na_2O powder, apparently derived from the calcium present in the red mud, and this compound is known as one of the major components of Portland clinkers. This indicates that this specific red-mud based binder can have a high reactivity when blended with water, as belite is not formed at lower calcination temperatures.

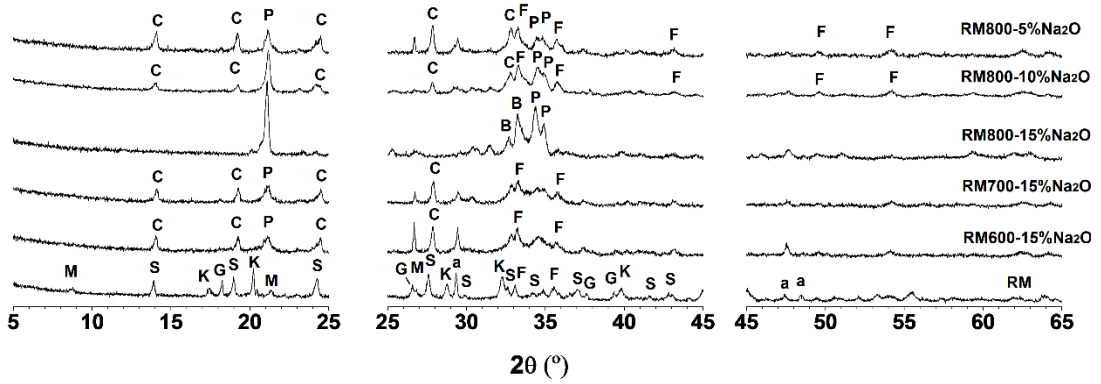

Fig. 6: *X-ray diffractograms of unreacted red mud and red mud treated with different alkali-thermal activation conditions, where S - cancrisilite, K - katoite, G - gibbsite, M - muscovite, a- calcite, F - hematite, C – cancrinite, B – belite, P – peralkaline Na-aluminosilicate.*

Compressive strength

Compressive strengths of the synthesised red mud one-part geopolymers are shown in Fig. 7. The compressive strength increased over the time of curing, except for the red mud treated at 700℃ with 15 wt.% alkali. There is not a consistent trend between the strength development and alkali-thermal activation conditions, as the performance of geopolymer is controlled by the dissolution rates of both Al and Si, which can be highly heterogeneous in the samples produced. The optimal strength was obtained when using the red mud powder treated at 800°C with 10 wt.% Na_2O, consistent with the high leachability of Si and Al species from this precursor, as observed in the alkali leaching tests (Fig. 5).

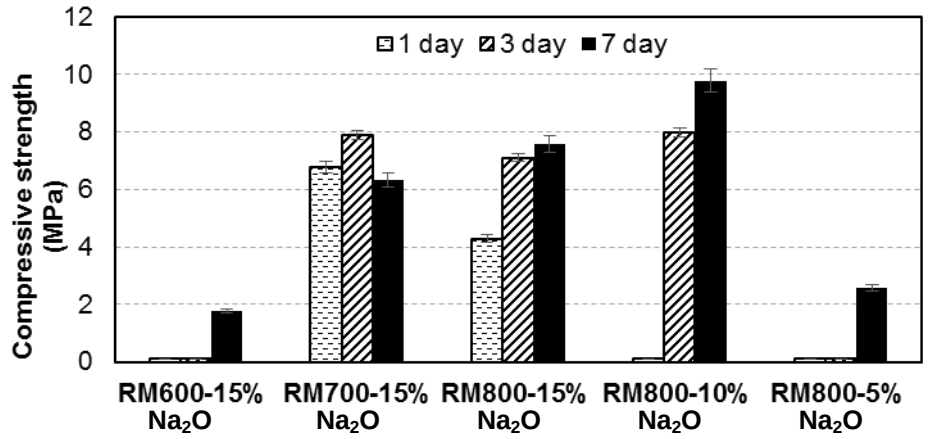

Fig. 7: *Compressive strength of pastes based on alkali-thermal activated red mud geopolymers. Data are reported as average and standard deviation of two replicate tests.*

CONCLUSIONS

- The solubility of Al from alkali-thermal treated red mud precursor increased at higher heating temperature and with alkali addition up to 10 wt.% Na_2O. The rise of solubility of Al is related to the formation of a disordered peralkaline aluminosilicate phase in the material. Solid precursors with higher Al solubility led to geopolymers with better mechanical strength.
- There is no direct correlation between the solubility of Si under the conditions tested, and the treatment conditions of the red mud. However, a high release of Si seems to promote high strength at early age, as RM700-15% Na_2O exhibited the highest 1 day strength among the samples tested.

ACKNOWLEDGEMENTS

The investigation was supported in part by the New Century Excellent Talents Project of the Ministry of Education (China) (NCET-09-0392). The participation of JLP and SAB was funded by the University of Sheffield.

REFERENCES

[1] Provis JL, Bernal SA. Geopolymers and related alkali-activated materials. *Annu Rev Mater Res.* 2014;44.

[2] van Deventer JSJ, Provis JL, Duxson P, Brice DG. Chemical research and climate change as drivers in the commercial adoption of alkali activated materials. *Waste and Biomass Valorization.* 2010;1(1):145-55.

[3] Provis J. Geopolymers and other alkali activated materials: why, how, and what? *Materials and Structures.* 2013:1-15.

[4] Provis JL, Brice DG, Buchwald A, Duxson P, Kavalerova E, Krivenko PV, et al. Demonstration Projects and Applications in Building and Civil Infrastructure. *Alkali Activated Materials: Springer*; 2014. p. 309-38.

[5] Duxson P, Provis JL. Designing precursors for geopolymer cements. *Journal of the*

American Ceramic Society. 2008;91(12):3864-9.

[6] Yang KH, Song JK. Workability loss and compressive strength development of cementless mortars activated by combination of sodium silicate and sodium hydroxide. *Journal of Materials in Civil Engineering*. 2009;21(3):119-27.

[7] Hajimohammadi A, Provis JL, van Deventer JSJ. One-part geopolymer mixes from geothermal silica and sodium aluminate. *Industrial & Engineering Chemistry Research.* 2008;47(23):9396-405.

[8] Hajimohammadi A, Provis JL, van Deventer JSJ. The effect of alumina release rate on the mechanism of geopolymer gel formation. *Chem Mater.* 2010;22(18):5199-208.

[9] Hajimohammadi A, Provis JL, van Deventer JSJ. The effect of silica availability on the mechanism of geopolymerisation. *Cement and Concrete Research.* 2011;41(3):210-6.

[10] Feng D, Provis JL, van Deventer JSJ. Thermal activation of albite for the synthesis of one-part mix geopolymers. *Journal of the American Ceramic Society.* 2012;95(5):565-72.

[11] Ye N, Zhu J, Liu J, Li Y, Ke X, Yang J. *Influence of Thermal Treatment on Phase Transformation and Dissolubility of Aluminosilicate Phase in Red Mud.* MRS Online Proceedings Library. 2012;1488: doi:10.1557/opl.2012.1546.

[12] Glasser LSD, Harvey G. The gelation behaviour of aluminosilicate solutions containing Na^+, K^+, Cs^+, and Me_4N^+. *Journal of the Chemical Society, Chemical Communications.* 1984(19):1250-2.

[13] Weng L, Sagoe-Crentsil K, Brown T, Song S. Effects of aluminates on the formation of geopolymers. *Materials Science and Engineering*: B. 2005;117(2):163-8.

[14] Felsche J, Luger S. Phases and thermal decomposition characteristics of hydro-sodalites $Na_{6+x}[AlSiO_4]_6(OH)_x \cdot nH_2O$. *Thermochimica Acta.* 1987;118:35-55.

RESEARCHING FUTURE STRUCTURAL CONCRETE

Philip L. Owens
Faculty of Science and Engineering, University of Wolverhampton,
Wulfruna Street, Wolverhampton, WV1 1LY, UK
p.l.owens@wlv.ac.uk

ABSTRACT: Often the standard approach used to evaluate the properties and performance of concrete is misleading, as the heat of chemical reaction during the process of 'cement' hydration is controlled in the laboratory at between 20 to 22°C; whereas in-situ and depending on a variety of conditions, it is impossible to stabilise to the temperatures imposed in the laboratory. This research is intended to relate standard tests to the performance of in-situ 'structural' lightweight concrete that has undergone significant temperature changes as a result of hydration. These changes modify the structure of the cement hydrate and thus the performance of concrete, particularly of that made with lightweight aggregates.
Keywords: concrete density, fly ash, in-situ concrete, lightweight-aggregate, lightweight-concrete.

INTRODUCTION

Ever since contemporary engineers became aware of the concrete used for the dome of the Pantheon in Rome, lightweight concrete has been of interest and often used in some unique and very demanding structures. [1] However, it has remained a niche solution because when compared to normal-weight concrete made with natural aggregates, some of the properties and behaviour of laboratory produced lightweight concrete often appear to have limitations. This however did not deter the construction of the 52 floor 'One Shell Plaza' Houston, USA in 1970 from deploying lightweight concrete for the whole of its sub and super structure.[2] Why this concept did not continue is possibly caused by the lack of sustainable sources of lightweight aggregate (LWA). Alternatively, 'normal' concrete is sustainable on the basis that when one source aggregate becomes exhausted, another suitable source can be found with relative ease.

However, the availability of LWAs is more complex, as they are manufactured and at first appear more expensive, this is caused by the integration of greater capital investment for production and the variable cost of manufacture.[3] This together with the requirement for suitable argillaceous resources, either deep clay, shale or slate and to site an adjacent factory is the main challenge for economic extraction and production. Without exception all five sources of LWA described in [4] available in the UK in 1974, have ceased production. The current UK sources of LWA are unsuitable for structural/reinforced concrete, as the variable

aggregate properties, size and high water absorption, are more suited for application in concrete blocks (masonry).

In consideration of the mineral resource for the production of LWA, the opportunity occurs to use the continuous supply of 'detritus' extracted from excavations and tunnelling in London's deep clay, this is a sustainable resource, which is heat 'bloatable' and when fired at 1185°C produces a low water absorption (lwa) LWA with a particle density (PD) of about 0.65Mg/m³. [5]

Structural concrete's fresh density is dependent on the coarse aggregate PD. For a coarse normal aggregate with a PD of 2.60 Mg/m³, the concrete fresh density is about 2400kg/m³, whereas for LWA with a PD of 0.65Mg/m³ it is about 1500kg/m³, but the maximum standard cube strength is about 25MPa, irrespective of any additional hydraulic binder (cement) [6]. To overcome this for a wider and designed density, the 'principle' of aggregate combinations has been developed, whereby the required fresh density of concrete can be specified between 1500 and 2400kg/m³ [7] to which the standard crushing strength can be related.

Principal to the definition of concrete whether lightweight or normal, is the specification of density. [8] Whether for reproducibility, conformity or convenience, it is often based on the *oven dry density*. For the commercial exchange or sale of goods relating to concrete the volume supplied is fundamental e.g. one cubic metre, thus there is a strict requirement for the purposes of batching, mixing and placement to produce a constant yield of fresh concrete [9]. In the case of concrete that is supplied ready-mixed both the volume and consistence are required to remain constant over a period of sufficient time to effect placement without the further addition of water. With an absorbent aggregate it is often normal practise to 'pre-soak' before application, thus the amount of water in concrete can be considerably increased. [7] Then given that in-situ concrete, particularly as the dimensions of an element increase, it is unlikely if ever, to 'totally dry' beyond its depth of carbonation. Even concrete elements when exposed to a dry internally heated environment and subjected to fire testing, water 'boils off' nominally dry concrete.

While it is often assumed that lightweight concrete is an ideal material for fire resistance, unfortunately unless the aggregate is of low water absorption or 'dry' in-situ, the intensity of fire loading make the application of highly absorbent LWA unsuitable. This is of particular concern for when there is a greater retention of water in the aggregate the risk of high vapour pressures developed during an intense fire makes this concrete potentially 'explosive'[10] rendering it totally unsuitable for enclosed spaces such as tunnels, etc.

Although not a fire test thermally stressing concrete for the determination of tensile strain capacity [11] found that Lytag concrete, with 310 litres/m³ of water of which 100 litres were absorbed by 1008kg of dried aggregate, showed that when the internal temperature of the concrete test specimen, 250mm wide x 150mm deep x 1200mm long, reached 135°C its failure mode was described as '*Specimen disintegrated instantaneously*! In other words it exploded.

The necessity of relating LWA absorption to concrete density is paramount, not only for its sale of goods description, but also for fire safety. The additional advantage of a 'lwa' LWA is that should a fire occur, the 'dry' voids in the aggregate particle not only provide thermal insulation to protect steel reinforcement, but also importantly allow for th relief of internal water vapour.

A NEW APPROACH FOR THE EVALUATION OF LIGHTWEIGHT CONCRETE

This submission presents the techniques that would be necessary to develop with 'lwa' LWA the principle of 'aggregate combinations' in order to vary the concrete density and the test methods used to simulate the early and later performance of in-situ structural concrete.

Without doubt any development new to the science of concrete, whether it be a new material or test method/technique it takes a considerable time for it to become established in practice. In the meantime between the scientific discovery and its adoption, the dogmas of concrete technology appear to override or thwart progress, unless there is a major failure that causes a fundamental reappraisal of the phenomena, e.g. carbonation and alkali-silica reaction.

In many respects the technology of concrete suppresses scientific progress, in that it obeys the standards that control any test method. Standards are concerned with reproducibility of tests, rather than addressing the performance of concrete in-situ. For instance, substituting 35% CEMI with fly-ash and making the concrete in the laboratory at 20°C, the 28-day cube strength is lower than concrete with CEMI alone, even correcting consistence by water reduction the fly ash concrete requires about 10% more 'cement' to achieve the same 28-day cube strength.[12]

This has proved beneficial to durability, but it has been quite unnecessary, not only for the 10% extra volume of 'hydraulic powder' provided by the fly ash, but also in-situ where the heat from the hydration of CEMI promotes the pozzolanic reaction, which develops an amorphous, rather than a crystalline hydrate 'gel' structure.

Another consequence of this is that in-situ high temperatures affect the manner of hydration, negatively with CEMI and positively when CEMI is partially substituted with fly ash. [13],[14],[15] While this can be replicated with mortars, it is more challenging with concrete where the size of the coarse aggregate relates to the size of the test specimen, i.e. 20mm aggregate is relative to 100mm cube. Thus the standard test, that combines normal weight aggregates with the mass of a steel mould provides a major 'heat sink' that absorbs any heat developed by hydration, further compounded later by storage in water. This has no relevance to the semi-adiabatic conditions of in-situ concrete, especially for larger elements [16], but it is nevertheless important to connect the relationship of standard tests with in-situ concrete, particularly for the reduced 'heat sink' of LWA that aids the same cement to develop even higher temperatures. [17]

The method for measuring the effect that maturity (time and temperature) has on concrete strength is known as temperature matched curing [18], which is used mainly to determine the early strength of concrete in pre-cast/stressed elements. However, LWA in concrete is an 'internal insulator' that causes an increase in the temperature generated by cement hydration [17], this has a synergy with fly ash, as the temperature developed by the heat of reaction of the cement not only depends on element size, [18] but also is increased by density reduction.

Exploiting this requires a means of adjusting concrete density with combinations of coarse normal and LWA, the application of fly ash and the development of a test method that simulates the semi-adiabatic conditions of in-situ concrete, with a minimum quantity of concrete cast in low density moulds to effect the temperature rise and fall of an in-situ concrete element.

THE MATERIALS

Fig.1: *The aggregates used.*

Fig. 1 shows the aggregates used and with the exception of the LWA, the normal aggregates both coarse and fines were selected on the basis of low water absorption. The two nominal sizes of coarse aggregate were 20mm and 10mm Midland quartzite gravels and two grades of silica sand fines nominated as 6/14 and 16/30 from Leighton Buzzard. Low water absorption LWA are not available to the UK and of the aggregates that were available Liapor 3G 8/16mm, ex Germany was the most spherical, but with a 30 minute water absorption of 17.7%.This high rate of water absorption was found difficult to accommodate, even pre-soaked with the other aggregates its effect reduced both yield and consistency , which confirmed the requirement for a low water absorption LWA.

The cements used were BS EN 197 -1 CEM I 52.5 ex Hope Construction Materials and to enable a combination cement BS EN450 Class S fly ash, ex Cemex Ltd, West Burton.

THE TEST METHODS

The approach here to concrete testing is designed for laboratory investigations and accepts the need for larger specimens in order to retain and maximise the temperature from cement heat of hydration, but this has to be balanced with the size of specimen to be tested within the limits of the equipment (usually) available in a typical concrete laboratory. The orientation of the specimens and their initial casting requires as many test specimens for as many test methods as possible, using the least amount of effort to obtain maximum data for analysis by a combination of non-destructive tests before physically testing specimens to destruction.

Part 1 Determination of the type of test specimen.

A cylinder was chosen in preference to a cube as it is easier to man-handle, however the main concerns for rejecting a 27 litre volume cube of concrete were,

i) For H&S reasons a cube made with normal aggregates has a mass of about 65kg that takes at least 3 people to man-handle.

ii) With each casting in a water-proof liner encased by a 200mm thickness of polystyrene stiff foam insulation and with due allowance of 100mm for a non-contact separation gap, 6-castings would cover a floor area of 2.3m x 1.5m, which in the laboratory after 3 consecutive weeks of casting would occupy too much of the laboratory space.

iii) Large cubes are difficult to hermetically seal in their inner casing and for the laboratory environment not to have an influence during the 20-day period before de-moulding and

iv) Not only for test specimens is removal of cores from these large cubes with a water flushed diamond tipped coring tool a process that interferes with the density and moisture of the concrete, but also is expensive, laborious, time consuming, particularly when accuracy of 'capping' parallel end surfaces to 100mm diameter cores requires to be very precise.

Fig.2: *The acrylic cylinder containing concrete with the 200mm encasing insulation removed.*

Thus a large cube is considered a less precise method for the simulation of in-situ conditions compared to a 194mm diameter concrete cylinder that has been moulded by a 3mm thick acrylic casing that is robust, water resistant and commercially available and when cut to length of 650mm contains 19.25 litres of concrete as shown in Fig.2, this can in effect be hermetically sealed at both ends with 200mm diameter acrylic discs. Lengthways the acrylic case/tube can be laser cut to allow for ease of de-moulding, but re-joined and sealed with heat resistant water proof duct tape.

After casting and when after 20-days the concrete has hardened the cylinder of concrete is easily removed from its acrylic casing, marked for cutting by circular diamond tipped saw allowing for 2 x 305 mm long cylinders and a 30mm thick disc to be removed from the central area that has experienced the maximum temperature. The sawn ends of both cylinders and disc are sealed with thin plastic film to prevent drying/moisture loss.

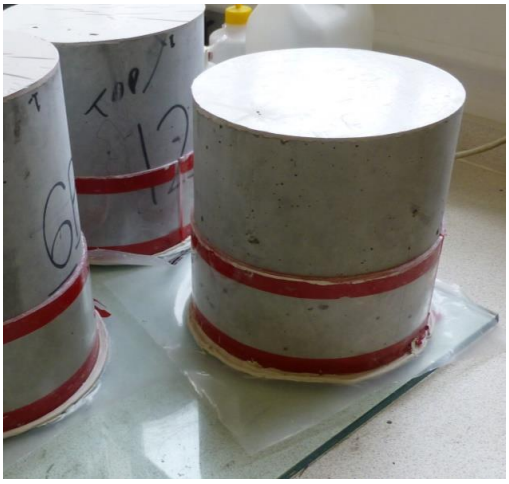

Fig. 3: *Capped cylinders with retaining collars lined with insulation tape to avoid adhesion.*

Before capping at 23 days the plastic film is removed and the 305mm cylinders are tested for:-
Density: By physical measurement and weighing top and bottom halves, as well as assessment for coarse aggregate distribution and floatation.

Crack detection: A 'fluid' is applied to the sawn areas for viewing under UV light to determine the amount of thermally induced micro-cracking. When the fluid has dried, images are taken for later analysis and

Ultrasonic pulse velocity: Scans are made of each half cylinder for evaluation of differences between top and bottom halves and aggregate dispersion.

Following these tests the cylinders are capped both ends with not more than 2.5mm thickness of 2-componet polyester hard filler resin as shown in Fig.3 and later Demec studs attached at peripheral ¼ points for E-Value determination, before crushing at 28-days for

comparison to standard cube test results. The 30mm thick disc also taken from the 'half' length is tested for water permeability by Initial Surface Absorption (ISAT) [19] Fig. 4 and thermal movement later. For ISAT and at 24 hours before testing the plastic film is removed to permit the specimen to condition in laboratory atmosphere and allow any surface moisture to evaporate. These tests were evaluated during Part 1 of the research and have been refined as a result. Due to the non-availability of (lwa) LWA the programme will be repeated in Part 2

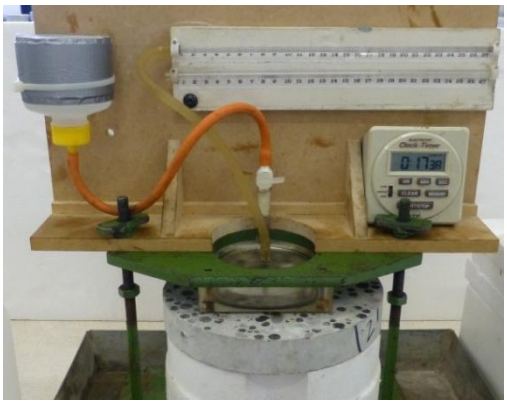

Fig. 4: *A 30mm thick disc clamped in the ISAT for water permeability*

.

Part 2. Overcoming the shortcomings of a highly absorbent coarse LWA for concrete.
To complete the research other work continues to manufacture (lwa) LWA. Nustone Ltd plan to produce sufficient quantity of this LWA, with the 'new concept' bench top rotary kiln under construction and funded by the Crossrail1 INNOVATE18 competition. Manufacture will take place at VINCI Technology Centre UK Ltd, Leighton Buzzard where there are appropriate facilities for kiln operations using the detritus London clay from tunnelling operations. With the refined test methods, research will continue during 2014 at the University of Wolverhampton

1. To confirm combinations of normal and (lwa) LWA are possible without segregation in concrete.
2. Determine the boundaries for concrete strength etc., with various aggregate combinations.
3. Find the uses for lightweight concrete that give the best environmental advantage.

ACKNOWLEDGEMENTS

Prof. Jamal Khatib; MSc Students Matthew Adams; (UK). Jian Hu;(CPR). Yodwara Wanamkang; (Thailand). Faculty of Science and Engineering, University of Wolverhampton.

Richard W F Boarder; Development Director, Nustone Ltd.
Crossrail Limited for funding via INNOVATE18 a 'new concept' bench top rotary kiln.

REFERENCES

[1] The Concrete Society Technical Report No. 16. *Structural lightweight-aggregate concrete for marine and offshore applications*. Concrete Society. ISBN 0-7210-1101-2, May 1978.

[2] Owens P L. Lightweight aggregates for structural purposes. Structural Lightweight Aggregate Concrete. Blackie Academic & Professional Chapman & Hall ISBN 0-7514-0006-8, 1993.
[3] Owens P L. One Shell Plaza shows the way. *Concrete* (December) pp 24-25, 1974
[4] Spratt B H. *The structural use of lightweight aggregate concrete*. Cement and Concrete Association, ISBN 0 7210 0973, 5 December 1974
[6] Nustone Ltd. UK Patent Application No 1305990.2 *A Lightweight Aggregate and a Concrete Comprising the Lightweight Aggregate.* INTELLECTUAL PROPERTY OFFICE. April 2013.
[7] Owens P L. Lightweight Concrete – Development of Mixes Suitable for Structural Application. *Advances in Concrete, Concrete Society Conference,* Birmingham, Day 2. Morning session, July 1971.
[8] BS EN 12390 – 7: 2009. Testing Hardened Concrete – *Density of Hardened Concrete*. BSI London, 2009.
[9] BS EN 12350 – 6: 2009. Testing Fresh Concrete – *Density.* BSI London, 2009.
[10] Lindgärd J and Hammer T A. Fire resistance of Structural Lightweight Concrete. A literature review with focus on spalling. Part of the Norwegian LIGHTCON project.
[11] Owens P L. *The influence of lightweight aggregates on the tensile strain capacity of concrete subjected to thermal stressing.* A thesis presented in partial fulfilment of the requirement for the Degree of Master of Philosophy, Department of Civil Engineering, The University of Leeds, October 1982.
[12] BS 8500-1:2002 – Concrete. Complimentary British standard to BS EN 206-1. *Method of specifying and guidance for the specifier*, BSI, 2006.
[13] Bamforth P B. In Situ Measurement of the Effect of Partial Portland Cement Replacement Using Either Fly Ash or Ground Granulated Blast-Furnace Slag on the Performance of Mass Concrete. *Proceedings of the Institution of Civil Engineers, London*, Vol. 69, Part2, pp. 777-800, September 1980.
[14] Owens P L. and Buttler F G. The Reactions of Fly Ash and Portland Cement With Relation to the Strength of Concrete as a Function of Time and Temperature. *7th International Congress on the Chemistry of Cement Volume III Communications* pp IV-60 to IV-65, Paris, July 1980.
[15] Owens P L. Effect of Temperature Rise and Fall on the Strength and Permeability of Concrete Made With and Without Fly Ash. *Temperature Effects on Concrete. ASTM STP 858*. T R Naik, Ed., American Society for Testing and Materials, Philadelphia, pp.134-149, 1985.
[16] Bamforth P B. *Early –age thermal crack control in concrete* CIRIA C660 978-0-86017-2 London, 2007.
[17] FIP Manual of Lightweight Aggregate Concrete 2nd Edition pp 86-87 ISBN 0-903384-43-4, 1983.
[18] BS 1881-130:2013 – Testing Concrete – *Method for temperature-matched curing of concrete specimens*. BSI, London, 2013.
[19] BS 1881-208:1996 – Testing Concrete – *Recommendations for the determination of the initial surface absorption of concrete.* BSI, London. 1996.

RESEARCH AND DEVELOPMENT OF THERMAL INSULATING ALKALI-ACTIVATED SYSTEMS

Stanislav Staněk
Faculty of Civil Engineering, VŠB-TU Ostrava, Ludvíka Podéště 1875/17, 70833 Ostrava, Czech Republic
stanislav.stanek@vsb.cz

ABSTRACT: The paper deals with a laboratory research and development of alkali activated system with thermal insulating properties, where, such as fillers were used low density materials, specifically Liapor (ceramic aggregates), expanded perlite, expanded vermiculite, Ekostyren (recycled polystyrene), SioPor (expanded sand), REFAGLASS (recycled foamed glass), recycled cork and waste wood flinders.
The experiment was focused on compressive strengths and heat conductivity of prepared materials. The purpose was to prepare durable but also isolating material based on alkali-activated blast furnace slag. In the research were prepared different kinds of mixtures. The values of compressive strengths and thermal conductivity of tested admixtures qualitatively correspond to commercially available building material. When thermal conductivity has ranged at 0.07 - 0.4 [$W.m^{-1}.K^{-1}$], the compressive strengths reached 5 to 25 MPa.
The results are a foundation for the next research and development of lightweight alkali activated systems with focus on practical applications in building.
Keywords: Alkali-activated, Geopolymer, lightweight Aggregate, low density material, thermal insulation.

INTRODUCTION

Current development in energy prices and also increasing demands on environmental performance of buildings, force each of us to choose the construction of building, or use in building reconstruction materials and systems, that the heat loss during its use was minimal.

In today's building market we can found a wide range of thermal insulation materials, which are vary in design, depending on properties of their location. Thermal insulation of buildings is performed in five ways, contact system, a system of sandwich walls, ventilated thermal insulating system, using of thermal insulating plaster, or the use of thermal insulating walls [8].

The best insulating materials, whose thermal conductivity ranges from 0.02 to 0.09 $W.m^{-1}.K^{-1}$, are mainly used in contact or sandwich system, these materials are anchored to the main load-bearing part of the structure. Among the most commonly used insulating materials in this group ranges expanded polystyrene, mineral wool and foam glass [8]. The advantage of these materials is easy workability and formability. Disadvantages are low resistance to mechanical damage, high demands for quality design and also decreased resistance to external influences, or flammability [7].

For insulating of ventilated insulation system, when the insulator is mounted on the carrier structure in free space behind the visual wall, are most commonly used polyurethanes, wool, or cellulose products. The disadvantage of this solution is high cost [7, 8].
In case of insulation with insulating plaster is used so-called thermal-plaster that in addition to conventional components includes insulating particles, mostly expanded perlite and polystyrene. These are used mainly for insulation of complicated facades of historic buildings [8]. The disadvantages are worse thermal insulation properties, surface treatment demands and occasion to follow exactly the technological process of prepared mixture.

Last eventuality of thermal protection is use of the structure that is itself a thermally insulating material. This widely used construction method mainly uses aerated concrete blocks and hollow brick blocks. The advantage of these systems is speed and simplicity of masonry, the disadvantage is low compressive strength and low heat accumulation, worse noise insulating properties and high water absorption [12].

In all mentioned systems is the base of the structure made of traditional building materials, mostly clay bricks, brick blocks and cement-based blocks. Production of these building materials significantly burdens the environment, particularly energy-intensive of firing. A suitable alternative to these materials are alkali-activated systems, also known as geopolymers. These are products of the geopolymerization that is controlled process of polycondensation of suitable particles. This creates zeolites, alkaline alumosilicates, alumosilicates alkaline earth metals, that are highly steady and resistant to external environmental influences and achieve excellent strength parameters [5].

The scope of the research was the development of thermally insulating material based on alkali-activated blast furnace slag, that would suit as strength as thermal insulation properties requirements for use in construction.

USED MATERIALS

Liapor.

It is commercial name for expanded clay aggregate. It is very porous with small bulk density. Liapor is prepared by burning of clay pellets at temperature 1100-1200°. Liapor aggregate has spherical grains and sintered surface. Grain size of liapor is up to 16mm. Its main advantage is very low thermal conductivity coefficient [9].

Table 1. *Properties of Liapor aggregate [10]*

Material name	Grain size [mm]	Loose bulk density [kg.m^{-3}]	Thermal conductivity coefficient [W.m^{-1}.K^{-1}]
Liapor 1-4/500	0/4	500	0.11
Liapor 4-8/450	4/8	450	0.11
Liapor 8-16/275	8/16	275	0.09

Expanded perlite.

Experlite is prepared by heating of a natural perlite. Natural perlite is a silicate material with a very high amount of closed water in the structure. Heating the experlite the water need to get out from material and causes expansion of perlite. Material expands up to 10times. The heating is done by temperatures between 900 and 1200°C. The experlite than has very low bulk density about 100kg/m^3. Grain size of experlite is 0-4mm [4, 11]. The used type of

experlite has a spherical shape and has very low water absorption, because the surface is hydrophobised [11].

Expanded vermiculite.
It is material prepared from natural silicate material vermiculite. It is classified as phyllosilicate. By heating on 1000°C the interlaminar water causes expansion of vermiculite up to 12times. The expanded vermiculite has very low bulk density about 100 kg/m^3, but its big disadvantage is very high water absorption [4].

Ekostyren.
It is a specially prepared crushed polystyrene. It has a very low water absorption and low bulk density about 30 kg/m^3 [6]. In experiment Ekostyren with coefficient of thermal conductivity 0.035 W.m^{-1}.K^{-1} was used.

Siopor.
It is porous (95%), mineral material, ball-shaped, natural origin, based on a particular type of silicate sand. It is produced by thermal method - the method of expansion. It has excellent heat and sound insulation properties, breathable and non-flammable.

Refaglass.
It is a Recycled foamed glass, a thermal insulation material made from one hundred percent recycled glass. It has excellent properties for use in many areas of construction and it is a highly efficient, non-absorbent, non-freezing and flame-resistant material.

Recycled cork.
In experiment a crushed recycled cork of grain size 0/8 mm from a thermal insulation of buildings was used.

Waste wood flinders.
Waste wood flinders from furniture production were used.

SAMPLE PREPARATION AND TESTING

Due to big differences among used aggregates, especially the water absorption, it was not possible to mix one type of mixture. For all type of materials was used blast furnace slag as activated material and alkaline activator prepared from modified sodium silicate solution. Modification was done by addition of 50% NaOH solution to get molar ratio of sodium silicate SiO2/Na2O on value 2.0. For comparison a standard mixture was prepared with verified mix design with a sand aggregate due to standard for cement testing. The mixture is in table 2.

Table 2. *Reference mixture composition*

Material	BFS (g)	Activator (ml)	Water (g)	Aggregate (g)
Amount	450	118.6	90	1350

Tested mixtures.

In mixtures with a lightweight aggregate, the dosage of aggregate must be done by the volume. The amount of a lightweight aggregate was used with the same volume as sand aggregate for cement testing due to testing standard [3]. On the base of continuously achieved results of fresh binders and strength properties of hardened materials the amount of blast furnace slag, water and activator were modified. Samples in table 3 are named according to used aggregate.

Table 3. *Composition of tested mixtures*

Sample	BFS (g)	Activator (ml)	Water (g)	Aggregate (ml)
Liapor 4/8	450	118.6	80	1300
Liapor 1/4+8/16	300	79.0	50	400+600
Vermiculite	585	154.0	300	1300
Experlite	585	154.0	220	1300
Ekostyren	450	118.6	90	800
Siopor	675	177.9	225	900
Refaglass	750	178.0	375	1500
Recycled cork	650	233.0	98	800
Waste wood flinders	650	233.0	276	800

Tested properties.

Hardened mixtures of lightweight alkali-activated materials were tested for mechanical and thermal properties. The thermal properties are most important but if the material is used in loaded structures, not only as insulation the strength is also important. Samples for testing were prepared in dimensions of 160x40x40mm according to testing standard for cement. For coefficient of thermal conductivity testing the cylinders with diameter of 6cm and 10cm high were prepared. Testing was done using Isomet 2114 device with surface contact probe [13].

RESULTS

Samples of prepared materials were tested for mechanical properties according to standard for testing of cement. Also bulk density was determined. Because of high water absorption of samples the bulk density was determined on dry and wet samples. The thermal conductivity was measured only on dry sample, because absorbed water increases the thermal conductivity coefficient. Results of measured properties on materials are in table 4.

Table 4. *Strength of samples after 28 days and bulk densities after 28days*

Sample	Compression strength 28days (MPa)	Bulk density Wet sample ($kg.m^{-3}$)	Bulk density Dry sample ($kg.m^{-3}$)	Coefficient of thermal conductivity $\lambda[W.m^{-1}.K^{-1}]$
Liapor 4/8	23.4	1250	1150	0.237
Liapor 1/4+8/16	7.1	860	810	0.165
Vermiculite	17.1	1570	1130	0.306
Experlite	21.7	1380	1070	0.219
Ekostyren	5.5	880	840	0.123
Siopor	4.8	1360	570	0.114
Refaglass	16.4	2000	1000	0.147
Recycled cork	5.3	1000	780	0.154
Waste wood flinders	6.1	1100	880	0.073

CONCLUSIONS

Experimentally were prepared materials with low density by using a lightweight aggregate. For thermal insulation materials is crucial a low bulk density and a low thermal conductivity. Prepared materials do not have as good thermal properties as commercial materials. But because of quite high compression strength these could be used for loaded structures with good thermal insulation properties. The best thermal insulation properties have material based on waste wood flinders, Siopor and crushed polystyrene. The strength of Siopor mixture is the lowest. Quite good ratio of strength and thermal properties has waste wood flinders mixture, refaglass mixture, experlite based material and Liapor 4/8. By changing the amount of lightweight aggregate component in mixture it could be possible to get better thermal properties. Next research of these materials will be focused on mix design to obtain optimal properties.

ACKNOWLEDGMENT

The paper was realized with the financial support of Ministry of Education, support of specific academic research - Student grant competition VŠB - TU Ostrava, the identification number SP2013/11 – Research and development of thermal insulating alkali-activated systems.

REFERENCES

[1] J. Boháčová. Preparation and verification of the geopolymers properties based on metakaolin and other binder, Diploma theses. VŠB - TUO, 2009, Ostrava.

[2] J. Boháčová. Study of influence of various types of an aggregate on properties of geopolymerous systems based on blast furnace slag. Bachelor theses, VŠB - TUO, 2008, Ostrava.

[3] ČSN EN 196-1 Methods of testing cement - Part 1: Determination of strength. Czech normalization institute, 2005

[4] Svoboda, L. a kolektiv: *Stavební hmoty*. JAGA, Bratislava, 2005, 471s. ISBN 80-8076-007-1

[5] V. Tomková, Alkali-activated composites based on slags from iron and steel metallurgy, Metallurgy, 48 (2009), 223-227

[6] Available at: http://www.ekostyren.cz/materialovy-list-2

[7] Available at: http://istavitel.cz/clanek/izolace/tepelne-izolace/zakladni-prehled-tepelneizolacnich-materialu_80

[8] Available at: http://istavitel.cz/clanek/izolace/tepelne-izolace/zpusoby-zatepleniobvodoveho-plaste-domu_81

[9] Available at: http://www.Liapor.cz/cz/keramicke-kamenivo-Liapor#technicke-info

[10] Available at: http:// www.Liapor.cz/dokumenty/technicke-listy/kamenivo/Liapor01.pdf

[11] Available at: http://www.perlit.cz/expand_perlit.php

[12] Available at: http://www.xstavba.eu/jaky-porobeton-ytong-hh-porfix-nebo-ift/

[13] Available at: http://www.appliedp.com/en/isomet.htm

CALCAREOUS GAIZE AS AN ACTIVE MINERAL ADMIXTURE FOR BLENDED CEMENT

M. Gawlicki, P. Stępień and W. Roszczynialski
AGH University of Science and Technology, Faculty of Materials Science and Ceramics, 30 Mickiewicza Av., 30-059 Krakow, Poland
wroszcz@gmail.com

ABSTRACT: The influence of the presence of gaize (a calcareous sediment rock) on the hydration of ordinary Portland cement (OPC) was investigated. Calcareous gaize was characterized by means of different techniques: X-ray diffraction, pozzolanic activity determination, scanning electron microscopy (SEM, EDS), and termogravimetric analysis. Three cements containing 15, 25 and 35% of calcareous gaize were produced by intergrinding. The following parameters of hydrating pastes and mortars were determined: water demand, initial and final setting time and compressive strength for mortars up to 90 days old. Hydration process of cement mixtures with gaize addition was also investigated using calorimetry and SEM microscopy. Additional properties were determined: density, Blaine surface area and particle size distribution. CEM I was used as a reference cement. It has been found that the addition of 15 to 35% of gaize allows to obtain binders meeting the requirements of cements CEM II/A-M 42,5R, CEM II/B-M 42,5R and CEM II/B-M 42,5N cement (if calcareous gaize is treated as a mix of natural pozzolan and limestone).
Keywords: Blended cement, calcareous gaize, limestone, mineral admixture, water demand.

INTRODUCTION

The most recent edition of EN 197-1:2012 standard sustains the approach of building materials industry professionals to accepted main components of Ordinary Portland cements, which aside Portland clinker may be: granulated blast furnace slag, certain types of fly ash, silica fume, burnt shale, limestone and pozzolans [1]. These definitions block the application of other than above mentioned materials as components of ordinary Portland cements. Nevertheless, there are natural raw materials combining characteristics of more than one main component but failing to meet the requirements for separate constituents of ordinary Portland cements. An interesting example of such material is calcareous gaize.

From the point of view of binding materials technology, calcareous gaize is a natural blend of pozzolanic active silica and dispersed calcium carbonate. This sedimentary mineral contains less calcium carbonate than required in EN 197-1:2012 standard from limestone (> 75% $CaCO_3$) and less active silica than required from pozzolans (> 25% SiO_2). Nevertheless, the application of calcareous gaize as a raw material for the production of Portland cement allows to obtain binding material meeting the requirements set by the standards for hydraulic binders (including physical and mechanical requirements for OPC) [1].

The purpose of this research was to thoroughly characterize calcareous gaize from the Ożarów region and assess its usability as an active component of clinker-based hydraulic binders.

CALCAREOUS GAIZE AS AN ACTIVE MINERAL ADMIXTURE FOR BLENDED CEMENT

Calcareous gaize properties

Samples of calcareous gaize from opencast deposit near Ożarów in Świętokrzyskie voivodeship were used for the binder preparation. Besides chemical analysis, phase composition was determined by the means of X-ray diffraction and thermal analysis (DTA/TG). Pozzlolanic activity was determined in accordance with ASTM C379-65 American standard [2]. Scanning electron microscopy was used to investigate the morphology of the examined mineral.

The chemical composition and pozzolanic activity (determined in accordance with ASTM C379-65 American standard) of calcareous gaize is shown in Table 1.

Table 1. *Chemical composition and pozzolanic activity of calcareous gaize*

	Chemcial composition, oxides								**Active oxides (pozzolanic activity)**	
	CaO	**MgO**	**SiO_2**	**Fe_2O_3**	**Al_2O_3**	**SO_3**	**Na_2O_e**	**L. O. I.**	**SiO_2**	**Al_2O_3**
Volume [mass %]	33,5	1,1	32,1	1,0	1,7	0,2	0,1	31,1	15,7	0,3

X-ray diffraction analysis results have shown that the main crystalline components of calcareous gaize are calcite, cristobalite and β-quartz. Based on the chemical analysis and the assumption that calcium oxide occurs only in the form of $CaCO_3$, it has been estimated that calcareous gaize contains about 60% of calcite ($CaCO_3$). What is more, thermal analysis results have shown that besides calcite the mineral contains dispersed calcium carbonate, which decomposes in much lower temperatures than calcite.

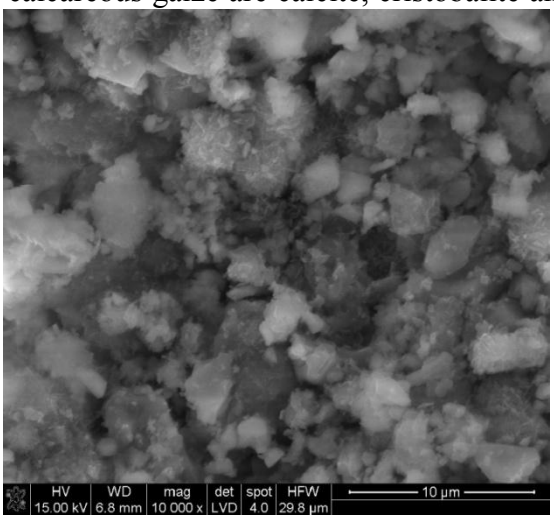

Fig. 1: *SEM image of Calcareous Gaize*

Scanning electron microscope images of gaize show a highly homogenous material with grains smaller than 5 µm in radius. The SEM image is shown in Figure 1.

Examination of hydraulic binders containing calcareous gaize

The research was carried on binders containing 15, 25 and 35% of gaize (described as B15, B25 and B35, respectively). The binders were prepared by intergrinding Portland clinker, natural gypsum and calcareous gaize in a laboratory ball mill. Grinding time was established at 50 minutes. Ordinary Portland cement CEM I 42,5R was used as reference binder, described as B0. Composition of examined binders is shown below in Table 2.

Table 2. *Composition of examined binders.*

Component [mass %]	B0	B15	B25	B35
Portland clinker	95	80	70	60
Calcareous gaize	0	15	25	35
Gypsum	5	5	5	5

The following physical and rheological properties of binders were determined: density, specific surface area (in accordance to Blaine method), particle size distribution, water/binder ratio for standard consistency of fresh paste and time of set. The examinations were carried in accordance with EN196-1:2006 and EN 196-3+A1:2011 standards [3, 4]. The results are shown in Table 3.

Table 3. *Physical and rheological properties of examined binders.*

Binder	Density [g/cm^3]	Blaine specific surface area [g/cm^2]	Water/Binder ratio for standard consistency	Time of set [min]	
				Beginning	End
S0	3,33	3500	0,26	180	275
S15	3,15	5150	0,28	175	280
S25	3,07	6320	0,30	155	295
S35	2,97	7740	0,32	135	285

Strength examination was carried out on mortars in accordance with PN-EN 196-1:2006 standard [3]. Compressive strength was measured after 1, 2, 7, 28 and 90 days of mortar hydration, and the results are shown in Table 4.

Table 4. *Compressive strength of examined hydraulic binders.*

Hydration time [days]	Compressive strength [MPa]			
	S0	S15	S25	S35
1	16,5	12,8	8,2	5,6
2	28,1	22,4	15,8	11,3
7	41,6	35,9	30,5	23,8
28	53,9	53,2	46,8	43,3
90	61,6	60,8	57,4	52,4

DISCUSSION OF THE RESULTS

The results of the examinations have shown that calcareous gaize from the Ożarów region is a fine-grained and homogenous material. It mainly contains the following phases: Calcium carbonate (60% of mass), quartz and cristobalite. The amount of active pozzolanic oxides (SiO_2 and Al_2O_3) allows to classify gaize as a moderately active pozzolanic additive [5]. The density of the binder decreases with the increase in the amount of added mineral [6]. Gaize is a grindable mineral which increases the specific surface area by 1200 cm^2/g for every 10% of Portland clinker mass substituted.

The addition of gaize shortens the beginning of time of set – it is believed that this effect is caused by very fine particles of calcium carbonate, which can serve as a nucleation centre for hydrating clinker phases [7,8].

Active influence of gaize positively alters cement hydration process - pozzolanic reaction of active silica and reaction of calcite ($CaCO_3$) with tricalcium

aluminate ($3CaO{\cdot}Al_2O_3$) yielding hydrated calcium carboaluminate ($3CaO{\cdot}Al_2O_3{\cdot}CaCO_3{\cdot}12H_2O$) positively influence properties of hardened cements such as compressive strength, durability and corrosion resistance.

The addition of calcareous gaize slightly decreases early strengths of mortars; after 7 days of hydration binder containing 15% of gaize has compressive strength 10% lower than reference binder, while the binder containing 35% of gaize has compressive strength 40% lower. Nevertheless, after 28 days of hydration, binder containing 15% of gaize shows nearly equal strength as the reference binder (53MPa), while the strength of other binders with gaize exceed 42,5 MPa. What is more, the difference in compressive strength of binders containing gaize in respect to the reference binder decreases with time, which can be observed after 90 days of hydration.

SUMMARY

Carried research show that calcareous gaize is an interesting material for hydraulic mineral binders production. It can be treated as a natural blend of pozzolan and limestone, two raw materials counted as major components of ordinary Portland cements by EN 197-1:2012 standard.

Prepared cements containing 15, 25 and 35% of calcareous gaize have satisfying functional properties meeting the requirements for 42,5N and even 42,5R strength class cements. Active influence of gaize positively influences properties of cements such as compressive strength, durability and corrosion resistance.

ACKNOWLEDGEMENTS

The financial support from the Polish State Committee for Scientific Research – KBN (grant n. NN506300139) is fully acknowledged.

REFERENCES

[1] EN 197-1:2012. *Cement – Part 1: Composition, specifications and conformity criteria for common cements*, European Committee for Standardization, 2012.

[2] ASTM C 379-65. *Specification for fly ash for use as a pozzolanic material with lime*, American Standard, 2002.

[3] EN 196-1:2006. *Cement testing methods – Part 1: Strength determination*, European Committee for Standardization, 2006.

[4] EN 196-3+A1:2011. *Cement testing methods – Part 3: Time of set and volume stability determination*, European Committee for Standardization, 2011.

[5] Roszczynialski W., *Application possibilities of materials with pozzolanic properties in cement industry*, Cement Lime Gypsum, Krakow, 8/9, 1980 (in Polish).

[6] Wyrwicka K., Roszczynialski W., *Assesment of calcareous gaize applicability as an active additive for cement production*, Polish Geological Institute Bulletin, Warsaw, 1986 (in Polish).

[7] Lothenbach B., Scrivener K., *Influence of limestone on the hydration of Portland cements*, Cement and Concrete Research 38, 2008.

[8] Tosun-Felekoglu K., *The effect of C_3A content on sulfate durability of Portland limestone cement mortars*, Constructions and Buildings Materials 36, 2012.

EFFECT OF DIFFERENT ADDITION METHODS OF NAPHTHALENE SUPERPLASTICISER ON RHEOLOGY, COMPRESSIVE STRENGTH AND DRYING SHRINKAGE OF NaOH-ACTIVATED SLAG PASTE

Jun Ren, Mengxia Sheng, Yicheng Shi, Qizhi Zhou, Yun Bai*
Department of Civil, Environmental and Geomatic Engineering, University College London, London, UK
Yun.bai@ucl.ac.uk

Martyn J. Earle
The Queen's University Ionic Liquid Laboratories (QUILL) Research Centre, Queen's University Belfast, Belfast, UK

Changhui Yang
College of Materials and Engineering, Chongqing University, China

ABSTRACT: The lack of workability has hindered the widespread applications of alkali-activated slag (AAS) -a novel, low carbon cementitious building material. In order to address this main barrier, the addition of superplasticiser is essential. However, many researchers have demonstrated that the conventional superplasticisers (SP) could not work properly in this novel system due to its interaction with the alkaline activator. Thus, adding SP and activator separately could be a potential method to improve the performance of SP in AAS. In this paper, the effect of different addition methods of conventional naphthalene derivation superplasticiser on the rheological properties of NaOH–activated slag paste was investigated. Then, the influence of different addition methods on the hardened properties, such as compressive strength and drying shrinkage, of AAS, was examined. The addition methods examined were simultaneous addition and separate additions including prior and delayed addition of SP by 3 min with respect to the addition of the activator. The results indicated that compared with simultaneous addition, separate addition methods showed better performance in the rheological properties of NaOH-activated slag paste. However, simultaneous addition has resulted in the highest compressive strength and the lowest drying shrinkage.
Keywords: Alkali-activated slag, compressive strength, hardened properties, naphthalene superplasticiser, rheology.

INTRODUCTION

Many attempts have been conducted over the past few decades to find suitable alternative low carbon building materials, which could potentially replace the Portland cement (PC) [1, 2].

Among various alternatives, alkali-activated slag (AAS) has been considered as the most attractive low carbon cementitious material due to its lower CO_2 emission and superior overall performance than PC [3]. However, AAS is still facing some challenges, notably, its poor rheological properties. To tackle this issue as well as to develop high performance AAS concrete, various chemical admixtures, especially superplasticiser (SP), need to be employed in order to improve the workability of AAS concrete.

Naphthalene derivation superplasticiser (NF SP) is one of the most commonly used superplasticisers in PC system [5-7]. Whereas the effects of commercial NF SP on PC systems have been well studied, its influence on AAS is largely unknown. Based on some limited studies available in the literature, it has demonstrated that NF SP could not significantly improve in the workability of AAS. On the contrary, sometimes, it even showed no effect on the workability and rheological property of AAS, especially in the AAS systems when waterglass was used as activator. This is presumably due to the possible interactions between the NF SP and the activators under highly alkaline environment [8-10]. The dysfunction of NF SP in AAS could be caused by the chemical instability and competitive adsorption between the activator and NF SP when adding them at the same time. Previous work reported by the authors indicated that adding lignosulfonate-based SP and waterglass activator at different mixing stage can improve the workability of AAS due to the increased stability of the SP and the reduced competition between the SP and the activator [12, 13]. However, the effect of addition method of NF SP on AAS has still not been explored, yet.

The aim of this study is, therefore, to investigate the effect of NF SP on some fresh and hardened properties of AAS paste. The effect of NF SP on rheological properties and compressive strength of AAS paste prepared by adding the NF SP and the activator separately at 3 min interval were examined. Meantime, the influence of different addition methods on the drying shrinkage of AAS pastes was also investigated. The suitability of different models for describing the rheological behaviour of NaOH-activated AAS was discussed.

EXPERIMENTAL PROGRAMME

Materials

The chemical composition of ground granulated blast furnace slag (GGBS, short for slag hereafter) is shown in Table 1 (Hanson Heidelberg Cement Group, UK). The fineness and specific gravity of the slag used were 518 m^2/kg and 2900 kg.m^3, respectively. The raw NaOH was obtained from Tennants Distribution. Naphthalene derivation superplasticiser (NF SP) was supplied by Tianjin Jiangong Special Material Co. Ltd.

Table 1. *Chemical composition of slag*

CaO	SiO_2	Al_2O_3	MgO	SO_3	TiO_2	MnO	Na_2O	Fe_2O_3	K_2O	LOI
39.03%	35.79%	12.28%	7.75%	1.66%	0.74%	0.71%	0.34%	0.30%	0.59%	0.39%

Mixing Procedure

The water to slag ratio for all the mixes was fixed at 0.48. The dosage of NF SP was controlled as 0, 0.125, 0.250, and 0.500% (by the mass of slag). NaOH solution was used as the activator and its content was controlled at 4 %(counted as Na_2O equivalent) by the mass of slag. Both the activator and NF SP were dissolved in water. Three different addition methods were studied, namely: 1) *simultaneous addition (**SA**)*: mixing slag with both NF SP and activator together; 2) *prior addition (**PA**)*: mixing slag with NF SP first, then adding

activator at 3 min interval; and 3) *delayed addition (**DA**)*: mixing slag with activator first, then adding NF SP at 3 min interval.

Test

The minislump test, which is carried out with a PVC plate and a cone with a lower inner diameter of 38.1 mm, an upper inner diameter of 19 mm, and a height of 52.7 mm, was used to determine the spread of AAS paste. The diameters at two perpendicular directions were measured and the average diameter was reported. The rheological property was measured by using a modified Rheomat 115 viscometer. The initial measurements of both the minislump and the rheological property were conducted at 7 minutes after mixing.

NaOH-activated slag paste specimens (25×25×25 mm) were prepared, and then cured at 20±2℃ under 100% relative humidity in sealed plastic bags with wet hessian. The compressive strengths of the specimens were determined after curing for 1, 7, 28, and 56 days. Drying shrinkage specimens (25×25×250 mm prism prepared with 0.500% dosage of NF SP) were cured for 24 hours at 20±2℃ under 100% relative humidity before demoulding. After demoulding, the prisms were cured for another 72 hours in water, and then was exposed to a drying condition in a room with constant temperature at 20±2℃ under 50±5% relative humidity. The change of length of prism was measured regularly with CONTROLS model 63-L0035/A apparatus.

RESULTS AND DISCUSSIONS

Rheological Property

The effect of different addition methods on rheological properties (in terms of plastic viscosity Vs yield stress) are illustrated in **Fig. 1**, which is plotted by using the vectorised-rheograph approach [14]. The results clearly demonstrated that with the addition of NF SP, both yield stress and plastic viscosity have been effectively reduced. In addition, compared with *simultaneous addition*, the *PA* and *DA* provided better plasticizing effect, especially at the lower dosage (dosage below saturation point 0.250%). Comparing both *separate addition* methods, lower yield stress can be observed from the *PA*, while a lower plastic viscosity was obtained from the *DA*.

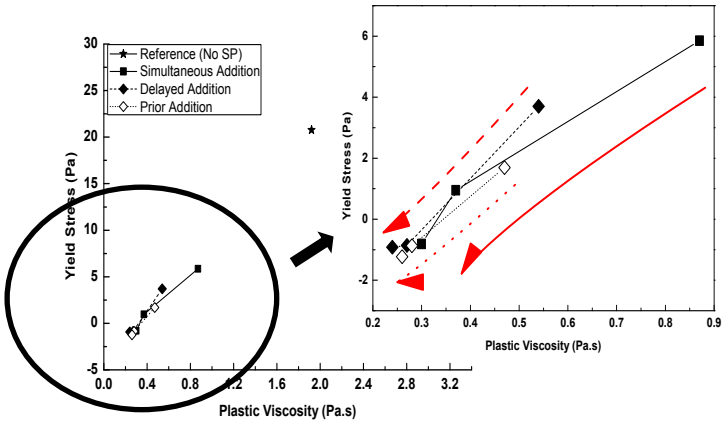

Fig. 1: *Effect of different addition methods of Naphthalene superplasticiser on rheological properties of NaOH-activated slag paste (The direction of arrow indicated the increase of SP Dosage).*

Minislump

The initial minislump test results for the NaOH-activated slag paste are shown in **Fig. 2**. The results indicated that the flowability of NaOH-activated slag improved with the addition of NF SP. It is obvious from **Fig. 2** that the minislump spread increased rapidly with dosages up to the saturation point of around 0.250%, which may be due to the availability of sufficient active sites on the surface of slag particles [15, 16]. When the dosage was over this point (0.250%), the flowability increased slowly and gradually reached a plateau. The results suggested that the NF SP showed a good plasticising effect on NaOH-activated slag, which also confirmed by Puertas's work [11]. In addition to the good plasticising effect, it is apparent from Figure 2 that the minislump spread was further improved by separate additions (both *DA* and *PA*). More than 10 mm improvement of the spread diameter was achieved by adding NF SP and NaOH at different mixing stages. The highest minislump was obtained from *PA*, which is similar to the author's previous finding [13].

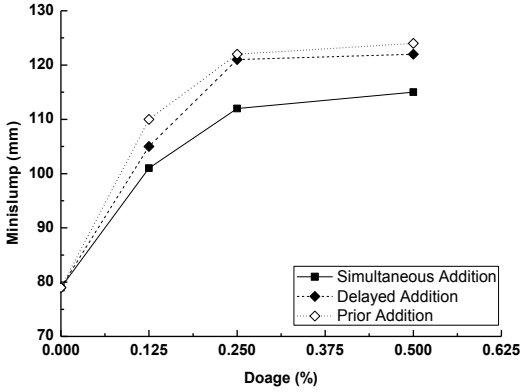

Fig. 2: *Effect of different addition methods of Naphthalene superplasticiser on initial minislump spread of NaOH-activated slag paste.*

Compressive Strength

The compressive strengths of NaOH-activated slag with NF SP are illustrated in **Fig. 3 (a-c)**. The results clearly demonstrated that compressive strength of all NaOH-activated slag pastes was gradually increased with the increase of curing time. Comparing these results, it is apparent that the reference NaOH-activated slag showed lower strength at all curing ages expect at 1 day, indicating that the addition of NF SP has increased the compressive strength. The reduction in the early strength could be due to the retarding effect by the addition of NF SP [17].

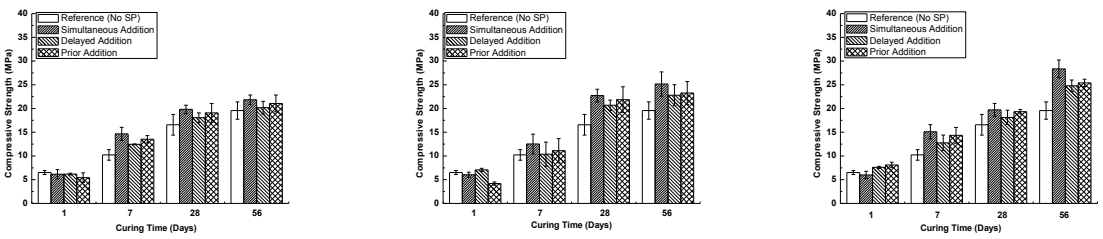

(a) at dosage of 0.125% *(b) at dosage of 0.250%* *(c) at dosage of 0.500%*

Fig. 3: *Effect of different addition methods of Naphthalene superplasticiser on compressive strength of*

NaOH-activated slag: (a) at dosage of 0.125%, (b) at dosage of 0.250% and (c) at dosage of 0.500%

In terms of the addition method of NF SP, **Fig. 3** also revealed that *SA* produced the highest compressive strength at all the dosages and curing ages except at 1 day. Nonetheless, the NaOH-activated slag pastes prepared by separate addition methods still offered comparable compressive strengths, with *PA* slightly higher than DA.

Drying Shrinkage

The effect of different addition methods of NF SP on drying shrinkage of NaOH-activated slag up to 175 days are shown in **Fig. 4.** Apparently, the drying shrinkage of the NaOH-activated slag prism was changed by adding NF SP. Among all the addition methods, *SA* caused the reduction in shrinkage with approximately 10% less than the reference specimen at 175 days. In contrast, both separate addition methods increased the final drying shrinkage of NaOH-activated slag paste. Interestingly, comparing with reference prism, the drying shrinkage of prism prepared by *PA* was smaller before 3 month, and it increased significantly over time. The reason could be attributed to the change of the microstructure of the NaOH-activated slag paste which still needs to be investigated in the future.

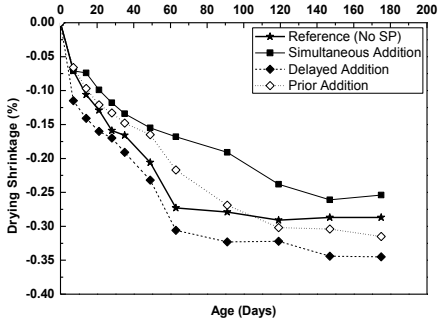

Fig. 4: *Effect of different addition methods of Naphthalene superplasticiser on drying shrinkage of NaOH-activated slag prism.*

CONCLUSIONS

(1) The effect of different addition methods of NF SP on rheological properties of NaOH-activated slag paste was presented in a rheograph using yield stress vs. plastic viscosity. Comparing with simultaneous addition, separate addition methods produced better plasticising effect from the addition of NF SP in NaOH-activated slag.

(2) In NaOH-activated slag paste, the spread diameter of minislump obtained from both delayed and prior addition methods was higher than that of simultaneous addition method, with the prior addition performed better than the delayed addition.

(3) The compressive strength of NaOH-activated slag was improved in the presence of NF SP. The highest compressive strength was obtained from simultaneous addition.

(4) Comparing with NaOH-activated slag paste without SP, lower drying shrinkage was obtained from simultaneous addition of NF SP. However, higher drying shrinkage was observed from both separate addition methods

ACKNOWLEDGEMENT

The authors would like to express their thanks to Hanson Heidelberg Cement Group, UK and Tianjin Jiangong Special Material Co. Ltd. China for their support in this research. Mr Jun Ren also wishes to thank Queen's University, Belfast and University College London for the sponsorship for his PhD study.

REFERENCES

[1] Li YD, Sun Y. Preliminary study on combined-alkali-slag paste materials. Cement and Concrete Research. 2000;30(6):963-6.

[2] Gong CM, Yang NR. Effect of phosphate on the hydration of alkali-activated red mud-slag cementitious material. Cement and Concrete Research. 2000;30(7):1013-6.

[3] Roy DM. Alkali-activated cements Opportunities and challenges. *Cement and Concrete Research.* 1999;29(2):249-54.

[4] Collins F, Sanjayan J. Early age strength and workability of slag pastes activated by sodium silicates. Magazine of Concrete Research. 2001;53(5):321-6.

[5] El-Gamal SMA, Al-Nowaiser FM, Al-Baity AO. Effect of superplasticizers on the hydration kinetic and mechanical properties of Portland cement pastes. Journal of Advanced Research. 2012;3(2):119-24.

[6] Collepardi M. Admixtures used to enhance placing characteristics of concrete. Cement and Concrete Composites. 1998;20(2-3):103-12.

[7] Hewlett PC. Lea's chemistry of cement and concrete: Butterworth-Heinemann; 2004.

[8] Douglas E, Brandstetr J. A preliminary study on the alkali activation of ground granulated blast-furnace slag. Cement and Concrete Research. 1990;20(5):746-56.

[9] Wang S-D, Scrivener KL, Pratt PL. *Factors affecting the strength of alkali-activated slag. Cement and Concrete Research.* 1994;24(6):1033-43.

[10] Palacios M, Banfill PFG, Puertas F. Rheology and setting of alkali-activated slag pastes and mortars: Effect of organ admixture. Aci Materials Journal. 2008;105(2):140-8.

[11] Palacios M, Puertas F. Effect of superplasticizer and shrinkage-reducing admixtures on alkali-activated slag pastes and mortars. Cement and Concrete Research. 2005;35(7):1358-67.

[12] Ren J, Bai Y, Earle MJ, Yang CH. A preliminary study on the effect of separate addition of lignosulfonate superplasticiser and waterglass on the rheological behaviour of alkali-activated slags. *Third International Conference on Sustainable Construction Materials & Technologies (SCMT3);* 2013; Kyoto.

[13] Ren J, Bai Y, Earle MJ, Yang CH.. Effect of Different Addition Methods of Lignosulfonate Admixture on the Adsorption, Zeta Potential and Fluidity of Alkali-activated Slag Binder. *Young Researchers' Forum in Construction Materials*; 2012; London.

[14] Wallevik OH, Wallevik JE. Rheology as a tool in concrete science: The use of rheographs and workability boxes. Cement and Concrete Research. 2011;41(12):1279-88.

[15] Nguyen V-H, Remond S, Gallias J-L. Influence of cement grouts composition on the rheological behaviour. Cement and Concrete Research. 2011;41(3):292-300.

[16] Aydın S, Hilmi Aytaç A, Ramyar K. Effects of fineness of cement on polynaphthalene sulfonate based superplasticizer–cement interaction. Construction and Building Materials. 2009;23(6):2402-8.

[17] Uchikawa H, Hanehara S, Shirasaka T, Sawaki D. *Effect of admixture on hydration of cement, adsorptive behavior of admixture and fluidity and setting of fresh cement paste. Cement and Concrete Research*. 1992;22(6):1115-29.

CEMENTITIOUS AND GEO-POLYMERIC MORTARS COMPARED WITH THE SAME MECHANICAL STRENGTH CLASS

Alessandra Mobili
Department of Sciences, and Engineering of Matter, Environment and Urban Planning, Università Politecnica delle Marche, Ancona, IT
a.mobili@univpm.it

Chiara Giosuè
Department of Sciences, and Engineering of Matter, Environment and Urban Planning, Università Politecnica delle Marche, Ancona, IT

Francesca Tittarelli
Department of Sciences, and Engineering of Matter, Environment and Urban Planning, Università Politecnica delle Marche, Ancona, IT

ABSTRACT: In the perspective of using environmentally friendly materials for the rehabilitation and restoration of ancient buildings, the behaviour of geo-polymeric mortars was studied. The research was developed into two main aspects: substitution of Portland cement with an alternative binder and recycling of industrial by-products. The experimentation was carried out comparing the performances of cementitious and geo-polymeric mortars with the same mechanical strength class (R1≥ 10 MPa, R2 ≥ 15 MPa, R3 ≥ 25 MPa, R4 ≥ 45 MPa), according to the European Standard. In particular, four geo-polymeric mixtures were prepared with a sodium silicate/sodium hydroxide proportion of 1:1 with different concentration of NaOH and a sand/fly ash proportion of 2.7:1. Four cementitious mortars were prepared with water/cement equal to 0.5, 0.65, 0.9 and 1.1 by weight, respectively. Different properties both in fresh and hardened state were evaluated and compared. The adherence with brick was reduced when geo-polymeric mortars were used. However, best results were obtained by geo-polymeric mortars with respect to cement ones for vapour permeability, capillarity water absorption, elastic modulus and resistance to salt crystallization.
Keywords: durability, fly ash, geo-polymer, mechanical properties, rehabilitation.

INTRODUCTION

In recent years, the eco-compatibility and the low environmental impact of materials in addition to the possible re-use of waste ones represented the central objectives of the research and the focus of new engineering studies. In fact, the production of the most common building material, Ordinary Portland Cement (OPC), generates an emission of carbon dioxide such that for every ton of cement worked, it emits into the atmosphere an equal amount of CO_2[1].

The aim of this research is to study the behaviour of mortars prepared with alternative binders, called geo-polymers, studied during the '70s for the first time by J. Davidovits.

The geo-polymers are constituted by a binary mixture of source materials and alkaline liquids. The former can be aluminosilicates, natural or deriving from waste products of special processing such as that of coal or rice, while alkali activators are usually solutions of hydroxide and silicate based on sodium or potassium [2].

The purpose of this research is to compare geo-polymeric and cementitious mortars with the same mechanical strength class by measuring their behaviour in terms of elastic modulus, adhesive strength on substrate, water vapour permeability, capillary water absorption and salt crystallization resistance.

EXPERIMENTAL PROGRAM

Materials

Geo-polimers were prepared with fly-ash (FA) and sodium-based alkaline liquid.

Fly ash is the by-product of the combustion of pulverized coal in coal-fired power plants, it could be of two types: Class C with an amount of CaO more than 10% and Class F with a low-calcium content. A Class F FA produced in Italy was used, kindly offered by General Admixture S.p.A. (Ponzano Veneto, Italy). Table 1 shows the chemical composition of fly ash.

Table 1. *Chemical analysis, weight (%) of fly ash used in this study.*

SiO_4	Al_2O_3	Fe_2O_3	CaO	MgO	K_2O	Na_2O	TiO_2	SO_3	Loss of Ignition
36 ÷ 52	22 ÷ 36	2 ÷ 10	1 ÷ 10	0.2 ÷ 3	0.2 ÷ 2	0.1 ÷ 0.6	0.1 ÷ 1.7	0.2 ÷ 2	1 ÷ 9

The alkaline activator was a mixture of sodium silicate solution (Na_2SiO_4) made of 30% of SiO_2 and 15% of Na_2O (by mass) with a SiO_2/Na_2O molar ratio of 2.10, kindly offered by Ingessil S.r.l. (Verona, Italy) and sodium hydroxide solution (NaOH) obtained by dissolution of NaOH pellets in distilled water.

Cementitious mortars were prepared with an ordinary Portland cement CEM II/A-LL 42.5R as binder and a calcareous filler with particles smaller than 100 μm as fine aggregate. A common calcareous sand with a maximum grain size of 8 mm was used for both mortars.

To reach the same workability, a superplasticizer based on modified acrylic polymer was added in the mix when needed.

Cement and geo-polymer mortars were prepared in order to cover the four different compressive strength class R1 (≥ 10 MPa), R2 (≥ 15 MPa), R3 (≥ 25 MPa), and R4 (≥ 45 MPa), according to UNI EN 1504-3:2006. The formers were prepared in accordance with UNI EN 1015-2:2007 as reported in Table 2. Concerning geo-polymers, the mixing procedure followed what said by Davidovits [3], who recommend to mix liquid solution 24 h prior to adding the liquid to the dry materials to prevent bleeding and segregation and to assist the polymerization process. Solids (fly ash and sand) were mixed first for two minutes, than the liquid activator was added and mixed for 3 minutes, at last superplasticizer, if required, was mixed for other 3 minutes. To reach different mechanical strength class, geo-polymers were prepared with different concentration as already demonstrated [4, 5].

The consistence of fresh cementitious and geo-polymeric mortars (slump) was investigated by flow table test according to the UNI EN 1015-3:2007. After casting, samples were conserved in climatic chamber at T = 20 ± 2 °C and RH = 95 ± 5% until the testing day.

To classify the eight mortars, compressive strength at 28 days was determined in accordance with UNI EN 1015-11:2007on 40 x 40 x 160 mm specimens.

Table 2. *Mix composition (g/l).*

	R4-CEM	**R3-CEM**	**R2-CEM**	**R1-CEM**	**R4-GEO**	**R3- GEO**	**R2- GEO**	**R1- GEO**
Cement (g)	450	450	250	205	-	-	-	-
Calcareous filler (g)	-	-	171	209	-	-	-	-
Water (g)	225	293	225	225	-	-	-	-
Sand (g)	1350	1350	1350	1350	1350	1350	1350	1350
Fly ash (g)	-	-	-	-	500	500	500	500
Distilled water (g)	-	-	-	-	102	90	114	126
NaOH (g)	-	-	-	-	48	60	36	24
Na_2SiO_4solution (g)	-	-	-	-	150	150	150	150
Superplasticizer (g)	-	-	-	-	-	20	-	-
aggregate/binder	3.0	3.0	6.0	7.7	2.7	2.7	2.7	2.7
water/binder	0.5	0.65	0.9	1.1	-	-	-	-
water/solids	-	-	-	-	0.30	0.28	0.33	0.35
Slump (mm)	135	140	135	140	130	135	130	135

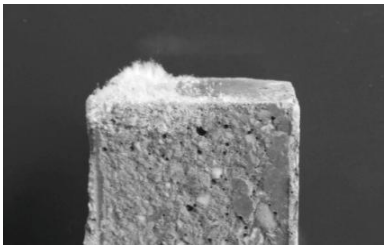

Fig. 1: *Efflorescence of geo-polymers with high NaOH concentration*.

After the curing period, the formation of efflorescence identified by X-ray diffraction as thermonatrite ($Na_2Co_3 \cdot H_2O$) on the surface of geo-polymers with high concentration of NaOH was observed (Fig. 1). This is a consequence of the exposition of the material to the atmosphere [6].

Tests and Results

Dynamic elastic modulus

To calculate the dynamic elastic modulus (E_d) three specimens of 40x40x160 mm dimension were used using the PUNDIT (Portable Ultrasonic Non-Destructive Digital Indicator Tester) by the equation reported in (1) where: v is the velocity of elastic wave in m/s, ρ is the density in kg/m^3 and γ_d is the Poisson modulus equal to 0.3.

$$E_d = \frac{v^2 \rho[(1+\gamma_d)(1-2\gamma_d)]}{(1-\gamma_d)} \quad (1)$$

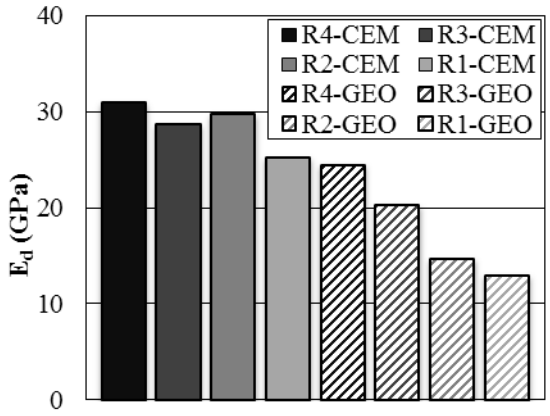

Fig. 2: *Dynamic elastic modulus at 28 days of geo-polymers and cementitious mortars.*

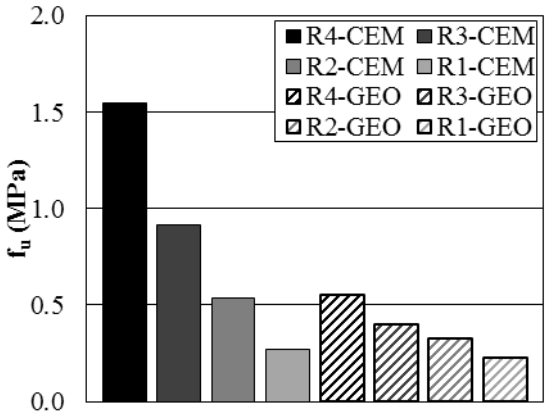

Fig. 3: *Adhesive strength at 28 days of geo-polymers and cementitious mortars.*

Fig.2 shows that in geo-polymer mortars higher is the compressive strength, higher the E_d is, moreover, all four geo-polymeric mortars obtained a lower E_d than cementitious ones.

Adhesive strength on substrate

The adhesion on solid brick surface was conducted according to the UNI EN 1015-12:2002 on five round samples. Results are reported in Fig.3. It can be observed that cementitious mortars obtained higher adhesive strengths (f_u) than geo-polymeric ones with the same compressive strength.

Porosimetry

Three specimens for each mortar were tested after 28 days of wet curing by mercury porosimetry. Results showed that total porosity of mortars with the same strength class was quite similar. However, in geo-polymers even if the mean radius decreases, the relative pore volume distribution is broader than that of cement mortars, with a volume of large diameter pores over 1 μm higher than cement ones.

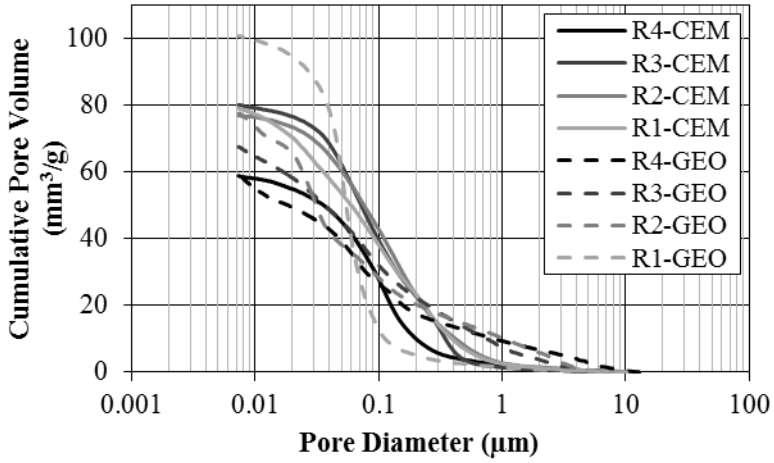

Fig. 4:*Cumulative pore volume of geo-polymers and cementitious mortars.*

Water vapour permeability

The test was developed according to UNI EN 1015-18:2004 on three round samples. Both mortars showed the same trend: the higher the strength class was, greater the resistance to water

vapour diffusion was, but results of cement mortars were about double than those of geo-polymeric ones. Permeability depends on open porosity, connectivity and tortuosity of the microstructure and connected pores size [7, 8]. Lower values of geo-polymers (Fig.5) could be explained by the higher volume of large diameter pores over 1 μm.

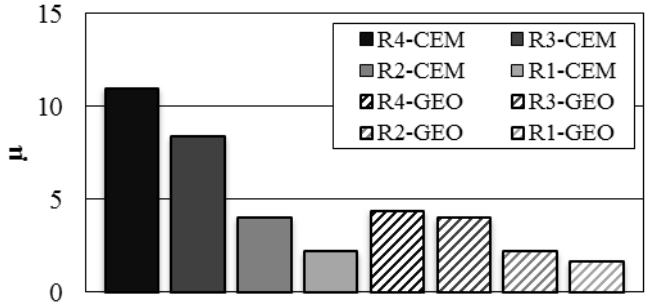

Fig. 5: *Water vapour diffusion resistance factor of geo-polymers and cementitious mortars.*

Capillary water absorption

Three specimens of 40 x 40 x 40 mm for each mortar were tested according to the UNI EN 1015-18:2004. Referring to the same strength class, cement mortars absorbed more water than geo-polymers. This trend could be explained by porosimetry tests: capillary water absorption depends on open porosity but also on connected pore size, with higher pressures when pores are smaller, according to Washburn equation (2) where: P is the pressure, r is the radius of the pore, σ is the surface tension of mercury and θ is the wetting angle. Lower values of geo-polymers with respect to cement one at the same strength class, could be due to higher volume of pores with diameter over 1 μm.

$$P = \frac{2\sigma}{r}\cos\theta \qquad (2)$$

Salt crystallization resistance

The test was conducted on three specimens partially immersed (40 mm) in common water as reference (1 specimen) and in a 16% Na_2SO_4 solution (2 specimens) for a period of 21 days. After the removal of specimens from the solutions the visual test was conducted (Fig.6). The two specimens immersed in the salt solution showed efflorescence; however, the efflorescence was much more evident in cement mortars affected also by diffuse cracks.

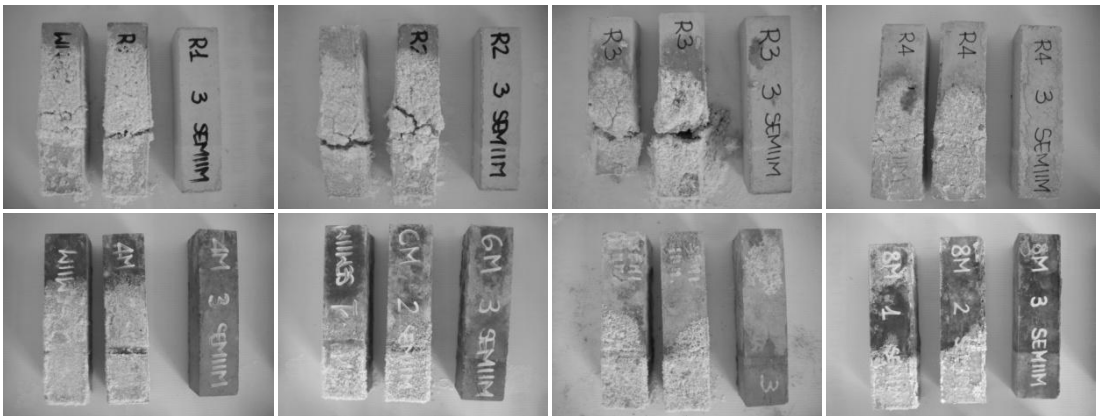

Fig. 6: *Visual observation of cement mortar (upper) and geopolymer mortars (bottom) exposed to semi immersion test after drying. In each photo, the specimen on the right was exposed in water, as reference.*

CONCLUSIONS

The properties of geo-polymeric and cementitious mortars with the same mechanical strength class was studied.
By varying the concentration of NaOH solution in geo-polymers, R1 ≥ 10 MPa, R2 ≥ 15 MPa, R3 ≥ 25 MPa, R4 ≥ 45 MPa strength class can be obtained, even if the formation of Na_2CO_3 efflorescence on specimens with highest compressive strength can be observed.
In addition, referring to the same mechanical strength class:

- the stiffness of geo-polymeric mortars is half of that of cement ones;
- the adherence to brick surface of geo-polymers is lower than cementitious mortars;
- geo-polymers are more permeable to water vapour;
- capillary water absorption is lower in geo-polymers than in cement-based mortars;
- the resistance to salt crystallization of geo-polymeric mortars is significantly higher with respect to cementitious ones.

REFERENCES

1. Leonelli C and Romagnoli M. Geopolimeri: Polimeri inorganici attivati chimicamente. ICerS: Bologna, 2011.
2. Rangan V B. *Concrete Construction Engineering Handbook*, Chapter 26. In: *Low-Calcium, Fly-Ash-Based Geopolymer Concrete*, ed. E.G. Nawy, 2008.
3. Davidovits J. *30 Years of Successes and Failures in Geopolymer Applications.* Geopolymer 2002 Conference, Melbourne, Australia, 2002, 1-15.
4. Palomo A, Grutzeck M W and Blanco M T. *Alkali-activated fly ashes. A cement for the future*. Cement and Concrete Research,1999, 29, 1323-29.
5. Komnitsas K, Zaharaki D and Perdikatsis V. *Effect of synthesis parameters on the compressive strength of low-calcium ferronickel slag inorganic polymers.* Journal of Hazardous Materials, 2009, 161, 760-8.
6. Rowles M R & O'Connor B H. *Chemical and structural microanalysis of aluminosilicate geopolymers synthesized by sodium silicate activation of metakaolinite*. Journal of the American Ceramic Society, 2009, 92, 2354-61.
7. Tittarelli, F. *Effect of low dosages of waste GRP dust on fresh and hardened properties of mortars: Part 2.* Construction and Building Materials, 2013, 47, 1539-43.
8. Aligizaki, Kalliopi K. *Pore structure of cement based materials. Testing interpretation and requirements.*Taylor & Francis, 2006, p. 75.

PERFORMANCE EVALUATION OF GALVANIC ANODES IN CHLORIDE CONTAMINATED CONCRETE

W Dodds
Centre for Innovative and Collaborative Construction Engineering, Loughborough University, School of Civil and Building Engineering, Loughborough, U.K., LE11 3TU.

C Christodouolou
AECOM Europe, Colmore Plaza, 20 Colmore Circus Queensway, Birmingham, U.K., B4 6AT.

C.I. Goodier
S.A. Austin
Loughborough University, School of Civil and Building Engineering, Loughborough, U.K., LE11 3TU.

ABSTRACT: This study examines the effectiveness of galvanic anodes installed both within the patch repair and surrounding parent concrete. Sodium chloride was added during casting of the concrete specimens to induce corrosion. The anodes were tested using surface potential mapping at 7 days after repair, 8 months and also 26 months. The results showed that galvanic anodes installed in the parent concrete had a greater polarisation effect on steel adjacent to the repair, which is generally considered to be at highest risk, as compared to galvanic anodes installed within the repair itself. It was also noted that, with increasing chloride content, the polarisation extent was reduced. However in all cases examined, the galvanic anodes in the parent concrete afforded a more dominant effect than similar galvanic anodes installed within the patch repair.
Keywords: Corrosion; galvanic anodes; potential mapping

INTRODUCTION

Corrosion of steel reinforcement is often considered the most significant deterioration process of reinforced concrete structures [1]. Chloride induced corrosion, in particular is caused by the ingress of chloride ions through the concrete cover from de-icing salts or exposure to marine environments [2, 3]. Hydrochloric acid is produced which causes a breakdown of the passive layer that protects the steel reinforcement and results in localised pitting [4]. The use of patch repairs and additional electrochemical treatment is a well-established method of restoring structural integrity [5] and re-establishing steel passivity [6]. Discrete galvanic anodes are connected directly to the steel and pass current through the surrounding concrete. They improve the environment around the steel and corrode preferentially by replacing the ions lost in the corrosion process [7, 8, 9]. A recent development of the galvanic technology is to install

the anode into pre drilled cavities in the parent concrete beyond the area for patch repair to prevent development of incipient anodic areas [3, 10, 11]. One particular advantage of this method over embedding the anode in the patch repair material is that a larger proportion of protective current will be directed to the steel [12].

Measuring steel potentials using a standard reference electrode is a well-established method of monitoring reinforced concrete structures for corrosion damage and determining localised anodic areas [13, 14, 15]. Recent research has shown factors such as moisture content, temperature and humidity can affect the potential of steel reinforcement [16]. Galvanic anodes have also been shown to distribute a higher protective current when the steel is in a passive environment [17].

The European standard for cathodic protection regulates the criteria required for an installed system. Galvanic anodes do not always achieve this criterion, therefore it has been suggested by Christodoulou et al (2014) and Holmes et al (2011) that galvanic systems are monitored based on a dominant effect over any steel anodic areas [12,16].

The aim of this study was to examine galvanic anodes installed both in parent concrete and patch repairs to identify performance differences using the two methods described above. Monitoring was undertaken by means of close-interval potential mapping.

METHODOLOGY

Casting and repair

A C20/25 mix design comprised of 1:2:4 ordinary portland cement, sand and coarse aggregate respectively with a water to cement ratio of 0.65 was used for the purposes of this study [18]. A 12mm diameter steel reinforcement bar was cast centrally in the beams and sodium chloride was added at 0%, 0.8% and 2.5% by weight of cement to initiate chloride-induced corrosion. A class R3 acrylic-polymer modified structural repair mortar was used [5] in this study and cast after 7 days of curing.

Two types of anodes were used in this work. Anode A is 65mm in diameter by 30mm height and was installed directly into the patch repair. Anode B is 18mm in diameter by 42mm height and was installed into a pre drilled cavity 25mm in diameter within the parent concrete. The arrangements are shown in Figure 1. The anodes were directly connected to the reinforcement by a titanium wire riveted to the steel.

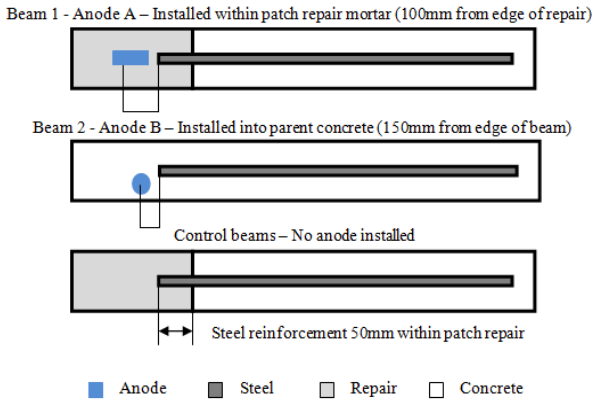

Fig. 1: *Arrangement of reinforced concrete specimens and patch repairs*

Testing

Potential readings were taken at 50mm intervals directly above the reinforcement in each beam using a portable Manganese (IV) oxide (MnO_2) reference electrode and a high impedance multi-meter [19]. Potential readings were taken along the beam before the repair, after the initial repair with the anode connected and after 7 days. The beams were then left outside to weather and further readings were taken after 8 and 26 months respectively.

ANALYSIS OF RESULTS

Effect of anode location

The polarisation effect afforded by anode types A and B at 26 months with varying chloride contents is illustrated in Figure 2. It can be seen that anode B located in the parent concrete afforded a greater polarisation effect on the steel at distances from the edge of the patch repair which is considered to be most at risk of chloride induced corrosion. This effect was also observed in the 7 day and 8 month potential readings.

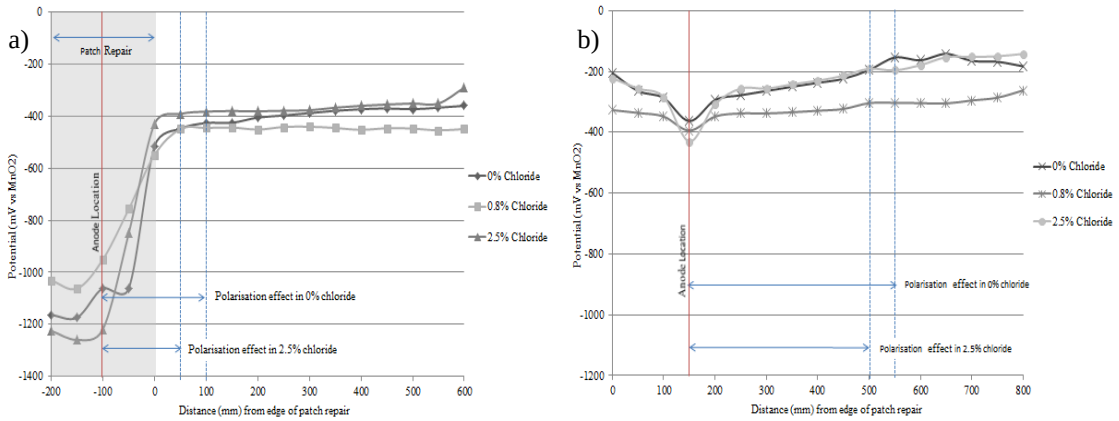

Fig. 2: *Polarisation effect in 2.5% chloride content for a) Anode A and b) Anode B*

At all 3 time intervals anode A only had a polarisation effect on steel reinforcement 50mm outside of the patch repair when installed in concrete with 2.5% chlorides, whereas anode B had a dominant effect over the steel up to 500mm when installed in concrete with 0.8% and 2.5% chlorides. It was observed for anode A that a large proportion of the dominant effect of the anode was lost at the interface between the patch repair mortar and the parent concrete.

Figure 3 shows the results for the two anodes installed into specimens with 0.8% chlorides and their effect over time. As expected when the anodes are first connected there is a significant drop in the potentials across the length of the beam as the anodes become active. Both anodes are showing a similar dominant effect on polarisation at this early stage. The results for anode A show a significant increase in the potentials within the first 100mm from the anode, which mainly occurs within the patch repair material. The change is then more gradual within the parent concrete. At all time intervals anode B had a greater influence on the steel potentials outside of the patch repair. The polarisation effect for anode A can be seen up to 50mm external to the repair and up to 250mm for anode B at 789 and 783 days respectively.

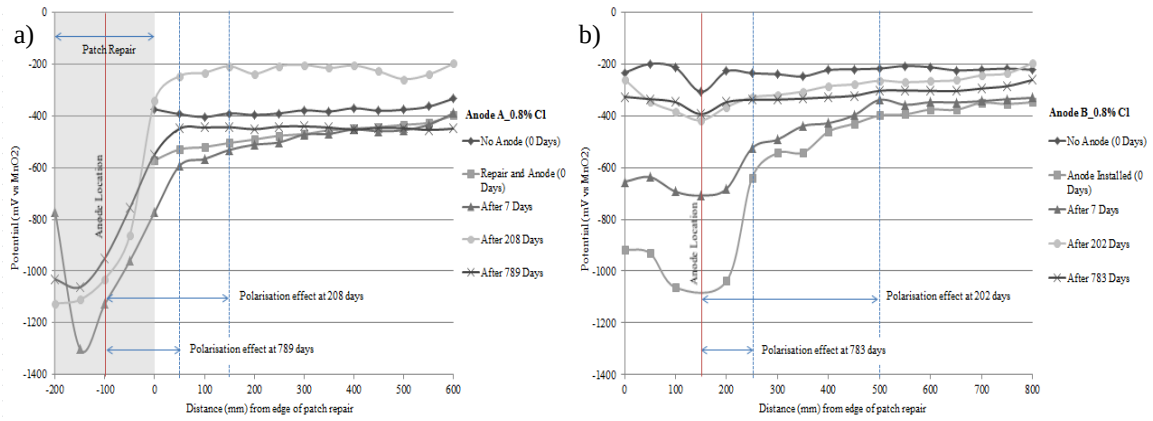

Fig. 3: *Polarisation effect in 0.8% chloride content for a) Anode A and b) Anode B*

Effect of chloride content

The potential of the steel was monitored in control specimens cast and repaired with no anodes installed. The results showed that there is a higher risk of corrosion in the parent concrete of the specimens cast with 2.5% chloride content at 8 and 26 months as localised anodic areas were observed along the length of the beam, indicated by a drop in potential readings. It was observed in the specimens with 0% and 0.8% chloride that the potential readings within the patch repair material were significantly lower than in the parent concrete.

The polarisation effects seen in Figure 2 indicate that the dominant effect of the anode over steel potentials is reduced with increasing chloride content.

DISCUSSIONS

Effect of anode location

The galvanic anodes installed into pre-drilled cavities in the parent concrete afforded a greater polarisation effect on steel adjacent to the patch repair (Fig. 2), which is considered to be at highest corrosion risk due to an incipient anode effect [3,10,11]. This observation agrees with the conclusions of Christodoulou et al (2014) in that a higher proportion of protective current will be directed to steel adjacent to the patch due to the higher resistance of the repair mortar [12].

A large polarisation effect was seen in the patch repair material when anode A was installed into the patch repair itself. This is possibly due to the high alkalinity of the repair causing a build-up of the passive layer on the steel reinforcement and allowing a greater polarisation effect from the anode. The work of Bertolini et al (2002) showed that galvanic anodes can have a large polarisation effect, even in highly resistive concrete, only when the steel is passive [17]. The polarisation effect rapidly reduces beyond the patch repair material which suggests that the passive film has been reduced due to the chlorides present in the parent concrete. However, the same observation was made on steel which should have remained passive in concrete containing zero chlorides. This indicates that the interface between the two materials may be affecting the performance of anode A.

The difference in polarisation effects seen at 7 days, 8 months and 26 months may also be due to the change of moisture content, temperature and humidity as the specimens were exposed to a changing environment [16].

Effect of chloride content

The results have shown that a higher proportion of chloride ions increased the corrosion risk, as expected. The potential readings from the beams cast with 2.5% chlorides show the formation of localised anodic areas along the length of the beam, which indicates chloride induced pitting corrosion [13, 14, 15].

Lower potential readings were seen within the patch repair material compared to the parent concrete. This effect was more significant in the specimens with lower chloride content. This, again, may be due to the high alkalinity of the repair material causing a greater polarisation effect.

The polarisation effect of both anodes was reduced with increasing chloride content. The breakdown of the passive layer at the surface of the steel reduces the amount of protective current that can be distributed from the anode and therefore the polarisation effect is reduced.

CONCLUSIONS

Galvanic anodes installed in the parent concrete, had a greater influence on the polarisation of steel reinforcement surrounding the patch repair, which is considered to be the highest corrosion risk, than anodes traditionally installed within the repair. The greater polarisation effect of the anode installed in the parent concrete was observed in all chloride contents used which allows for larger anode spacing.

The polarisation effects of galvanic anodes installed either in parent concrete or within the patch repair were reduced with increasing chloride content. This effect was more dominant when the anode was installed into the patch repair itself. In the specimens cast with a 2.5% chloride content the polarisation effect of anodes installed in the patch was just 50mm beyond the edge of the repair compared to 500mm with anodes installed in parent concrete.

REFERENCES

[1] Page, C.L. 2007. Corrosion and protection of reinforcing steel in concrete. In: Page, C.L. Page, M.M. 2007. *Durability of concrete and cement composites*. pp136-186. Woodhead Publishing Limited.

[2] Bertolini, L. Elsener, B. Pedeferri, P. Polder, R. 2004. Corrosion of steel in concrete: Prevention, diagnosis, repair. p 91. WILEY-VCH.

[3] Christodoulou, C. Webb, J. Glass, G. Austin, S. Goodier, C. 2011. A new approach for the patch repair of car parks using galvanic anodes. In: GRANTHAM, M. MECHTCHERINE, V. SCHNECK, U. (eds). *Concrete Solutions 2011: Proceedings of the International Conference on Concrete Solutions 2011*. London: CRC Press.

[4] Glass, G.K. Reddy, B. Clark, L.A. 2007. Making reinforced concrete immune from chloride corrosion, Proceedings of the Institution of Civil Engineers, *Construction Materials*, Vol 160, pp. 155–164.

[5] British Standards Institution. 2005. BS EN 1504-3. *Products and systems for the protection and repair of concrete structures – Part 3: Structural and non-structural repair*. London, BSI.

[6] British Standards Institution. 2008. BS EN 1504-9. *Products and systems for the protection and repair of concrete structures – Part 9: General principles for use of products and systems*. London, BSI.
[7] British Standards Institution. 2012. BS EN ISO 12696, *Cathodic protection of steel in concrete*, London: BSI.
[8] Glass, G. Christodoulou, C. Holmes, S. 2012. Protection of steel in concrete using galvanic and hybrid electrochemical treatments. In: Alexander, M.G. Beuhausen, H.D. Dehn, F. Moyo, P. (eds). 2012. *Concrete Repair, Rehabilitation and Retrofitting III:* 3rd International Conference on Concrete Repair, Rehabilitation and Retrofitting, ICCRRR-3, 3-5 September 2012, Cape Town, South Africa. Taylor and Francis Group.
[9] Christodoulou, C. Goodier, C. Austin, S. Webb, J. Glass, G. 2013. Hybrid corrosion protection of a prestressed concrete bridge. European Corrosion Conference 2013, *EUROCORR 2013*, Estoril, Portugal, 1st-5th September 2013.
[10] Broomfield, J.P. (2000). *The principles and practice of galvanic cathodic protection for reinforced concrete structures*. Monograph No: 6. Corrosion Prevention Association, Bordon, UK.
[11] Page, C.L. Sergi, G. 2000. Developments in cathodic protection applied to reinforced concrete, *Journal of Materials in Civil Engineering*, Volume 12 February (2000), Issue 1, pp. 8 - 15.
[12] Christodoulou, C. Goodier, C.I. Austin, S.A. Glass, G.K. Webb, J. 2014. A new arrangement of galvanic anodes for the repair of reinforced concrete structures, *Construction and Building Materials*, Vol. 50, pp. 300–307.
[13] Christodoulou, C. Glass, G. Webb, J. Austin, S. Goodier, C. 2010. Assessing the long term benefits of impressed current cathodic protection, *Corrosion Science*, Vol. 52, pp. 2671–2679.
[14] Elsener, B. 2003. Half-cell potential measurements – potential mapping on reinforced concrete structures, RILEM TC 154-EMC: electrochemical techniques for measuring metallic corrosion, *Mater. Struct*. Vol. 36, pp. 461–471.
[15] British Standards Institution, 1990. BA 35/90, *Inspection and repair of concrete highway structures*, London: BSI.
[16] Holmes, S.P. Wilcox, G.D. Robins, P.J. Glass, G.K. Roberts, A.C. 2011. Responsive behaviour of galvanic anodes in concrete and the basis for its utilisation, *Corrosion Science*, Vol. 53, pp. 3450–3454.
[17] Bertolini, L. Gastaldi, M. Pedeferri, M. Redaelli, E. 2002. Prevention of steel corrosion in concrete exposed to seawater with submerged sacrificial anodes, Corrosion Science, Vol. 44, pp. 1497-1513.
[18] British Standards Institution. 2000. BS EN 206-1, *Concrete – Part 1: Specification, performance, production and conformity*, London: BSI.
[19] American Society for Testing and Materials, 2009. ASTM C 876, *Standard test method for corrosion potentials of uncoated reinforcing steel in concrete*, Pennsylvania, USA.

EXPLICIT AND REFLECTIVE MODELLING AS A METHOD OF LEARNING ABOUT THE LIFE CYCLE ENVIRONMENTAL IMPACTS OF BUILDING MATERIAL APPLICATIONS

Bengt Cousins-Jenvey
Department of Architecture and Civil Engineering/IDC in Systems, University of Bath/University of Bristol, Bath/Bristol, UK

ABSTRACT: If a whole life cycle analysis of a building is undertaken, it is frequently based upon extremely precise assumptions about the future. Critics of this deterministic approach suggest that probabilistic modelling provides a better understanding of the actual life cycle environmental impact of a building. This extended abstract introduces the idea that this probabilistic modelling could be more rigorous and useful if it was also explicit and reflective. Its aim is to learn from modelling how a range of UK specific inputs influence the greenhouse gas emissions associated with three different applications (the envelope, finishes and structure of a building) of one cubic metre of concrete, steel and timber. Only in 16 of the 27 material application scenarios modelled does the largest proportion of 'embodied' emissions occur during the product phase. Subsequent research should examine, critique and improve a number of specific model inputs and the model logic.
Keywords: buildings, environment, life cycle, materials, modelling

INTRODUCTION

Any analysis of a new building's 'embodied' environmental performance in the UK is frequently limited to greenhouse gas emissions during the product phase of a building's life. If a more ambitious, whole life cycle analysis (LCA) is undertaken , Fawcett et al.[1] observed that it is likely to be unrealistically precise because deterministic models dominate current practice. A deterministic type of model constrains users to a single value for each model input, which Fawcett et al. argue is inferior to a probabilistic approach. They propose that triangular probabilistic modelling (with low, likely and high values for each model input) provides decision-makers with a better understanding of where they should focus their attention during the design process and beyond.

Although Fawcett et al. do not explicitly address the issue that their life cycle model is untested against data from real buildings, this may be because an accurate prediction is not actually the purpose of their modelling. Epstein [2] expands upon this idea by highlighting 16 reasons for building a model even if its predictive accuracy is unknown. He emphasises the rigour and value of models that are explicit because they provide others with sufficient detail to examine, criticise, improve and fundamentally reproduce results. Blockley and Godfrey[3]

have also discussed these steps in relation to complex engineering problems as a process of "continuous learning".

This extended abstract shows that it is possible to explicitly, but concisely describe the logic, inputs and outputs of a life cycle model and then reflect on all three. The purpose of the modelling is to learn about how a range of values influence the life cycle greenhouse gas (GHG) emissions associated with a cubic metre of concrete, steel and timber when each one is the primary material of three different building components (the envelope, finishes and structure).

METHODOLOGY

The methodology has two parts. The first is the model logic, which is based closely on BS EN 15978: 2011, the method proposed by Adalberth [4] and knowledge of the GHG conversion factors available. The second is the choice of a reasonable range and likely value for all model inputs based upon a review of UK specific literature and informal discussions with practitioners.

Modelling logic: mass of materials

The mass of material used prior to practical completion is the product phase material *PM*. During the design process, the mass is calculated from the volume of the material *V*, its density ρ and a percentage increase to account for losses during both transporting $P_{Transporting}$ and installing $P_{Installing}$ (1).

$$PM = (V \cdot \rho) \cdot (1 + P_{Transporting} + P_{Installing}) \quad (1)$$

The use phase material *UM* is also important. This is the mass of a material *M* added to the building during maintaining and repairing or replacing and refurbishing (MRRR) (2).

$$UM = M_{\text{Maintaining \& Repairing}} + M_{\text{Replacing\& Refurbishing}} \quad (2)$$

$$M_{Maintaining\ \&\ Repairing} = \left(P_{Maintaining\ \&\ Repairing} \cdot PM\right) \cdot \left(\left\lceil \frac{L_{Building}}{L_{Application}} \right\rceil - 1\right) \quad (3)$$

$$M_{Replacing\ \&\ Refurbishing} = \left(P_{Replacing\ \&\ Refurbishing} \cdot PM\right) \cdot \left(\left\lceil \frac{L_{Building}}{L_{Component}} \right\rceil - 1\right) \quad (4)$$

The quantities of material for each MRRR process are a percentage *P* of the product phase materials multiplied by the number of times that process occurs during the life of the building. Occurrences are calculated from the life of the building $L_{Building}$ and the life of the material in that application $L_{Application}$ or the life of the whole component $L_{Component}$.. Based upon the EeBGuide[5], the result is rounded up before subtracting one (3)(4).

Modelling logic: mass of waste categorised by treatment process

All of the product phase materials *PM* (including the losses described above) are assumed to become waste and its treatment is based upon a percentage recovered $P_{Recovered}$ (5) and incinerated $P_{Incinerated}$ (6) with the remainder assumed to end up in landfill (7).

$$PM_{Recovered} = PM \cdot P_{Recovered} \quad (5)$$

$$PM_{Incinerated} = PM \cdot P_{Incinerated} \quad (6)$$

$$PM_{Landfilled} = PM - \left(PM_{Recovered} + PM_{Incinerated}\right) \quad (7)$$

(5)(6)(7) also apply to all material during the use phase, but with *UM* replacing *PM*.

Modelling logic: carbon dioxide equivalents and other pollution

Whether quantifying carbon dioxide equivalents or other impacts, conversion factors provide a way to simplify the modelling. One example is the Inventory of Carbon and Energy[6], which summarises numerous 'cradle to gate' material studies. This facilitates the calculation of the product phase impact $I_{Product}$ of the product phase material mass *PM* by simply multiplying it by an appropriate conversion factor $C_{Producing.}$ The conversion factor represents the impacts of obtaining the raw material, transporting it to the factory and then processing it or manufacturing the finished product (8).

$$I_{\text{Product}} = I_{CradleToGate} = \left(PM \cdot C_{\text{Producing}}\right) \quad (8)$$

The construction phase impact is just the impact of transporting product phase materials to site $I_{GateToSite}$ as the impact of all site activities is not quantified by the model. The end of life phase is the sum of transporting the product phase materials to different treatment facilities $I_{SiteToGrave}$ with an appropriate conversion factor applied to the different categories of waste to acknowledge the impacts of treating them (9). Transporting impacts during both phases are the mass of material or waste multiplied firstly a generic conversion factor $C_{Transporting}$ and then a phase specific distance *D* (10)(11).

$$I_{Grave} = \left(PM_{\text{Recovered}} \cdot C_{\text{Recovering}}\right) + \left(PM_{\text{Incinerated}} \cdot C_{\text{Incinerating}}\right) + \left(PM_{\text{Landfilled}} \cdot C_{\text{Landfilling}}\right) \quad (9)$$

$$I_{GateToSite} = PM \cdot D_{GateToSite} \cdot C_{Transporting} \quad (10)$$

$$I_{SiteToGrave} = PM \cdot D_{SiteToGrave} \cdot C_{Transporting} \quad (11)$$

The impact of the use phase is found by calculating the impacts of all use phase material from cradle to grave. (8)(9)(10)(11) are all used to calculate this impact, but with *UM* substituted for *PM*.

Notably, the model does not include the use of machinery and site activities during the construction, use and end of life phases. In the absence of any appropriate conversion factors, these impacts would be laborious to calculate and are generally thought to be small in the context of the entire life cycle. Another notable simplification is the grouping of construction and end of life waste as *PM*.

Modelling inputs: ranges and references

Table 1 details the range of UK appropriate values for each material application input and lists all of the references used to support them.

Table 1. *A summary of the UK specific ranges for each model input with supporting references*

Input	Units	Concrete			Steel/Stainless Steel			Timber			Ref.
		Envelope	Finishes	Structure	Envelope	Finishes	Structure	Envelope	Finishes	Structure	
ρ	kg/m^3	500 - 2100	1440 - 2400	1440 - 2400	7800 - 8000	7800 - 8000	7800 - 8000	450 - 630	400 - 1000	500 - 930	[6]
$P_{Transporting}$	%	0 - 10	0 - 10	0 - 10	0 - 10	0 - 10	0 - 10	0 - 10	0 - 10	0 - 10	
$P_{Installing}$	%	0 - 20	0 - 20	0 - 20	0 - 10	0 - 10	0 - 10	0 - 10	0 - 10	0 - 10	[4]
$P_{Maintaining}$	%	0 - 5	0 - 5	0 - 5	0 - 5	0 - 5	0 - 5	0 - 5	0 - 5	0 - 5	
$P_{Repairing}$	%	5 – 10	5 – 10	5 – 10	5 – 10	5 – 10	5 – 10	5 – 10	5 – 10	5 – 10	
$P_{Refurbishing}$	%	10 – 50	10 – 50	10 – 50	10 – 50	10 – 50	10 – 50	10 – 50	10 – 50	10 – 50	
$P_{Replacing}$	%	100	100	100	100	100	100	100	100	100	
$P_{Recovered}$	%	75 – 95	75 - 95	75 - 95	90 - 100	90 - 100	90 - 100	57 - 95	57 - 95	57 - 95	[7]
$P_{Incinerated}$	%	0	0	0	0	0	0	5	5	5	
$L_{Application}$	years	5 - 25	5 - 15	5 - 25	5 - 25	5 - 15	5 - 25	5 - 25	5 - 15	5 - 25	
$L_{Component}$	years	25-75	10-30	25-75	25-75	10-30	25-75	25-75	10-30	25-75	
$D_{GateToSite}$	km	20 - 1200	20 - 1200	20 - 1200	20 - 1200	20 - 1200	20 - 1200	20 - 1200	20 - 1200	20 - 1200	[5]
$D_{SiteToGrave}$	km	20 - 1200	20 - 1200	20 - 1200	20 - 1200	20 - 1200	20 - 1200	20 - 1200	20 - 1200	20 - 1200	[8]
$C_{Producing}$	kg $CO2_e$/kg	0.05 - 0.16	0.05 - 0.16	0.05 - 0.53	1.38 – 3.27	1.38 - 6.15	1.38 - 6.15	0.20 – 1.43	0.41 – 1.10	0.20 - 0.87	[6]
$C_{Transporting}$	(kg $CO2_e$/kg)/km	$3{\cdot}10^{-6}$ - $3{\cdot}10^{-4}$	$3{\cdot}10^{-6}$ - $3{\cdot}10^{-4}$	$3{\cdot}10^{-6}$ - $3{\cdot}10^{-4}$	$3{\cdot}10^{-6}$ - $3{\cdot}10^{-4}$	$3{\cdot}10^{-6}$ - $3{\cdot}10^{-4}$	$3{\cdot}10^{-6}$ - $3{\cdot}10^{-4}$	$3{\cdot}10^{-6}$ - $3{\cdot}10^{-4}$	$3{\cdot}10^{-6}$ - $3{\cdot}10^{-4}$	$3{\cdot}10^{-6}$ - $3{\cdot}10^{-4}$	[9]
$C_{Recovering}$	kg $CO2_e$/kg	0	0	0	0	0	0	0	0	0	
$C_{Incinerating}$	kg $CO2_e$/kg	0	0	0	0	0	0	0.021	0.021	0.021	[9]
$C_{Landfilling}$	kg $CO2_e$/kg	0.002	0.002	0.002	0.002	0.002	0.002	0.851	0.851	0.851	[9]

RESULTS

Figure 1 breaks down total CO_{2e} by building life cycle phase based upon a building life of 25 years ($L_{Building}$) for each material application scenario. The 'best' and 'worst' scenarios (smallest and biggest quantity of emissions) shown for each material application were produced by an appropriate combination of the lowest and highest values from Table 1.

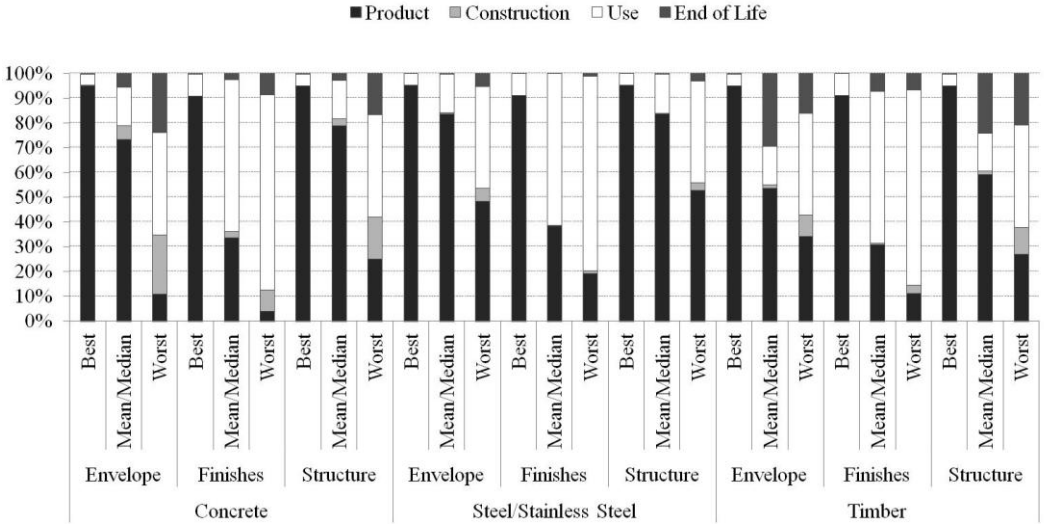

Fig.1: *Breakdown of life cycle CO2e in different material application scenarios*

DISCUSSIONS

Figure 1 shows the significant proportion of CO_{2e} that would be outside the scope of a product phase analysis of a building. In fact, the product phase is the most significant part of the life cycle in only 16 of the 27 model outputs, even if a short 25 year building life is assumed. (If the actual building life was 60 years, the number decreases to just six.) Such a general observation is more interesting than a comparison of the best material for each component, because a cubic metre is not an appropriate functional unit of comparison. As a result, it was a conscious decision not to present the results as absolute quantities.

Although $L_{Application}$, $L_{Component}$ and all of the MRRR percentages in Table 1 clearly need supporting with peer-reviewed research, they are currently constant for each material application. If a greater distinction could be made between these model inputs, then the differences between material applications might become more pronounced. Furthermore, with a more detailed review of the model inputs, particularly the conversion factor methodologies, it would be possible to translate them into specific guidance for designers, contractors or asset managers.

A clear limitation of the model is that all inputs are constant throughout the building's long life, but it is feasible to address this in some instances with life cycle averages rather than complicating the model logic. The methodology has also noted that all site activities are currently outside of the scope of this model, but there are other questions about its boundaries. Concrete coatings, steel paint and wood preservatives might have a significant impact if they were included too. Conversely, a concrete finish might be achievable without any additional material if it is possible to expose the structure.

The limitations of the model logic and inputs should all be addressed when they are applied to other components or, more ambitiously, a whole building.

CONCLUSIONS

A description and critique of a model's outputs, logic and inputs is possible even within the page constraints of this short extended abstract. The probabilistic, explicit and reflective approach it demonstrates could translate to other materials, components, and potentially whole buildings with the purpose of learning about embodied life cycle GHG emissions (or other environmental impacts) in different scenarios. Although a number of modelling improvements are detailed, the outputs do suggest that the 'cradle to gate' or product phase may not be the most significant even if a building's life is only 25 years. Priorities for further study include the demands for use phase materials as well as the distance and mode of transporting them to or (as waste) from the site. However, this research should also conduct a more systematic analysis of how modifying the modelling logic and inputs influences its outputs.

ACKNOWLEDGEMENTS

This research was funded by the UK Engineering and Physical Sciences Research Council, Expedition Engineering Ltd. and Useful Simple Projects Ltd.

REFERENCES

[1] Fawcett W, Hughes M, Krieg H, Albrecht S, Vennström A. *Flexible strategies for long-term sustainability under uncertainty*. Build Res Inf 2012;40(5):545–57.
[2] Epstein JM. Why model? J Artif Soc Soc Simul 2008;11(4):12.
[3] Blockley D, Godfrey P. *Measuring judgements to improve performance*. Proc ICE - Civ Eng 2005;158(3):124–9.
[4] Adalberth K. *Energy use during the life cycle of buildings: a method*. Build Environ 1997;32(4):317–20.
[5] EeBGuide Project [Internet]. Available from: http://www.eebguide.eu/
[6] Jones C, Hammond G. Inventory of Carbon and Energy (ICE), V2.0 [Internet]. Available from: http://www.circularecology.com/ice-database.html
[7] WRAP. Waste Recovery Quick Wins. 2007.
[8] Environmental Protection Agency. WARM Waste Reduction Model.
[9] DEFRA/DECC. *GHG Conversion Factors for Company Reporting*. 2013.

EVALUATION OF Ag/AgCl SENSORS FOR IN-SITU MONITORING OF FREE CHLORIDE CONCENTRATION IN REINFORCED CONCRETE STRUCTURES

Farhad Pargar, Dessi Koleva, Oguzhan Copuroglu, Eduard Koenders, Klaas vab Breugel
Department of Materials & Environment, Delft University of Technology, Delft, The Netherlands
f.pargar@tudelft.nl

ABSTRACT: The level of free chloride concentration in reinforced concrete structures essentially determines the onset of steel corrosion initiation and further propagation . One of the well-known methods for monitoring free chloride concentration is using silver/silver chloride electrodes (Ag/AgCl). These electrodes are sensitive mainly to chloride ions and establish a certain electrochemical potential depending on the chloride ion activity in the environment. Although the functioning principles of these electrodes are well-established, their use in concrete is challenging when durability and practical engineering issues are considered. In order to be able to accurately determine free chloride content in concrete, it is important to evaluate the performance of Ag/AgCl electrodes (sensors) in strong alkaline environments i.e. those existing in non-carbonated concrete (pH~12–13.5). Furthermore the linear response of these sensors to a wide range of chloride concentrations in highly alkaline medium, as well as their sensitivity to pH changes, need a more in-depth investigation.

In this paper the response of Ag/AgCl electrodes in simulated pore solutions having different chloride concentrations and different pH values was studied. The electrodes were calibrated in cement extract solution, distilled-water and simulated pore solution. The results show that at chloride concentrations of > 4 mM the effect of pH on the response of the sensors is insignificant which makes using Ag/AgCl sensors in concrete feasible i.e. this concentration is much lower than the generally reported thresholds for corrosion initiation.
Keywords: Ag/AgCl electrode, cement extract solution, free chloride, pH value, pore solution.

INTRODUCTION

Corrosion of the steel reinforcement in concrete is recognized as the major problem within maintenance of civil structures. The concrete pH, usually in the range 12–13.5, provides chemical protection to the re-bars due to steel passivation. However, with time, severe corrosion problems may occur in reinforced structures [1]. Chloride ions are the major contributing factor that affects the corrosion state of the steel rebar embedded in concrete. Analysis of the chloride content in hardened cement based materials is not an easy task. The traditional way of powder drilling, dissolution in acids and chloride analysis by potentiometric titration shows quite a wide scatter [2]. Having the drawbacks of destructive techniques, attempts have been made to measure the free chloride concentration in the concrete pore solution by means of embedded ion selective electrodes. A perfect embeddable

electrode must obey several conditions: it must be stable, invariant to chemical and thermal changes in concrete, able to pass small currents with a minimum of polarization and hysteresis effects, display long-term performance, be cost effective and result from an environmentally safe manufacturing procedure [1].

Because of its good stability and easy preparation, the common Ag/AgCl electrode has been widely used as a reference electrode in electrochemistry. Solid Ag/AgCl electrodes (or commonly known as ion-selective probes) have been also developed to monitor the chloride content in model solutions or concrete structures [2, 3]. The first documented attempt to measure chloride ion activities with Ag/AgCl electrodes in hardened mortar was reported in the early 1990s [4].

In this study, Ag/AgCl electrodes were prepared by anodizing metallic silver in acidic environment with high chloride concentration. During the anodization process the silver wire is "coated" with AgCl packed-piled particles. This electrode, when in contact with the relevant external environment, establishes a quasi-equilibrium potential (Fig. 1). This potential depends on the chloride concentration in the environment and as long as this electrolyte concentration is maintained, the electrode potential is constant.

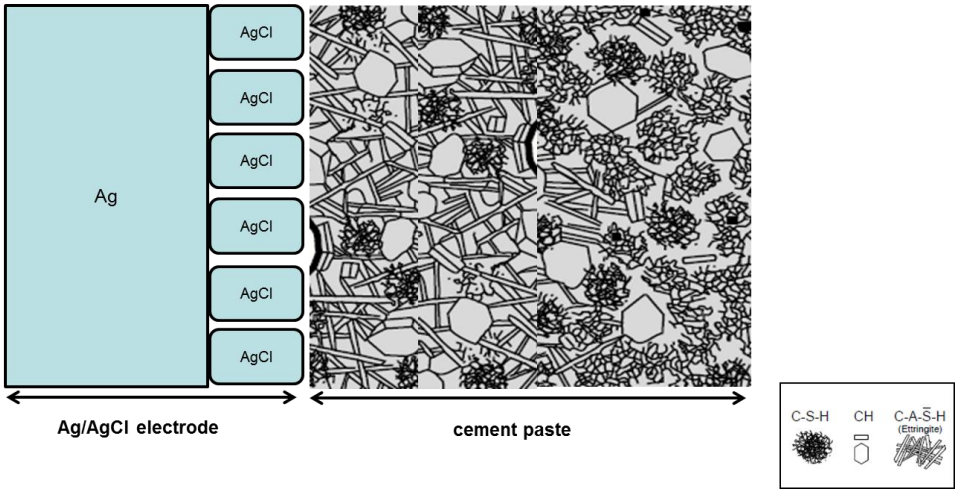

Fig. 1: *Schematic representation of Ag/AgCl electrode in contact with cement paste*

Some authors reported that Ag/AgCl electrodes embedded in mortar specimens are stable only for a short period, while others found good long-term stability. Consequently, these electrodes still remain a potentially interesting choice in what concerns chloride ion monitoring in reinforced concrete structures [1]. Their equilibrium potential value depends on the chloride ion activity (concentration) in the surrounding medium according to Nernst's Law [5]. In high alkaline solution and in the presence of hydroxyl ions (as within concrete environment), silver activity near the surface (and hence electrode potential response) is determined by an exchange equilibrium, Eq.(1) [7]:

$$2AgCl+2OH^- \longleftrightarrow Ag_2O+2Cl^-+H_2O \quad (1)$$

` At high pH values, the AgCl membrane becomes unstable and is, partly or completely, turned into Ag_2O. By continuous transformation of the electrode surface into Ag_2O, a mixed potential will be developed at the electrode/solution interface. As reported in previous studies, pH has a significant influence on the potential value of the sensor at low chloride concentration and further studies need to quantify the interference of pH in order to establish a suitable calibration method for low chloride concentration environments [5]. Some authors discussed the limit of detection of the chloride ion selective electrode, due to hydroxyl ion interference, varies with pH. For the pore solution of ordinary Portland cement paste or concrete, this limit can be

set between $3*10^{-3}$ molal, and $7*10^{-3}$ molal, i.e. just below a chloride concentration value of $1*10^{-2}$ molal. This effect can prevent the reliable measurement of free Cl^- concentrations, when these are below the corresponding limit of detection [6].

Therefore, in order to be able to accurately determine the free chloride content in concrete, it is important to evaluate the performance of Ag/AgCl electrodes (sensors) in strong alkaline environments i.e. those existing in non-carbonated concrete (pH~12–13.5) and intensely carbonated concrete (pH~7.5) [8].

In this paper the response of Ag/AgCl electrodes in simulated pore solutions with different chloride concentrations and different pH values was studied. The electrodes were calibrated in distilled water (pH=6) and simulated pore solution (pH=13.6). The range of employed chloride concentrations in the above environments allows quantification of the interference of pH and establishing a suitable calibration method for low chloride concentration environments.

EXPERIMENT

Silver wires, 1 mm in diameter (99.99% purity) were cleaned for 2 hours in concentrated ammonia and immersed in distilled water overnight. Next, they were anodized for one hour in 0.1M HCl solution at current density of 0.5 mA/cm^2 (Pt mesh served as cathode). The electrodes were stored in closed and out of direct sunlight environment until needed.

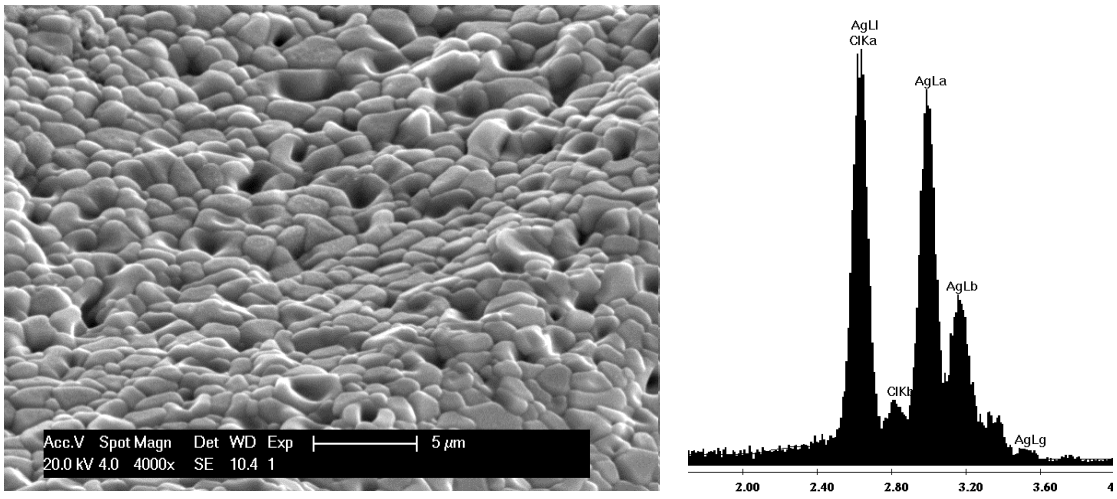

Fig. 2: *SEM micrograph and EDS analysis of AgCl layer deposited at 0.5mA/cm^2 current density*

Electrical connection for further tests was made through welding of the anodized silver wire to a copper wire; the non-anodized and welded zones were insulated by epoxy resin.

Fig. 2 shows the surface morphology of a Ag/AgCl electrode, anodized in 0.1 M HCl. Scanning electron microscopy (SEM) observations show the uniformly packed and piled particles, deposited on the silver substrate; Energy dispersive x-ray analysis (EDS) confirms the presence of AgCl through the observed Ag and Cl peaks in the EDS pattern. The electrode (sensor) potential was measured in distilled water (pH~6) and in simulated pore solution (0.63 M KOH+0.05 M NaOH+Sat. $Ca(OH)_2$ in the presence of various chloride concentrations.

RESULTS

Fig. 3 shows the fast response of the sensors to the various levels of Cl^- concentration in

different solutions, establishing stable potential values. This is essentially a potentiometric measurement: when exposed to solutions with various amounts of Cl^- ions, the Ag/AgCl electrode responds in a few seconds and reaches a constant potential depending on the Cl^- concentration in less than 1 min. The final potential increases (becomes more anodic or positive) with decreasing Cl^--ions concentration and more negative (more cathodic) with increasing chloride concentration. These potential changes follow fundamental principles and Nernst law, but are also determined by the ease of the electrochemical process i.e. the response of the sensor is also influenced by the morphology and microstructural properties of the AgCl layer, shown in Fig.2 (the dependence of sensor response on AgCl layer properties is not subject to this work)

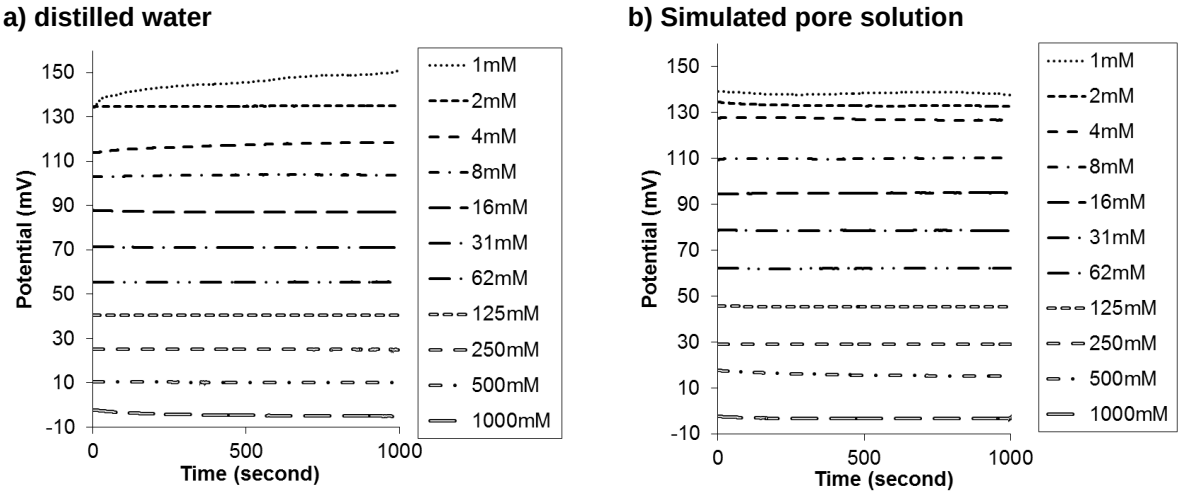

Fig. 3: *Potential response of Ag/AgCl electrode in solutions with various amounts of Cl^-*

As can be observed (Fig.3) the type of solution determines slightly different response of the Ag/AgCl sensor under the same chloride ion concentration. For instance, for 1 mM Cl-concentration, the sensor potential in distilled water presents 13.1 mV higher value, compared to the potential reading in simulated pore solution. This decreased potential values in simulated concrete pore solution, which has a notably higher pH value (13.5) than distilled water (pH of 6.0), is mainly due to the interference from hydroxyl (OH^-) ions. This deviation at low chloride contents could be attributed to the formation of Ag_2O, AgOH or $Ag(OH)^-_2$. When the chloride ion concentration increases to 1000 mM, the potential of the sensor in simulated pore solution is a slightly higher (1.9 mV) than that in distilled water and simulated pore solution, containing 1007 mM chloride concentration. Therefore, the influence of pH on the potential of the sensor in 1000 mM chloride concentration is different from those in 1 mM chloride solution so the potential variation is less significant at higher chloride concentrations. This interference has seldom been quantified before for the case of concrete pore solution.

According to the literature, it was shown that in conditions of the same chloride concentration the potential of Ag/AgCl electrode in simulated pore solution containing NaCl is always more positive than that in pure NaCl solution [7]. However, in the current study the potential of Ag/AgCl electrodes in distilled water with 1 mM and 2 mM was more positive than the corresponding potential in simulated pore solution. This indicates that the high pH affects the senor behavior at low chloride concentration.

To investigate the effect of pH on the potential of the sensor at different chloride concentrations, simulated pore solutions with different pH (7.0, 9.0, 12.6, 13.6) and chloride concentrations (1 mM, 2 mM, 4 mM, 16 mM, 62 mM and 250 mM) were prepared and the potential of the sensors was measured in these solutions. In order to prepare the solutions at

different pH, and chloride concentrations but with similar ionic strength (to minimize the effects due to the presence of ions other than hydroxyl ions), concentrated nitric acid was added drop-wise to the solution to adjust the pH at the relevant values. After pH adjustment, the potential of the sensor in the solutions was recorded.

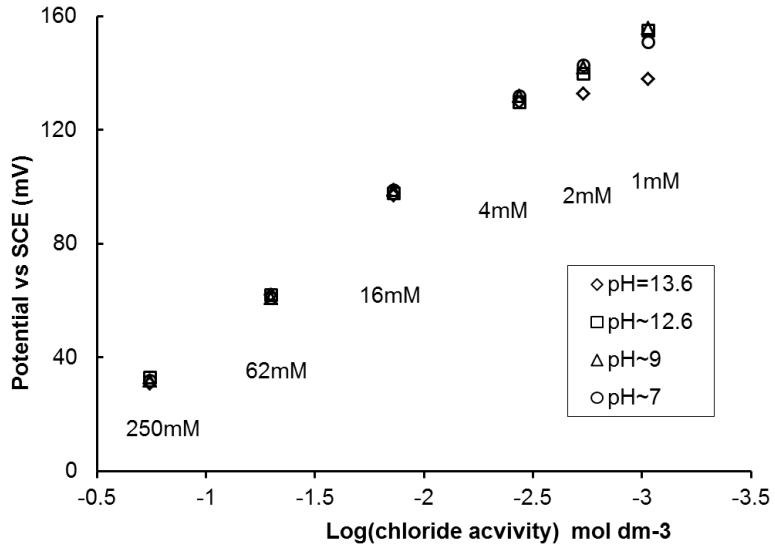

Fig. 4: *The effect of pH on the response of the sensor*

Fig. 4 shows the pH sensitivity is lower at higher chloride concentration. At low chloride concentration the potential difference between the solutions with different pH is larger than the potential difference at higher chloride concentration. In the case of 1 mM and 2 mM the difference between the maximum and the minimum potentials is about 18 mV and 10 mV, respectively. At 4 mM chloride concentration there is only 2 mV difference between the highest and lowest potential of the sensor. At higher chloride concentrations the effect of pH on the response of the sensor is less than 1 mV which is insignificant. Therefore, in solutions with chloride concentration lower than 4 mM, the effect of pH on the response of the sensor is not negligible. Therefore, the Ag/AgCl electrodes (sensors) can be used to determine chloride concentrations in cement-based materials with high accuracy at chloride concentration higher than 4 mM. Considering pH of 12.6 as the maximum value results in higher accuracy at low chloride concentrations and the difference between the maximum and the minimum potential of sensor at 1 mM and 2 mM chloride solutions decreases to 5 mV and 3 mV, respectively. Consequently, pH has a significant influence on the response of the senor when a pH increase from 12.6 to 13.6 is relevant (12.6 – 13.6 being the pH range for pore solution in concrete environment).

These results indicate that (ideally) the chloride-content should be determined along with simultaneous detection of pH values, especially when low chloride concentrations are concerned. The performance of the Ag/AgCl sensors in embedded conditions (cement paste, mortar and concrete specimens) is an on-going investigation, focusing on sensor readings' interpretation and defined field application.

CONCLUSIONS

The following conclusions can be drawn from the present investigation:

- At 1000 mM chloride concentration, the solution composition has a minimum effect on the response of the sensor.
- The pH has a significant influence on the potential value of the sensor at chloride concentration lower than 4 mM.
- The pH value should be simultaneously detected in order to precisely determine the chloride content in concrete with low or minimal chloride concentration.

REFERENCES

[1] Duffo G S, Farina S B and Giordano C M. Characterization of solid embeddable reference electrodes for corrosion monitoring in reinforced concrete structures. *Electrochimica Acta*, 2009, Vol. 54 (3), 1010–1020.

[2] Elsener B, Zimmermann L and Bohni H. Non destructive determination of the free chloride content in cement based materials. *Materials and Corrosion*, 2003, Vol. 54 (6), 440–446.

[3] Atkins C P, Carter M A and Scantlebury J D. Sources of error in using silver/silver chloride electrodes to monitor chloride activity in concrete, *Cement and Concrete Research*, 2001, Vol. 31(8), 1207-1211.

[4] Angst U, Elsener B, Larsen C K and Vennesland O. Potentiometric determination of the chloride ion activity in cement based materials. *Journal of Applied Electrochemistry*, 2010, Vol. 40 (3), p. 561–573.

[5] Gao X, Zhang J, Yang Y and Deng H. Fabrication and performance of all-solid-state chloride sensors in synthetic concrete pore solutions, *Sensors*, 2010, Vol. 10(11), 10226-10239.

[6] de Vera G, Climent M A, Anton C, Hidalgo A and Andrade C, Determination of the selectivity coefficient of a chloride ion selective electrode in alkaline media simulating the cement paste pore solution, *Journal of Electro analytical Chemistry*, 2010,Vol. 639(1-2), 43-49.

[7] Du R G, Hu R G, Huang R S and Lin C J. In Situ Measurement of Cl- Concentrations and pH at the Reinforcing Steel/Concrete Interface by Combination Sensors, *Analytical Chemistry*, 2006, Vol. 78 (9), 3179-3185.

[8] Chang C F, Chen J W. The Experimental Investigation of Concrete Carbonation Depth. *Cement and Concrete Research*, 2006, Vol. 36 (9), 1760-1767.

THE INFLUENCE OF CRACKS ON CHLORIDE-INDUCED CORROSION OF REINFORCED CONCRETE STRUCTURES – DEVELOPMENT OF THE EXPERIMENTAL SET-UP

Andrija Blagojević
Department of Structural Engineering - Concrete Structures, Delft University of Technology, Delft, The Netherlands
a.blagojevic@tudelft.nl

Dessi A. Koleva
Department of Materials and Environment, Delft University of Technology, Delft, The Netherlands
d.a.koleva@tudelft.nl

Joost C. Walraven
Department of Structural Engineering - Concrete Structures, Delft University of Technology, Delft, The Netherlands
j.c.walraven@tudelft.nl

ABSTRACT: Chloride-induced corrosion of steel reinforcement is one of the major threats to durability of reinforced concrete structures in aggressive environmental conditions. When the steel reinforcement starts to corrode, structures gradually lose integrity and service life is shortened. Cracks are inevitable in practice and they facilitate ingress of chloride ions, moisture and oxygen through the concrete cover. This work discusses the experimental set-up, developed with an emphasis on the effect of cracks on chloride-induced corrosion of reinforced concrete structures. The test series consist of 32 reinforced concrete beams (1500×100×150 mm), designed in manner to monitor both mechanical and corrosion (embedded steel, reference cells, counter electrodes) properties. Four-point bending was applied in order to induce cracks with predefined and variable width. The variable mean crack width, number of cracks and total crack width were investigated in correlation to different concrete cover and types of loading in the experiments. In order to simulate aggressive environment within the designed loading conditions, the specimens were exposed to alternating wetting and drying cycles i.e. once a week for 2 days ponding using a 3.5 % NaCl solution and a 5 days drying phase. The half-cell potential and linear polarization resistance methods were applied for assessing the corrosion state of the steel reinforcement (this is an on-going experiment, hereby reported are the details of experimental set-up).

Keywords: chloride-induced corrosion, concrete cover, crack width, crack frequency, durability, reinforced concrete.

INTRODUCTION

Common knowledge, e.g. considering Tutti's [1] diagram, is that within the service life prediction for reinforced concrete structures, two main phases can be distinguished and defined: the corrosion-initiation phase and the corrosion-propagation phase. During the initiation phase chloride ions, water and oxygen penetrate through the concrete cover and reach the vicinity of the steel reinforcement. The initiation period is defined to be completed when the chloride concentration at the steel surface reaches a critical value, thus destroying the passive layer protecting the steel reinforcement. This is the point when the propagation phase starts. In this phase corrosion products form, accumulate, volume expand and hence induce concrete cover cracking, which even further facilitates accelerated penetration of aggressive substances, through already an increased number of cracks. Furthermore, corrosion can lead to spalling of the concrete cover, reduction of the cross-sectional areas of the reinforcement and as such impair structural safety.

The unavoidable presence of cracks in concrete structures can, essentially, determine a rapid start of the corrosion initiation phase, e.g. even within a few days-scale [2]. However, this process is supposed to slow down and even to stop as a result of "self-healing". This early corrosion is therefore, in the case of small cracks, not believed to be very influential on the service life of a structure. However, tests with regard to the role of this autonomous "self-healing" of cracks have been generally carried out under static loading and it is questionable whether the already drawn conclusions hold for other situations as well, for instance for non-static conditions in bridges.

RESEARCH SIGNIFICANCE

It is remarkable that in the Model Code for Service Life Design [3] the width of the cracks is not considered as an influencing factor, whereas in nearly all building codes the service life of concrete structures is directly related to the surface crack width. This leads to a confusing situation, because increasing the concrete cover is supposed to improve service life, whereas increasing the concrete cover leads as well to an increased surface crack width (due to the truncated shape of the cracks), which – according to the codes – means a reduction of service life at the mean time. Hence, it would be already an improvement to adopt the surface crack width – concrete cover ratio as a criterion for service life design, instead of the current width of surface cracks [4]. Furthermore, it is unsatisfactory that in current codes for structural concrete the maximum allowable crack width only depends on the exposure class and the type of structure (reinforced or prestressed), whereas anyhow the concrete composition and the level of loading are influencing parameters, together with the possibility for crack frequency, crack orientation and crack depth to play a significant role. Regarding those uncertainties, it is obvious that the influence of cracks on service life should be re-considered. To that aim, an appropriate experimental set up should be developed, which is subject to discussion in this work.

DEVELOPMENT OF THE EXPERIMENTAL SET-UP

As far as the durability provisions for chloride-induced corrosion of reinforced concrete structures are concerned, the following issues are prescribed by codes: exposure class (X0, XC, XD, XS, XF, XA), sometimes the concrete mixture (w/c ratio, cement content, binder type), maximum allowable crack width and minimum concrete cover. All of these were

considered for the experimental set-up. Additionally, to account for the influence of cracks on chloride-induced corrosion, the following parameters were altered: crack width, crack frequency, total (summed) crack widths, concrete cover and type of loading.

Exposure class

The exposure classes for concrete structures are defined in Eurocode 2 [5]. In the experiments the most severe conditions were applied by alternating wetting and drying cycles to simulate environmental class XD3. Examples of this exposure class are car park slabs, pavements, and parts of bridges exposed to de-icing salts. Several researchers used a different chloride ponding-drying ratio to simulate corresponding exposure conditions. For example, in a study by Otieno [2], 3 days ponding by 5% NaCl and 4 days drying (weekly cycles) were applied to accelerate steel corrosion. Mohammed[6] and Otsuki[7], reported 24 hours ponding and 60 hours drying cycles, twice a week , using 3.5% and 3.1% of NaCl respectively. However, the most realistic conditions were applied in a study by Schießl [8], where 1 day of ponding using 1% NaCl and a 6 days drying period were applied twelve times, followed by two wetting periods with chloride-free solution. After that, the specimens were exposed to 80% RH in a climatic chamber without further wetting cycles for one year. After one year, the same procedure was conducted once again to simulate exposure conditions as closely as possible in the splash zone of a motorway near Düsseldorf during the harsh winters of 1986 and 1987. Research should be carried out during limited time, but it is not desirable to exaggerate with acceleration of steel corrosion in comparison with real exposure conditions. Considering the aforementioned reports and in order to simulate aggressive environment, the cracked reinforced beams in this study were exposed to alternating wetting and drying cycles once a week for 2 days ponding (3.5 % NaCl solution) and a 5 days drying phase.

Concrete mixture

In order to reduce the number of parameter combinations, and regarding that the role of the concrete composition is not the subject of the research, only one concrete mixture was used for all experiments. The research project aims at investigating the influence of cracks on chloride-induced corrosion during a limited period of time. Consequently, a relatively low value of the concrete strength class was aimed at for the concrete mixture, C20/25 (w/c ratio 0.60 and cement content 260 kg/m3).

Casting and curing

The reinforced concrete beams 1500×100×150 mm were cast with one ribbed bar which was embedded at the desired position. High yield ribbed reinforcing bars B500A were used, diameter of 12 mm and length of 1460 mm. Before casting, the reinforcing bars were degreased. The internal reference electrode (platinized titanium) was fixed next to the reinforcing bar using strips (Fig. 1). The side of the beam, which was later exposed to a chloride solution, is situated at the bottom of the mould. The concrete was vibrated in three layers. Titanium mesh (MMO Ti) was embedded at the opposite side at 15 mm from the cover in order to act as counter electrode for corrosion measurements (Fig. 2). Several cubes were cast from each batch to monitor the compressive strength. Three cubes per batch were cast in order to be exposed to a chloride solution under the same conditions as the beams and for the purpose of finding chloride profiles in uncracked concrete. After casting, the beam specimens and the cubes were covered with plastic sheets for 72 hours under laboratory conditions. Subsequently, all specimens were cured in a climate-controlled (fog) room (20±2°c and 95±5% RH) until the age of 28 days. Then, three cubes were tested to check the compressive strength, while the reinforced concrete beams were exposed to air drying under laboratory conditions for additional 7 days.

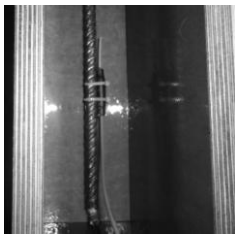

Fig. 1: *Pt/Ti reference electrode*

Fig. 2: *MMO Ti mesh counter electrode*

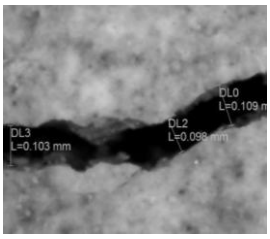

Fig. 3: *Crack width 0.1 mm*

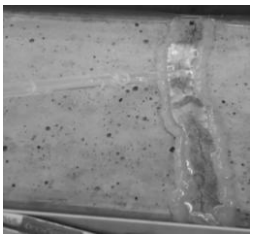

Fig. 4: *Crack sealing by epoxy*

Concrete cover

During casting three different concrete covers were applied: 20 mm, 30 mm and 40 mm. The larger the concrete cover, the longer is the distance from the concrete surface to the steel reinforcement i.e. the larger is the limitation for aggressive substances penetration. Consequently, a thicker concrete cover theoretically provides better corrosion protection of the steel reinforcement. A larger concrete cover, on the other hand, leads to a higher surface crack width. Therefore, it is logic that the surface crack width-concrete cover ratio is a parameter which has to be taken into consideration. Four-point bending was applied in order to induce predefined crack widths in reinforced concrete specimens. Steel beams were needed for the purpose of accommodating supports (steel rods) on them and to use a downer bracket in interaction with threaded rods, bolts and upper bracket to apply the force on the concrete beam. The experimental set-up is shown in Fig. 5. The series of different mean crack widths, number of cracks and total crack widths were tested in combination with various concrete covers and types of loading during the experiments. Crack widths were measured by a digital microscope and the average value was compared with the desired target value (Fig. 3). In order to control the number of cracks in some series undesired cracks had to be sealed by epoxy (Fig. 4). The containers for NaCl solution were made of PVC and placed on the top of the beam. The cracks in depth along both sides of the beams were sealed by silicone.

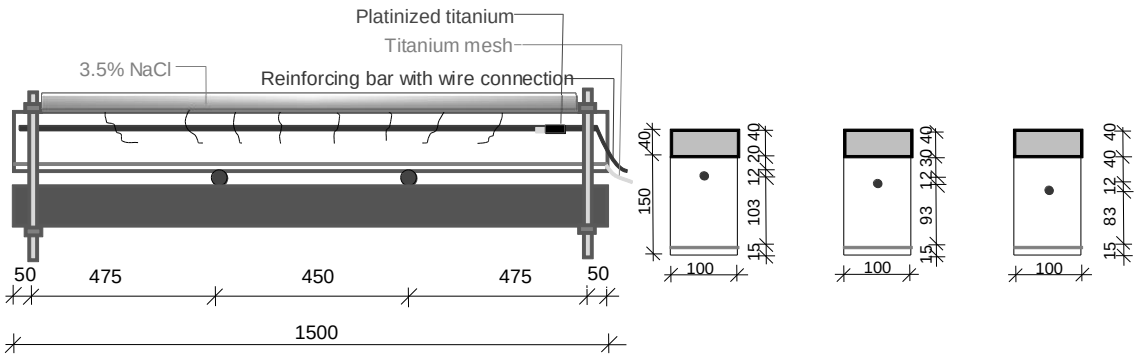

Fig. 5: *Experimental set-up*

MEASUREMENT OF STEEL CORROSION

Half-cell potential

The half-cell potential (HCP) measurement is the most widely used standard and non-destructive technique for assessing the active or passive state of steel in concrete. The HCP, in a simplified way, provides a potential reading (voltage difference between the steel reinforcement and a reference electrode). Based on standards, requirements and experience, the probability of corrosion initiation and further propagation is judged, based on the recorded

potential values. Different reference electrode (cells) can be used, including external and embedded ones. In this experiment silver-silver chloride (Ag/AgCl) was applied as an external reference electrode. HCP measurements were conducted using an electrical connection to the reinforcement and the external reference electrode, placed on the concrete surface – this was the so-called, "point" measurement. The steel electrode potential was further recorded through the embedded Pt/Ti reference cell, which gives the average value for the whole re-bar. The HCP measurements were conducted as point measurements twice a week, at the end of wetting and drying cycles, aiming to assess the probability of steel corrosion [9]. Information on the corrosion rate is not available via HCP. After steel de-passivation, linear polarization resistance technique was applied in order to quantitatively assess the corrosion state of the steel reinforcement. Potentiostat was used for all corrosion tests.

Linear polarization resistance

The linear polarization resistance (LPR) technique can be considered as a non-destructive, mostly straight-forward rather then complex technique for corrosion rate measurements in civil structures. The principle of LPR is steel polarization in a window of at least +/- 10 mV around the HCP and record of the corrosion current response within polarization. For this set-up, the steel reinforcement was the working electrode, the titanium mesh was the counter and Ag/AgCl (or the embedded Pt/Ti) was the reference electrode. A polarization window from -20 mV to +20 mV with a scan rate of 0.1 mV/s and a step of 0.5 mV were applied. The fundamental principle of this and other electrochemical techniques can be found in more details in specialised literature and reports [10]. For the purpose of this investigation, it will be only mentioned that linear regression was applied to derive the R_p values (eq.1), whereas the Stern-Geary equation (eq. 2) was employed to calculate the corrosion currents. Normalization to corrosion current densities was performed through considerations of geometrical constants (equations 3). Automated calculation (via the relevant in this case NOVA software) is also possible and additionally employed in this study.

$$R_p = \frac{\Delta E}{\Delta I} \tag{1}$$

$$I_{corr} = \frac{B}{R_p} \tag{2}$$

$$i_{corr} = \frac{I_{corr}}{A} \text{ , where } A = \pi D l \tag{3}$$

B is a constant which varies and depends on many factors and conditions (which are not subject to discussion hereby). According fundamental principles and literature and also considering reinforced concrete, B = 52 mV is used for passive and B = 26 mV is used for active state of the steel reinforcement [10], therefore these range of values were employed in the calculations of corrosion rate for this study as well. As aforementioned, the experiment is on-going. The exposure and monitoring time will be 2 years.

CONCLUSIONS

This experimental program is focused on the relation between surface crack width and corrosion initiation and propagation in reinforced concrete members. The purpose of this experimental set-up is to investigate the interconnected influence of surface crack width, crack density (frequency), total crack width, concrete cover and loading conditions on the corrosion of steel reinforcement. Actually, this experimental set-up was developed in order to take a step towards improved regulations for cracked reinforced concrete members in aggressive environmental conditions.

REFERENCES

1. Tutti, K., *Corrosion of Steel in Concrete*. Swedish cement and concrete Research Institute Report, Stockholm, 1982.
2. Otieno, M.B., Alexander, M.G., Beushausen, H.-D., *Corrosion in cracked and uncracked concrete - influence of crack width, concrete quality and crack reopening.* Magazine of Concrete Research, 2010, 62(6), pp. 393-404.
3. Fib, *Model code for service life design in fib Bulletin 34.* International Federation for Structural Concrete (fib), Lausanne, Switzerland 2006.pp126.
4. Gowripalan, N., Sirivivatnon, A., Lim, C.C., *Chloride diffusivity of concrete cracked in flexure.* Cement and Concrete Research, 2000, Vol. 30, pp. 725-730.
5. EN 1992-1-1-2005, *Design of Concrete Structures, Part 1-1: General Rules and Rules for Buildings*. Committee of European Normalisation, Brussels, (1992–2005a)
6. Mohammed, T.U., Otsuki, N., Hisada, M., Shibata, T., *Effect of crack width and bar types on corrosion of steel in concrete.* Journal of Materials in Civil Engineering, 2001, Vol. 13(3), pp.194-201.
7. Otsuki, N., Miyazato, S.I., Diola, N.B., Suzuki, H., *Influences of bending crack and water-cement ratio on chloride-induced corrosion of main reinforcing bars and stirrups.* ACI Materials Journal, 97(4), 2000., 454-464.
8. Schießl, P., Raupach, M., *Laboratory studies and calculations on the influence of crack width on chloride-induced corrosion of steel in concrete.* ACI Materials Journal, 1997, 94(1), pp. 56-61.
9. C876-91, ASTM, *Standard test method for half-cell potential of reinforcing steel in concrete*. American Society for Testing and Materials, 1991.
10. Andrade, C., Alonso, C., *Corrosion rate monitoring in the laboratory and on-site.* Construction and Building Materials, 1996, 10(5), pp. 315-328.

EFFECT OF SPACERS ON CONCRETE TRANSPORT PROPERTIES AND CHLORIDE PENETRATION

S.Alzyoud, H.S. Wong, N.R. Buenfeld
Concrete Durability Group, Department of Civil and Environmental Engineering, Imperial College London, United Kingdom
s.alzyoud11@imperial.ac.uk

ABSTRACT: Despite concerns over the effect of spacers on concrete durability, no studies have been carried out to establish the behaviour of the different types and materials of spacers in concrete. This paper investigates the effect of concrete, plastic, and steel spacers on gas diffusion, gas permeation and water absorption (sorptivity) in concrete cover. Concrete specimens made using different types of spacers were subjected to different curing and drying regimes reflecting real site conditions. Transport properties were then measured and µXRF was utilised to study chloride ingress, particularly near the interface between spacers and concrete matrix. The results show that plastic spacers consistently give the least resistance to transport, followed by samples with concrete spacers and steel spacers. The control samples (samples without spacers) had the most resistance to transport in all cases. This behavior is probably due to the poor interface between spacer and concrete and differential shrinkage, due to drying or cooling, between spacer and concrete which lead to cracking.

Keywords: Chloride penetration, interface zone, spacer, transport properties, µXRF.

INTRODUCTION

A rebar spacer is a device that is placed to secure the reinforcing steel prior to concreting so that the required concrete cover between the reinforcement and formwork or blinding is achieved [1]. Adequate cover is essential to protect the reinforcement from corrosion. The spacer is left permanently in the structure and it may have an important influence on the properties of the hardened concrete. A detailed search of the literature on the effect of spacers on the microstructure and durability of concrete showed there has been little research on this subject. It appears that its significance has largely been ignored by the concrete construction industry.

Spacers are manufactured from three basic materials: plastics, cementitious material or steel wire. Although spacers represent only a small proportion of the concrete cover, their presence could interrupt the microstructure of the concrete cover and provide potentially easy access of deleterious agents to the reinforcement. Despite some concerns over the effect of spacers on concrete durability, no studies have been carried out to establish the effect of the different types of spacers on the properties of concrete. There is a lack of research on understanding the effect of spacers on the mass transport properties and durability of concrete, in particular chloride or carbonation induced reinforcement corrosion.

EXPERIMENTAL WORK

Material

Concrete mixes were prepared at a water to cement ratio (w/c) of 0.4. The mix proportions are shown in Table 1. The cement used was CEM I complying with BS EN 197-1:2011 [2]. Tap water was used as batch water. The aggregates were Thames Valley gravel (5–10 mm) and sand (<5 mm) complying with the BS 882 Medium grading. Three types of spacers were tested in this study: a) concrete single cover spacer without tying wire, b) plastic "A shaped" spacer, and c) continuous lattice steel wire spacer.

Table 1. *Concrete mix design*

Mix ID	w/c ratio	Cement (kg/m^3)	Sand (kg/m^3)	Gravel (kg/m^3)
C1	0.4	345	726	1090

Sample preparation, curing and conditioning

More than one hundred cylindrical samples of 100 mm diameter and 50 mm height were cast in steel moulds. Spacers were tightly secured to the mould by clamping the rebar onto the base plate using the assembly shown in Figure 1. Concrete was placed in three layers and each layer was compacted using a vibrating table until no significant amount of air bubbles escaped the top surface.

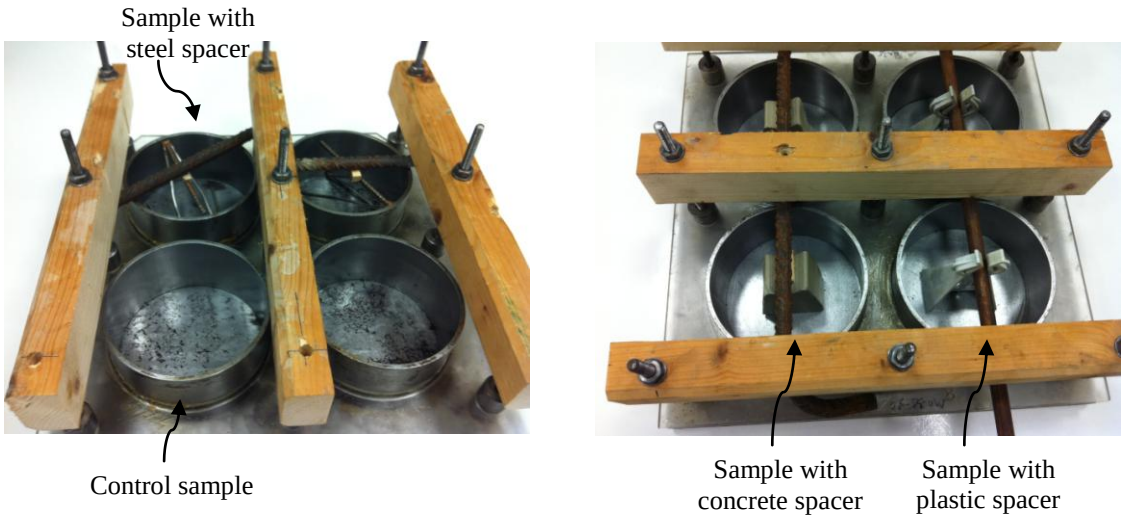

Fig. 1: *Sample setup*

Samples for transport testing were covered in plastic sheets and wet hessian for the first 24 hours, de-moulded, sealed in cling film and polythene bags and then kept in the laboratory at 20°C for a predetermined curing period of 3 or 28 days. Samples were conditioned at 20°C, 50% RH to constant mass prior to transport testing. Samples for chloride penetration were cured in a fog room (20˚C, 100%RH) for 28 days. Subsequently, samples were dried in an oven at 40˚C until constant weight was achieved.

Transport testing

Three replicates of each sample type were tested for oxygen diffusion, oxygen permeation, water absorption, and chloride penetration. These transport tests were selected because of their relevance to reinforcement corrosion. Water ingress via capillary suction is an important transport mechanism in non-saturated concrete. Full details of the test methods are described

in [3]. In the chloride penetration test, samples were placed in a tray containing shallow sodium chloride (3M) solution for 40 days. The solution level was about 5 mm above the lower surface of the sample.

Micro X-ray fluorescence (µXRF)

µXRF is a non-destructive technique for mapping and measuring elemental composition. It uses an X-ray beam to excite the sample instead of a beam of high-energy electrons as in the case of energy dispersive X-ray microanalysis (EDX). The main advantage of µXRF over EDX is its ability to map large and irregular samples, under ambient pressure environment, without requiring destructive and time-consuming sample preparation. Depth profiles of the chloride penetration were measured on split samples using this technique.

RESULTS

Figures 2-4 show the average oxygen diffusivity, oxygen permeability, and water sorptivity measured after the various curing and conditioning regimes. Error bars indicate +/- one standard error of the average. Figure 5 shows an example of a chloride distribution map for a sample with a plastic spacer, obtained using µXRF. The results consistently show that samples with spacers have significantly higher mass transport properties regardless of the curing age. Samples with plastic spacers consistently recorded the highest transport properties, followed by samples with concrete spacers and steel spacers. The control samples (i.e. samples without spacers) had the lowest transport coefficients in all cases.

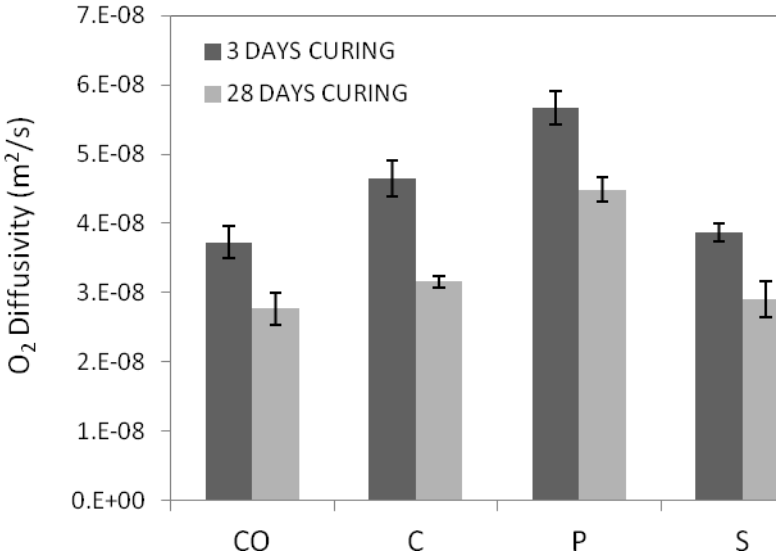

Fig. 2: *Oxygen diffusivity of samples after 3 and 28 days curing, conditioned at 20◦C, 50% RH. (CO = Control; C = Concrete spacer; P = Plastic spacer; S = Steel spacer)*

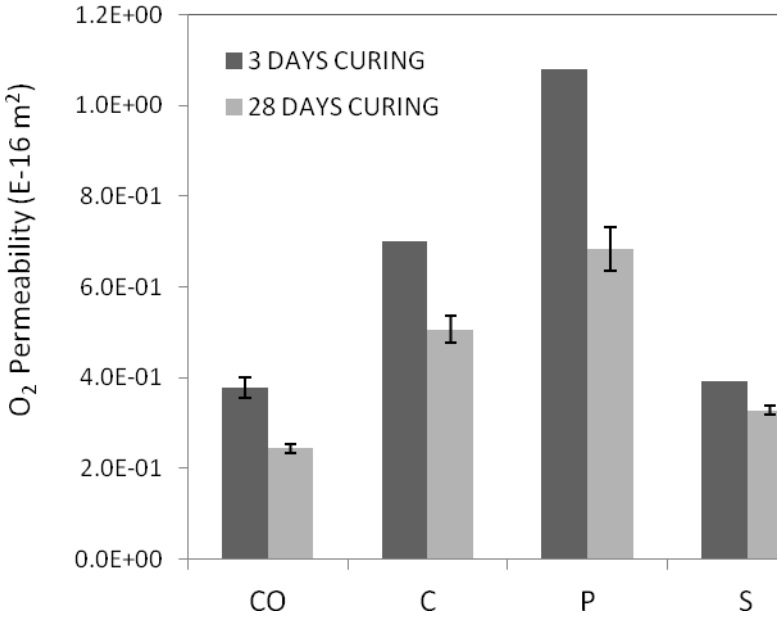

Fig. 3: *Oxygen permeability of samples after 3 and 28 days curing, conditioned at 20◦C, 50% RH. (CO = Control; C = Concrete spacer; P = Plastic spacer; S = Steel spacer)*

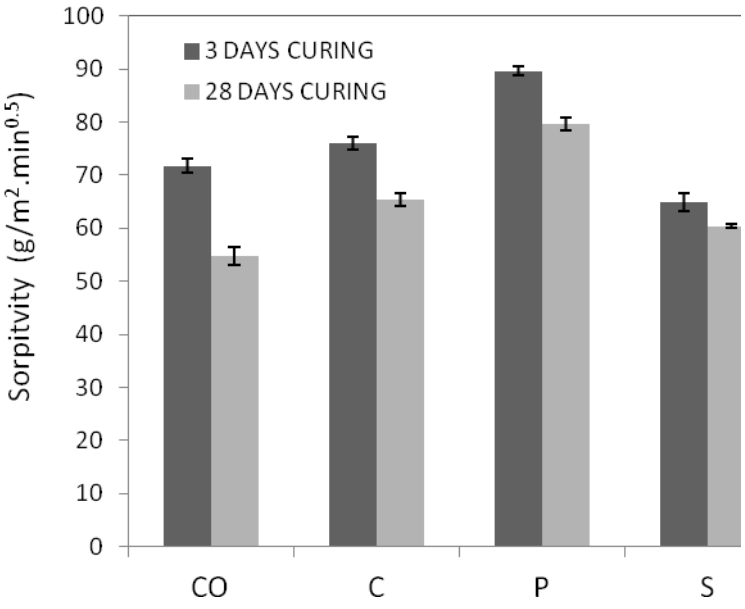

Fig. 4: *Water sorptivity of samples after 3 and 28 days curing, conditioned at 20◦C, 50% RH. (CO = Control; C = Concrete spacer; P = Plastic spacer; S = Steel spacer)*

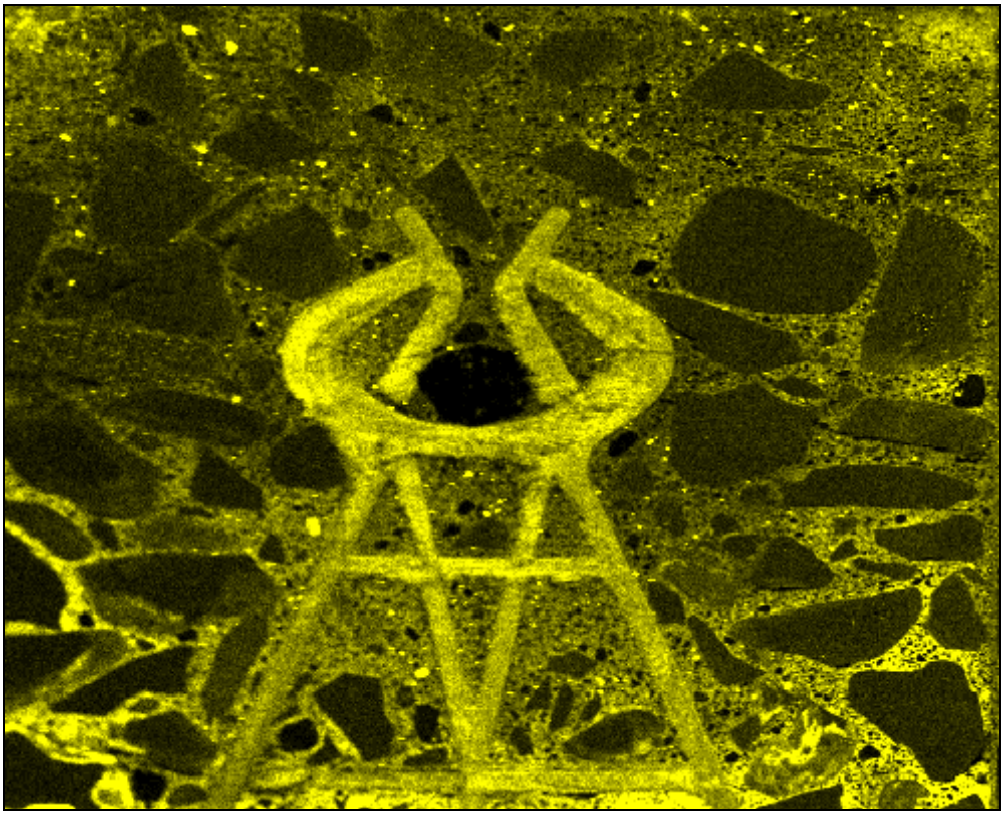

Fig. 5: *Elemental map from µXRF showing the distribution of chloride in a concrete sample containing a plastic spacer. The sample was exposed to 3M sodium chloride solution for 40 days. Higher intensity indicates higher concentrations of chlorides.*

CONCLUSIONS

The results from this study show that reinforcement spacers have a negative effect on mass transport properties of concrete regardless of curing age and curing condition. Concrete samples with plastic spacers consistently give the least resistance to transport, followed by samples with concrete spacers and steel spacers. The control samples (samples without spacers) had the most resistance to transport in all cases. This behavior is probably due to the poor interface between spacer and concrete and differential shrinkage, due to drying or cooling, between spacer and concrete which lead to cracking. Further work is on going to verify this and to determine its impact on long-term durability.

REFERENCES

[1] British Standards Institution. *Spacers and chairs for steel reinforcement and their specification. Product performance requirements*. BS 7973-1: 2001. BSI, London, 2001.

[2] British Standards Institution. *Cement composition, specifications and conformity criteria for common cements*. BS EN 197-1:2011. BSI, London, 2011.

[3] H.S. Wong, N.R. Buenfeld, J. Hill, A.W. Harris Mass transport properties of mature wasteform grouts. Adv. Cem. Res., 2007, 19 (1) 35-46.

MgO BASED MINERAL ADDITIVES FOR SELF-HEALING IN CONCRETE

Tanvir Qureshi and Dr. Abir Al-Tabbaa
Department of Engineering , University of Cambridge, Cambridge, UK
tsq20@cam.ac.uk

ABSTRACT: Self-healing within certain limits in traditional Portland cement (PC) concrete called autogenous healing has been acknowledged for many years. This research aims to increase the autogenous self-healing ability of PC concrete using expansive mineral additives, such as magnesium oxide (MgO), bentonite clay and, quicklime. Minerals are expected to improve the self-healing in the nano-micro scale. Preliminary laboratory investigations were carried out in which up to 10% of the three mineral additives were mixed with PC. Cube samples were prepared for compressive strength analysis, and prism samples for crack forming through a three-point bend test and subsequent crack healing analysis over 28 day periods. Healing was found to be more promising for crack width smaller than 100 µm. Furthermore, addition of the three expansive mineral additives improved the self-healing potential of PC, where most of the mixes showed better performance compared to only PC mix. MgO and bentonite was also found to reduce the pH level in mixes which is promising to create friendly environment for biological agent incorporation and healing in micro-meso scale.
Keywords: Crystallisation, Expansion, MgO, Portland cement (PC), Self-healing.

INTRODUCTION

Modern PC concrete is currently the most used construction materials in the world. PC concrete strength gradually decreases due to hydration, shrinkage, fatigue and other environmental conditions. Thus, concrete structures require repair and maintenance during its design life period. However self-healing technology can extend the repair requirement period which not only can longer the material life span but also reduce repair and maintenance costs[1].

Expansive minerals such as MgO have great prospects for increasing the self-healing capacity of PC concrete. This expensive mineral addition in the PC, process is to improve the autogeneous self-healing of PC concrete. Autogenous self-healing is a natural repairing process in the cementitious materials[2]. This process is initiated by hydration of un-hydrated cement particles in the crack surface. There are five principle steps in autogeneous self-healing, i) Further reaction of the unhydrated cement; ii) Expansion of the concrete in the crack flanks; iii) Crystallization of calcium carbonate; iv) Closing of the cracks by solid matter in the water; v) Closing of the cracks by spilling-off loose concrete particles resulting from the cracking[3]. Reactions involved in deposition of calcium carbonate are as follows[4].

$H_20+CO_2 \Leftrightarrow H_2CO_3 \Leftrightarrow H^+ + HCO_3^- \Leftrightarrow 2H^+ + CO_3^{2-}$ (1)
$Ca^{2+}+CO3^{2-} \Leftrightarrow CaCO_3$ ($pH_{WATER}>8$) (2)

$Ca^{2+}+HCO_3^- \Leftrightarrow CaCO_3+H^+$ ($7.5<pH_{water}<8$) (3)

Reactions illustrated in the above three equations have leads towards the calcite crystal formation which causes the autogeneous self-healing. Permeability found to have gradually decrease over time when water flowed through cracked concrete within a specific hydraulic gradient[4,5]. Expensive minerals MgO have potential to increase the self-healing materials formation in the crack surface. MgO based mineral addition with PC cement is hypothesized to improve intrinsic material property for better self-healing in micro scale and may encourage the bacterial self-healing in meso scale.

MATERIALS AND METHODS

Materials

CEM 1 (52.5N) Ordinary portland cement (PC) was used as the typical cement material. Principal self-healing minerals was light burnt Magnesioum Oxide (MgO 92/200). Furthermore, local bentonite clay (supplied by Kentish minerals) and quicklime have been used for assisting and comparing MgO self-healing activity with PC. Four different mixes of PC up to 10% additives was used for investigation and compared with a control mix (100% PC). Different mixes are illustrated in the Table 1 below.

Table 1. *Mix proportions of five different cement mixes.*

Mix	OPC (PC)	MgO (M)	Bentonite Clay (B)	Quicklime (L)	Water	Superplasticiser
M1(PC100)	100	-	-	-	28.5	0.3
M2(PC95M5)	95	5	-	-	30	0.3
M3(PC95B5)	95	-	5	-	32	0.3
M4(PC95L5)	95	-	-	5	30.5	0.3
M5(PC90M5B5)	90	5	5	-	33.5	0.3

Methods

Mechanical and image analysis on cube (100X100X100mm) and prism (160X40X40mm) samples was conducted to investigate the self-healing performance. Compression test on cubes were performed following (BS EN 196-1)[6] in different period. Prism samples were used for forming cracks using three point bend test following (BSEN 12390-5)[7] and (ASTM: D790-10)[8], and monitoring subsequent crack healing in different period. Flexural stress, strain and elasticity was calculated using equation 4,5 and 6 below.

$$\sigma_f = \frac{3PL}{2bd^2} \quad (4)$$

$$\varepsilon_f = \frac{6Dd}{L^2} \quad (5)$$

$$E_f = \frac{L^3 m}{4bd^3} \quad (6)$$

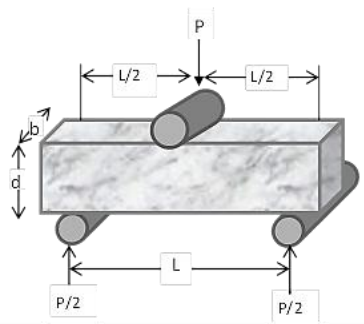

Fig. 1: *Three point bend test setup.*

In those equations, σ_f= Stress in outer surface at midpoint (MPa), ε_f= Strain in the outer surface (mm/mm), E_f= flexural Modulus of elasticity (MPa), P= load (N), L= Support span (mm), b = Width (mm), d= Depth (mm), D= maximum deflection of the prism center (mm), and m= The gradient (i.e., slope) of the initial straight-line portion of the

load deflection curve (P/D), (N/mm). Three point bend test setup is illustrated in Fig.1. Prism samples were cracked on day 1 after casting and left in the water curing tank for self-healing. The healed samples were cracked again under three point bend test for measuring the flexural strength regain in 28 days. The healing was also monitored under digital microscope.

RESULTS AND DISCUSION

Compressive strength development

Addition of 5% MgO increased the compressive strength of mixes as evident in M2(PC95M5). Quicklime up to 5% did not have much impact on the overall compressive strength development. However, bentonite clay had reduced the compressive strength, although it had increased the self-healing capacity significantly. Substitution of 10% cement with MgO and bentonite clay in M5(PC90M5B5) found to have reduce the compressive strength. Strength development is illustrated in Fig.2 below.

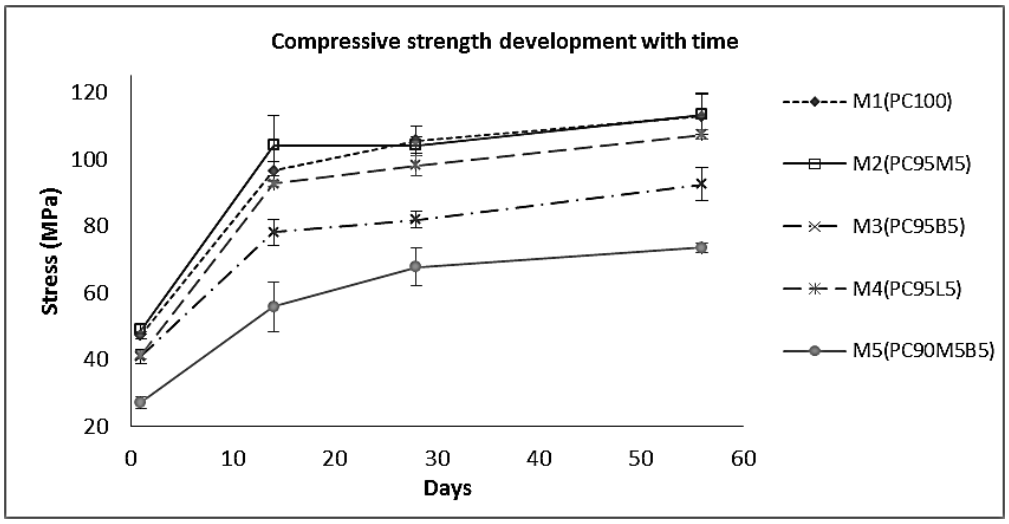

Fig. 2: *Compressive strength development.*

Three-point bend test

In the three point bend test, M2 and M5 found to have regained flexural strength up to 40% and 80% after 28 day healing. In comparison, M1, M3 and M4 have not gained considerable amount of strength (Fig.3). Hence, addition of MgO, and combined MgO and bentonite clay have greater prospects in terms of strength regain due to self-healing.

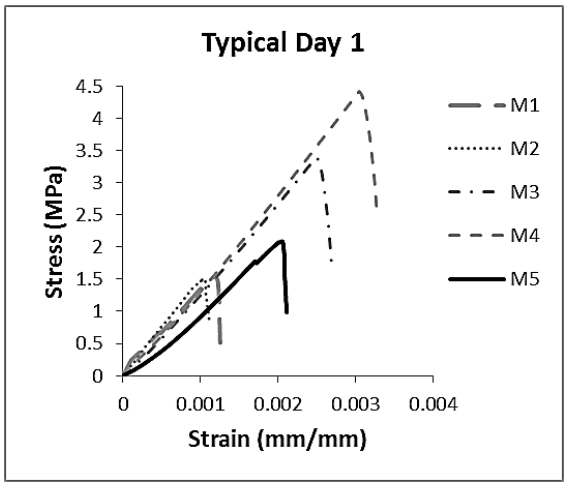

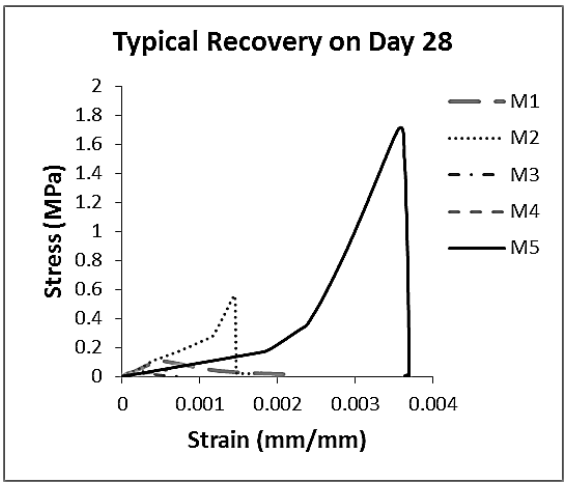

Fig.3: *Three-point bend test on day 1 and recovery on day 28.*

Crack healing visualization

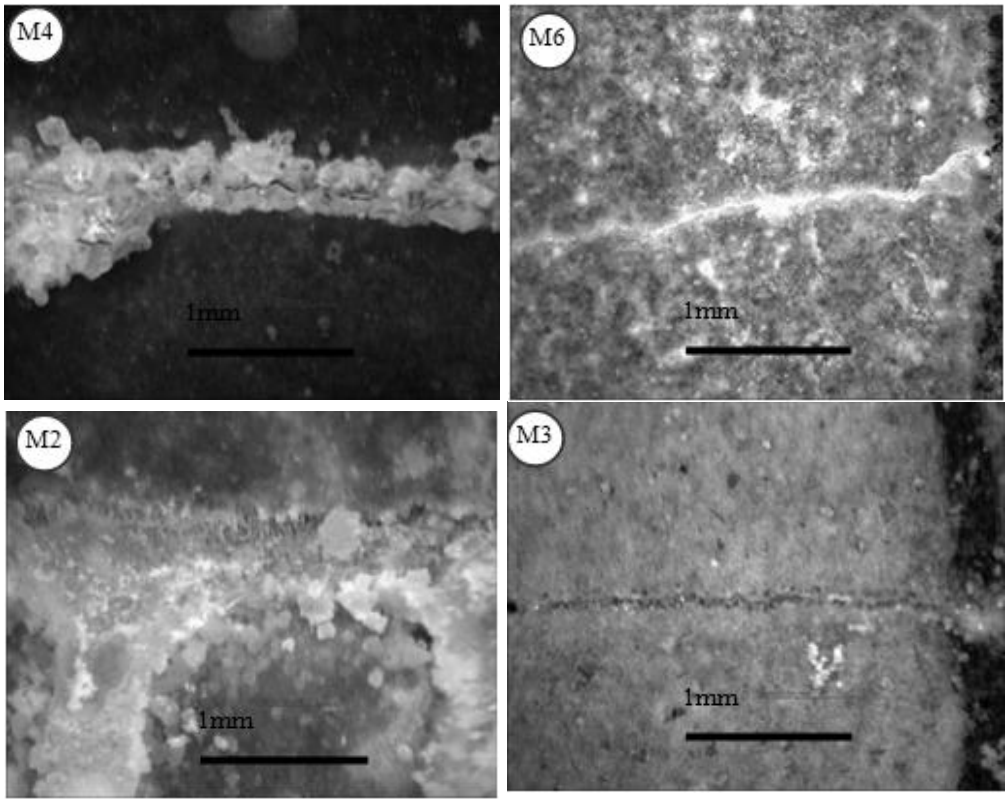

Fig.4: *Crack healing of M2, M3, M4 and M5 after 28 day curing.*

Cracks in M2 and M5 were found to heal faster and gain considerable amount of mechanical strength after 28 day healing (Fig.4). Good crystallisation was found in M3 and M4, however mechanical strength regain was not satisfactory.

Furthermore, reactive MgO has great potential to decrease the pH level of concrete[9]. As concrete formed with stone aggregate has a void space for survival of bacterial spore, lower pH further have benefits for bacterial growth and survival for a longer period. The hydration and carbonation reaction of MgO in the concrete demonstrated by Vandeperre et al[10] is illustrated in equation 7 and 8 below:

$$MgO + H_2O \rightarrow Mg(OH)_2 \quad (7)$$

$$Mg(OH)_2 + CO_2 + 2H_2O \rightarrow MgCO3 \cdot 3H_2O \quad (8)$$

CONCLUSIONS

Overall, MgO individually in M2(PC95M5) and MgO and bentonite clay combination in M5(PC90M5B5) have improved both healing and sealing performance of PC cement. Quicklime also has potential in crack sealing due to extensive crystallisation. Hence, optimum combination of MgO, bentonite clay and quick lime have great prospects for increasing concrete self-healing. Further, investigation is underway for finding optimum mix proportion and characterise self-healing materials.

REFERENCES

[1] Ghosh, S.K. *Self-healing Materials, Fundamentals, Design Strategies, and Application*, Wiley-vch Verlag GmbH & Co., Germany. ISBN: 978-3-527-31829-2, 2009. Aavailable at: http://japanlinkcenter.org/DN/JST.JSTAGE/jact/10.185?lang=en&from=CrossRef&type=abstract, [Accessed January 10, 2013].

[2] Wagner E.F. *Autogenous Healing of Cracks in Cement-Mortar Linings for Gray-Iron and Ductile-iron Water Pipe.* Journal of the American Water Works Association, Vol. 66, pp 358-360.1974,

[3] Ramm, W. & Biscoping, M. *Autogenous healing and reinforcement corrosion of water-penetrated separation cracks in reinforced concrete.* Nuclear Engineering and Design, 179(2), pp.191–200. 1998. Available at: http://linkinghub.elsevier.com/retrieve/pii/S0029549397002665. [Accessed February 1, 2013]

[4] Edvardsen. *Water permeability and autogenous healing of cracks in concrete.*" ACI Material Jounral, 96(4), pp.448-454. 1999. Web: http://www.unitedstatesconcrete.com/AutogenousHealingofCracks.pdf [Accessed on. February 1, 2013]

[5] Reinhardt and Jooss, *Permeabilitiy and selfhealing of cracked concrete as a function of temperature and crack width.* Cement and Concrete Res 33:981–985. 2003.

[6] British Standards Institution. Methods of testing cement. Determination of strength. BS EN 196-1:2005, BSI, London, 2005.

[7] British Standards Institution, *Testing Hardened Concrete* Part 5: Flexural Strength Test Specimens. BS EN 12390-5:2009. 2009.

[8] American Society for Testing and Materials, *Standard Test Methods for Flexural Properties of Unreinforced and Reinforced Plastics and Electrical Insulating Materials*, ASTM D790 – 10, 2010.

[9] Zhang, T., Cheeseman, C.R., Vandeperre, L.J. *Development of novel low pH cement systems.* DIAMOND'09 Conference, York, UK. pp.1–4. 2009.

[10] Vandeperre, L., Liska, M., and Al-Tabbaa, A. *Reactive MgO cements : Properties and Applications*. in *International conference on sustainable construction materials and technologies*. Coventry: Taylor and Francis. 2007.

EFFECT OF SURFACE PRE-TREATMENT OF WASTE TIRE RUBBER AGGREGATE ON WORKABILITY AND COMPRESSIVE STRENGTH OF CONCRETE

Jian Yang, Haolin Su, Gurmel S. Ghataora and Samir Dirar
School of Civil Engineering, University of Birmingham, Birmingham, UK

ABSTRACT: Crumb rubber has found a novel use in concrete in recent years. Given the common observation of weak bond between rubber and cement matrix, it is of practical use to understand the effect of rubber surface modification on the resulting concrete performance. In this paper, the effect of waste tire crumb rubber surface modification on the workability and compressive strength of concrete properties is studied. Mixed sized crumb rubber particles were prepared by blending different size of rubber particles so that its particle size distribution (PSD) curve is similar to the sand grading curve. They were pre-treated by silane coupling agent (SCA) and saturated NaOH solution, respectively, prior to replacing 20% of natural fine aggregate by volume. Control concrete specimens with the same percentage of untreated rubber were also prepared to compare their properties. Results reveal that the concrete with the SCA pre-treatment crumb rubber is found to have a better compressive strength but a worse workability as compared to that with untreated rubber or saturated NaOH solution pre-treated rubber. The scanning optical microscopic inspection was performed to study the interfacial properties between the rubber and cement matrix and it is found that the rubber-matrix adhesion is enhanced by SCA, but there is almost no effect by saturated NaOH solution by comparing to control concrete.
Keywords: compressive strength, concrete, silane coupling agent, waste tire rubber, workability.

INTRODUCTION

The rapid growth of vehicle use has brought about a huge increase in waste tires. This has created a pressing problem called as ‘black pollution’, which poses a potential threat to the environment and the wellbeing [1]. These waste tires may produce fire hazards and occupy a large volume of decreasing landfill sites with components that do not biodegrade [2]. Several means of recycling or reusing waste tires have been proposed, including the use as lightweight aggregates in asphalt pavement, as fuel for cement kiln, as feedstock for making carbon black and as artificial reefs in marine environment [2]. However, some of these proposals are economically and environmentally unattractive.

Many studies have been carried out on the subject of using waste tire rubber as aggregate substitutes for making concrete [3-5]. Similar to the use of recycled construction or demolition aggregate [6], recycling waste tire rubber in concrete can be a feasible option for

the sustainable and eco-friendly construction development. The use of crumb rubber as aggregate in concrete will reduce the workability and strength, but improve the ductility, impact resistance and dynamic energy dissipation capacity, and this is attributed to the rubber aggregate's own properties (e.g. high resilience, low density). One of the most important influencing factors on the properties of rubber concrete is rubber replacement percentage, which has been widely studied and reported [3, 4]. However, research on the effect of rubber surface modification on the properties of concrete is still scarce. Segre and Joekes [5] exercised surface-treatment on rubber particles with saturated NaOH solutions for 20 minutes at the room temperatures by stirring before the mixture was filtered. The rubber was washed with tap water and dried at the ambient temperature before using. The results from this treatment showed that the NaOH treatment enhanced the adhesion of tire rubber particles to surrounding paste, leading to an improvement in mechanical properties such as compressive strength, flexural strength and fracture energy. In contrast, Albano etc. [3] pointed out that prior treatment of rubber with NaOH did not produce obvious changes on compressive and splitting tensile strength of resulting concrete when compared to the untreated rubber concrete.

This study aims to further the understanding of the effect of pre-treated crumb rubber on the properties of concrete. Saturated NaOH solution and SCA were used to modify the surface of rubber particles. Tests of workability at the fresh stage as well as the cube compressive strength at the hardened stage were conducted.

EXPERIMENT STUDIES

The materials used in this study comprised cement, tap water, sand, natural gravels, recycled aggregates and crumb rubber. Cement (CEM II/B-V 32.5) with 30% pulverized fuel ash (PFA) was used as a binder for the concrete mixture. Clean crushed stones with a nominal maximum particle size (NMPS) of 10 mm were used as coarse aggregate. Recycled aggregates from local demolishing plant, with the same NMPS, were used to replace 50% of natural coarse aggregates by mass for all four concrete mixes. The composition of the recycled aggregates is about 82.3% recycled concrete aggregate, 15.1% crushed clay bricks and 2.6% impurities. Natural river sand comprising a NMPS size of 5 mm was used as the fine aggregate. Waste tire rubber (CSR) with continuous grading similar to the natural sand were sourced from local recycling plant to replace 20% of river sand by volume. Saturated NaOH solution and SCA were prepared to modify the surface of rubber particles. Two batches of rubber particles were soaked in saturated NaOH solution for 2 hours and 24 hours respectively under the ambient condition. Then they were washed with tap water and kept in the air dry condition prior to using. Another batch was soaked in SCA untill all the surface was coated by the agent before being added into the mixture.

The British Department of Environment (DoE) method that is widely used for concrete mix design in the UK was adopted in this study. Saturated surface dry (SSD) density and SSD water absorption of aggregates and crumb rubber are shown in Table 1. The mix design of control concrete was aimed to achieve a target mean strength (grade C30) of 43 MPa at 28 days with a slump value of 60-180 mm. A total of four concrete mixes were prepared, that is, the control mix with untreated rubber (indicated as REF), the mix with the rubber particles pre-treated by a saturated NaOH solution for 2 hours (indicated as CCSR20-N2h), the mix with the rubber particles pre-treated by a saturated NaOH solution for 24 hours (indicated as CCSR20-N24h) and the mix with the rubber pre-treated by the silane coupling agent (CCSR20-SCA). All mix design parameters (water-to-binder ratio of 0.37) were kept constant throughout the rntire experiment programme (see Table 2).

To evaluate the workability of fresh concrete, slump were measured according to BS EN 12350-2. For the hardened concrete, three specimens from each mix were used for determining the compressive strength in conformity with BS EN 12390-3 at the age of 28-day after casting. Scanning optical microscopy was also performed to characterize the rubber particles and to observe the interface between the rubber and the matrix.

Table 1. *SSD density and SSD water absorption of natural and rubber aggregates.*

Item	Sand	Gravel	CSR
SSD* density (kg/m3)	2512	2581	973
SSD water absorption (%)	1.37	1.26	8.46

*SSD – saturated surface dry

Table 2. *Mix proportions of the mixtures.*

Notation	Water	Cement + PFA	Sand	Gravel	Rubber
REF	0.37	1	0.66	1.60	0.064
CCSR20-N2h	0.37	1	0.66	1.60	0.064
CCSR20-N24h	0.37	1	0.66	1.60	0.064
CCSR20-SCA	0.37	1	0.66	1.60	0.064

Note: the values are the mass ratio under SSD condition

RESULTS AND DISSCUSSION

Workability

All the concrete mixes were observed (by visual inspection) to be cohesive with no segregation during the mixing, placing or compaction. Fig. 1 shows the slump for all four concrete mixes. A slump of 66 mm was recorded for the REF. The slump for CCSR20-N2h, CCSR20-N24h and CCSR20-SCA is 4.5% (3 mm) higher, 3.0% (2 mm) higher and 13.6% (9 mm) lower than the REF mix, respectively. This result indicates that the pre-treatment by NaOH does not affect workability concrete significantly as the slump values from REF, CCSR20-N2h and CCSR20-N24h are rather close.

On the contrary, the pre-treatment by SCA reduced the workability noticeably. This is mainly ascribed to the sticky nature of SCA-treated rubber surface that tends to bond the rubber particles and the matrix, thus making the concrete mixture less workable. SCA is an organosilicon compound which contains two different reactive groups – one functional group is organophilic and the other is inorganophilic. The general formula of SCA is $YSi(OR)_3$, where Y is a non-hydrolytic group which tends to well bond the synthetic resin, rubber etc. in organic materials, and OR is a hydrolyzable group that will hydrolyze in water to generate SiOH group which tends is liable to chemically react with hydroxyl on the surface of inorganic materials to form the hydrogen bond. Then the further condensation reaction will form oxygen covalent bond, and eventually the surface of inorganic material is covered by the reaction products, thereby enhancing the cohesiveness [7]. The reaction process is shown in Fig. 2. Because of the special molecular structure of SCA that can react with both organic and inorganic materials to form chemical bond, two kinds of materials with

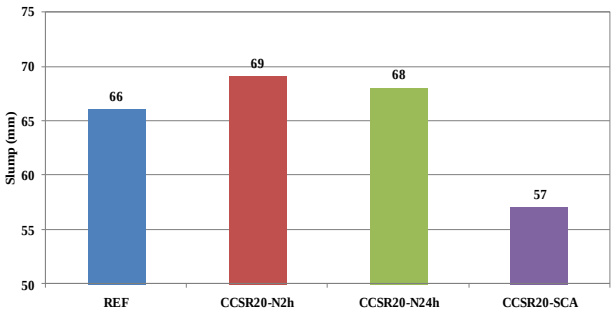

Fig. 1: *Slump test results of all the mixes.*

different type of chemical structures can be well connected on their interface, thus improving the bonding strength.

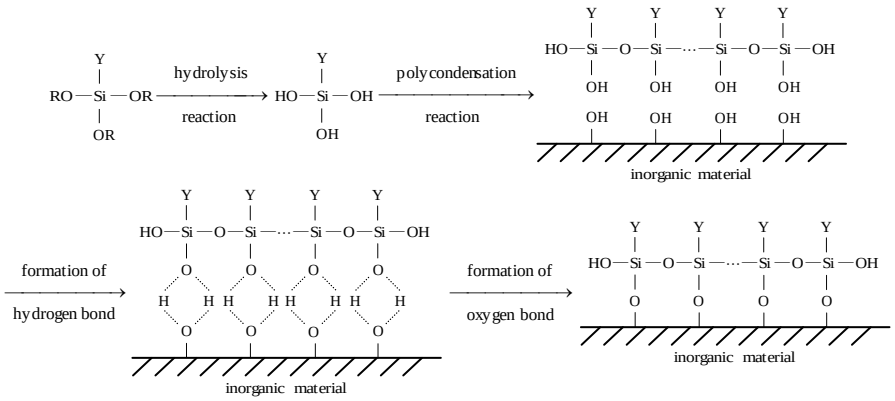

Fig. 2: *Reaction process of SCA with inorganic materials.*

Compressive strength

Compressive strength tests for different mixes at 1 day, 7 days and 28 days were carried out, respectively. It is observed from the results shown in Fig. 3 that the difference in compressive strength between the mixes containing untreated rubber and NaOH pre-treated (less than 24 hours) rubber is rather modest. The 1 day compressive strength of CCSR20-N2h and CCSR20-N24h is 2.4% (0.2MPa) lower and 1.2% (0.1MPa) higher than REF, respectively. However, the value of CCSR20-SCA is 1.6MPa, namely, 19.3% higher than that of REF. The 7-day strength of CCSR20-N2h, CCSR20-N24h and CCSR20-SCA are 5.2% (1MPa) lower, 2.6% (0.5MPa) higher and 9.3% (1.8MPa) higher than REF, respectively. The 28-day strength was 2.2% (0.8MPa) lower, 0.8% (0.3MPa) higher and 6.8% (2.5MPa) higher, respectively. Those results suggest that the surface modification of rubber particles by SCA has a better effect on the improvement of the compressive strength than by saturated NaOH solution (less than 24 hours).

The above observation is also confirmed by the microscopic inspection and analysis of 28-day crushed cube samples. The rubber-matrix interface was inspected by a scanning optical microscopy. Detailed investigations on 10 rubber particles of each specimen were performed. Micrographs of typical fracture surfaces are shown in Figs. 4-6. Most fracture surfaces of REF specimens show that rubber particles seemed to be pulled-out. As shown in Fig. 4a, it is quite clear that there is a distinct crack highlighted with the white curve in Zone I. From the 3D image (Fig. 4b), significant discontinuity in Zone II was found. Faults and cracks observed at the rubber-matrix interface indicate that the untreated rubber-concrete matrix adhesion is poor. Similar phenomena are also found in the concrete samples of CCSR20-N2h and CCSR20-N24h, as shown in Fig. 5. No obvious difference is discovered after rubber was treated by NaOH. From the micrograph of CCSR20-N24h (Fig. 5b), it can be seen that two cracks initiate from the surface of the rubber particle. This may be ascribed to the lower stiffness of rubber as compared to the mineral aggregates. In the context, rubber particles behave as voids and a stress concentration usually arises at the interface between rubber particles and matrix. In the micrograph of CCSR20-SCA (Fig. 6), a well developed adhesive

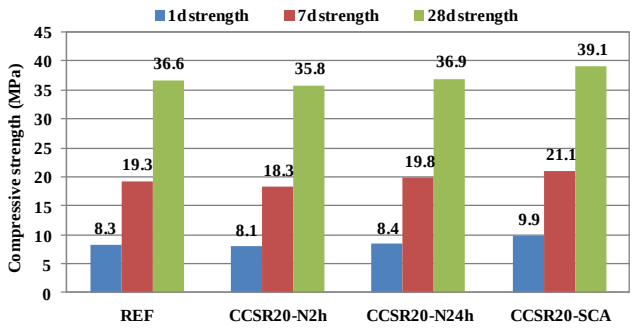

Fig. 3: *Compressive strength test results of all the mixes.*

joint section is observed between the SCA-treated rubber particles and the matrix, where the adhesion promoting agent has diffused to both substrate materials. From its 3D image, it can be seen that the transition zone between the rubber particle and concrete matrix is very smooth, in contrast to the counterpart of REF as shown in Fig. 4b, where a clean trough can be observed in Zone II. The observation for the CCSR20-SCA specimen suggests that there is a relatively strong bond at the interface. The mechanism illustrated above suggests that the nature of SCA enhances the bonding between organic and inorganic materials, leading to an improvement in compressive strength by nearly 20% at day 1. However, the enhancement of compressive strength at day 7 and day 28 days is only about 9% and 7%, respectively. A highest enhancement rate can be seen at the early age, indicating that the effect of SCA is more active when the concrete is weak.

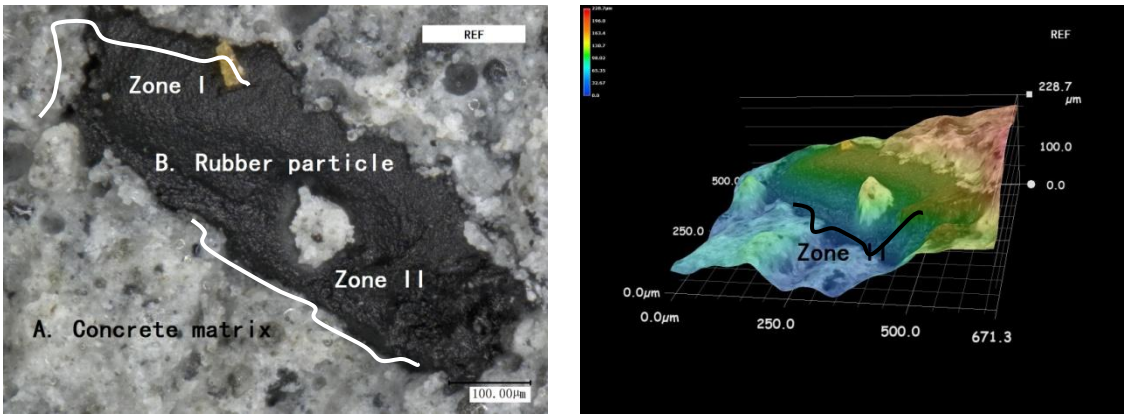

(a) rubber-matrix interface of REF *(b) 3D image of rubber-matrix interface of REF*

Fig. 4: *Rubber-matrix interface micrograph of (a) REF and (b) its 3D image.*

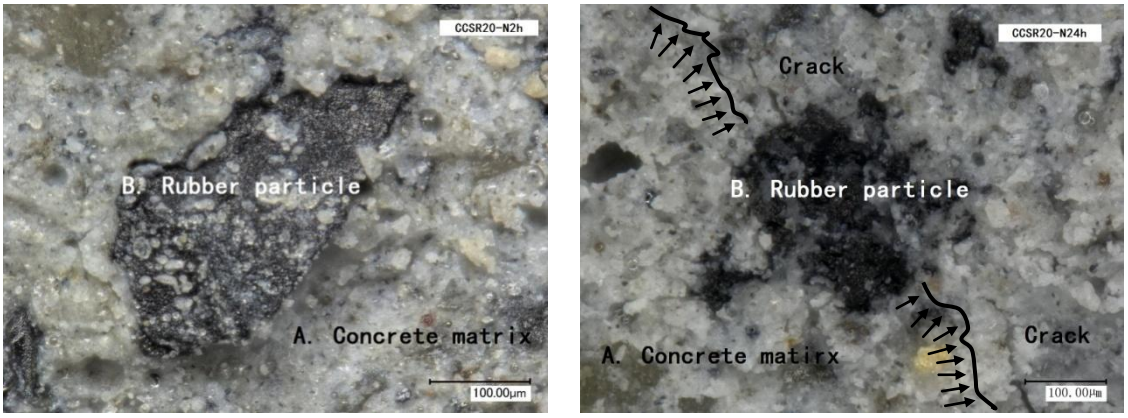

(a) rubber-matrix interface of CCSR20-N2h *(b) rubber-matrix interface of CCSR20-N24h*

Fig. 5: *Rubber-matrix interface micrographs of (a) CCSR20-N2h and (b) CCSR20-N24h.*

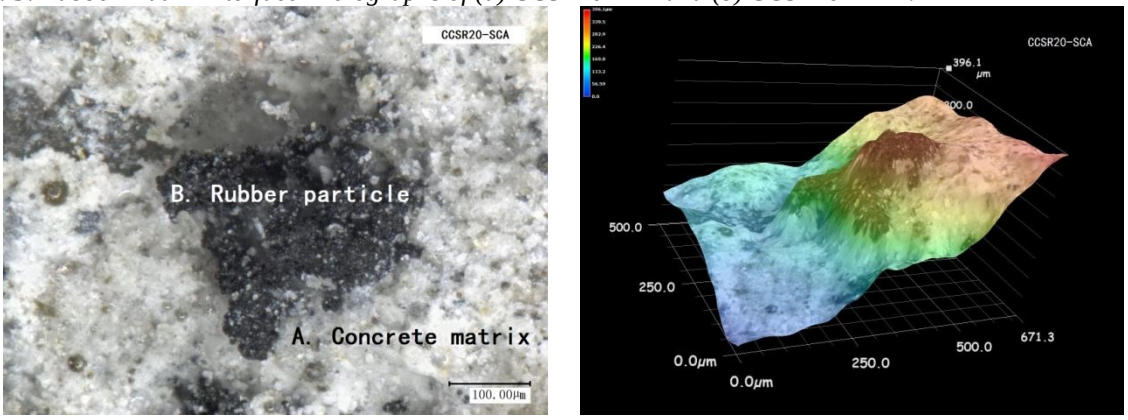

(a) rubber-matrix interface of CCSR20-SCA *(b) 3D image of CCSR20-SCA*

Fig. 6: *Rubber-matrix interface micrograph of (a) (CCSR20-SCA) and (b) its 3D image.*

SUMMARY

The main findings of this work include that the surface modification of rubber particles by saturated NaOH solution less than 24 hours does not produce significant changes on workability and compressive strength of the composites. The pre-treatment by SCA enhances the adhesion of tire rubber particles to cement matrix, as observed by scanning optical microscopy, resulting in the improvement of concrete compressive strength and reduction of concrete workability. Micrographs show that the transition area between SCA-treated rubber and cement matrix is better than untreated or NaOH-treated rubber.

ACKNOWLEDGEMENT

The financial support of the Institution of Structure Engineers (IStructE) research grant is gratefully acknowledged.

REFERENCES

[1] Nehdi M and Khan A. Cementitious composites containing recycled tire rubber: an overview of engineering properties and potential applications. *Cement Concrete and Aggregates*, 2001, 23(1): 3-10.

[2] Raghavan D, Huynh H and Ferraris CF. Workability, mechanical properties, and chemical stability of a recycled tyre rubber-filled cementitious composite. *Journal of Materials Science*, 1998, 33: 1745-1752.

[3] Albano C, Camacho N, Reyes J, Feliu JL and Hernandez M. Influence of scrap rubber addition to Portland I concrete composites: destructive and non-destructive testing. *Composite Structures*, 2005, 71(3-4): 439-446.

[4] Aiello M and Leuzzi F. Waste tyre rubberized concrete: properties at fresh and hardened state. *Waste Management*, 2010, 30(8-9): 1696-1704.

[5] Segre N, Joekes I. Use of tire rubber particles as addition to cement paste. *Cement and Concrete Research*, 2000, 30(9): 1421-1425.

[6] Yang J, Du Q and Bao YW. Concrete with recycled concrete aggregate and crushed clay bricks. *Construction and Building Materials*, 2011, 25(4): 1935-1945.

[7] Xanthos M. *Functional Fillers for Plastics*. Germany, Wiley-VCH, 2005.

PRODUCTION OF LIGHTWEIGHT FILLERS FROM WASTE GLASS AND PAPER SLUDGE ASH

C. Spathi
Department of Materials, Imperial College London, London, SW7 2BU, UK
Department of Civil and Environmental Engineering, Imperial College London, London, SW7 2BU, UK
charikleia.spathi10@imperial.ac.uk

L. Vandeperre
Department of Materials, Imperial College London, London, SW7 2BU, UK

C.R. Cheeseman
Department of Civil and Environmental Engineering, Imperial College London, London, SW7 2BU, UK

ABSTRACT: The production of lightweight fillers (LWFs) has been investigated using recycled glass and paper sludge ash (PSA). This represents a relatively high value re-use application for these two waste materials. Milled glass undergoes liquid-phase sintering in the temperature range where decomposition of calcium carbonate present in PSA occurs. The gas generated produces lightweight porous foamed glass particles suitable for use as LWFs. The effect of key process parameters such as PSA content, particle size of the raw materials and sintering conditions (temperature and time) have been studied and optimised. Processing glass containing 20 wt.% PSA at 800°C produces LWF particles with physical and mechanical properties comparable to leading commercially available products.
Keywords: Lightweight fillers, waste glass, paper sludge ash, liquid phase sintering.

INTRODUCTION

The production of lightweight fillers (LWFs) is a potential reuse application for recycled glass given that demand for lightweight and thermal insulating products is increasing. LWFs have low density and low water absorption and are typically supplied in sizes ranging from 0.1 to 4mm. They provide low-thermal conductivity and sound insulation in additional to lightweight and are used in a range of architectural products and other applications. Manufactured LWFs are normally formed by rapid sintering using components in the mix which decompose to produce porosity. Two requirements have to be met during sintering [1]:

- Evolution of gases from thermally instable constituents;
- Presence of a viscous liquid phase to encapsulate the gases.

Recycled glass can be used to form a viscous material. It has high silica content and an amorphous structure and has previously been used for the production of lightweight materials [2,3]. The high sodium oxide (Na_2O) and calcium oxide (CaO) content in soda lime silica glass lowers the sintering temperature, reducing the firing time and energy consumption [4].

Expanded glass particles can be produced by mixing finely ground glass with a suitable expanding agent and firing this mix at a temperature above the softening point of the glass where the viscosity is less than $10^{6.6}$ $N \cdot s \cdot m^{-2}$ [5]. Amongst various potential expanding agents, the use of paper sludge ash PSA has been investigated. This provides CO_2 from decomposition of calcium carbonate. PSA is currently used in the manufacture of construction blocks, as an animal bedding material and it is used on agriculture land as a liming agent, although significant quantities are also still landfilled [6]. The development of LWF manufactured from recycled glass and PSA would be a novel, added-value application for PSA.

In this work, glass-PSA LWFs were prepared and optimised. The physical and mechanical properties were determined and compared with commercially available products that are currently imported into the UK.

EXPERIMENTAL

Materials

Glass cullet

Mixed-colour glass cullet free of any significant contamination was used. It was ground by attrition milling for 60 s in 50g batches to produce a fine glass powder which was used in all the experiments. Chemical composition data for recycled glass were determined by X-ray fluorescence (XRF Spectro 2000 Analyser) as shown in Table 1.

Paper sludge ash

Paper sludge ash (PSA) was supplied by a major paper mill in South East England, producing newsprint from recycled paper. They use combustion in a fluidized bed boiler at 850 °C to manage waste paper sludge. The ash produced is a fine grey powder with pH~12. The chemical composition is presented in Table 1.

The particle size distribution of as-received PSA samples was determined by laser diffraction (Beckman Coulter LS-100). PSA has a d_{10} (10% by volume of particles having a diameter smaller than this size) of 23 μm, d_{50} (mean diameter) of 156 μm and d_{90} of 395 μm. The absolute density, excluding the pores between particles, was measured using a helium gas pycnometer (Micromeritics, AccuPyc II 1340, Georgia, USA) was 2.85 $g.cm^{-3}$.

Crystalline phases present in PSA were determined by X-ray diffraction (XRD, Philips PW 1830 diffractometer system with 40 mA and 40 kV, Cu radiation). As shown in Figure 1, the major crystalline phases present are gehlenite ($Ca_2Al_2SiO_7$), mayenite ($Ca_{12}Al_{14}O_{33}$), calcite ($CaCO_3$), calcium silicate (a'–Ca_2SiO_4), lime (CaO) and quartz (SiO_2). PSA particles are porous and heterogeneous as shown by the SEM micrographs in Figure 2. Separate grains form agglomerates as a consequence of combustion.

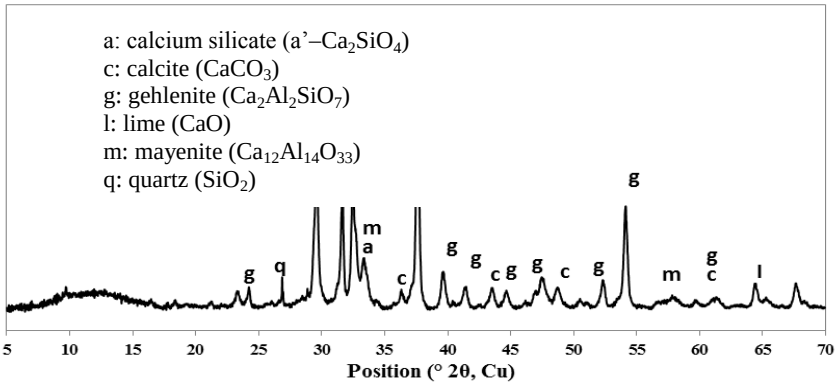

Fig. 1: *X-ray diffractogram of as-received paper sludge ash.*

Table 3. *Chemical composition of PSA and waste glass.*

	CaO	SiO_2	Al_2O_3	MgO	Fe_2O_3	K_2O	Na_2O	TiO_2	SO_3	P_2O_5	Others
PSA	61.2	21.2	12.6	2.8	0.9	0.4	nd	0.3	0.2	0.1	0.1
Waste glass	12.0	75.8	1.4	2.3	0.3	0.6	7.3	nd	0.2	nd	-

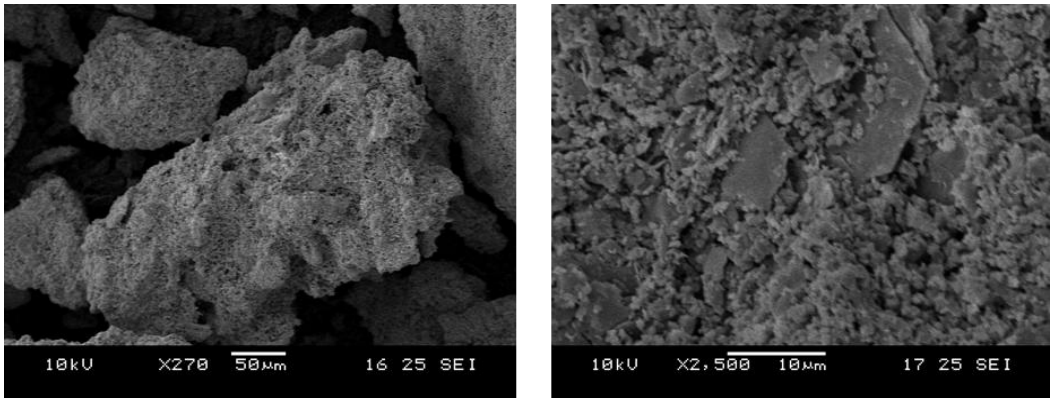

Fig. 2: *Scanning electron micrographs of PSA particles*

Characterisation of sintering behavior

The sintering behavior of recycled glass and PSA has been characterized using dilatometry (Netzsch 402E). Pressed glass and PSA samples were heated to 800 °C and 1400 °C respectively at a constant rate of 10 °C/min. Thermogravimetric analysis of PSA (Netzsch STA 449 F1 Jupiter®) used dried powder weighing ~35mg (rate of 10 °C/min).

Preparation of PSA-glass lightweight fillers (LWFs)

Milled recycled glass was mixed with various amounts (0-50 wt.%) of PSA by wet milling (Pascal Engineering ball mill) at a constant rate of 45 rpm for 1 hour using 19mm alumina balls as the milling media. 500g batches of raw materials were used with 1000mL of water with a solid: milling media ratio of 1: 5. Wet-milling resulted in thick slurry that was dried at 105 °C for 24 hours. The dried glass-PSA powder was manually ground using a pestle and mortar and sieved to <475 µm. Spherical particles were formed using a disc-pelletiser with the addition of 50% (w/v) water. Green pellets ranging in diameter from 0.5–4 mm were fired in a Carbolite rotary tube furnace. This had a 150 cm long tube with a 90 cm central heated zone. The speed of rotation was 10 rpm and it was kept horizontal to control the sintering time.

Characterisation of sintered products

The dry density of the sintered LWFs (apparent specific gravity) was determined using Archimedes Principle [7]:

$$\rho_{rd} = \rho_w \cdot \frac{m_{dry}}{m_{sat} - m_{imm}} \text{ g cm}^{-3},$$

where the dry mass is m_{dry}, immersed mass is m_{imm} and 24-h saturated surface-dry mass is m_{sat}. In order to ensure full saturation, samples were kept under water and under vacuum for 24 hours.

The water absorption (WA_{24}) was calculated according to the following formula:

$$WA_{24} = \frac{m_{sat} - m_{dry}}{m_{dry}} \times 100\%.$$

The compressive strength of LWFs produced was determined by loading a bulk amount of 3-4 g of LWFs between two parallel plates until 10% deformation is achieved. The confined compressive strength CS(10) was calculated using [8]:

$$CS(10) = \frac{F_{10}}{A},$$

where F_{10} is the load recorded at 10% deformation, and A is the area of the load distribution plate.

RESULTS AND DISCUSSION

Sintering properties of recycled glass and PSA

Dilatometer data for PSA and glass is presented in Figure 3 and thermogravimetric analysis for PSA is shown in Figure 4. Recycled glass powder exhibits shrinkage of 23.2% between 594°C and 664°C, which indicates the temperature range within which glass softening occurs. PSA has low reactivity as particles did not sinter together to form a rigid body and samples fell apart after heating to 1180 °C. TGA of PSA shows an initial weight loss between ambient and 120°C associated with the evaporation of residual water. Weight loss at higher temperatures is caused by thermal degradation of PSA. Weight loss between 600°C and 780°C is due to the decomposition of calcite ($CaCO_3$) to lime (CaO) with simultaneous generation of CO_2. Evolution of CO_2 within this temperature makes PSA a potential expanding agent for preparing foamed glass.

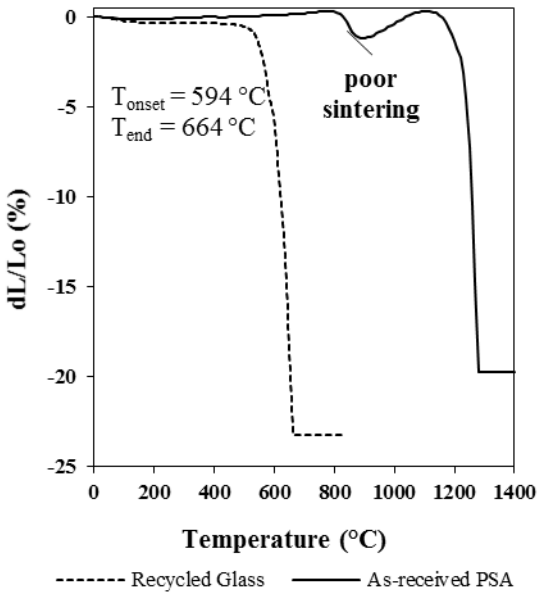

Fig. 3: *Dilatometer results for glass and PSA.*

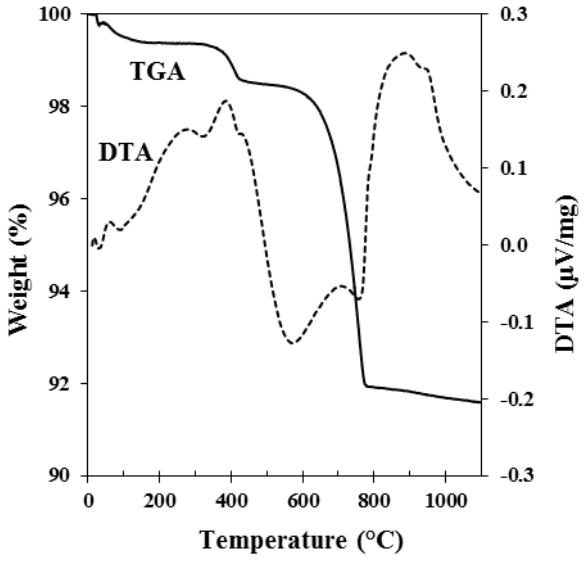

Fig. 4: *TGA and DTA results for PSA.*

Physical and mechanical properties of sintered products

The effect of PSA addition on density and water absorption of various glass-PSA mixes is shown in Figure 5 which also contains data for a commercial LWF.

Samples prepared with PSA additions up to 20% have similar or lower densities than 4mm commercial LWFs. However, further increases in the PSA content resulted in increased density. The optimum samples contained 80 wt.% glass and 20 wt.% PSA and these had a density of 0.75 g cm^{-3} and water absorption of 75%.

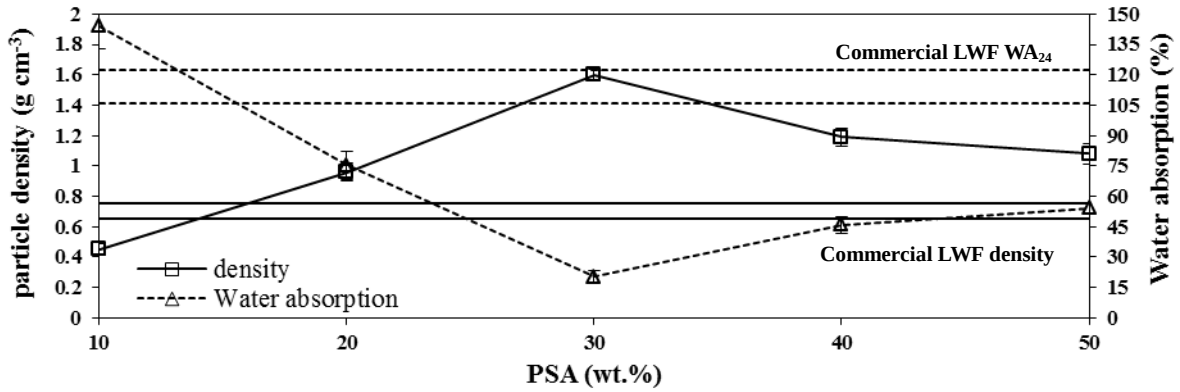

Fig. 5: *Effect of PSA addition on the density and water absorption of sintered glass-PSA pellets at 800 °C.*

The effect of sintering time on the 80/20 glass/PSA pellets fired at 800 °C is shown in Figure 6. Microstructural evolution can be described by four distinct stages: a) heating, b) glass softening/gas evolution, c) stabilisation and d) further densification. The optimum sintering time was 15 minutes with LWFs having a density of 1 g·cm^{-3} and WA of 17%. Microstructures of both optimum 80/20 glass/PSA LWFs and commercial LWFs are shown in Figure 7. This shows that a uniform distribution of approximately spherical pores with typical diameters of 50-150 μm is formed in glass/PSA pellets.

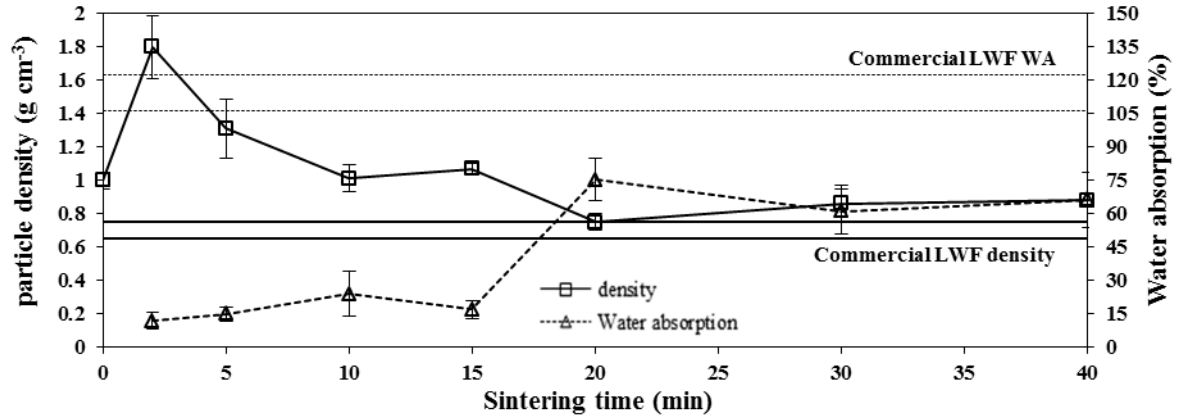

Fig. 6: *Effect of sintering time on density and water absorption of 80/20 glass/PSA mixes sintered at 800 °C.*

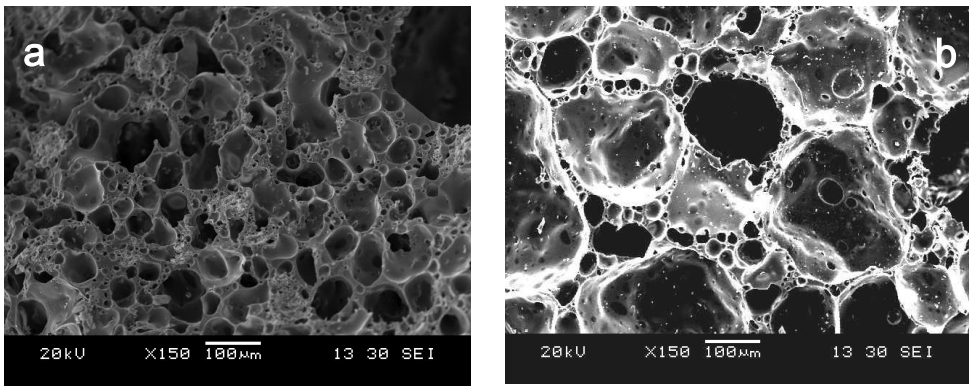

Fig. 7: *Morphology of optimum LWFs tested: a) Fracture surfaces of 80/20 glass/PSA LWFs sintered at 800 °C for 15 min. b) Commercial LWF.*

The confined compressive strength CS(10) for 80/20 glass/PSA LWFs sintered at 800 °C for 15 minutes with a diameter of 1-2 mm and 2-5 mm are compared against commercial

LWFs in Table 2. Artificial glass-based LWFs with 20% addition of PSA have consistent mechanical properties regardless of the LWF size.

Table 2. *Mechanical properties of 80/20 glass/PSA LWFs and commercial LWFs.*

Sample ID	CS(10) (MPa)
Commercial LWF 1-2 mm	1.3
80/20 glass/PSA LWFs 1-2 mm	2.9
Commercial LWF 2-5 mm	1.1
80/20 glass/PSA LWFs 2-5 mm	2.9

CONCLUSIONS

A glass-PSA system can form foamed materials using simple processing technology involving wet milling, pelletising and low temperature sintering. Glass provides a low-viscosity phase that encapsulates CO_2 evolving from PSA particles. Lightweight fillers containing 80% glass and 20 wt.% PSA sintered at 800 °C for 15 minutes have density of 1 g cm^{-3} and water absorption of 17% compared to 115% for the commercial LWFs tested. The crushing strength is 2.9 MPa and this is three times higher than values for typical commercially available LWF.

REFERENCES

[1] Wei Y-L, Lin C-Y, Ko K-W and Wang H.P. Preparation of low water-sorption lightweight aggregates from harbour sediment added with waste glass. *Marine Pollution Bulletin*, 2011, 63: 135-140.

[2] Ducman V, Mladenovic A and Suput J S, Lightweight aggregate based on waste glass and its alkali-silica reactivity. *Cement and Concrete Research*, 2002, 32: 223–226.

[3] Kourti I and Cheeseman C R. Properties and microstructure of lightweight aggregate produced from lignite coal fly ash and recycled glass. *Resources, Conservation and Recycling*, 2010, 54: 769-775.

[4] Karamberi A and Moutsatsou A. Participation of coloured glass cullet in cementitious materials. *Cement and Concrete Composites*. 2005, 27: 19–27.

[5] Kingery W D, Bowen H C and Uhlmann D R. *Introduction to Ceramics*, 2nd Edition, John Wiley and Sons, New York, 1976.

[6] WRAP. *Paper Sludge Ash: A technical report on the production and use of paper sludge ash*, Environment Agency, UK, 2007.

[7] British Standards Institution. Lightweight aggregates. Part 1: Lightweight aggregates for concrete, mortar and grout. BS 13055-1:2002. BSI, London, 2002.

[8] British Standards Institution. *Tests for mechanical and physical properties of aggregates*. BS 1097-11:2013. BSI, London, 2013.